Dynamiques de synchronisation de lasers bifréquence à état solide et DFB soumis à une réinjection décalée en fréquence : applications en photonique micro-onde

Aurélien Thorette

UNIVERSITE MATIERE BRETAGNE MOLECULES LOIRE ET MATERIAUX

UNIVERSITÉ DE RENNES 1

THESE DE DOCTORAT DE

L'UNIVERSITE DE RENNES 1
COMUE UNIVERSITE BRETAGNE LOIRE

ECOLE DOCTORALE N° 596
Matière, Molécules, Matériaux
Spécialité : « *Physique* »

Par **Aurélien THORETTE**

Synchronization dynamics of dual-mode solid-state and semiconductor DFB lasers under frequency-shifted feedback. Applications to microwave photonics.

Unité de recherche : **Institut FOTON / DOP**

Thèse soutenue à Rennes le 30 novembre 2018
devant le jury composé de :

Hervé GILLES, *président*	Professeur, ENSICAEN
Stéphane BLIN, *rapporteur*	Maître de conférences, Université de Montpellier 2
Frédéric GRILLOT, *rapporteur*	Professeur, Telecom ParisTech
Giovanna TISSONI, *examinatrice*	Maître de conférences, Université de Nice-Sophia Antipolis
Frédéric VAN DIJK, *invité*	Ingénieur, III-V Lab Palaiseau
Marc VALLET, *co-directeur de thèse*	Professeur, Université de Rennes 1
Marco ROMANELLI, *co-directeur de thèse*	Maître de conférences, Université de Rennes 1

Remerciements

La grande qualité de l'environnement de travail dans lequel j'ai évolué durant ces trois années de thèse doit beaucoup à la présence constante et aux échanges scientifiques quotidiens que j'ai pu avoir avec mes directeurs, Marco Romanelli et Marc Vallet (ex-æquo). Je me suis rendu compte au fil des rencontres avec d'autres thésards de tous horizons qu'il est finalement bien rare de bénéficier d'un encadrement d'un tel acabit.

Entre les lignes de cette thèse, il faut aussi voir la compétence de très haut niveau, et plus généralement la patience et la pédagogie des électroniciens Ludovic Frein et Steve Bouhier, et de l'ingénieur ès fibres optiques, Goulc'hen Loas. J'y associe également Anthony Carré pour la partie optique et informatique, et Cyril Hamel pour la mécanique. Marc Brunel mérite une mention particulière, pour avoir gardé une attention sur ces travaux, et pour sa disponibilité à discuter des problèmes rencontrés.

Une partie du matériel utilisé est issu du projet EDA HIPPOMOS, dont je remercie les différents partenaires pour les composants uniques dont j'ai pu bénéficier. Sur ce volet, je me contenterais de mentionner que les efforts de Mehdi Alouini y sont pour beaucoup.

Marie Guionie a droit à sa propre phrase complète, au titre de collègue de bureau presque agréable, stagiaire M2 efficace, et grande cheffe de Pint of Science à Rennes, qui fut une belle expérience. J'en profite pour en saluer les autres participants.

Dans le désordre, salutations amicales aux collègues du DOP : Julien, François P. Romain, François B., John, Kévin, Gwennaël, Gaëlle, Hongzhi, ainsi qu'à ceux que je n'ai que brièvement croisés et que j'oublie peut-être : Swapnesh, Nolwenn, Céline, Noé, Tron, Esteban, Tore, Ayman, Emmanuel, ...

Cette thèse s'est achevée à l'Institut FOTON et a débuté au sein de l'Institut de Physique de Rennes (IPR). J'adresse donc une salutation globale aux collègues des deux instituts, notamment aux personnels administratifs, et aux chercheurs que j'ai pu rencontrer lors de mon expérience d'enseignement. J'adresse un remerciement plus particulier à Guillaume Raffy, Alexandra Viel et Jérémy Gardais de l'équipe SIMPA, pour m'avoir prêté jusqu'au bout du temps de calcul, et apporté le soutien technique associé.

Enfin, je remercie Fréderic Grillot et Stéphane Blin d'avoir accepté de rapporter ces travaux, Hervé Gilles d'avoir bien voulu présider le jury, Giovanna Tissoni en qualité d'examinatrice, et Frédéric Van Dijk pour sa présence lors de la soutenance.

RÉSUMÉ DES RÉSULTATS

CE manuscrit présente des travaux effectués autour de la problématique de synchronisation en phase de deux lasers. Plus précisément, est étudiée une méthode appelée réinjection décalée en fréquence, qui vise à obtenir le verrouillage sur une référence de la différence de fréquence entre deux lasers. En pratique, cette différence de fréquence se situant dans le domaine micro-onde, ces travaux sont à l'intersection de la dynamique des lasers et de la photonique micro-onde.

LE PREMIER CHAPITRE est introductif et vise à rappeler les principes fondamentaux et les équations de base régissant la dynamique de lasers de classe B. Une dérivation des "rate equations" standards est proposée. Une partie est consacrée plus précisément au facteur de Henry (α), en raison de sa grande influence lors de l'étude de dynamiques sous injection. Sa définition est rappelée, et est poursuivie par une brève revue des différentes méthodes permettant de le mesurer. Disposant de ces éléments, quelques résultats élémentaires sont rappelés pour le cas d'un laser injecté, et d'un laser soumis à une rétroaction (feedback). Les concepts de bifurcations, de plage d'accrochage, de modes de cavité externe sont présentés. La suite du chapitre permet de présenter le contexte de la photonique micro-onde, et notamment la technique de génération hétérodyne, c'est-à-dire utilisant le battement entre deux fréquences optiques comme source de fréquence dans le domaine micro-onde. Les avantages de cette approche et les difficultés rencontrées sont énumérés, en aboutissant au besoin d'une stabilisation supplémentaire du battement. Une revue des techniques existantes est présentée, en insistant particulièrement sur le fort intérêt qu'il y a à générer les deux fréquences optiques dans un unique laser. Une option, le laser bipolarisation bifréquence, utilise la levée de dégénérescence des modes de polarisation d'une cavité laser pour générer deux modes orthogonaux de fréquences différentes. Les résultats existants sur ce type de configuration sont rappelés.

LE SECOND CHAPITRE porte sur l'application de la méthode de stabilisation par réinjection décalée en fréquence à un laser bipolarisation à état solide Nd:YAG. Il s'agit de réaliser une injection optique d'un mode de polarisation du laser sur l'autre. Or, une injection résonante n'est possible que pour un faible désaccord de fréquence entre le champ injecteur et celui de la cavité. Une étape de décalage en fréquence, utilisant ici un modulateur acousto-optique est donc utilisée. De plus, la séparation en polarisation des deux modes permet une injection unidirectionnelle.

Lorsque le désaccord de fréquence est faible, ou que l'injection est forte, un

verrouillage de phase entre les modes est observé. Il correspond à un report complet de la stabilité de la référence (ici, le signal de décalage) sur le battement laser. Un modèle basé sur des rates equations est présenté, incluant les termes d'injection et de saturation croisée liés au fonctionnement bipolarisation. Ce modèle, sous une forme normalisée, est à la base de l'étude numérique. L'étude des bifurcations de l'état stationnaire permet en effet d'identifier, outre la zone d'accrochage de phase, une zone de verrouillage partiel. Dans cette région, un régime de phase bornée est observé numériquement et expérimentalement. Il correspond à un verrouillage de la fréquence moyenne, malgré des oscillations d'amplitude et de phase. Une étude numérique plus exhaustive est menée pour les cas de faible injection, pour lesquels de nombreux régimes chaotiques existent. On peut ainsi mettre en évidence un régime particulier, combinant des propriétés de phase bornée et des fluctuations chaotiques. Ce régime dit de chaos borné est également observé expérimentalement. L'étude du bruit de phase montre qu'il s'agit toujours d'un régime de synchronisation moyenne forte.

D'autres études sont menées autour de ces zones de faible injection. Premièrement, un retard est ajouté dans le bras de réinjection sous la forme d'une bobine de fibre. On montre que pour des retards correspondant à quelques périodes des oscillations de relaxation, une réduction de la plage d'accrochage est observée, ainsi qu'une dégradation du bruit de phase. D'autre part, un mécanisme de type excitabilité est mis en évidence sur les bords de la plage d'accrochage. On peut en particulier conserver le caractère borné de la phase pendant le déclenchement d'un événement. Enfin, les études précédentes ont été reproduites pour plusieurs valeurs du coefficient de saturation croisée β et du facteur de Henry α.

Ce dernier facteur, rarement pris en compte dans les lasers à état solide, a en effet été ajouté dans le modèle pour rendre compte d'observations expérimentales. Les asymétries observées sur la plage d'accrochage, et notamment la différence de type de décrochage observé en fonction du signe du désaccord, sont en effet un marqueur typique d'un facteur α non nul. Une méthode de mesure ad-hoc de ce coefficient a été développée, en tirant partie d'une légère modification du dispositif expérimental. L'introduction d'une perturbation de phase par injection optique se reporte sur l'intensité de sortie via le couplage phase-amplitude lié à α. Or, il existe une valeur critique du désaccord pour laquelle ce n'est pas le cas. La mesure de celle-ci permet de remonter à α. La mise en œuvre de cette méthode «FM/AM» se réduit dans notre cas à introduire une modulation de fréquence sur le signal de référence. À l'aide du modèle, on obtient ainsi une mesure précise et originale $\alpha = 0.28 \pm 0.04$.

Finalement, cette méthode de stabilisation par réinjection décalée en fréquence a aussi été appliquée à un autre type de laser bipolarisation, un laser fibré de type

DFB. Dans ce début d'étude, nous avons constaté que le verrouillage est possible et robuste, mais que le facteur de Henry probablement plus élevé mène à des formes plus complexes de la plage d'accrochage.

LE CHAPITRE III est consacré à la transposition de cette méthode de réinjection décalée en fréquence à un système plus proche des applications potentielles. Il s'agit cette fois de deux lasers semi-conducteurs distincts, de type DFB, situés sur une même puce. Ces composants originaux sont développés et produits par le III-V Lab, en tant que générateurs hétérodyne pour des applications télécom, radar, etc. Dans cette optique, ils présentent une faible largeur de raie, autour de 300 kHz ainsi qu'une large bande passante de modulation. Leur accordabilité est large, et dans notre cas, nous utilisons un battement de 10 GHz entre les deux lasers.

Afin de verrouiller en phase ces deux lasers, une boucle fibrée de réinjection décalée en fréquence est réalisée, incluant un modulateur d'intensité. L'utilisation de ce dernier, motivée par les hautes fréquences à atteindre, a pour conséquence un mécanisme de couplage plus complexe que précédemment entre les deux lasers. En effet, chaque laser est injecté optiquement par l'autre laser, mais il subit aussi son propre feedback. De plus, ces lasers ayant des temps caractéristiques rapides (de l'ordre de la nanoseconde), le temps de parcours dans la boucle de feedback ne peut être négligé, ce qui nous met en présence de dynamiques à retard long. Néanmoins, nous montrons expérimentalement, mais aussi numériquement que le verrouillage de phase est possible. Un modèle numérique basé de type "rate equations" a en effet été développé pour décrire le couplage retardé entre les lasers. À cette fin, une bonne connaissance des paramètres du système est nécessaire. Ainsi une caractérisation poussée des lasers a-t-elle été réalisée, notamment les différents temps de vie (obtenus par l'intermédiaire d'une mesure de la fonction de transfert en modulation) et le facteur de Henry (obtenu par une méthode d'injection optique statique).

Outre le régime de verrouillage de phase, qui permet, comme dans le cas du laser bipolarisation, de transférer la pureté spectrale de la référence vers le battement, des régimes de synchronisation partielle sont observés expérimentalement et numériquement. À la différence du cas bipolarisation, on observe un morcellement de la zone de stabilité en fonction du désaccord, qui forme des « bandes d'accrochage ». La périodicité de ces bandes est reliée à la fréquence de la cavité externe, c'est-à-dire au retard. Cette alternance de zone de verrouillage, avec des zones de décrochage ou de synchronisation partielle, type phase bornée, a pu être observée très nettement que ce soit expérimentalement et numériquement.

Parmi les nombreux paramètres présents dans ce système, les phases optiques liées à chaque terme de couplage ont fait l'objet d'une attention particulière. En effet, ces paramètres sont mal contrôlés expérimentalement, et peuvent être sujets à de fortes

dérives. Or leur valeur peut changer de façon importante l'état stationnaire atteint par le système. C'est pourquoi nous avons étudié numériquement l'influence de ces phases optiques sur l'état final du système, et ce en fonction des différents taux de couplage, ainsi que pour différents retard. Il apparaît qu'il est possible de minimiser l'influence de ces paramètres sur le régime verrouillé en privilégiant l'injection croisée entre les lasers et en minimisant le feedback pour chacun d'entre eux. D'autre part, il semble que la présence d'un retard long permette également de diminuer l'influence de ces phases.

DANS LE CHAPITRE IV, le système précédent est réutilisé, mais dans une configuration « boucle fermée », c'est-à-dire en s'affranchissant de la référence externe. Un retard, sous la forme d'une bobine de fibre, est utilisé pour verrouiller le battement sur lui-même. En ajoutant un filtre passe-bande électrique dans cette boucle résonante, on obtient une configuration assez similaire ce qui est couramment connu sous le nom d'oscillateur opto-électronique (OEO). À la différence de ces montages, qui se basent habituellement sur un modulateur d'intensité, notre signal de sortie contient uniquement les deux fréquences optiques associées à chaque laser. Cette propriété, dite de bande latérale unique, rend le taux de modulation du signal insensible à la dispersion chromatique, et donc approprié à la transmission dans une longue liaison fibrée.

Ce montage expérimental, réalisé sans grande isolation de l'environnement, permet d'obtenir de bonnes performance de bruit de phase, jusqu'à $-95\,\mathrm{dBc/Hz}$ à $10\,\mathrm{kHz}$ de la porteuse à $10\,\mathrm{GHz}$. Le bruit de phase présente les caractéristiques typiques d'un OEO : décroissance en basse fréquence relative, puis pics de résonances liés au retard utilisé. Ces derniers peuvent être réduits en utilisant des techniques issues des développements sur les OEO. Par exemple, nous avons montré l'efficacité d'un schéma basé sur deux retards différents formant un interféromètre dans le domaine micro-onde.

Finalement, la présence d'une longue cavité externe dans le système de réinjection décalée en fréquence impose l'usage d'un filtre RF sur-mesure, avec une bande passante particulièrement faible. Cette contrainte peut être levée en réduisant la cavité externe. Nous avons développé un système beaucoup plus compact, qui utilise une simple réflexion comme cavité externe, et une faible modulation directe du courant de pompe d'un des lasers comme mécanisme de décalage en fréquence. On peut dès lors utiliser un filtre RF beaucoup plus standard, et obtenir, avec un montage très simple, un signal optique micro-onde quasiment à bande latérale unique.

Dès lors, de nombreuses perspectives apparaissent, comme l'intégration du modulateur, voire du retard sur le composant, chose qui a déjà été réalisée au III-V Lab. Enfin, l'utilisation du modèle développé au chapitre III peut permettre de réaliser une

analyse plus quantitative du système pour guider son amélioration.

EN CONCLUSION, cette étude de la réinjection décalée en fréquence dans deux cas différents permet de mettre en avant les propriétés globales de cette méthode de couplage entre deux lasers, ou deux modes du même laser. L'influence d'un grand nombre de paramètres a été étudiée, que ce soit pour le régime de verrouillage, ou pour des régimes de synchronisation partielle. La combinaison d'études expérimentales et numériques a permis de garder une perspective résolument tournée vers les applications et la caractérisation des performances, sans pour autant négliger l'étude de la dynamique et des régimes instables. La versatilité de cette technique et la bonne compréhension de son fonctionnement amène finalement à envisager des développements futurs pour d'autres types de lasers, que ce soit dans des milieux actifs différents (Erbium, fibre, semiconducteurs multifonctionnalités) ou encore pour des fonctionnements multimodes.

TABLE OF CONTENTS

Table of symbols **15**

General introduction **17**

I Introduction to injection and feedback in lasers, and to microwave photonics **21**

1 Dynamical modeling of class-B lasers 21

1*a* The laser rate equations 21

Evolution of the field 22

Population inversion 25

Rate equations and their properties 26

1*b* The linewidth enhancement factor α 29

Definition, consequences and typical values 29

How to measure it? 30

2 Interaction dynamics and their usages 32

2*a* Injection and synchronization 32

The Adler equation 33

Beyond the Adler equation 34

2*b* Feedback in lasers 36

Lang-Kobayashi equation and external cavity modes . . 37

3 Microwave photonics 39

3*a* Characteristics of a microwave signal 40

3*b* Dual-frequency lasers 42

Heterodyne microwave generation 42

Dual-polarization lasers 43

4 Conclusions 46

II Frequency-shifted feedback in dual-frequency solid state lasers **47**

1 Dual-frequency dual-polarization laser 47

Frequency separation 48

Pump diode 49

2 Frequency difference locking using feedback 50

2*a* Experimental setup 51

2*b* Rate equations model 52

Analytical study 54

2*c* Coupling coefficient β 55

3 Results . . . 58
3a Locked state, bounded phase . . . 58
Steady state and bifurcation diagram . . . 58
Bounded phase oscillations . . . 60
3b Exhaustive mapping for $\Gamma \lesssim 1$ . . . 61
4 Bounded phase chaos . . . 65
Numerical prediction . . . 65
Experimental observation . . . 66
Phase noise properties . . . 67
4a Influence of the feedback delay . . . 69
4b Bounded chaotic "spike triggering" (excitable-like) . . . 73
4c Arguments in favor of a non-zero α . . . 77
4d Alternate results for $\alpha = 0$ and $\beta = 0.6$ . . . 79
5 Application to the measurement of the small linewidth enhancement factor . . . 82
5a Theory . . . 82
5b Dual-frequency laser . . . 84
5c Result for Nd:YAG bulk laser . . . 87
6 Fiber laser . . . 89
7 Conclusions . . . 94

III Synchronization and complex dynamics of two coupled semiconductor lasers 95
1 The dual-DFB component . . . 95
1a Tunability . . . 98
1b Frequency stability . . . 99
1c Linewidth . . . 100
1d Lifetimes measurements . . . 102
Principle . . . 102
Results . . . 104
1e Linewidth enhancement factor . . . 104
Principle . . . 105
Experimental realization . . . 107
Results . . . 108
2 Setup and model for frequency-shifted feedback . . . 110
2a Experimental setup . . . 110
2b Delayed rate equations . . . 111
Resonant approximation and the relevant terms . . . 111
Rate equations and normalization . . . 112
Injection rates . . . 114
Summary of the parameters . . . 115
Estimating the drift of the feedback phases . . . 116
2c Analytical considerations . . . 117

2*d* Injection rate estimation 118
2*e* Modulation ratio 120
3 Comparison of numerical and experimental results 120
3*a* Observed regimes 121
Experiments 121
Simulations 122
"Full" model simulations 123
3*b* Multistability 124
3*c* Phase dependency 125
3*d* Influence of frequency detuning: locking range 127
3*e* Locking bands 129
3*f* Overall stability and phase noise 130
4 Conclusions 132

IV Hybrid opto-electronic oscillator **135**
1 The opto-electronic oscillator 135
1*a* Principle 135
1*b* Phase noise 137
1*c* Dispersion losses in long fiber links 138
2 Long-delay setup 139
2*a* Setup 140
2*b* Performances and challenges 141
2*c* Dual-loop 143
3 Shorter delays, towards integration 145
3*a* Straight feedback and direct modulation 145
4 Transfer functions: towards a full model of the hybrid OEO. 149
4*a* On-chip feedback 151
5 Perspectives 153

Conclusions and perspectives **155**

Annexes **159**
A Eigenstates of a cavity with two quarter-wave plates 159
B Estimation of α from gain asymmetry 162
C Coupling factor β for an non-isotropic pumping 165
D Comparison of integrators for phase noise calculation 169
E A Python wrapper for the DDE integrator RADAR5 171

Associated publications **173**

References **175**

TABLE OF SYMBOLS

Through this work, for a variable x, $\widehat{x}$ denotes the associated steady-state value. The symbol i is used for the imaginary unit without exception, while j is used for indexing.

The following global notations are used in different places through the document. The more local notations, used a few times in a single section, are not included in this table.

c	Speed of light in the vacuum.
E	Complex amplitude of the slowly-varying electric field.
E_{inj}	Complex amplitude of the injected field.
$\mathcal{E}_j$	Complex electric field.
f_0	Reference microwave frequency.
f_{AO}	Driving frequency for the acousto-optic modulator.
f_M	Frequency modulation frequency.
$f_R^{(j)}$	Relaxation oscillations frequency (possibly of laser j).
g	Normalized laser gain.
G	Amplifier gain.
I	Optical intensity (Chapter I) or power (Chapters II to IV).
$\mathcal{I}, \mathcal{Q}$	In-phase and quadrature components of a demodulated signal.
K	Feedback or injection strength.
ℓ	Cavity length.
$\mathcal{L}$	Phase noise (in dBc/Hz).
L	Feedback length (Chapter II and III). Fiber coil length (Chapter IV).
m	Modulation ratio associated to the Mach-Zehnder modulator.
n	Optical index of the active medium (Chapter I), or of the fiber (Chapter II to IV).
N	Difference of population inversion density from the threshold level.
$\mathcal{N}$	Population inversion density.
$\mathcal{N}_{\text{th}}$	Population inversion density at laser threshold.
P	Pump term. In the case of semiconductor lasers, pump current.
$\mathcal{P}$	Electric polarization of the active medium.
q	Ratio of the field transmissions of the output coupler.

r Pumping ratio.
R_p Pumping rate.
$R_{\mathrm{p,th}}$ Pumping rate at laser threshold.
s Normalized time, related to the relaxation oscillations pulsation.
S_φ Phase noise (in dBrad^2/Hz).
t_0 Field transmission coefficient for the modulator.
$t_{1,2,C}$ Field transmission of the output coupler for each laser, or for one of them.
T Feedback delay.
X Demodulated beatnote amplitude.

α Linewidth enhancement factor.
β Cross-saturation coefficient.
Γ Normalized injection rate.
Δ, δ Normalized frequency detuning.
Δ_0 Mean detuning (Chapter II). Half-width of locking range (Chapter III)
Δ_m Mean detuning of minimal amplitude response (Chapter II).
Detuning of unchanged intensity output (Chapter III).
$\delta\nu$ Frequency detuning.
$\Delta_{+,-}$ Normalized locking range boundaries.
ε Damping coefficient.
η Effective pumping ratio.
θ Angle of a quarter-wave plate, either in the cavity or for the pump (Chapter I).
Phase difference between the two lasers (Chapter III).
κ Normalized feedback strength.
λ Laser wavelength.
$\nu_{x,y,1,2}$ Optical frequency of mode x/y, or of laser 1/2.
τ Normalized feedback delay (Chapters I, II and III). Opto-electronic delay, unnormalized (Chapter IV).
τ_c Carrier lifetime (even for solid-state lasers), related to the decay of population inversion.
τ_p Photon lifetime, related to cavity losses.
χ, χ_r, χ_i Electric susceptibility of the active medium, and its real and imaginary part respectively.
φ Phase of the electric field under injection (Chapter I).
Phase difference between the two modes (Chapter II).
$\varphi_{1,2,x}$ Optical feedback phases (Chapter III).
ϕ Output phase of the microwave signal (Chapter IV).
ψ Phase of the injected field.
ω Pulsation of the monochromatic field under study.
ω_0 Resonant optical pulsation of the cavity.
Ω Pulsation of the external cavity mode (except in IV.1c).

GENERAL INTRODUCTION

THE first lasers appeared in the early 60s, from a series of experimental and theoretical advances. While the theoretical background was already there, most notably due to Einstein [Einstein17], the experimental breakthrough came from first realization of microwave-domain masers by Gordon, Zeiger and Townes [Gordon55]. The latter, along with Schawlow, then predicted that a similar device, but operating in the visible spectrum could be made [Schawlow58]. The same suggestions were made by Basov and Prokhorov [Prokhorov58], and it was not long since the first laser was indeed realized by Maiman using a crystal of ruby [Maiman60]. At that time, the booming of researches on semiconductors and the premises of the associated industry quickly allowed the fabrication of semiconductor-based lasers [Basov61; Hall62; Nathan62]. Ever since then, they have become ubiquitous, and an integral part of many consumer systems or research equipment.

While lasers have completely revolutionized optics, they also made their way into almost every field of science and technology. To illustrate this, we will cite only two very different examples. First, we cannot but admire the success of fiber-optics communication networks, which use laser diodes as transmitters, and allow for ever-rising transfer speed and volumes [Agrawal02]. Second, the recent detection of gravitational wave signals with the LIGO and VIRGO detectors [Abbott16] has been made possible also thanks to the ultrastable solid-state lasers at the core of the giant interferometers [Bondu96; Acernese09].

While these two examples seem quite remote from each other, they were chosen to illustrate the vast area in which this thesis takes places, namely the stabilization of lasers, or even more generically the dynamics of lasers. Indeed, the evolution of telecommunication systems or the increasingly finer metrology experiments require even more stable lasers, or lasers with particular behaviors.

This very wide problem has attracted a lot of attention and generated countless developments. Putting aside pulsed regimes such as mode-locked lasers, for which considerable efforts have been made [Udem02], and focusing only on continuous-wave lasers, many solutions have been proposed and successfully applied. For inten-

sity stabilization, the most common are based on “noise-eating” electronic feedback loops, which use a measurement on the laser’s output and a counter-reaction on one of its parameter, such as pump or temperature. For frequency stabilization, it is common to use the interaction with a frequency etalon, such as the absorption by a molecular transition in a gas cell, or the reflection from a Fabry-Perot cavity. The most prominent example of this is the Pound-Drever-Hall method and its variations [Drever83]. A different scheme uses the optical locking of the laser on an external cavity, such as a Fabry-Perot resonator [Salomon88] or a long fiber [Kéfélian09]. This is usually obtained by allowing a certain level of feedback from the external resonator into the laser.

In this work, we will focus on a subset of laser stability problem: rather than the absolute stabilization of a laser, we will study a method that allows to stabilize the frequency difference between two lasers. This frequency difference corresponds to a beatnote usually falling in the microwave domain. Thus, our work falls at the intersection between optics and the high-frequency electronics needed to process these beatnotes. This quite new domain called *microwave photonics*, arises partly from the fact that large microwave frequencies, i.e. over 10 GHz, are sometimes much easier to handle, generate, transport or process when placed on an optical carrier, rather than on a coaxial cable [Yao09].

Among the most obvious problems addressed by microwave photonics are the “radio-over-fiber” cases, for instance in high-speed telecommunications, or antenna remoting for wireless systems such as radar [Xu14] or radioastronomy [Montebugnoli05].

The generation of microwave signals can also benefit from interactions with optics. Indeed, it is well known that the higher the frequency, the harder it is to generate it with conventional methods. This applies in terms of complexity, cost, and output signal quality [Rohde14]. For all these points, the use of optical beatnotes shines as an attractive alternative. Indeed, such *heterodyne methods* are conceptually simple and inherently widely tunable with few frequency-dependent noise.

To illustrate this, one of the main interests of such heterodyne methods is that very high frequencies, often barely reachable with all-electronic techniques can be obtained [Rolland14]. For instance, fast progresses in the the field of terahertz waves [Tonouchi07] and their potential applications in biology [Pickwell06], defense [Davies08], chemistry [Mouret13] or wireless communications [Federici10] drive the search for tunable and high-quality sources.

However, heterodyne methods suffer from the fact the fluctuations of each laser’s wavelength and amplitude are reported on the beatnote. Thus, stabilization techniques have to be applied, and no standard, widely usable method has arisen yet.

Methods derived from the stabilization of a single laser can be used, by applying them on the two sources [Day92; Hallal16]. Otherwise, sole stabilization of the beatnote can be obtained using similar methods, based on feedback loops and locking on an external reference [Alouini01; Rolland11b].

The optical frequencies involved in the generation of the beatnote can be obtained from either two different lasers, or from multiple modes of a laser. For instance, optical frequency combs are commonly used [Fortier11]. In our lab, we develop and propose another approach: we generate the two frequencies from a single laser, that functions on its two orthogonal polarization axes. Such *dual-polarization dual-frequency* lasers [Bretenaker90] have interesting properties in terms of tunability and free-running stability, that led to some achievements in terms of THz beatnote generation [Alouini98; Brunel04; Danion14] and optically-carried high-purity microwave signals [Pillet08]. Stabilization techniques have been developed for these lasers, with extensions towards very high frequency beatnotes [Rolland11a]. More details on the properties of dual-polarization lasers, along with a quantitative description of some realizations will be given in Chapter I.3*b*.

We see here that a lot of stabilization techniques are based on a mechanism of controlled optical feedback or injection. However, in the history of the laser, injection and feedback have not always been seen as stabilizing features. On the contrary, feedback is often seen as destabilizing [Henry86], and so can be an external injection [Tredicce85]. The experimental observations, combined with numerical models of such phenomena form the raw material of a field known as *laser dynamics*. The viewpoint here is to consider lasers under different couplings as dynamical systems. How they react under variations of their parameters is studied, and a wide range of effects are found, from self-sustained oscillations, to chaotic behavior, or synchronization mechanisms between multiple lasers [Erneux10; Sciamanna15].

In this thesis, we will study in more depth an injection-based method called *frequency-shifted feedback* (FSF). This technique is based on the resonant injection from one laser into the other, and allows to synchronize their phase. In turn, the difference between the frequencies of the two lasers produces a much more stable beatnote. It was originally proposed a few years ago [Kervevan07], and has shown promising results when applied to the two modes of a dual-frequency solid-state laser [Thévenin12c]. Here, we will continue this study, and also try to adapt the technique to separate semiconductor lasers. All this will be done from a twofold point of view: first, the applicative microwave photonics viewpoint of beatnote stabilization, and second also the more fundamental framework of the study of coupled laser dynamics.

Outline

This manuscript is structured in four chapters. The first one will be devoted to a short and simplified recall of the rate equations theory, and how they can be used to describe the dynamics of a class-B laser. Namely, they can be successfully applied to the case of lasers subjected to the optical injection from another laser, or to feedback from themselves. The microwave photonics framework of this work will be also presented, and specifically the heterodyne generation of microwave signals. With respect to that challenge, we will see that dual-polarization dual-frequency lasers are particularly fit for the task but require stabilization mechanisms.

In the second chapter, we will focus on a form of stabilization using frequency-shifted feedback, applied to a solid-state dual-frequency dual-polarization Nd:YAG laser. Building on previous results from our lab, we will show experimentally and numerically that depending on a number of parameters, different types of synchronization regime between the two polarization modes can be obtained. We will also measure the value of the often ignored linewidth enhancement factor, and highlight its influence in the reinjection dynamics.

Chapter III will be devoted to another type of beatnote-generating device. This time, two separate semiconductor lasers provided by III-V Lab will be used, with the particularity of being located on a single semiconductor component. We will see that FSF can still be applied, but that more complex phenomena take place, namely because of the higher number of couplings between the lasers, and the fact they are ruled by delayed dynamics. Nevertheless, thanks to a careful characterization of the components, we will develop a numerical model and see that its results compare well with experimental observations.

Theses results will be used in Chapter IV in order to build a proof-of-concept of a self-referenced heterodyne oscillator. By combining FSF and the concept of the opto-electronic oscillator (OEO), we will show that microwave signals over optical carriers can be obtained with good phase noise performances. Perspectives, among which integration on photonic components and precise model-driven design will be discussed.

A short conclusive section will summarize the different achievements, and discuss the horizon of perspectives, suggesting future work to be done.

CHAPTER I
INTRODUCTION TO INJECTION AND FEEDBACK IN LASERS, AND TO MICROWAVE PHOTONICS

1 Dynamical modeling of class-B lasers

In this thesis, one of our task will involve modeling of lasers. Thus, in this first part, we will recall some standard concepts, results and make a brief derivation of the tools that will be extensively used afterwards.

1.a The laser rate equations

THE principle of the laser emission is well described by the original meaning of the acronym LASER, namely "Light Amplification by Stimulated Emission of Radiation". Indeed, it is based on a light-matter interaction process called stimulated emission, where the deexcitation of elements in an active medium allows to coherently amplify a light field. This process can be summarized as the effective duplication of an incident photon, accomplished during this deexcitation. The energy of the supplementary photon corresponds to the difference between the upper, excited level and the lower level after the transition. This is sketched on Fig. I.1. While the principle is the same for all lasers, widely different active media exist, from gas molecules, ions trapped in crystalline, glass matrices or fibers, to semiconductor lasers where laser emission relies on electron-hole recombination. Alongside, the process of pre-excitation of the active medium, called pumping, can differ a lot, and can be provided for instance by another light source, an electric spark, or an electric current [Verdeyen95; Svelto10]. Having realized a "light amplifier", it is placed in an optical cavity, schematically two face-to-face mirrors, so that each photon makes

multiple round-trips, and has multiple chance to trigger stimulated emission. When the gain of the amplification compensates the losses in the cavity or at its ends, the *laser threshold* is reached, and the laser phenomenon begins.

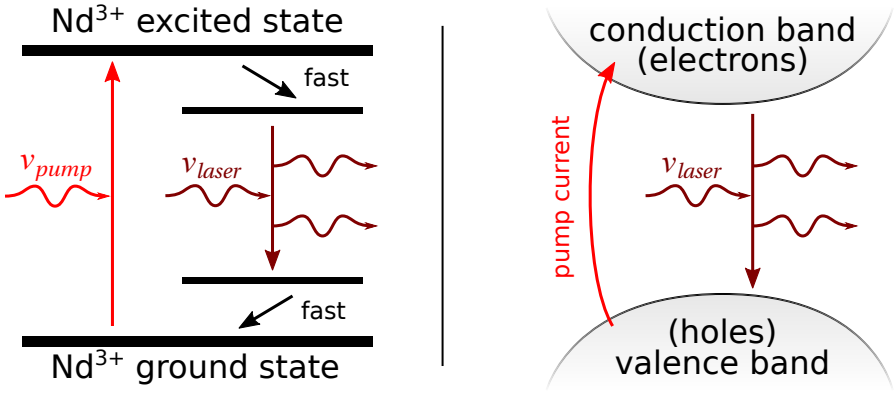

Figure I.1: Principle of stimulated emission amplification, in a four-level solid state medium, such as Nd:YAG (left) and in a semiconductor (right).

The fact that some elements of the active medium are being pumped into an excited level comes unavoidably with the fact that they may randomly decay into a state of lower energy. By doing so, they will generate non-coherent light, composed of photons with random direction, polarization and wavelength. This phenomenon, called spontaneous emission, is one of the main sources of noise in lasers. However, in all the following, we will not be interested in the intrinsic noise of our lasers, so this phenomenon will be neglected in all our models. This approximation is justified for solid-state lasers, which have a low level of spontaneous emission above threshold [Koechner06]. This is not the case in many types of semiconductor lasers, but we will only be interested in models that have a sufficiently low noise levels, and used way above threshold, so that spontaneous emission can be neglected.

Evolution of the field

First modeling of the laser phenomenon was done almost as soon as the first observation of the effect, and was built upon the previous model of the MASER, the microwave domain predecessor of the laser [Schawlow58; Lamb64]. Afterwards, numerous approaches to describe the laser phenomenon have been developed with varying complexity. A semi-classical treatment uses the density matrix formalism and leads to the Maxwell-Bloch equations, that may also be designated as Arecchi-Bonifaccio equations after their discoverers [Arecchi65; McNeil15]. Other approaches, either generic or more specifically applied to certain types of lasers, are also common and lead to similar results in the usual cases [Agrawal86; Tartwijk95; Petermann88; Lugiato15; Ōtsubo17]. The semi-classical treatment of the laser phenomenon takes

schematically this form:

$$\text{field } \mathcal{E} \xrightarrow[\text{acts on}]{①} \text{ions, atoms, electrons, etc.} \xrightarrow[\text{generate}]{②} \text{polarization } \mathcal{P} \xrightarrow[\text{drives}]{③} \text{field } \mathcal{E}$$

Here the electric field in the cavity $\mathcal{E}$ interacts with the active medium (step ①). The interaction process can be rather complex, and its accurate description is often only possible using a quantum mechanics point of view. However, ultimately, it will lead to an electric polarization $\mathcal{P}$ of the medium (step ②) so that it is possible to phenomenologically account for this response. Conversely, the response can be simply experimentally measured. Finally, this electric polarization acts as a driving force for the electric field (step ③), and the loop is repeated again [Sargent74]. We will present here a simplified derivation of the laser equations, based on this principle.

Wave equation. We will assume that the laser cavity selects an axis z, and will neglect any transverse aspect of the field. Also, the model will be scalar, and will not take polarization effect into account, although this can be done in extensive models [Chartier00]. We will not make any assumption on the shape of the active medium, or on whether it occupies the whole cavity or not. Starting from the Maxwell equations, and with all these assumptions, we can write the following wave equation for the time evolution of the cavity field $\mathcal{E}$ along the cavity axis z:

$$\frac{\partial^2\mathcal{E}}{\partial z^2} - \frac{n^2}{c^2}\frac{\partial^2\mathcal{E}}{\partial t^2} - \frac{n^2}{c^2\tau_p}\frac{\partial\mathcal{E}}{\partial t} = \mu_0\frac{\partial^2\mathcal{P}}{\partial t^2} \tag{I.1}$$

There, c is the speed of light in vacuum, n is the index in the cavity. Here we consider a non-magnetic medium, so that μ_0 is the vacuum magnetic permittivity. We have introduced phenomenologically a decay term with time scale τ_p, that corresponds to the distributed losses along the cavity, including what is due to output mirrors, optical elements, conductivity of the medium, etc. This quantity is often called the "photon lifetime". Finally, the right-hand side is a driving term, that corresponds to the interaction of the field with the gain medium. This produces an electric polarization $\mathcal{P}$, which in turn drives the evolution of the field.

We consider a monochromatic field with an arbitrary pulsation ω, $\mathcal{E}(z,t) = E(t)e^{i\omega t - ikz} + \text{c.c.}$, and are only interested in its complex amplitude $E(t)$. Here k is the wavenumber corresponding to the resonant mode of the cavity, so that $k = n\omega_0/c$ where ω_0 is the resonant pulsation. We note here a first approximation, that is that the intensity $|E|^2$ of the field does not vary appreciably along the cavity. This is obviously true for cavities with good mirrors, but may not be correct for some long

semiconductor lasers. However, we will only be interested in distributed feedback semiconductors (DFB), which have low photon lifetimes. This gives the following time and space derivatives:

$$\frac{\partial \mathcal{E}}{\partial t} = \left(\frac{\mathrm{d}E}{\mathrm{d}t} + i\omega E\right) e^{i\omega t - ikz} + \text{c.c.} \tag{I.2a}$$

$$\frac{\partial^2 \mathcal{E}}{\partial t^2} = \left(2i\omega \frac{\mathrm{d}E}{\mathrm{d}t} - \omega^2 E + \frac{\mathrm{d}^2 E}{\mathrm{d}t^2}\right) e^{i\omega t - ikz} + \text{c.c.} \tag{I.2b}$$

$$n^2 c^2 \frac{\partial^2 \mathcal{E}}{\partial z^2} = -n^2 c^2 k^2 E e^{i\omega t - ikz} + \text{c.c.} = -\omega_0^2 E e^{i\omega t - ikz} + \text{c.c.} \tag{I.2c}$$

We suppose that the rotating frame pulsation ω is close to the resonant frequency ω_0, so that $\frac{\omega^2 - \omega_0^2}{\omega} \approx 2(\omega - \omega_0)$. This will add a frequency detuning term in the final wave equation.

Slowly Varying Envelope Approximation (SVEA). As we suppose that the complex amplitude E varies slowly compared to the optical frequencies, we can remove most terms of the previous derivatives using what is often called the slowly variable envelope approximation (sometimes abridged as SVEA), which is applicable when $\left|\frac{\mathrm{d}E}{\mathrm{d}t}\right| \ll \omega|E|$ and $\left|\frac{\mathrm{d}^2 E}{\mathrm{d}t^2}\right| \ll \omega\left|\frac{\mathrm{d}E}{\mathrm{d}t}\right|$ [Butcher98]. These condition hold as long as we do not deal with ultrashort pulses or very intense fields [Sanborn03], or when we are not interested in boundaries effects in the laser [Dumont14].

Linear response. Finally the lasers we are interested in, solid-state lasers and semiconductor lasers, are class-B lasers. This means that their polarization density $\mathcal{P}$ adjusts to the cavity field much faster than the variations of the field itself, or than the lasing transitions in the active medium. Thus, it can be described proportional to the electric field in the frequency domain: $\mathcal{P} = \epsilon\chi(\omega, \mathcal{N})\mathcal{E}$, where χ is the electric susceptibility. Lasers in which it is not the case are called class-C lasers (often operating in far-infrared), and show more complex dynamics on three different time scales.[1] As χ contains the information on the stimulated emission process, it will also depend on the state of the active medium through the quantity $\mathcal{N}$, described shortly after.

Eventually, we obtain the evolution equation for the complex amplitude E:

$$\frac{\mathrm{d}E}{\mathrm{d}t} + i(\omega - \omega_0)E + \frac{1}{2\tau_p}E = -\frac{i\omega}{2}\chi E \tag{I.3}$$

[1] On the contrary, class-A lasers such as VCSELs, dye or He-Ne lasers, have even simpler one-variable dynamics because the population also has a much faster dynamics than the intracavity field, and can be adiabatically removed.

Population inversion

We now have to model the evolution of the active elements, and we will try to do so in a quite general approach, that can be later used for the two types of lasers we will study. In the case of the solid-state Nd:YAG laser, we will consider a population of ions with different possible energy levels. In the second case of the DFB semiconductor, it will be a population of electrons, either in the valence or conduction band. While the complete description of the transition processes is indeed quite complex, and involves different cascades of level changes, we will here make a simple "two-levels" model, such as the ones of Fig. I.1. We consider that the stimulated emission occurs between level 2 and 1, that are described by the densities $\mathcal{N}_1$ and $\mathcal{N}_2$. The higher level 2 is continuously populated by the pumping mechanism, at a rate R_p. Finally, each of these level experiences various losses to lower levels, so that the *population inversion* $\mathcal{N} = \mathcal{N}_2 - \mathcal{N}_1$ decays with rate $1/\tau_c$ [Erneux10].

Finally, as the stimulated emission process depends on the intensity of the field, the evolution equation for $\mathcal{N}$ can only depend on the optical intensity $I = \frac{1}{2}\epsilon_0 nc|E|^2$:

$$\frac{\mathrm{d}\mathcal{N}}{\mathrm{d}t} + \frac{1}{\tau_c}\mathcal{N} = -G(\omega, \mathcal{N}, I) + R_p \tag{I.4}$$

The term G quantifies the rate of decay of the population inversion caused by the stimulated emission. From Eq. (I.3), if we write the evolution of the optical intensity I, we obtain:

$$\frac{\mathrm{d}I}{\mathrm{d}t} + \frac{1}{\tau_p} I = \omega \mathrm{Im}(\chi) I \tag{I.5}$$

The energy of a photon being $\hbar\omega$, we can deduce that the stimulated emission process generates $\frac{\omega \mathrm{Im}(\chi)}{\hbar\omega} I$ photon per second, per arbitrary surface unit. In a four-level system, this corresponds to the same amount of decrease for the population[2]. The gain term G is thus proportional to the imaginary part of the susceptibility, and we have:

$$\frac{\mathrm{d}\mathcal{N}}{\mathrm{d}t} + \frac{1}{\tau_c}\mathcal{N} = -\frac{\epsilon_0 nc}{2\hbar}\mathrm{Im}\left(\chi(\omega, \mathcal{N})\right)|E|^2 + R_p \tag{I.6}$$

[2] In a three-level system, such as a ruby laser, it only corresponds to half the decrease, because the stimulated emission is not followed by another fast transition, as the lower level already corresponds to the ground level. This situation, and more complex intermediary cases, are often accounted for by a constant coefficient with the notation "2^*".

Rate equations and their properties

What remains to be expressed is the susceptibility $\chi = \chi_r + i\chi_i$. Without making any assumption on the physical phenomena involved, we can proceed to a linearization around the level of population inversion $\mathcal{N}_{\text{th}}$ so that $\omega\chi_i(\mathcal{N}_{\text{th}}) = \frac{1}{\tau_p}$. This means that for this value, the gain in the medium compensates the losses in the cavity. This is called the threshold level. Some authors such as [Agrawal93] choose to rather develop around a "transparency level" for which $\chi_i = 0$, but this does not correspond well to the case we will study, and lead to atypical definitions of parameters. Finally, we will ignore the dispersion term $\chi_r(\mathcal{N}_{\text{th}})$ as it will only shift the resonant frequency of the cavity ω_0.

$$\chi(\omega,\mathcal{N}) \approx \frac{i}{\omega\tau_p} + \left(\frac{\partial\chi_r}{\partial\mathcal{N}} + i\frac{\partial\chi_i}{\partial\mathcal{N}}\right)(\mathcal{N}-\mathcal{N}_{\text{th}}) \tag{I.7}$$

We define the gain $g = \omega\frac{\partial\chi_i}{\partial\mathcal{N}}$ and the coefficient $\alpha = -\frac{\partial\chi_r/\partial\mathcal{N}}{\partial\chi_i/\partial\mathcal{N}}$. This last term is called the linewidth enhancement factor [Henry82], a name that will be explained in the next section. There seems to be some dispersion in the literature on the choice of its sign. We have chosen it so that it appears as $(1+i\alpha)$ in the gain term of the rate equations. The two equations write:

$$\frac{\mathrm{d}E}{\mathrm{d}t} = -i(\omega-\omega_0)E + \frac{1}{2}g(1+i\alpha)(\mathcal{N}-\mathcal{N}_{\text{th}})E \tag{I.8a}$$

$$\frac{\mathrm{d}\mathcal{N}}{\mathrm{d}t} = -\frac{1}{\tau_c}\mathcal{N} + R_p - \frac{\epsilon_0 nc}{2\hbar\omega}\left(g(\mathcal{N}-\mathcal{N}_{\text{th}}) + \frac{1}{\tau_p}\right)|E|^2 \tag{I.8b}$$

If we define $N = \mathcal{N}-\mathcal{N}_{\text{th}}$, and the pump term $P = \tau_c(R_p - R_{p,\text{th}})$ where $R_{p,\text{th}} = \mathcal{N}_{\text{th}}/\tau_c$ is the threshold pumping rate, we obtain:

$$\frac{\mathrm{d}E}{\mathrm{d}t} = -i(\omega-\omega_0)E + \frac{1}{2}g(1+i\alpha)NE \tag{I.9a}$$

$$\frac{\mathrm{d}N}{\mathrm{d}t} = -\frac{1}{\tau_c}N - \frac{\epsilon_0 nc}{2\hbar\omega}\left(gN + \frac{1}{\tau_p}\right)|E|^2 + \frac{1}{\tau_c}P \tag{I.9b}$$

It is very common to use alternate units for electric field, so that the complex amplitude $|E|^2$ corresponds to the number of photon per surface unit. This can be done by doing the following scale change $E \to \sqrt{\frac{2\hbar\omega}{\epsilon_0 nc}}E$, which we will do in all the following equations. This leads to the following usual equations:

$$\frac{\mathrm{d}E}{\mathrm{d}t} = -i(\omega-\omega_0)E + \frac{1}{2}g(1+i\alpha)NE \tag{I.10a}$$

$$\frac{\mathrm{d}N}{\mathrm{d}t} = -\frac{1}{\tau_c}N - \left(gN+\frac{1}{\tau_p}\right)|E|^2 + \frac{1}{\tau_c}P \tag{I.10b}$$

This important set of equations are the class-B laser rate equations, and are sometimes called the Statz and de Mars after their purely phenomenological derivation [Statz60]. They are the foundation of many numerical and theoretical studies of laser dynamics. For instance, they can be used to estimate the influence of noises on the intensity output and on the frequency of the laser [Sargent74]. The latter is described at the first order by the linewidth $\Delta\nu$ of the laser, given by Schawlow-Townes formula [Schawlow58], which reads:

$$\Delta\nu = \left(1+\alpha^2\right)\frac{hc}{4\pi\lambda I_{\text{out}}\tau_p^2} \tag{I.11}$$

Here I_{out} is the output power of the laser, assuming that the cavity losses are only due to the output coupling. Note that this is only a coarse order-of-magnitude estimation obtained from Eqs. (I.10), and that some refinements may be needed, for instance when dealing with semi-conductor lasers. Yet, this allows to see for instance that solid-state lasers, where τ_p is usually in the microseconds range produce a much sharper linewidth than semiconductor lasers, for which a value of τ_p in the picoseconds region is often found.

Equations (I.10) can be further simplified by choosing the optical frequency as the resonant frequency of the cavity so that $\omega-\omega_0 = 0$. In that case, only three physical parameters are involved. One is the ratio of the photon and population lifetimes τ_c/τ_p, the other quantifies the pumping, and is often written in terms of the pumping ratio $r = \tau_p gP+1$, and finally the linewidth enhancement factor α, that quantifies the phase drift.

The rate equations present two steady states, one with no field in the cavity, so that $|E| = 0$ and $N = P$ is often called the "off" state. Once the pump P crosses the threshold P_{th} (i.e. for $r \geq 1$) it becomes unstable and the other steady state, called the "on" state as $|E| \neq 0$, becomes stable.

An important feature of these equations, and a characteristic of the class-B lasers, is that small oscillations can happen around this steady state. Indeed, as two different time scales exist, two-way exchanges of energy between the field and the population can take place. This results in a phenomenon called the relaxation oscillations. Their frequency f_R can be obtained by linearizing around the steady state, and is:

$$f_R = \frac{1}{2\pi}\sqrt{\frac{r-1}{\tau_c\tau_p} - \left(\frac{r}{2\tau_c}\right)} \approx \frac{1}{2\pi}\sqrt{\frac{r-1}{\tau_c\tau_p}} \tag{I.12}$$

The last expression is obtained for class-B lasers, thanks to the fact that in most of them $\tau_p < \tau_c$ by a factor of at least ten [Siegman86]. This will be the case for the Nd:YAG and semiconductor lasers we will be brought to study.

These relaxation oscillations create sidebands around the optical frequency, so they appear as a beatnote on the intensity noise of the laser and can be observed on the power spectral density of the photocurrent delivered by a photodiode. This appears clearly on the simulated intensity noise spectrum presented on Fig. I.2. These oscillations may be detrimental in certain use cases such as noise reduction, and way to avoid them are often looked after [Audo18].

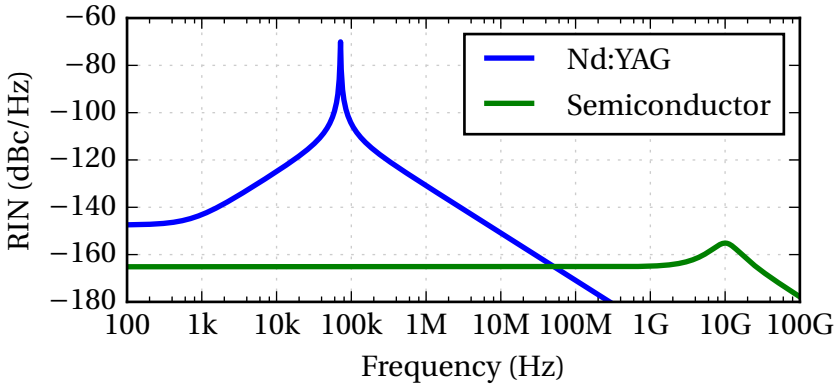

Figure I.2: Example of computed reduced intensity noise (RIN) for two lasers, assuming only spontaneous emission (Schawlow-Townes) noise. First a solid-state 1.06 µm Nd:YAG laser from Chapter II ($\tau_c = 230\,\mu s$, $\tau_p = 4.3\,ns$, $I_{out} = 1\,mW$, $r = 1.2$), second the 1.55 µm DFB semiconductor laser from Chapter III ($\tau_c = 60\,ps$, $\tau_p = 8\,ps$, $I_{out} = 1\,mW$, $r = 3$).

It is usual to proceed to more normalizations of these equations, and various conventions exist in the literature. One of the most common is to use an alternate time scale t/τ_p. However, by doing so, the equations for the field and for the population still evolve on quite different time scales. The system of equation is then called “stiff”, and is not well suited to numerical integration. As we will heavily resort on numerical integration in the following, we will adopt another time scale based on the relaxation oscillation $s = 2\pi f_R t$ [Erneux10]. This, along with normalizations $e = \frac{1}{2\pi f_R}\sqrt{\frac{g}{\tau_p}}E$ and $n = \frac{g}{2\pi f_R}N$, and with the definition of the damping coefficient $\varepsilon = \sqrt{\frac{\tau_p/\tau_c}{r-1}}$ and pumping ratio $r = \tau_p g P + 1$, gives the following reduced equations:

$$\frac{\mathrm{d}e}{\mathrm{d}s} = \frac{1}{2}(1+i\alpha)ne \tag{I.13a}$$

$$\frac{\mathrm{d}n}{\mathrm{d}s} = 1 - |e|^2 - \varepsilon n\left(1+(r-1)|e|^2\right) \tag{I.13b}$$

1.b The linewidth enhancement factor α

Definition, consequences and typical values

In the previous section, we derived the rate equations governing the time evolution of the field amplitude and of the population inversion. They depend on a certain number of parameters, the value of which will alter the possible dynamics. Thus, a way to measure each of them is needed. Here, we will focus particularly on the linewidth enhancement factor α, that was previously introduced when linearly expanding the electric susceptibility. The approximation of a constant coefficient for the ratio of the imaginary and real parts of the first order term is justified as long as we are not dealing with ultrashort pulses in mode-locked lasers, or very fast carrier density oscillation [Agrawal93]. This factor is defined as

$$\alpha \equiv -\frac{\partial\chi_r/\partial N}{\partial\chi_i/\partial N} = \frac{1}{\lambda}\frac{\partial n/\partial N}{\partial\mathcal{G}/\partial N} \tag{I.14}$$

We see that it can be rewritten as the ratio of the variation of optical index with respect to the population inversion, on the gain variation. The term $\partial\mathcal{G}/\partial N$ is linked to the laser gain curve by $\partial\mathcal{G}/\partial N = \lambda\sigma(\lambda)$ where σ is the cross-section of stimulated emission. The other term $\partial n/\partial N$ quantifies the variation of optical index caused by the population inversion. As the susceptibility χ is supposed to be an analytical complex function of the frequency, its imaginary and real parts are linked by the Kramers-Kronig relation, so they are not independent [de L Kronig26]. More details on this can be found in Annex B. Notably, this means that the α coefficient depends on the asymmetry of the gain curve with respect to the operating frequency of the laser. If the laser operates at the maximum of its gain curve, an asymmetric gain, frequently encountered in semiconductor lasers, corresponds to $\alpha \neq 0$. Conversely, a symmetric gain as found in most gas or solid-state lasers means that $\alpha \approx 0$. This explains why this terms only appeared in laser models with the advent of semiconductor lasers [Haug67; Lax67].

Indeed, this α factor is sometimes also named Henry factor after [Henry82], who popularized it as a way to explain the observed linewidth of semiconductor lasers, which is quite higher than what would be expected from Schawlow-Townes estimations [Schawlow58]. Namely, it was shown that the linewidth is larger by a factor

$(1+\alpha^2)$. It was quickly discovered that this α factor also played a key role in the phase dynamics of semiconductor lasers. This becomes apparent when an external field is injected into the laser, be it another laser [Chow83], or a partial reflection of the output [Lang80]. This will be particularly discussed in the following sections.

As can be seen in the rate equations, the α factor introduces an effective phase-amplitude coupling for the field, so that it is also sometimes called the phase-amplitude coupling coefficient. Thus, it follows that the laser cannot be purely modulated in amplitude by varying its pumping rate: an amplitude modulation is necessarily accompanied by a phase –or frequency– modulation. This phenomenon of optical frequency chirp under current modulation is rather detrimental to high-speed communications systems, so that an external modulation of the light is often used above 10 GHz. This motivates the search for laser sources with low α for communications purposes.

Typical values in semiconductor lasers range from 0 to 15, and depend on the geometry of the active medium, and ultimately on the gap of the semiconductor [Westbrook87]. In practice, this full range of values is addressed by different active medium. Low values can be found in certain quantum dot lasers, for instance $\alpha < 1$ in 1.22 µm lasers [Newell99], or $\alpha \approx 1$ in dash-in-a-well structures [Moreau06]. Standard DFB lasers, such as the quantum-well-based commercially available for telecommunication applications often feature α in the range 2–3 [Kikuchi85; Osinski87]. Higher values have been observed in certain quantum well-based VCSEL lasers [Moller94] or other kind of quantum dot lasers [Dagens05].

Moreover, the α coefficient can also depend on other parameters of the laser, either directly, or indirectly through its dependency on the operating frequency. Obviously, in most lasers, different values of α can be measured when varying the pumping ratio, but temperature may also have a strong influence through thermo-optical effect. More surprisingly, it has been reported that an external injected field can alter the linewidth enhancement factor in some lasers [Naderi09; Chuang14].

How to measure it?

Very extensive literature exist on α-factor measurements performed in all main types of semiconductor lasers, i.e., quantum wells, dots, quantum cascade lasers, VCSELs and so forth. An extensive, although a bit outdated review can be found in [Osinski87]. The oldest measurement methods include direct estimation of the gain asymmetry [Hakki75]. However, this can only be done under the laser threshold by measuring the optical spectrum of the amplified spontaneous emission, and the resulting α value can differ strongly from the actual one above threshold, which is often the only one of

interest.

Another straightforward measurement is the direct estimation from the optical linewidth, and a fit with the predicted model [Toffano92]. However, this method assumes a very good knowledge of all the other parameters involved in the linewidth, so that it is seldom usable in practice.

The most popular measurement method is based on an amplitude modulation of the pump. A non-zero linewidth enhancement factor will turn this amplitude perturbation into an optical phase perturbation. This kind of method, often nicknamed "AM/FM", is of practical interest because it corresponds to the situation for telecommunications, where the laser is used as a data transmitter [Harder83; Kikuchi85].

There is various ways of measuring the output optical phase perturbation. This can be done using heterodyne methods [Harder83] or Mach-Zehnder interferometry [Provost11]. Also, chromatic dispersion in a long fiber provides a simple way to do this measurement, and has the advantage of being even closer to a real data transmission situation [Royset94]. These modulation methods are interesting from an applicative point of view, however changes in the pump current often induce important thermal fluctuations, which can in turn change the refractive index through the thermo-optic effect. To compensate, either faster modulation is needed, but the required bandwidth, often of more than a few GHz, is not always available, or subsequent processing must be done to account for this thermal amplitude-phase coupling. To sum up, it is sometimes not so clear what is measured using these methods, and some care should be given to the precise measurement parameters.

Finally, the last class of measurement methods is based on the laser's behavior under optical injection or feedback, which usually show a strong dependency on α. Such effects will be discussed in more details in the next section, but clever methods of measuring α have been suggested, including the monitoring of the output amplitude while varying the frequency detuning between a master laser and the one under study [Hui90; Iiyama92]. Variations of the relaxation oscillation frequency during optical injection experiments [Szwaj04], or asymmetry of the locking range [Fordell05] have been used. More complex methods have also been proposed, for instance based on the master-slave optical frequency detuning for which an instability appears [Chlouverakis03]. Finally, optical feedback with a varying or modulated delay has been used, using an effect known as self-mixing [Yu04]. All these methods, that we can classify as based on the injection or feedback dynamics, are interesting because they give access to the value of α in the operating conditions, hopefully without affecting significantly the other parameters of the laser, and namely with few thermal changes.

To sum up on the different measurement methods of α, it should be noted that

it remains an active research domain, with sometimes controversial results. Indeed, what is actually measured often depends on the measurement method, on the operating conditions, and on the type of laser under study. This fact has been illustrated by a 2007 round-robin study, where different labs were asked to measure α on the same lasers, using different methods. The results gave a clear advantage to the fiber dispersion, optical injection and feedback methods for physically meaningful, reproducible above-threshold measurements of commercial DFB lasers [Villafranca07].

2 Interaction dynamics and their usages

Now that we have recalled the main concepts around laser modeling and rate equations, we will add new ingredients to the mix, and do a brief review on how the dynamics of a laser are altered by the interaction with an external field, either from a completely different source, or by a reflection of its own output.

2.a Injection and synchronization

The idea of injecting an external light beam into an operating laser is almost as old as the laser itself [Pantell65; Stover66]. At first, it was observed that the laser would amplify the injected light, as long as its wavelength was kept in the gain region. This phenomenon was called regenerative power amplification [Buczek73]. As the wavelength of the injected field gets closer to the wavelength of the laser, the amplification phenomenon gets stronger, up to the point where most of the available gain is used to regenerate the injected field. When it happens, the cavity mode cannot be sustained anymore, and the output of the laser becomes a single wavelength, controlled by the injected field. The span of frequency difference in which this happens is called the locking range. Indeed, this can be also understood as a synchronization (or locking) phenomenon, i.e. the optical frequency of the laser synchronized with the input frequency [Sargent74]. In that, the laser, as an optical oscillator, inherits of the same property than many other types of oscillators: the ability to synchronize to a driving frequency. Indeed, this phenomenon has been widely observed, for instance from the pendulums of Huygens [Huygens90] to the electronic circuits of Van der Pol [van der Pol27].

One of the most prominent usages of optical injection is the stabilization of power lasers. Indeed, a low-power, but highly stabilized laser can be injected into a much more powerful laser in order to lock its wavelength, reduce its amplitude noise, slightly tune its frequency or induce a modulation. One spectacular achievement of this principle are the ultra-stable Nd:YAG source lasers used in gravitational wave

detectors [Barillet96], which played indeed a key role in the recent successful detections [Abbott16].

Indeed, changes in the intensity and frequency noise of a laser when it is subjected to injection has been widely studied [Farinas95]. However, optical injection can also be used to induce instabilities in a laser, so that it is interesting from the point of view of the non-linear dynamics [Tredicce85].

The Adler equation

Going back to the model, a term accounting for the injected field is added to the normalized rate equation (I.13a) for the complex amplitude. It is composed of the field E_{inj}, and of an injection rate Γ. This coefficient depends on the transmission of the output mirror, and of geometric parameters that quantify the overlap between the injected field and the intracavity mode. The frequency difference $\delta\nu = \nu - \nu_{\text{inj}}$ between them, called frequency detuning, appears as a normalized term quantified by $\Delta = \delta\nu / f_R$.

$$\frac{\mathrm{d}E}{\mathrm{d}s} = \frac{1}{2}(1+i\alpha)NE + i\Delta E + \Gamma E_{\text{inj}} \tag{I.15}$$

If we split the phase and amplitude as $E = |E|e^{i\varphi}$ this corresponds to:

$$\frac{\mathrm{d}|E|}{\mathrm{d}s} = \frac{1}{2}N|E| + \Gamma E_{\text{inj}}\cos\varphi \tag{I.16a}$$

$$\frac{\mathrm{d}\varphi}{\mathrm{d}s} = \frac{1}{2}\alpha N + \Delta - \Gamma\frac{E_{\text{inj}}}{|E|}\sin\varphi \tag{I.16b}$$

Combining the two equations (I.16), and recalling that $\sin\varphi + \alpha\cos\varphi = \sqrt{1+\alpha^2}\sin\varphi'$ where $\varphi' = \varphi + \arctan\alpha$, we obtain the following equation for the time evolution of the phase:

$$\frac{\mathrm{d}}{\mathrm{d}s}\left(\varphi' - \alpha\ln|E|\right) = \Delta - \Gamma\sqrt{1+\alpha^2}\frac{E_{\text{inj}}}{|E|}\sin\varphi' \tag{I.17}$$

For simplicity, we will then suppose that the amplitude $|E|$ does not vary much. In practice, this hypothesis is equivalent to a low injection rate $\Gamma E_{\text{inj}}/|E| \ll 1$. We obtain:

$$\frac{\mathrm{d}\varphi'}{\mathrm{d}s} \approx \Delta - \Gamma\sqrt{1+\alpha^2}\frac{E_{\text{inj}}}{|E|}\sin\varphi' \tag{I.18}$$

This equation is called the Adler equation, and it is the first order model for any

problem of synchronizing oscillators [Adler46]. The main lesson it teaches is that two regimes are possible: for $|\Delta| < \sqrt{1+\alpha^2}\Gamma E_{\text{inj}}/|E|$, the system converges toward a steady state, called a phase locked solution. In this region, named the locking range, the frequencies of the two oscillators are the same. In our case, the output of the laser consists in a single wavelength, controlled by the injected field. Here we see clearly that as announced in the previous section, the linewidth enhancement factor plays a key role, as it widens the locking range by a factor $\sqrt{1+\alpha^2}$. Now, when leaving the locking region, the steady state disappears in what is called a saddle-node bifurcation, and the phase starts to experience a monotonous drift. For our laser, there are two different wavelengths in the output, the one of the injected signal, and the one of the laser, which will be slightly pulled toward the injected wavelength because of the phase drift [Armand69; Blin00].

Beyond the Adler equation

However, this analysis is only valid in the very particular situation of low injection, and considerably different behaviors can be obtained when a stronger field is injected into a laser. Indeed, the shape of the locking range becomes more complex, the unlocking may be different, and peculiar spectral properties can appear [Blin03; Wieczorek05].

For instance, unlocking can happen through a Hopf bifurcation, which consists in growing oscillations around the now unstable equilibrium point [Simpson97]. It has been proposed to use these oscillations, sometimes referred as "period-one" (or P1) as source of easily tunable microwave signal [Zhuang13; Hung15]. Indeed, their period depends on the injection rate and frequency detuning. More complex outputs may include spiking regimes with short pulses, and this has been proposed as an alternate way to enforce mode-locking in diode lasers [Moses76].

Also, chaotic regimes exist outside of the locking region, so that the injected semiconductor laser is a convenient device for the generation of wide-band chaotic spectrums. Furthermore, it has been shown that the chaotic regimes of two identical lasers can be synchronized using injection of light from one to the other [Murakami03; Kim06]. This phenomenon of chaotic synchronization is widespread in dynamical systems [Pikovsky97], but particularly interesting in semiconductor lasers, as it has potential uses in secure chaotic communications [Sciamanna15].

One important tool in the theoretical study of the possible behaviors are the bifurcation diagrams, which show the locus and type of the relevant bifurcations of the equilibrium with respect to the parameters of the system. They are often produced using numerical methods based on continuation algorithms. They allow to follow an equilibrium of the system while varying a parameter, but can also be used to follow

a bifurcation while varying two parameters at once [Kuznetsov04]. Some examples of such diagrams for an injected semiconductor laser have been produced using the venerable AUTO program[3] [Doedel12], and are shown on Fig. I.3. There we clearly see the locking range, and the complex shape it can take for strong injection and higher values of α. What is not shown on these diagrams are the different behaviors outside the locking range, which can go from oscillations to chaotic regimes.

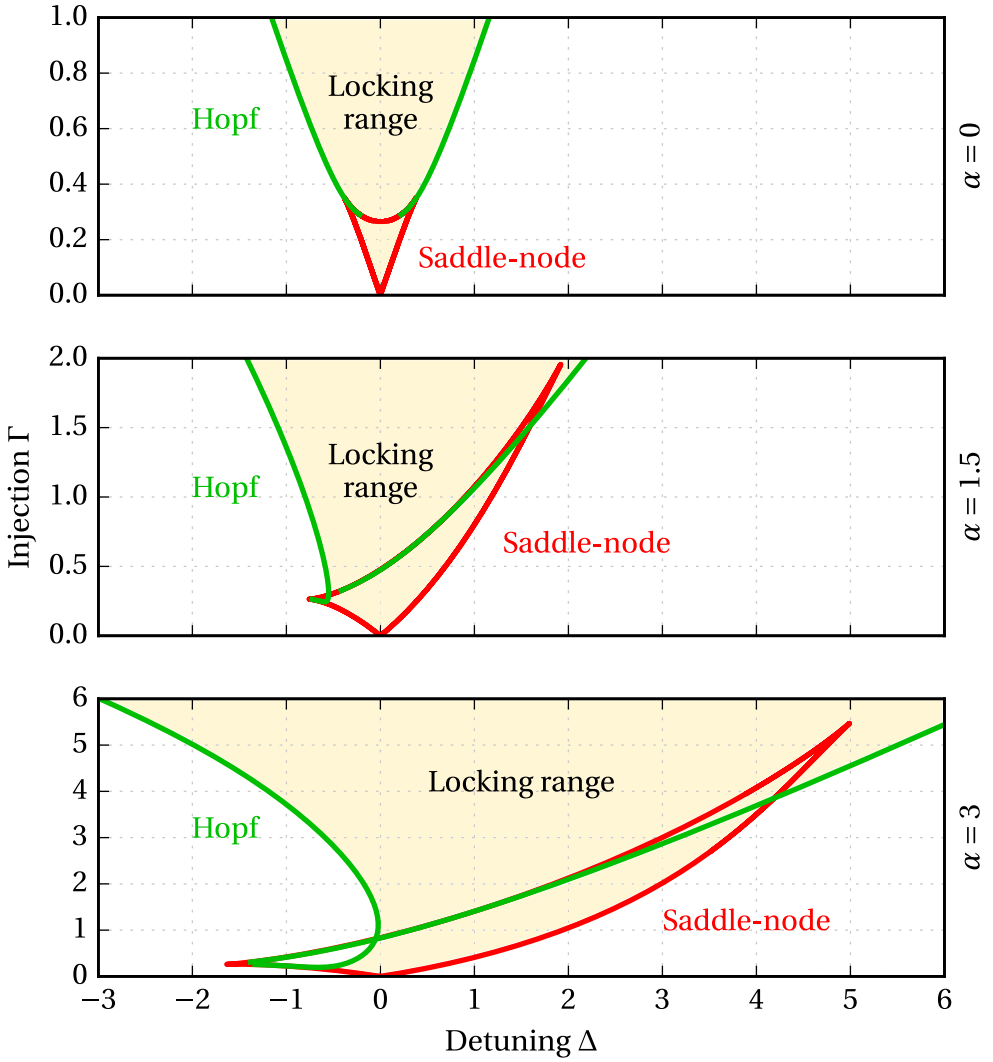

Figure I.3: Bifurcation diagram of an injected laser, for $\varepsilon = 0.2$, $r = 1.5$, and various values of α.

It should be noted that advanced usages of continuation algorithm are possible, for instance they can be used to follow limit cycle oscillations and study their stability. Such instances of a precise study of cycles, along with more bifurcation diagrams and discussions of available dynamic regimes can be found in [Wieczorek05], which

[3] http://indy.cs.concordia.ca/auto

presents an extensive study of the injected semiconductor laser.

2*b* Feedback in lasers

A subtly different case of the interaction of a laser with an external field is the reflection of the output light itself into the laser. It is a very obvious observation for anyone who has worked with lasers that even a very small reflection can lead to dramatic changes in the stability of the output. This fact was first precisely described in He-Ne lasers, where a modulation of the output intensity was observed as the position of the feedback mirror changed [Hilsum63]. This behavior, which experimentally does not look unlike an interferometric effect, was later called self-mixing interferometry [Wang94]. While in some cases it is only detrimental to the stability of the laser output, it has also been proposed to take profit of it for telemetry and Doppler velocimetry applications [Scalise04].

Since then, many additional effects of feedback have been identified, depending on its intensity and on the time delay T between the injected and the cavity field [Tkach86b]. Another viewpoint is that feedback corresponds to an *external cavity* of length c/T coupled to the laser and that the fields of the two cavities interact. For instance, self-modulation has been observed in diode laser subjected to feedback, and relaxation oscillations have been shown to lock on the external cavity frequency [Broom70]. This concept has been extended so that "compound cavity" lasers use feedback to induce single mode operation [Bogatov73]. A short external cavity, using a close mirror (at less than 0.3–2 cm from the output) can be very effective at suppressing the relaxation oscillations, and damping much of the noise in a laser [Chinone78]. Appending an external cavity on lasers has since then become common practice. For instance, in telecommunication applications, it can be used to widen the modulation bandwidth. For instance, a short external cavity was used in [Radziunas07] to enlarge the current modulation bandwidth from 10 to 40 GHz.

As previously mentioned, the effect of feedback depends strongly on the time delay T introduced by the external cavity, on the injection ratio and other parameters of the laser. Indeed, with different values, effects on the optical linewidth can range from a narrowing [Agrawal84] to a broadening [Miles80]. Using a "short" feedback, for instance in the 10 cm range for semiconductor lasers often results in chaotic regimes. The experimental simplicity of such a setup, compared to other chaos-generating devices opens interesting perspectives, as it can be used for instance as a random number generator [Uchida08], or as a source for chaotic communications [Rogister01].

Some authors have also proposed semiconductor lasers with feedback as a nonlinear building block for the physical implementation of machine learning algorithms,

such as reservoir computing [Bueno17].

Finally, using a particular form of feedback, namely including a frequency-shifting element in the optical path, it is possible to greatly favor the sensibility to the reflected power. This has been suggested as a novel imaging technique, called Laser Optical Feedback Imaging (LOFI), with potential applications in microscopy [Hugon11].

Note that a review of the different use cases of feedback in semiconductor lasers can be found in [Kane05].

Lang-Kobayashi equation and external cavity modes

Similarly to the case of externally injected light, the rate equations can be modified to include a feedback term, that takes into account the time delay T between the output field from the laser, and the feedback field that is injected back. Neglecting the higher-order successive reflections in either cavity, we obtain the following equation for the cavity field, which along with the unchanged equation for the population inversion are called the Lang-Kobayashi equations [Lang80].

$$\frac{\mathrm{d}E}{\mathrm{d}s} = \frac{1}{2}(1+i\alpha)NE + \kappa e^{i\psi}E(s-\tau) \tag{I.19}$$

The injection rate κ is now called the feedback rate but has the same definition than in the injection case. The delay appears in its normalized form $\tau = 2\pi f_R T$. The optical phase acquired by the field during its travel outside the laser is ψ.

If one tries to find the steady states of the previous equation, it will soon become clear that there are none. Instead, solutions with constant amplitude $|E|$ and population inversion N, but with rotating phase exist. These solutions, sometimes called rotating waves, but most often referred as *external cavity modes* take the form $E(t) = E_c e^{i\Omega t}$, where E_c and Ω are the complex amplitude and pulsation of the mode. Thus, it is current practice to modify the equation so that it directly describes the evolution of these external cavity modes. We define $E_c(t) = E(t)e^{-i\Omega t}$ and obtain:

$$\frac{\mathrm{d}E_c}{\mathrm{d}s} = \frac{1}{2}(1+i\alpha)NE_c - i\Omega E_c + \kappa e^{i\psi - i\Omega\tau}E_c(s-\tau) \tag{I.20}$$

This equation presents usual steady states, but only for certain values of Ω. The corresponding external cavity modes frequencies can be obtained by solving the steady state equations for the three unknown parameters $|E_c|$, Ω, N. An additional condition on the phase, which is physically irrelevant in the steady state, has to be set, such as $\mathrm{Im}(E_c) = 0$. Note that the number of possible external cavity modes and their stability depends on the parameters in a non straightforward way [Haegeman02].

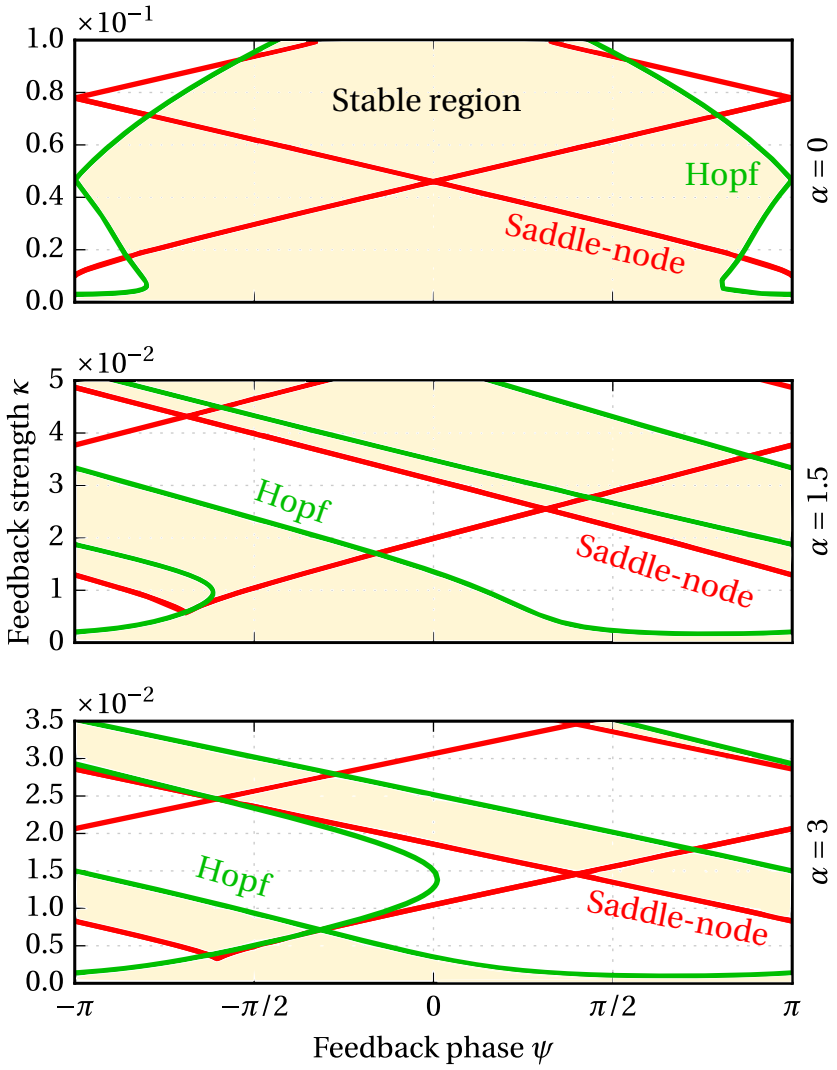

Figure I.4: Bifurcation diagram for feedback, for $\tau = 100$, $\varepsilon = 0.2$, $r = 1.5$, and different values of α. The filled region represent the domain of stability of the steady state.

As for the injection case, we have computed some bifurcation diagrams for a laser subjected to optical feedback. However, as the rate equations are now delayed differential equations (DDE), specific continuation algorithms are needed. Here, we used the Matlab/Octave package "ddebiftool" [Engelborghs02][4]. Fig. I.4 shows some bifurcation diagrams for parameters κ and ψ. We see that a strong dependence on these parameters is to be expected, and that except in the case of very low feedback, stable regions alternate with unstable ones depending on the phase ψ. More details, and a thorough study of the bifurcations in the Lang-Kobayashi model can be found in [Green10].

Finally, simultaneous optical injection and feedback has also been widely studied,

[4] http://twr.cs.kuleuven.be/research/software/delay/ddebiftool.shtml

and can indeed combine the complexity of the two mechanisms. For instance one can look at the theoretical study from [Nizette04a] and the experimental counterparts from [Liao13; Song15]. In this situation, reproduced in Fig. I.5, a piecewise locking range can appear, separated by Hopf or saddle-node bifurcations. Other phenomena, such as damping of the transients have been reported [Dellunde95].

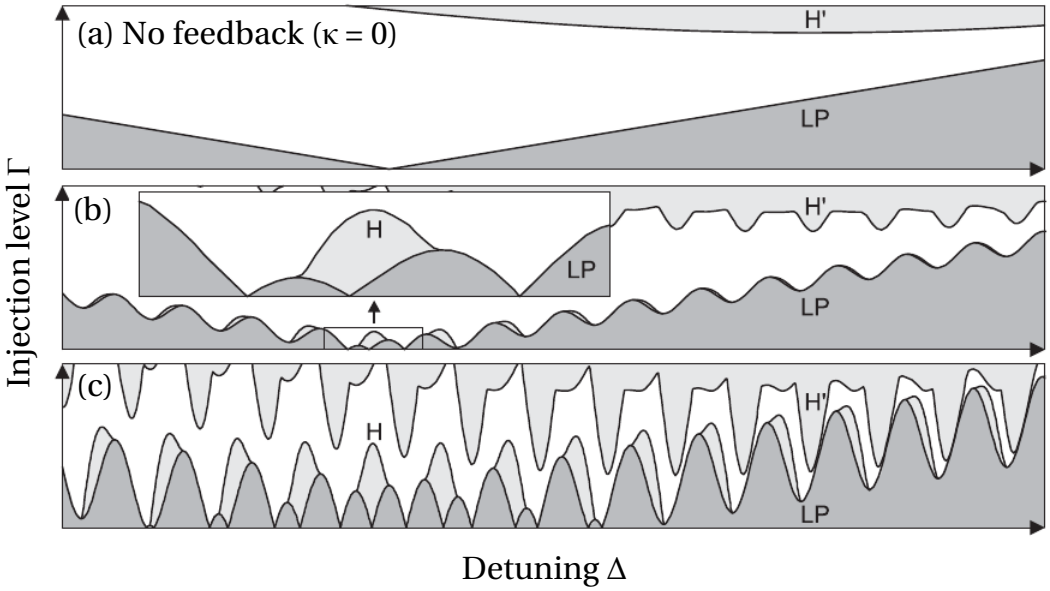

Figure I.5: Typical shape of the computed bifurcation diagram for an injected laser, also subjected to an optical feedback. From [Nizette04b]. H and H' refers to Hopf bifurcations, and LP to Limit Point (saddle-node). From (a) to (c), with growing feedback level κ.

3 Microwave photonics

The ease of use and the mass production of diode lasers, along with the flexibility and impressively low losses in optical fiber systems, led the combination of these two elements to the core of telecommunication systems. Schematically, their goal is to use light in order to carry a certain signal, with the fastest possible data rate. The object it manipulates is then an optical wavelength, which carries a modulation in the microwave domain. The set of techniques that are used to carry, process, amplify, filter or generate these signals is gathered under the term of *microwave photonics*. In this work, we will focus on this last item, the generation of optically-carried microwave signals.

3a Characteristics of a microwave signal

In this introductory section, we will recall some properties of microwave signals, that allow for quantitative comparison of their quality between different sources. The following notions will be used through the rest of this work. In the time domain, a real-world noisy signal at frequency f_0 can be represented as $x(t) = A(t)\sin\big(2\pi f_0 t + \varphi(t)\big)$, where $A(t)$ is a slower varying amplitude and $\varphi(t)$ a slower varying phase, as depicted on Fig. I.6. This means that the signal is amplitude modulated, and phase modulated, so that its power spectral density is more complex than just a single peak at f_0. This modulation accounts for the noise superimposed on the signal, and A and φ usually show erratic variations. However, their power spectral density will depend greatly on the process used in the signal generation. These power spectral densities $S_A(f)$ and $S_\varphi(f)$ are called the amplitude and phase noise respectively [Rubiola08].

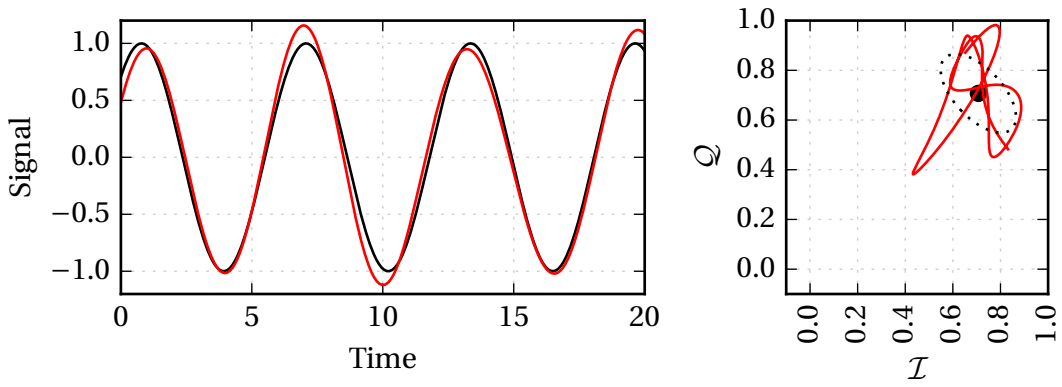

Figure I.6: Sinusoidal signal $x(t)$ with phase and amplitude noise.

If we inspect this signal on an electrical spectrum analyzer, the linewidth of the signal, related to the power spectral density $S_x(f)$ around f_0 will be a combination of the phase and amplitude noise, that cannot be easily disentangled.

In order to measure the two different noises, complex methods and devices exist, but they share the same principle and goal: to obtain the in-phase signal $\mathcal{I}(t)$ and its quadrature counterpart $\mathcal{Q}(t)$ using a demodulation process. The signal of interest $x(t)$ is multiplied twice by a local reference at frequency f_0, with a $\frac{\pi}{2}$ phase difference each time. The result is low-pass filtered, so that we obtain:

$$\mathcal{I}(t) = 2x(t)\sin(2\pi f_0 t) = A(t)\cos\big(\varphi(t)\big) + \text{(higher frequency term, filtered)} \quad \text{(I.21a)}$$

$$\mathcal{Q}(t) = 2x(t)\cos(2\pi f_0 t) = A(t)\sin\big(\varphi(t)\big) + \text{(higher frequency term, filtered)} \quad \text{(I.21b)}$$

Then the amplitude of the signal is extracted as $A(t) = \sqrt{\mathcal{I}(t)^2 + \mathcal{Q}(t)^2}$ and its phase as $\varphi(t) = \arctan\frac{\mathcal{Q}(t)}{\mathcal{I}(t)}$. This process can either be done in software or by a dedicated hardware. The latter usually also computes the power spectral density of the phase $S_\varphi(f)$, and is thus called a phase noise analyzer. Assuming the usual hypothesis of ergodicity and stationarity of the signal, and using the Kramers-Kronig theorem, $S_\varphi(f)$ can be defined as:

$$S_\varphi(f) = \int_{-\infty}^{+\infty} \langle \varphi(t)\varphi(t+\tau) \rangle e^{-2i\pi f\tau} \mathrm{d}\tau \tag{I.22}$$

where the mean value $\langle\dot{}\rangle$ is taken over a large number of samples, effectively corresponding to the statistical expected value.

Alternately, when the phase has been recorded, the power spectral density can be computed numerically, using Fourier transform, or more precisely using a multitaper spectral method that relies on Slepian sequences [Thomson82]. In this work, we used the implementation[5] [Prieto09] and its Python wrapper[6]. As it was defined before, and because it is often expressed in a logarithmic scale, the unit of phase noise is $\mathrm{dBrad}^2/\mathrm{Hz}$. On that topic it must be noted that most measurement devices use a slightly different quantity, that reflects the fact that only one side of the noise around the carrier is considered. Though also called phase noise, it is noted $\mathcal{L}(f)$. The relationship between the two is simply $\mathcal{L}(f) = \frac{1}{2}S_\varphi(f)$, or a 3 dB offset in logarithmic scale. The two quantities can be safely distinguished by their unit, as $\mathcal{L}$ is given in dBc/Hz. As the latter seems to be more common, we will only use $\mathcal{L}$ and its unit dBc/Hz in this work.

Finally, it is sometime useful to think in terms of frequency noise rather than phase noise, but as $\nu = f_0 + \frac{1}{2\pi}\frac{\mathrm{d}\varphi}{\mathrm{d}t}$, the conversion between them is straightforwardly $S_\nu(f) = f^2 S_\varphi(f)/(4\pi^2)$.

When one considers a standard electronic synthetizer in the microwave domain, the amplitude noise is often not the main concern, because feedback loops can be used to efficiently regulate the amplitude of the output. However, the stabilization of the frequency, and hence the phase noise, is a core issue. Indeed, Fig. I.7 shows the problem with standard electronic oscillators, that are based on the multiplication of a crystal resonance and a phase-locked loop. It is clear that with this technique the phase noise rises steadily with the output frequency f_0, approximately by 20 dB by decade. Many clever mitigations have been developed and proposed over the years [Rohde14; Leeson16], but ultimately the problem of phase noise degradation as the carrier frequency rises remains.

[5] http://wwwprof.uniandes.edu.co/~gprieto/software/mwlib.html
[6] http://github.com/krischer/mtspec

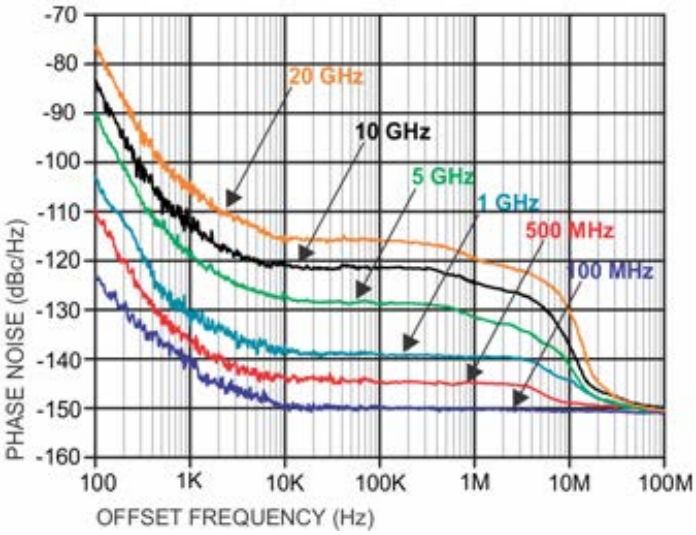

Figure I.7: Phase noise of an electronic commercial synthesizer, the National Instrument FSW-0010, for various use frequencies. Reproduced from constructor website: http://ni-microwavecomponents.com/quicksyn-full (July 2018).

Applications such as telecommunications, radar, or metrology being evermore demanding on phase noise quality, the development of very different approaches is required. With respect to this urge, hybrid techniques, combining optical elements with electronic parts, have been showing very good results for the past twenty years. Perhaps the most prominent concept, the opto-electronic oscillator, will be discussed in more details in Chapter IV, section 1.

3*b* Dual-frequency lasers

Heterodyne microwave generation

We saw previously than most microwave generating techniques face the problem of a growing phase noise as the frequency rises. This is why we will focus on a completely different principle, that consists in generating a microwave signal from a beatnote between two optical frequencies. The basic principle of such heterodyne methods is shown on Fig. I.8.

The most prominent feature of heterodyne methods is that the output noise do not depend on the microwave frequency f_0. Another interesting feature is that the optical output contains only two wavelengths, contrary to the carrier plus two sidebands of the modulation scenario. We will see in Chapter IV that this makes the signal insensitive to chromatic dispersion in fibers, which can be a relief for long-distance applications. Finally, and contrary to most other generation techniques, arbitrary high microwave frequencies can be obtained, often with continuous tuning.

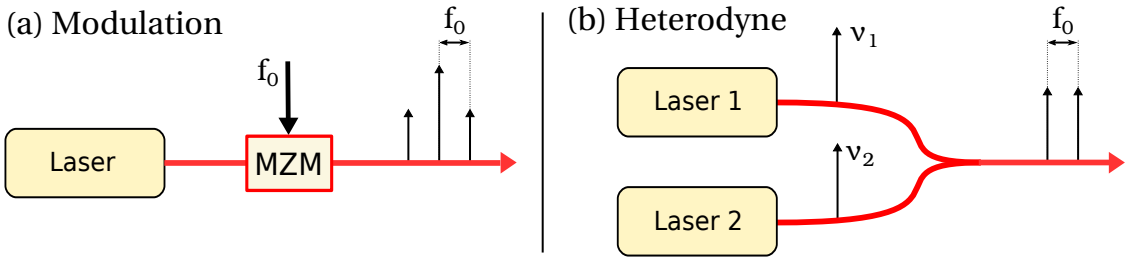

Figure I.8: Generation of a microwave-over-optical signal, the common modulation method, for instance using an amplitude Mach-Zehnder Modulator (MZM) (a), versus the heterodyne method (b).

However, heterodyne methods suffer from stability and low frequency noise problems, as the two lasers are subject to environmental noises, fluctuations and drift of their wavelength. Indeed, the large scale factor between optical frequencies and microwave frequencies will turn even a small relative optical noise into a large, usually unacceptable relative noise in the microwave domain. This brings up the need of some kind of stabilization mechanism, either for the two lasers' wavelengths, or for their difference. For the first case, standard methods of frequency stabilization can be applied on each laser [Drever83; Hallal16], but at the cost of some complexity. The second idea, which is the stabilization of the frequency difference can be implemented using a feedback loop, such as an optical phase-locked loop [Gliese92].

Dual-polarization lasers

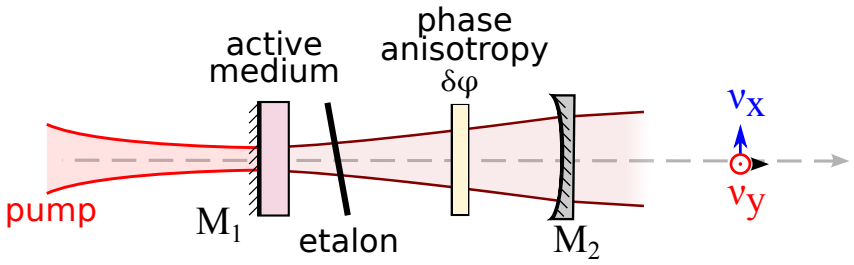

Figure I.9: Principle of the dual-polarization dual-frequency laser.

Having two separate lasers means that each of them experiences different and often uncorrelated fluctuations and drifts. Hence, it is interesting to seek ways to combine the generation of the two wavelengths on a single device, i.e. to look for a dual-frequency laser. A first option would be to let the laser operate on two different longitudinal modes. While this approach is promising and has been heavily investigated [Wake95; Gu98; Grillot11], the tuning of the frequency difference can be quite inconvenient, and the two output modes cannot be easily separated. This can be a problem for stabilization mechanism or data transfer. A comparable alternative,

which has seen recent developments is the use of two transverse modes [Paquet16; Blin17]. A second choice, on which we will focus, is to use a single longitudinal mode but with a different frequency for each polarization axis of the cavity. By doing this, we create a *dual polarization dual-frequency laser*, that outputs slightly different optical frequencies on its two orthogonal polarization axes [Bretenaker90]. This can be achieved simply by altering the effective optical length of the cavity depending on the polarization, i.e. by inserting a phase anisotropy $\delta\varphi$ in the cavity, as shown on Fig. I.9. This creates two polarization modes, which are orthogonal at each end of the cavity. See Annex A for more details. The difference between their frequencies ν_x and ν_y can be computed in this simple case and is:

$$\nu_y - \nu_x = \mathrm{FSR} \times \frac{\delta\varphi}{2\pi} \tag{I.23}$$

where FSR is the free spectral range of the cavity. This also fixes a limitation on the maximum reachable frequency difference, given by half the free spectral range of the cavity.

Since its introduction, this compact dual-polarization dual-frequency source has been the subject of quite a number of researches, and has made a few steps toward a commercial product. Early prototypes at Thales Research and Technology of an Er:Yb laser with an opto-electronic phase-locked loop stabilization showed the generation of a tunable beatnote in the 2–6 GHz range, with a phase noise down to −117 dBc/Hz at 10 kHz from the carrier [Pillet08]. Later, an enhanced version was able to reach 100 GHz, while keeping a good phase noise level of −90 dBc/Hz at 10 kHz offset from the carrier [Pillet14]. However, the frequency rigidity of the stabilization loop limited the tunability to a 3 GHz range.

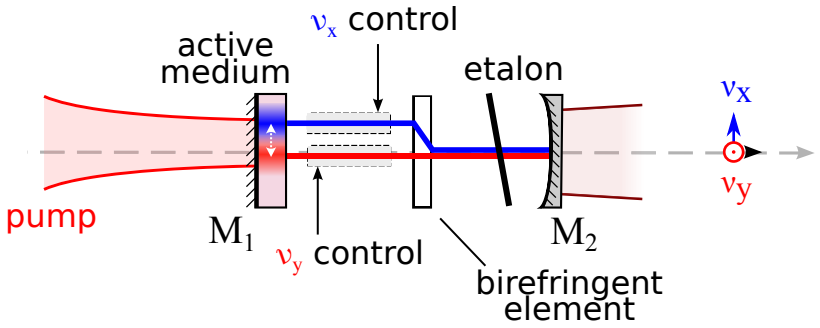

Figure I.10: Principle of the dual-polarization dual-frequency laser with a separated states cavity. The path of the two modes are split by a birefringent element.

One of the main drawbacks of this setup is the frequency limitation, and the relative inability to individually act on each polarization mode. Indeed, they share exactly the same cavity, and are furthermore coupled in the gain medium. A slightly

different scheme was developed to address this problem. Shown on Fig. I.10, it uses birefringent element inserted in the cavity to split the optical path depending on the polarization [Brunel97a]. This approach has two advantages: first, it allows to lift the constraint on the reachable beatnote frequencies, so it can reach the THz domain seamlessly [Alouini98]; second, each polarization mode can be controlled individually, for instance by inserting an electro-optic modulator on each path. Impressive performances were reached using this scheme, for instance a Er:Yb:glass laser reached $-150\,\mathrm{dBc/Hz}$ at 1 MHz from the carrier. As this was obtained without any stabilization loop, the beatnote tuning from 0 to 900 GHz remained possible [Danion14]. Other achievements in the realm of the THz beatnote include the use of the biaxial Yb:$KGd(WO_4)_2$ active medium for high power output, around 120 mW [Czarny04]. Note that several steps have already been made to turn a dual-frequency source into a useful proof-of-concept of a THz communication system [Rolland14].

Declinations of the dual-frequency dual-polarization laser have been made in the microchip format, that allows for more compact and robust design, at the cost of a more noisy output. Different teams were able to reach a 100 GHz with good power outputs. For instance in [Brunel05], a continuously tunable Er,Yb:glass laser including an intracavity birefringent $LiTaO_3$ could generate a continuously tunable beatnote up to 60 GHz. Slightly later, [McKay09] reached 150 GHz using glued quarter-wave plates.

Among the other usages of dual-polarization dual-frequency lasers, proposals have been done in the domain of metrology, for instance for atomic clock distribution over fiber links [Dumont14]. Using second harmonic generation, green dual-frequency light has been investigated for underwater LIDAR-RADAR applications [Morvan02; Vallet13]. Also, in imaging, the frequency difference between the two modes has been used to probe polarization features [Fade12].

While mainly Nd:YAG and Er:glass were mentioned, it must be noted that different active media can be used, and a wide panel of wavelengths can be addressed. For instance, Ti:Sa at 780 nm [Loas14], fiber lasers in DFB [Li14; RotaRodrigo14; Loh97] or ring configuration [Li97], vertically-external cavity surface-emitting semiconductors (VECSELS) [Baili09]. For the latter, we can note that they have class-A dynamics, and thus do not feature relaxation oscillations, which is an advantage in terms of amplitude and phase noise.

For completeness, it must be noted that dual-frequency laser can be operated not only in a continuous regime, but also in pulsed regimes, for instance Q-switch, by inserting a saturable absorber such as Cr:YAG in the cavity [Lai03], or in mode-locked solid-state [Thévenin12c] or semiconductor lasers [Pelusi97]. They can also be used to produce optical combs on orthogonal polarization axes [Link17].

Dual-frequency lasers also present interesting properties when subjected to feedback. Without going into much details, as this will precisely be the topic of the next chapter, we can say that the fact that two laser modes coexist can turn an optical feedback into a sort of external coupling between them. Thus, different regimes of synchronization, or of externally-driven oscillations are possible. This has been described under the label "self-mixing" in the works [Nerin97; Tan07].

The topic of the next chapter will be the study of a method based on a feedback coupling between the modes, that allows to synchronize their phase and stabilize their frequency difference. This technique of *frequency-shifted feedback* relies on the resonant injection of one mode onto the other, and has shown interesting results before [Kervevan07; Thévenin11a].

4 Conclusions

In this introductory chapter, we have recalled the basic principles of the laser phenomenon, and have derived the rate equations governing the electric field amplitude, phase, and the population inversion for a class-B laser. We presented the parameters involved, with a sharp focus on the linewidth enhancement factor, that will be of a certain interest in the next chapter. We showed that these rate equations can be used to describe the dynamics of a laser subjected to an injected field from another laser, or to feedback from itself. The next chapter will present more complex situations, where rate equation analysis will be applied to the case of dual-frequency lasers, that were also presented here. Finally, a brief domain overview of microwave photonics was made, as this will be the context and motivation behind most of this work.

CHAPTER II

FREQUENCY-SHIFTED FEEDBACK IN DUAL-FREQUENCY SOLID STATE LASERS

STARTING from the fact that frequency-shifted feedback is an interesting and quite general synchronization mechanism for two lasers, and building up on the good knowledge we have of the Nd:YAG dual-frequency dual-polarization laser [Romanelli14], we will try to dive deeper into the synchronization dynamics it presents. This will be done with two goals in mind. On the one hand, a better understanding and a good model-experiment agreement is likely to provide a sturdy foundation for the development of more complex stabilization mechanisms. Also, this can facilitate the transposition of this technique to other kind of lasers, that may not be as well controlled and characterized as the one we study. On the other hand, from a more fundamental point of view, we are interested in exploring the different regimes and instabilities that appear in this system. Using the good stability of the experiment and the fine control we have on the different parameters, we can use it as a testbed of some regimes.

1 Dual-frequency dual-polarization laser

As already explained, lasers can be made to oscillate simultaneously on the two polarization modes of their cavity. Then, by inserting a phase anisotropy in this cavity, the frequency of the two modes can be split, so that a dual-polarization dual-frequency laser is obtained [Brunel16]. In the following, we will consider a free-space laser, composed of a plano-concave cavity and of a Nd:YAG crystal as a gain medium. As a reminder, a Nd:YAG laser operates at 1064 nm when pumped with a 808 nm beam. It is a four-level system, with two fast non-radiative decays (with durations around 0.1 ns) surrounding a slower transition in the 230 µs range, that provides stimulated emission (see Fig. I.1, p. 22). For that reason, when studying the dynamics of the field

and population, it can be considered as a two-level system [Siegman86].

Our dual-frequency laser is composed of a $\ell = 65\,\text{mm}$-long cavity, pumped by a focalised beam from a laser diode. At one end of the cavity is the active medium, a 2%-doped Nd:YAG crystal whose outside face is also the input mirror. This crystal is 5 mm long, and is cut along its (111) crystallographic axis, so that it is isotropic and only has a low residual birefringence of $\Delta n \approx 7 \times 10^{-6}$. At other end of the cavity, the output mirror has a radius of curvature 10 cm and a transmission of 1% at 1064 nm. This setup, shown on Fig. II.1, defines a resonant Gaussian mode that has a waist of 130 µm in the active medium, and a divergence of 2.6 mrad.

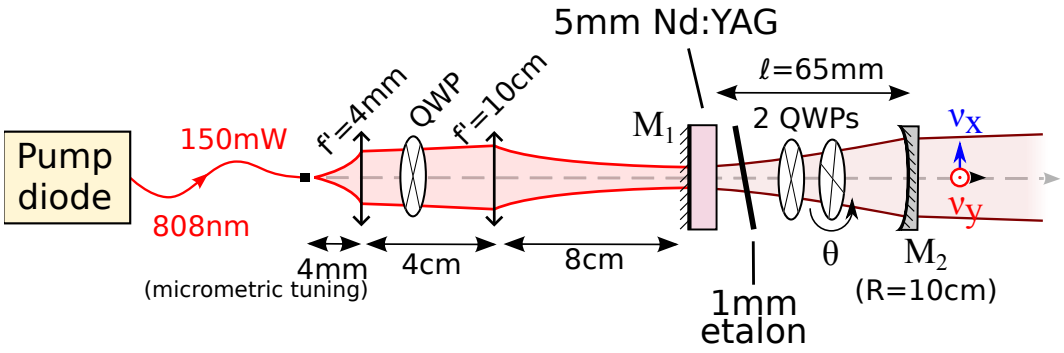

Figure II.1: Dual-frequency laser used through this chapter.

Inside the cavity, two quarter-wave plates (QWP) have been inserted, placed on rotating mounts. The first one has been aligned so that its principal axis forms a 45° angle with the axis associated with the small birefringence of the crystal. The second wave plate is tilted by an angle θ from the previous one, and is used to tune the difference of optical phase experienced by the two polarization modes of the cavity. Finally, a 1 mm silica etalon with a 40% reflection is added in the cavity, close to the active medium, so that only one longitudinal mode is selected for each polarization state. The full setup is summarized on Fig. II.1, and a photograph can be seen on Fig. II.2.

Frequency separation

The detailed computation of the polarization states in the laser involves the Jones matrix formalism [Jones41; Bretenaker91]. In our case, we would have to consider the matrices of the two rotated QWP (see Annex A). The main result is that the resonant frequency ν is different for the two polarization axes x and y, and that their difference is directly related to the angle between the waveplates. Similarly to Eq. (I.23), we have:

$$\nu_y - \nu_x = \frac{c}{2\ell} \times \frac{2\theta}{\pi} \tag{II.1}$$

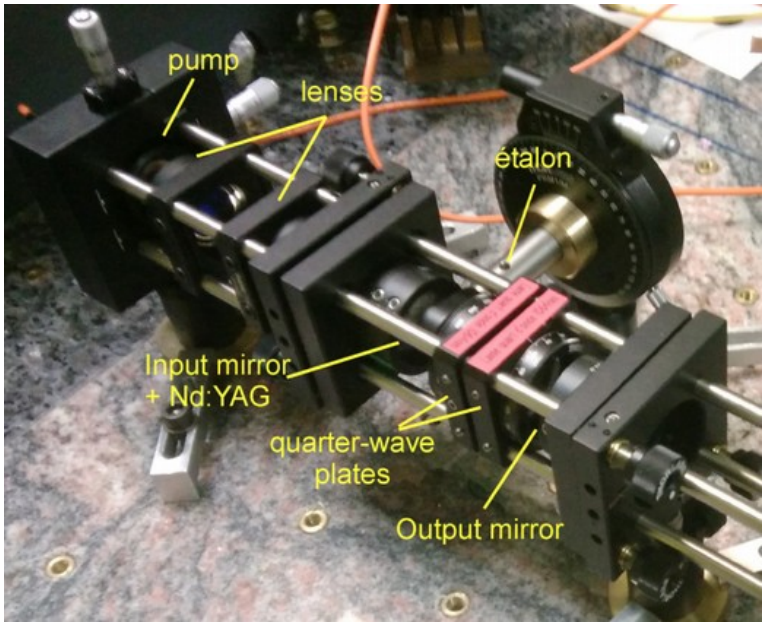

Figure II.2: Photograph of the dual-frequency laser used.

Note that in the following, we will stick to the convention that the axes x and y are chosen so that $\nu_y > \nu_x$. The maximum frequency difference is thus limited to $c/4\ell$, obtained for $\theta = \pi/4$, which is directly related to the free spectral range of the cavity. For instance, in our setup, this corresponds to a maximum frequency separation of roughly 1 GHz. However, this will not be a problem for now: as other discussed in subsection 2*a*, we will use a rather low frequency difference of 180 MHz. The beatnote associated with this frequency difference can be transformed into an electrical signal in the RF domain, by mixing the two polarizations using a polarizer at angle 45°, and recording it on a photodiode.

Pump diode

Two pigtailed pump diodes at 808 nm have been used: first, a multimode laser diode from Opto Power with a maximum output of 2 W. It is connected to a multimode fiber, whose core diameter is 130 µm. In the pumping layout, two identical lenses of focal 5 cm have been used, so that the pump spot diameter on the active medium was also 130 µm.

We later replaced it by a single mode laser diode, model LU0808M250, delivering up to 250 mW of continuous wave light at 808 nm. The model we used was followed by a fiber Bragg grating (FBG), which allows to reach a spectral width of 0.2 nm. As shown of Fig. II.1, a QWP inserted between the focalising lenses allowed to change the pump polarization, as described in Section 2*c*. We decided to keep a pump spot diameter identical to the previous multimode pumping, so we calculated the configuration of

two lenses needed to focus the output of the fiber using Gaussian beam formalism, often expressed in terms of "ABCD" matrices [Kogelnik66]. The fiber core is 6 µm, a short-focal lens of 4 mm is placed close to the output of the fiber, and a larger lens of focal 10 cm is placed 4 cm after (Fig. II.1). This allows the waist of the pumping beam to be 130 µm at 8 cm of the second lens, which is where we place the active medium. The use of this new pump diode permitted a better stability of the dual-polarization state, eliminating the need for daily adjustments of the etalon.

The characteristic curve on Fig. II.3 shows that with all the intracavity elements, the output power can be go up to 6 mW, with a different efficiency and threshold for the different pumps, nearly 200 mW for the multimode pump, against 80 mW for the single mode pump.

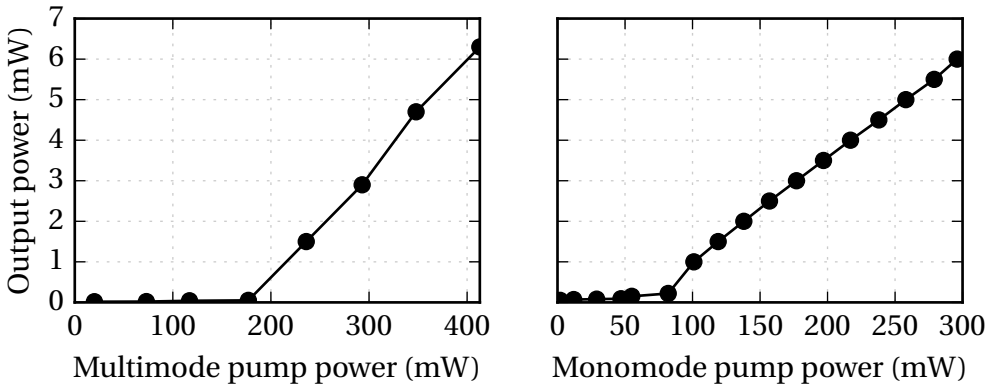

Figure II.3: Output power for dual-polarization Nd:YAG laser, versus pump power for the two different pumps used.

2 Frequency difference locking using feedback

As highlighted in Chapter I, the goal we would like to achieve is the stabilization of the output beatnote. In particular, in order to keep the good spectral quality of the laser, we would like to do so without any modification to the laser itself. This rules out methods based on phase-locked loops, because they require a way to directly alter the frequencies of the modes. Although this can be done, for instance by inserting an internal actuator such as an electro-optic element (see I.3*b*), it is at the cost of a modification of the laser, and enhanced complexity. Thus, we will rather try to introduce some kind of controlled coupling between the modes, that we will use to achieve synchronization between them. In the rest of this chapter, we will investigate how this can be done by optically injecting one mode on the other one, and how it affects the dynamics of the laser.

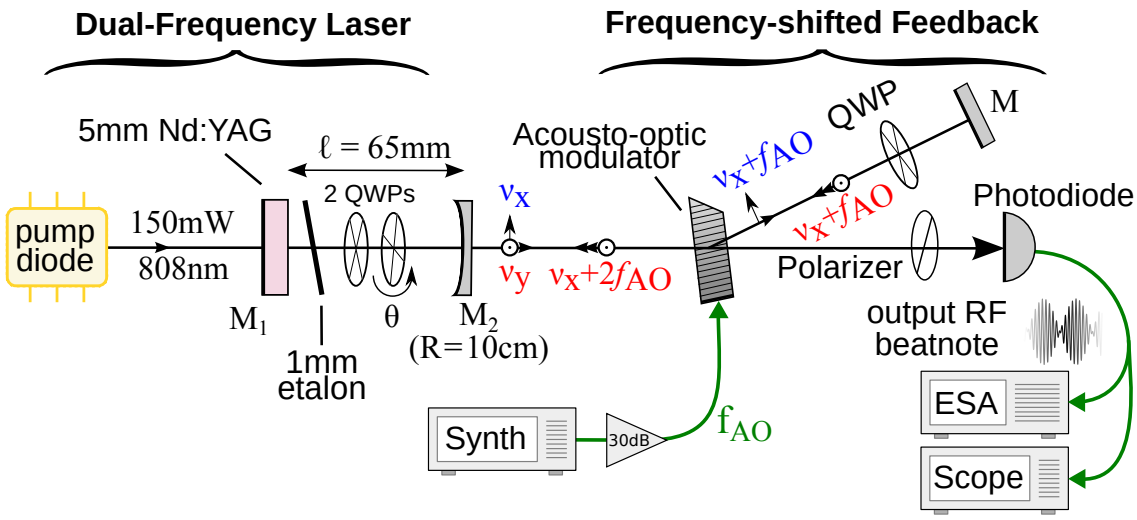

Figure II.4: Frequency-shifted feedback applied to a dual-frequency Nd:YAG laser.

2a Experimental setup

Starting from the dual-frequency laser described in previous section, we add a feedback arm, as presented on Fig. II.4. At the output of the laser, the light goes through a TeO_2 Bragg cell, acting as an acousto-optic modulator (model AA MT80). A piezoelectric element is used to create an acoustic wave in the crystal. It is driven by a sinusoidal voltage at frequency f_{AO}, generated by a reference synthetizer (Adret 740A), and amplified to a maximum of +30 dBm using a MHW592 amplifier. The standing acoustic wave creates a grating, which causes the modulator crystal to deflect the input light by 7 mrad, and to shift its frequency by $+f_{AO}$. The deviated beam goes through a quarter-wave plate, whose neutral axes are oriented at 45° with respect to the polarization direction. Then, the beam ends on a mirror which is adjusted to make it go back on itself, so that it passes through the waveplate, and through the modulator again. To sum up, before being injected back into the laser, the frequency of each mode has been shifted by $+2f_{AO}$ and its polarization rotated by 90°, so that x and y have been exchanged.

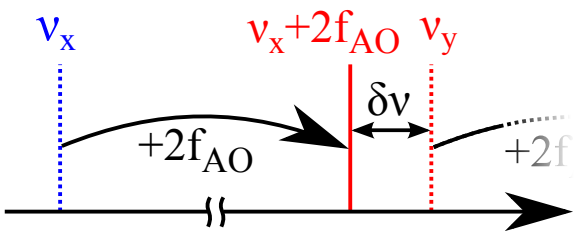

Figure II.5: Principle of the polarization-rotated frequency-shifted feedback. The color denotes the polarization. The dashed frequencies are the output of the laser, while the solid one is the resonant injected signal.

The coupling principle is summarized on Fig. II.5. The driving frequency f_{AO} is chosen so that its double $2f_{\mathrm{AO}}$ is close to the frequency separation of the two modes $\nu_y - \nu_x$. This makes the frequency of the field that is reinjected on the y axis ($\nu_x + 2f_{\mathrm{AO}}$) nearly resonant with the intracavity field on that axis at frequency ν_y. The remaining frequency difference $\nu_y - \nu_x - 2f_{\mathrm{AO}}$ will be referred to as the frequency detuning $\delta\nu$, and will be kept below a few MHz. As the acousto-optic modulator is a resonant element, the range of available shifting frequencies is only 80–100 MHz, and we had to choose $f_{\mathrm{AO}} \approx 90\,\mathrm{MHz}$. In order for the reinjected light to be resonant, the frequency difference $\nu_y - \nu_x$ between the modes has thus to be set to $2f_{\mathrm{AO}} \approx 180\,\mathrm{MHz}$. These values will be used in all the following experiments.

The output of this system is the beatnote between the polarization modes, and can be observed on a photodiode after having been projected by a polarizer at 45°. The resulting RF signal is amplified, and monitored on a Rohde&Schwarz FSV electrical spectrum analyzer, that also acts as a real-time demodulator at $2f_{\mathrm{AO}}$. Its 10 MHz reference is phase-locked to the one of the reference synthetizer, so that it is able to compute not only the beatnote amplitude X, but also the phase difference φ between the beatnote and the reference.

2b Rate equations model

In solid-state lasers, the optical gain comes from the interaction of the field with the doping ions in the crystalline matrix. The "population" that will be taken into account in the laser rate equations is the number of ions in the excited state. However, it is clear that the interaction between the laser field and the ions' dipoles is going to depend on the polarization of the field. This can lead to separate the active ions into three distinct populations, aligned along orthogonal axes [Schwartz09]. However, considering only two populations, each associated with a polarization mode, has been shown to be a sufficient description of the system [Zeghlache95a; Chartier00]. Thus, the following model, introduced in [Bielawski92] and previously studied by [Thévenin12c], describes the evolution of the two polarizations of the electric field $\mathcal{E}_x$ and $\mathcal{E}_y$, and the corresponding normalized population inversion densities N_x and N_y. We recall that, as in Chapter I, the units for electrical field are chosen so that $|\mathcal{E}|^2$ is a density of photons.

$$\frac{\mathrm{d}\mathcal{E}_x}{\mathrm{d}t} = g(1+i\alpha)\left(N_x+\beta N_y\right)\mathcal{E}_x + 2i\pi\nu_x\mathcal{E}_x \tag{II.2a}$$

$$\frac{\mathrm{d}\mathcal{E}_y}{\mathrm{d}t} = g(1+i\alpha)\left(N_y+\beta N_x\right)\mathcal{E}_y + 2i\pi\nu_y\mathcal{E}_y + Ke^{i\psi}\mathcal{E}_x(t-T)e^{4i\pi f_{\mathrm{AO}}t} \tag{II.2b}$$

$$\frac{\mathrm{d}N_{x,y}}{\mathrm{d}t} = -\frac{N_{x,y}}{\tau_c} - \left(\frac{1}{\tau_p}+gN_{x,y}\right)\left(|\mathcal{E}_{x,y}|^2+\beta|\mathcal{E}_{y,x}|^2\right) + \frac{1}{\tau_c}P \tag{II.2c}$$

Similarly to Chapter I, the lifetime of the photons in the cavity is τ_p, while the lifetime of the excited level of the ions population is τ_c. These notations, more usually found in the domain of semiconductor lasers, are chosen for coherence with Chapter III. The factor g quantifies the laser gain. Here we notice that the linear gain includes an imaginary part quantified by the linewidth enhancement factor α. While this is unusual for a solid-state laser, the reasons for its inclusion will be discussed afterwards (Section 4*c*, p. 77), and its value precisely measured in Section 5 (p.82). Finally, P quantifies the density of pumping, assumed to be equal for both polarizations.

A particularity of this model is the presence of a coupling factor β, that quantifies the interplay between the two populations, and highlights the fact that they are not actually two separated populations. More details on this cross-saturation coefficient will be found in Section 2*c* (p. 55). Finally, T is the time delay of the reinjected field, which corresponds to the round-trip time in the feedback arm. In our experiment, the length of the feedback arm is $L = 75\,\mathrm{cm}$, so that $T = c/2L = 5\,\mathrm{ns}$. This means that unless otherwise stated, this delay can be safely ignored, as it is much shorter than the characteristic time scale of the laser, i.e. its oscillation relaxation time, in the tens of microseconds range.

We will now proceed to some normalizations on the model, in order to identify the relevant parameters. When injection is off, the frequency of the relaxation oscillations for the dual-polarization laser is $f_R = \frac{1}{2\pi}\sqrt{\frac{2gP(1+\beta)-1}{\tau_c}}$. As this frequency corresponds to the characteristic time scale of the laser's dynamics, we choose accordingly to use a normalized time $s = 2\pi f_R t$. Numerically, this allows to make the equation non-stiff, i.e. all the variables evolve more or less with the same time scales [Erneux10]. This is known to make numerical simulations much faster and reliable. Also, the reference frequencies for the fields are chosen so that no explicitly time-dependent term appears in the equation. By setting $e_x = \frac{1}{2\pi f_R}\sqrt{\frac{g}{\tau_p}}\mathcal{E}_x e^{2i\pi\nu_x t - i\psi}$, $e_y = \frac{1}{2\pi f_R}\sqrt{\frac{g}{\tau_p}}\mathcal{E}_y e^{2i\pi(\nu_x+2f_{\mathrm{AO}})t}$ and $m_{x,y} = \frac{g(1+\beta)}{2\pi f_R}N_{x,y}$, Eqs. II.2 become:

$$\frac{\mathrm{d}e_x}{\mathrm{d}s} = (1+i\alpha)\frac{m_x+\beta m_y}{1+\beta}\frac{e_x}{2} \tag{II.3a}$$

$$\frac{\mathrm{d}e_y}{\mathrm{d}s} = (1+i\alpha)\frac{m_y+\beta m_x}{1+\beta}\frac{e_y}{2} + i\Delta e_y + \Gamma e_x(s-\tau) \tag{II.3b}$$

$$\frac{\mathrm{d}m_{x,y}}{\mathrm{d}s} = 1-(|e_{x,y}|^2+\beta|e_{y,x}|^2) - \varepsilon m_{x,y}[1+(\eta-1)(|e_{x,y}|^2+\beta|e_{y,x}|^2)] \tag{II.3c}$$

There, we have introduced the following reduced parameters. The factor $\eta = 1 + g\tau_p P(1+\beta)$ is the effective pumping ratio, meaning that $\eta = 1$ corresponds to the laser threshold, i.e. that the lasing starts as soon as $\eta \geq 1$. Then we define the normalized injection delay $\tau = 2\pi f_R T$, for which we have $\tau \ll 1$, so that it will be neglected (except in subsection 4*a*). Finally, we define the normalized injection strength $\Gamma = K/2\pi f_R$, detuning $\Delta = (\nu_y - \nu_x - 2f_{\mathrm{AO}})/f_R$ and damping coefficient $\varepsilon = \sqrt{\frac{\tau_p/\tau_c}{\eta-1}}$.

Analytical study

These rate equations can be rewritten in a slightly simpler form if we write $e_x = |e_x|e^{i\varphi_x}$, we obtain from first equation $\frac{\mathrm{d}\varphi_x}{\mathrm{d}s} = \alpha\frac{1}{|e_x|}\frac{\mathrm{d}|e_x|}{\mathrm{d}s}$. This can be integrated so that $\varphi_x = \alpha\ln|e_x| + \text{const.}$ at any time. This last integrating constant can be arbitrarily set to zero, because the equations are unchanged by the transformation $e_x \to e_x e^{i\psi}$ for any ψ.

$$\frac{\mathrm{d}|e_x|}{\mathrm{d}s} = \frac{m_x+\beta m_y}{1+\beta}\frac{|e_x|}{2} \tag{II.4a}$$

$$\frac{\mathrm{d}e_y}{\mathrm{d}s} = (1+i\alpha)\frac{m_y+\beta m_x}{1+\beta}\frac{e_y}{2} + i\Delta e_y + \Gamma|e_x(s-\tau)|e^{i\alpha\ln|e_x(s-\tau)|} \tag{II.4b}$$

$$\frac{\mathrm{d}m_{x,y}}{\mathrm{d}s} = 1-(|e_{x,y}|^2+\beta|e_{y,x}|^2) - \varepsilon m_{x,y}[1+(\eta-1)(|e_{x,y}|^2+\beta|e_{y,x}|^2)] \tag{II.4c}$$

This transformation is necessary if one wishes to study the bifurcations using the numerical continuation tools introduced in Section I. 2*a*. Also, this reduces the number of equations for the real variables from 6 to 5, which allows for faster numerical integration. Finally, the equations can be rewritten in terms of phase and amplitude by letting $e_y = |e_y|e^{i\varphi}$. Here φ is, up to an additive constant, the phase difference between the two modes. Thus, it also corresponds to the difference of microwave phase between the output beatnote and the reference, that we observe experimentally. Neglecting the time delay τ, Eq. (II.4b) writes:

$$\frac{\mathrm{d}|e_y|}{\mathrm{d}s} = \frac{m_y+\beta m_x}{1+\beta}\frac{|e_y|}{2} + \Gamma|e_x|\cos\left(\varphi-\alpha\ln|e_x|\right) \tag{II.5a}$$

$$\frac{\mathrm{d}\varphi}{\mathrm{d}s} = \frac{\alpha}{2}\frac{m_y+\beta m_x}{1+\beta} + \Delta + \Gamma\sqrt{\frac{|e_x|}{|e_y|}}\sin\left(\varphi-\alpha\ln|e_x|\right) \tag{II.5b}$$

If we consider the steady state of this system, we find that it corresponds to a fourth order polynomial, that can be written for instance in terms of $\widehat{m_y}$:

$$\begin{aligned}0 &= -\beta\varepsilon^2 x\left(\alpha^2+1\right)\left(\beta-1\right)^3\widehat{m_y}^4 + \varepsilon(\beta-1)^2\left(4\alpha\beta\varepsilon\Delta x - \left(\alpha^2+1\right)\left(\beta^2+2\beta x+1\right)\right)\widehat{m_y}^3\\ &+ (\beta-1)\left(4\alpha\varepsilon\Delta\left(\beta^2+2\beta x+1\right) - \left(\alpha^2+1\right)(\beta-1)^2 - 4\beta\left(\Delta^2-\Gamma^2\right)x\varepsilon^2\right)\widehat{m_y}^2\\ &- 4\left(\varepsilon\Delta^2(\beta+1)^2(x+1) - \alpha\Delta(\beta-1)^2 - \varepsilon\left(\Delta^2-\Gamma^2\right)\left(\beta^2 x-2\beta-x\right)\right)\widehat{m_y} - 4\left(\Delta^2-\Gamma^2\right)(\beta-1)\end{aligned} \tag{II.6}$$

with $x=\eta-1$. Each steady state corresponds to a root of this polynomial, so this shows that there are either four, two, or zero steady states. Yet, usually at most two of them have physically reasonable values and only one is stable. When we consider $\varepsilon=0$, the degree of equations (II.6) falls to 2, and steady states can be expressed as $\widehat{m_y} = -2\frac{\alpha\Delta\pm\sqrt{(1+\alpha^2)\Gamma^2-\Delta^2}}{(1+\alpha^2)(1-\beta)}$. The discriminant being proportional to $(\alpha^2+1)\Gamma^2-\Delta^2$, we notice that the steady states merge, then disappear in a saddle-node bifurcation when $|\Delta|=\sqrt{1+\alpha^2}\Gamma$ (see I.2*a*). This usual result in injection-locked system [Wieczorek05; Erneux10] gives the maximum size of the locking range[1]. However, the approximation $\varepsilon=0$ does not allow to compute the stability of this steady state, as the real part of the eigenvalues depends on ε. In particular it cannot be used to locate eventual Hopf bifurcations that could shorten the stable region. In the following we will see that this is indeed the case, and that Hopf bifurcations play an important role.

2*c* Coupling coefficient β

As noted when introducing the model (Section II.31, p. 52), it includes a coupling between each field and the opposite population and vice-versa. This coupling term, that reflects how the light-matter interaction depends on the polarization of the field, has already been introduced by Lamb for gas and solid-state lasers [Sargent74; Brunel97b]. It is commonly quantified in the literature by a factor C, and defined as

[1] We point out that at the first order in ε, the positions of these saddle-node bifurcation are slightly modified, at $\Delta=\pm\sqrt{1+\alpha^2}\Gamma - \alpha\varepsilon\eta\Gamma^2\left(\frac{1+\beta}{1-\beta}\right)^2$, but the maximum size of the locking range is not.

$$\mathcal{C} = \frac{\left.\frac{\mathrm{d}I_x}{\mathrm{d}\gamma_y}\right|_{\mathrm{eq}} \times \left.\frac{\mathrm{d}I_y}{\mathrm{d}\gamma_x}\right|_{\mathrm{eq}}}{\left.\frac{\mathrm{d}I_x}{\mathrm{d}\gamma_x}\right|_{\mathrm{eq}} \times \left.\frac{\mathrm{d}I_y}{\mathrm{d}\gamma_y}\right|_{\mathrm{eq}}} \tag{II.7}$$

Here, $x|_{\mathrm{eq}}$ denotes variations of x around the steady state. $I_{x,y}$ being the intensity of the modes, and $\gamma_{x,y}$ the corresponding laser gain.

In our model, we have $\gamma_{x,y} = N_{x,y} + \beta N_{y,x}$ in the $\varepsilon \approx 0$ approximation. In the steady state, $N_{x,y} \approx r(1 - I_{x,y} - \beta I_{y,x})$, so that $\gamma_{xy} = r\left((1+\beta) - (1+\beta^2)I_{xy} - 2\beta I_{yx}\right)$. We obtain the following correspondences between the notations:

$$\mathcal{C} = \left(\frac{2\beta}{1+\beta^2}\right)^2 \tag{II.8}$$

$$\beta = \frac{1}{\sqrt{\mathcal{C}}}\left(1 - \sqrt{1-\mathcal{C}}\right) \tag{II.9}$$

If we consider the steady state of the non-injected system ($\Gamma = 0$), and linearize around it, we find that it displays two eigenvalues, which correspond to frequencies of small oscillations. One is the usual relaxation oscillation at f_R, and the corresponding eigenvector shows that the oscillations are in phase on each polarization mode. The other, called antiphase oscillation, has a lower frequency f_A, and the property that the corresponding oscillations are on the contrary in phase opposition on each polarization mode [Otsuka92; Lacot96]. Their frequencies are related by the following relationship:

$$\frac{f_A}{f_R} = \frac{1-\beta}{1+\beta} \tag{II.10}$$

This means namely that the measurement of these two frequencies can be used to retrieve the coupling coefficient. As the oscillations at f_A are in phase opposition, they cannot be seen as sidebands of the beatnote produced after mixing the two polarization modes with a polarizer at 45° from the two polarization axes. However, they can be observed on each polarization's intensity noise. As explained in Section I.1, this can be done by measuring the electrical spectrum of the photocurrent at low frequencies. As this noise is very low, for this measurement, we use a 50 dB amplifier. A typical spectrum is shown on Fig. II.6.

In that case we obtain $\beta = 0.20 \pm 0.05$. While we will particularly focus on this value in the following, we happened to also measure another value $\beta = 0.6$ in a different pump configuration. The reason for this is still under study, and may for instance be due to residual intracavity birefringences, that would result in variations of the mode overlapping in the active medium [Pal10]. Section 4*d* will be dedicated to results obtained with $\beta = 0.6$.

The measurement in Fig. II.6 was obtained with a symmetric pumping. By that,

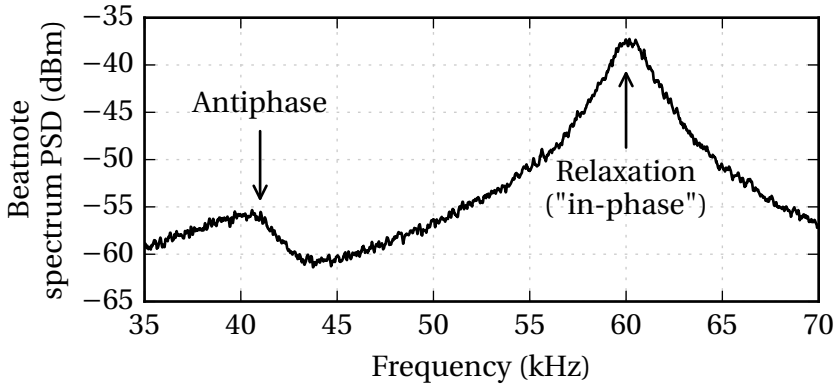

Figure II.6: Intensity noise of the dual-polarization laser, i.e. low-frequency electrical spectrum of the beat-note, showing relaxation and antiphase oscillations.

we mean either an unpolarized beam from a multimode source, or a circularly polarized monochromatic beam with the same diameter. Other cases have been briefly investigated, for instance linearly polarized or elliptic pumping. In such cases, it is expected that the coupling depends strongly on the orientation of the pumping polarization [Schwartz09]. For instance, Fig. II.7 shows the dependence of the coupling on the angle of the pump quarter-wave plate (see Fig. II.1). From this result it is clear that β depends on the ellipticity of the pump polarization. Yet, this result could not be fully explained using a model based on dipoles orientation (see Annex C). Interestingly, the interplay between the polarization of the pump and the light-matter interaction has already been observed before and seem to be a common feature [Zeghlache95b; Verschaffelt08]. Therefore, this topic would indeed benefit from further investigation in future work.

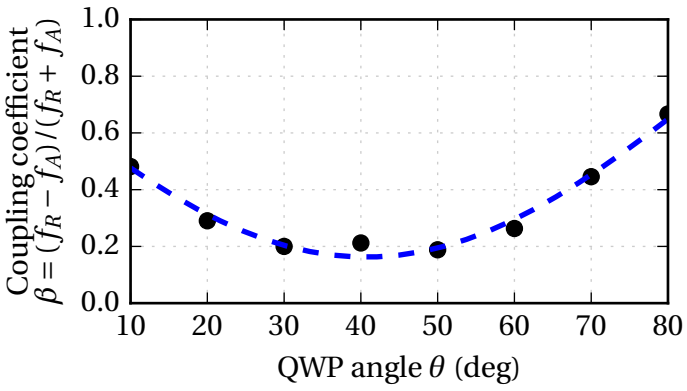

Figure II.7: Coupling factor, in function of the angle of the pump quarter wave plate θ. Dashed curve is the best fit $\beta = 0.77 - 0.6\sin(2(\theta + 0.08))$

3 Results

Being familiarized with the model and its parameters, we will now compare experimental and numerical results obtained on this setup, with a focus on the particular dynamics, and on the stability of the beat-note. Namely, the interesting and measurable outputs of the system that will be studied are the RF amplitude $X = |e_1 e_2|$ and phase $\varphi = \arg e_x e_y^*$ of the beatnote $|e_1 + e_2|^2$. The influence of most of the parameters are studied, but when not otherwise stated the parameters from the following table will be used:

Pump rate $\eta = P_{\text{pump}}/P_{\text{threshold}}$	1.2
Photon (or cavity) lifetime τ_p (sometimes referred as $1/\gamma$)	4.3 ns
Population inversion lifetime τ_c (sometimes referred as $1/\gamma_\parallel$)	230 μs
Damping factor $\varepsilon = \sqrt{\frac{\tau_c/\tau_p}{r(1+\beta)-1}}$	0.01
Coupling factor β	0.20 ± 0.05
Linewidth enhancement factor α	0.28 ± 0.04
Relaxation oscillations frequency f_R	≈ 70 kHz

Table II.1: Summary of parameters

The linewidth enhancement factor α was only precisely measured after some of the following studies were made, so that in many of them, a less precise value $\alpha = 0.2$ has been used. We do not expect this to greatly alter the results. Also, in the thesis from J. Thévenin that preceded this work [Thévenin12c], and in some previous studies such as [Thorette16; Romanelli14; Romanelli16; Thévenin12a], the coupling factor β has been measured to be 0.6 and the linewidth enhancement factor was not identified ($\alpha = 0$) so these values are of a particular interest.

3.a Locked state, bounded phase

Steady state and bifurcation diagram

Experiments have shown that frequency-shifted feedback allows to lock the frequency difference on the external RF reference [Thévenin11b]. In the terms of our model, this means that the phase of the beatnote φ is kept constant, along with the output intensities of each mode. This corresponds to a stable steady state of the rate equations. In the previous section it was shown that this can be only achieved for $|\Delta| < \sqrt{1+\alpha^2}\Gamma$, i.e. that there is a *locking range* in which phase locking can happen.

The range of existence and stability of this steady state can be studied when varying parameters of the model. In a similar process to the example of Section I.**??**. The

corresponding bifurcation diagrams, showing the location of bifurcations, have been computed using the AUTO program, with fixed parameters from Table II.1 and varying Δ and Γ. The result is shown on Fig. II.8.

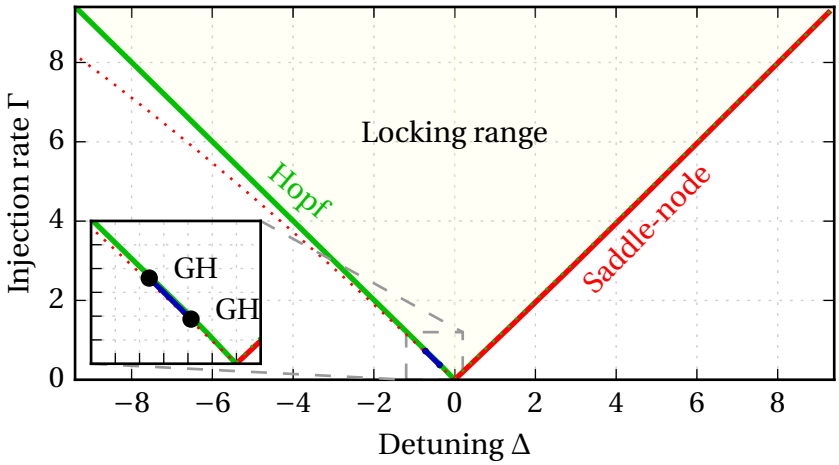

Figure II.8: Bifurcation diagram, showing the range of existence of a stable equilibrium. Green: Supercritical Hopf bifurcation, dark blue: subcritical Hopf bifurcation, red: saddle-node bifurcation. The dotted red line is a saddle-node bifurcation of the unstable equilibrium. GH: Generalized Hopf point, i.e. change of criticality of the Hopf bifurcation.

We first notice that the bifurcation diagram is asymmetric with respect to the detuning Δ. As said in Chapter 1, this is a consequence of a non-zero α factor. Yet, as long as $\alpha \ll 1$ the unlocking happens roughly for $|\Delta| \approx \Gamma$ on each side of the locking range. We will see that this is partly due to the internal coupling $\beta \neq 0$. The asymmetry with respect to Δ concerns the unlocking process, that depends on the sign of the detuning, and on the injection rate Γ. According to the bifurcation diagram, for $\Delta < 0$, the steady state meets a Hopf bifurcation. For high injection, when $\Gamma > 1$, this bifurcation is what is called a *supercritical* Hopf bifurcation. This means that crossing the bifurcation line leads to small oscillations around the now unstable equilibrium point, and that this limit cycle grows with the detuning Δ. When $\Gamma < 1$, there is a also small region in which the Hopf bifurcation is on the contrary *subcritical*. This means that the limit cycle is unstable, and that the change at the border of the locking range is not smooth [Strogatz01]. This is seen in the inset of the diagram, between the two GH (Generalized Hopf) points, that correspond to a change of the criticality of the Hopf bifurcation. For $\Delta > 0$, the equilibrium first encounters a saddle-node bifurcation, i.e. it simply vanishes. The system then jumps on another attractor. A Hopf bifurcation still exists, but it concerns the remaining unstable equilibrium, and happens slightly after.

Bounded phase oscillations

While the bifurcation diagram gives information on the steady states, and thus on the locking range, it doesn't say much on what happens outside of it. Thus, we resort on numerical integration of the equations, and compute "numerical" bifurcation diagrams, by time integrating the model for various parameters. Some results for large values of Γ can bee seen on Fig. II.9. The rate equations are integrated for $\Delta = 0$ until a stationary regime is reached, and the extrema values for φ and e_x are plotted. Then the detuning value Δ is slightly changed, and the simulation is restarted from the previous values. This has been done for $\Delta > 0$ and $\Delta < 0$.

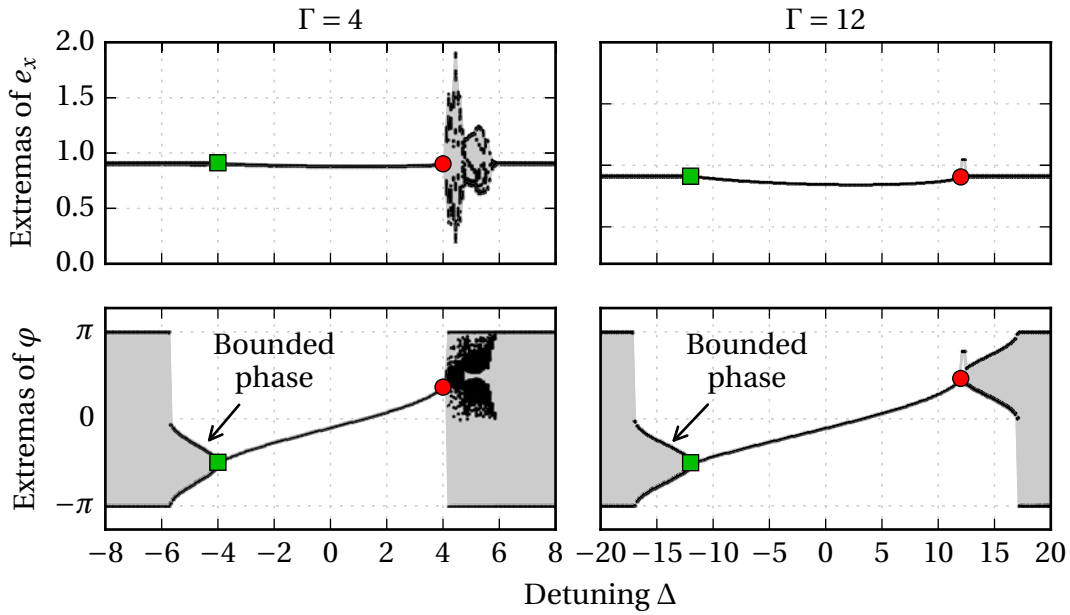

Figure II.9: Numerical bifurcation diagrams, obtained by integration of the rate equations. Green square: Hopf bifurcation, red circle: saddle-node bifurcation.

Once the system leaves the locking range, one possibility is that it goes through a smooth bifurcation (supercritical Hopf) and a limit cycle appears. This oscillation has initially a small amplitude, and grows as $|\Delta|$ moves farther from the locking point. What is interesting is that as the oscillation is initially small, the phase difference φ between the beatnote and the reference remains in the $[-\pi, \pi]$ range for values of the absolute detuning not too far from Γ. The bounded phase region corresponds to the range in which it happens [Braza90; Kelleher10; Thévenin11a]. At high injection rates ($\Gamma \gg 1$), it is located near the boundaries of the locking range, even for $\Delta > 0$. Indeed, as seen on the right panel of Fig. II.9, for positive detuning values, the first bifurcation of the steady state is a saddle-node. Yet, after a very short chaotic span, the system will settle again on a limit cycle. Note that this is not the case for lower values of Γ, as seen on the

left panel of the same figure. The “threshold” value depends on α, and allows a rough estimation of its value.

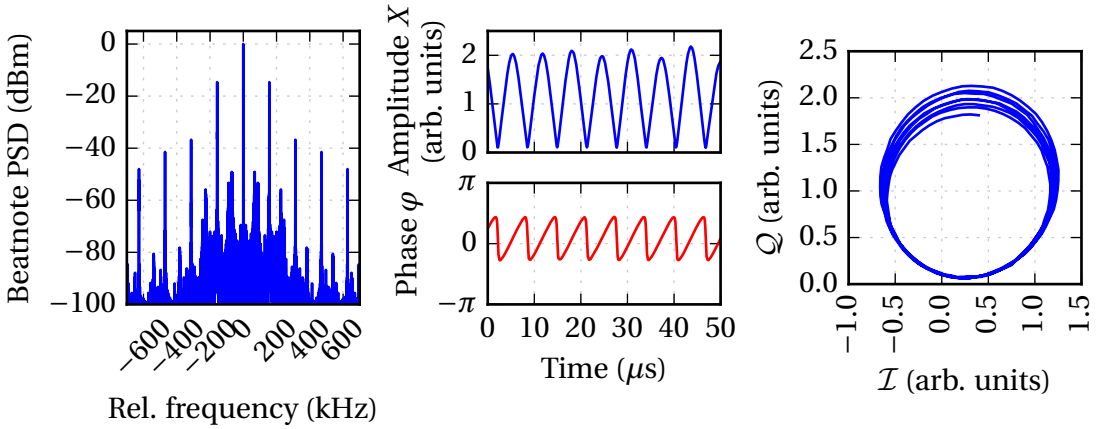

Figure II.10: Experimental observation of the bounded phase regime, using IQ demodulation with a bandpass of 10 MHz around $2f_{\mathrm{AO}}$. The slight changes in amplitude at each cycle, visible on the right panel is due to experimental drifts.

Bounded phase regimes are a common feature in a lot of dynamical systems and various fields of science, from simple optically injected lasers [Kelleher12], to cavity solitons [Vahed11], electronic oscillators [Chakraborty88], biological systems [Kronauer82], hydrodynamics [Li13], or nanomechanics [Barois14]. Each time, they are intimately linked to the presence of a Hopf bifurcation. In such regimes, the mean value of the phase taken on the time scales of a few oscillations remains constant. This signifies that the mean output frequency is constant and thus that the beatnote frequency can be said to remain effectively locked on the reference. This is why this phenomenon has been dubbed “frequency locking without phase locking” [Thévenin11a]. Indeed, on the electrical spectrum of Fig. II.10, we see a sharp peak at the reference frequency $2f_{\mathrm{AO}}$, that does not drift and remains very stable. But it features harmonic sidebands that correspond to the bounded phase oscillation, as seen on the other panels of the figure. This will be confirmed by phase noise measurements and simulations, which will be presented on Fig. II.19 and Fig. II.20 in Section 4. There we will see that the long-term stability of the reference is still present on the beatnote, as the phase noise remains as close to the one of the reference as for the locked regime [Romanelli14].

3b Exhaustive mapping for $\Gamma \lesssim 1$

Until now, we have mostly considered the case of large injection $\Gamma > 1$. This would allow large locking ranges $|\Delta| > 1$, and an extended partial synchronization region, where bounded phase is observed. However, it is known that if the detuning is close

to or lower than the relaxation oscillation frequency, the system can become very sensitive to the changes of its parameters, and that chaotic dynamics are commonly found [Hugon11; Thévenin12a]. Thus, we have investigated precisely the different behaviors outside the locking range, particularly in the domain $\Gamma \lesssim 1$.

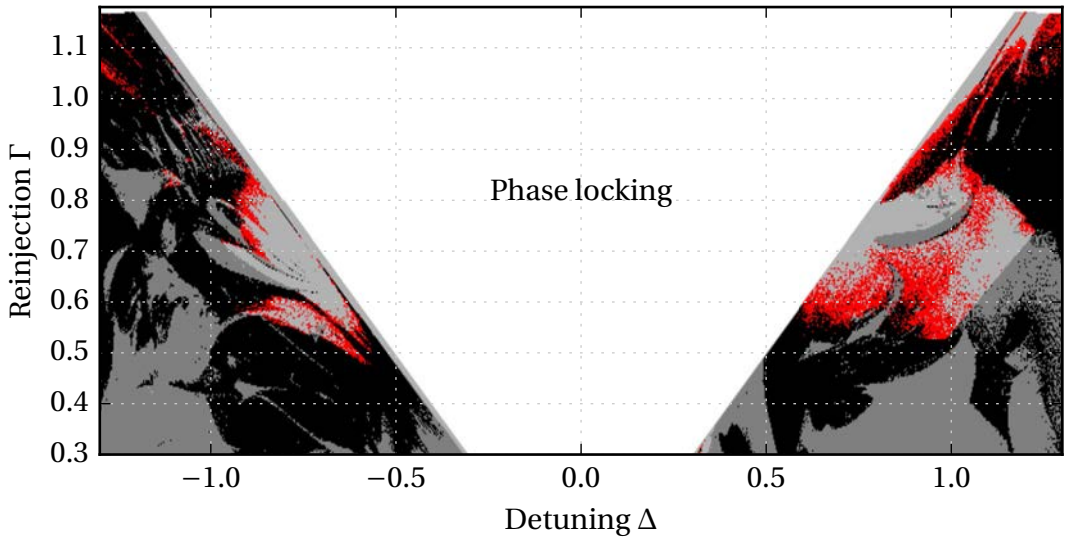

Figure II.11: Map of the different regimes for $\beta = 0.2$ and $\alpha = 0.28$. □ White: locking range, ■ gray: unbounded, ■ light gray: bounded phase (existence of at least a stable limit cycle for which φ is bounded), ■ black: existence of at least one unbounded chaotic attractor, ■ red: existence of bounded chaos.

The mapping of all the available regimes in this region of interest $\Delta, \Gamma \lesssim 1$ is shown on Fig. II.11. Some considerations on how it has been obtained are necessary. Namely, it has been produced using the following steps. For each point (Δ,Γ), numerical integrations have been performed starting from 100 random initial values, taken arbitrarily in the range $[0,3]$ for $|e_{x,y}|$, $[-\pi,\pi]$ for φ and $[-6,6]$ for $m_{x,y}$. Then, the resulting asymptotic states for $s > 40000$, that are called attractors, have been studied and compared to each other using the Hausdorff distance[2]. As a criterion to discriminate identical attractors from different ones, we found that an arbitrary chosen threshold of 1 on their Hausdorff distance would give good results. This allowed us to group them by similarity, and to obtain a list of attractors, including chaotic ones, for each (Δ, Γ) point.

Then, we would like to classify each attractor according to two properties: (i) is it

[2]The Hausdorff distance is often used as a measure of the similarity of two sets of points X and Y. It is defined for finite sets as $\max\left(\max_{y\in Y} d(y,X), \max_{x\in X} d(x,Y)\right)$ where $d(x,Y)$ is the distance between the point x from the set X and the set y. Here we have used Euclidean distance, so that $d(x,Y) = \sqrt{\min_{y\in Y} \sum_k (x_k - y_k)^2}$ where $\sum_k$ is a sum on the components of the points. By doing so, we compare the geometrical likeness of the two attractors, not taking in account the time evolution.

For the ordinary differential equation $\dot{y} = f(y)$, where y is a vector of N rows, we define a perturbed trajectory vector ε, initialized with $\varepsilon_k = |\varepsilon_0|/\sqrt{N}$. We have taken $|\varepsilon_0| = 10^{-6}$. The first Lyapunov exponent is initially $\lambda_1 = 0$, and we compute it by steps using the following algorithm:

1. Integrate the equations $\mathrm{d}y/\mathrm{d}t = f(y)$ from time t to $t+\theta$. We used $\theta = 1$.
2. Integrate the same equation on the same time span, but with perturbed initial conditions equations $y'(t) = y(t) + \varepsilon$.
3. Compute the norm of the final perturbation $\varepsilon = y'(t+\theta) - y(t+\theta)$: $|\varepsilon| = \sqrt{\sum_k \varepsilon_k^2}$. The first Lyapunov exponent λ_1 is increased by $\frac{1}{\theta}\log|\varepsilon|/|\varepsilon_0|$.
4. Scale down the perturbation to $\varepsilon\frac{|\varepsilon_0|}{|\varepsilon|}$, and integrate again, starting at $t+\theta$ (step 1). Repeat while $t < T$ (we used $T = 10000$).

Figure II.12: Algorithm used for the computation of Lyapunov exponents.

chaotic ? (ii) does it features bounded or unbounded oscillations of the phases ? The second property is trivially obtained from the integrated solution, and the first one can be answered by computing the first Lyapunov exponent λ_1 of the solution. This number quantifies the convergence or divergence of very close trajectories in phase space. While a non-chaotic attractor will show a convergence of infinitesimally spaced trajectories, a characteristic feature of chaotic evolution is that two initially different trajectories will ultimately diverge. Thus, it is quite common to consider the sign of the largest Lyapunov exponent as a criterion for deciding whether a trajectory can be considered as chaotic or not [Skokos10]. It was computed using a simple method, described in [Sprott94], that consists in studying the evolution of a small perturbation along the trajectory. We have summarized the corresponding algorithm in Fig. II.12.

Note that we tried other methods, such as the Cayley decomposition method, or QR decomposition method, but they were not found as effective in our case [Skokos10]. Finally, we combined the data on Lyapunov exponents, multistability, and phase extrema on the map shown on Fig. II.11.

As it appears, various attractors exist and co-exist. They are of different kinds, for instance some feature periodic oscillations, either with a single period (limit cycles) or with two periods (limit torus). The oscillations of the phase φ can be bounded or unbounded. With respect to this fact, we note that the loss of frequency locking is not a strict bifurcation of the system, as it does not correspond to a change in the topology of the attractor.

Chaotic attractors can also be found, sometimes in combination with the other ones. The associated time dynamics are often a kind of quasi-periodic spiking behavior, with chaotic intensity and slight variations of the period.

A regime of particular interest is highlighted on this mapping in red, and corresponds to chaotic attractors for which the phase excursion never exceeds 2π. This means that while the time evolution is chaotic, the phase remains bounded, and the frequency locking is maintained. We named this regime "bounded phase chaos", and will study it in details in the next section.

To conclude with Fig. II.11, note that it is often possible to get different results if different initial conditions are used. This phenomenon, called multistability, corresponds to the coexistence of multiple attractors. For instance, Fig. II.13 shows how the choice of different initial values for $|e_x|$ and m_x affects the final attractor reached by the system. In that case, they are very different indeed, as one is chaotic, and the other is not. As seen of the figure, there is no simple pattern, and a zoom on the map shows ever finer details, a feature which could point to a fractal nature of theses attraction basins.

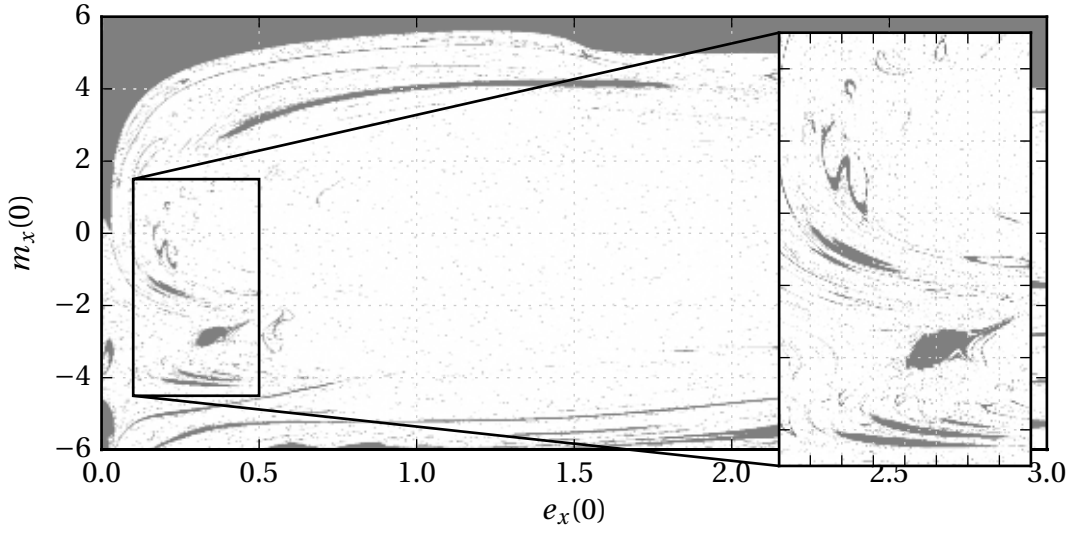

Figure II.13: White: non-chaotic limit torus. Dark: chaotic attractor. Parameters are $\Delta = 0.6$, $\Gamma = 0.5$, $\beta = 0.6$ and $\alpha = 0$. Other initial conditions are $e_y = 0$ and $m_y = 0$.

4 Bounded phase chaos

Numerical prediction

The chaotic regime with bounded phase oscillations we have observed on the previous mapping is quite unique, because it combines chaotic oscillations of the beatnote amplitude and phase, while keeping the mean frequency synchronized on the reference. Another viewpoint is that it is a regime of chaotic synchronization between the two polarization modes, and that this synchronization is strong enough to keep the phase difference under 2π. We will present here some results obtained for $\alpha \neq 0$. It should be noted that the same results were also obtained for $\alpha = 0$ and $\beta = 0.6$ when it was not known that a linewidth enhancement factor had to be included, and have been published in [Thorette16].

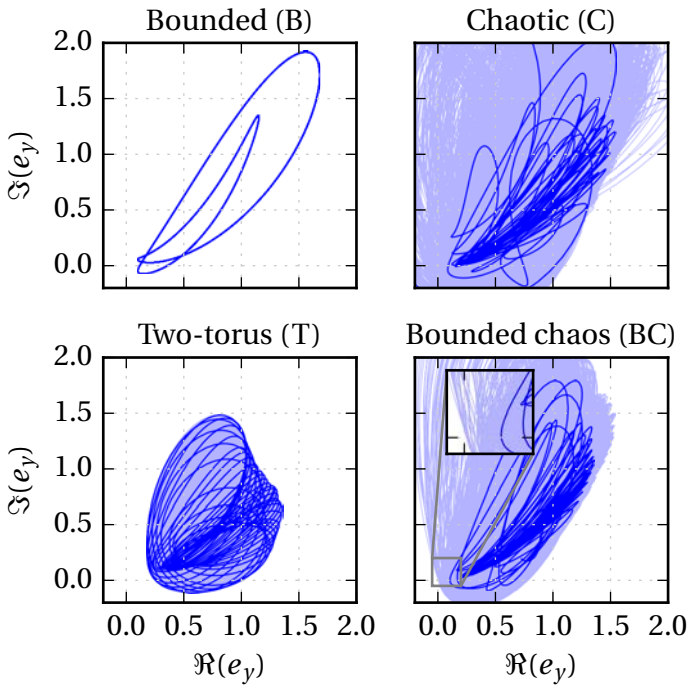

Figure II.14: Numerical time series in the bounded chaos regime, for $\Gamma = 0.85$ and different values of the detuning: (B) $\Delta = -1$, (C) $\Delta = -0.9$, (T) $\Delta = -0.95$, (BC) $\Delta = -0.87$. Solid blue line corresponds to 200 time units, and light blue to 50000.

Fig. II.14 shows some regimes that can be obtained for an identical value of the injection $\Gamma = 0.85$, and different values of the detuning. What we can see ranges from complex bounded phase cycles with two peaks, plain chaotic regimes, and bounded phase oscillations with two periods (two-torus). Finally, close to the locking range, we encounter the bounded chaos regime, which combines chaotic oscillations and a

bounded phase property. Fig. II.15 shows more clearly the evolution of the amplitude and phase in this regime. It is a regime of spiking with pseudo-period of approximately 120 normalized units, modulated by roughly 20 faster oscillations with quite variable amplitudes.

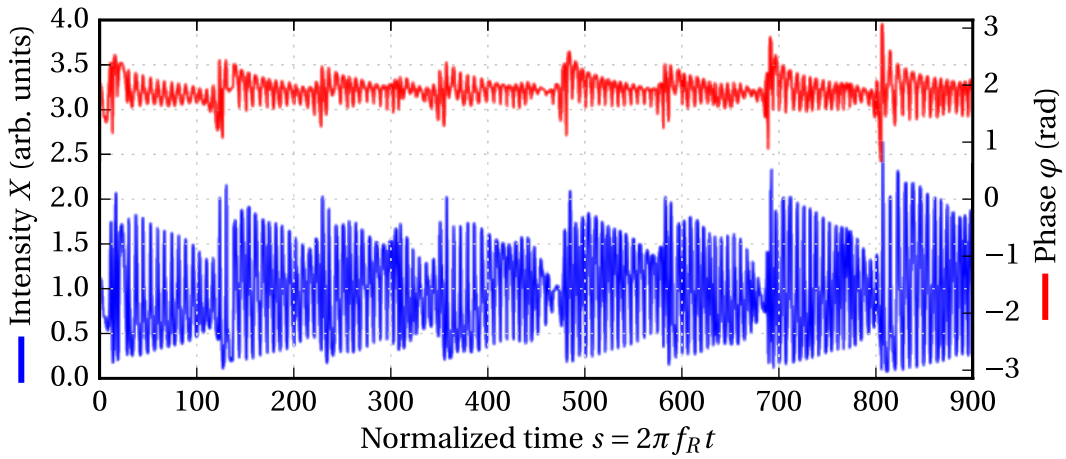

Figure II.15: Computed amplitude (blue) and phase (red) of the beatnote for the bounded phase chaotic regime, at $\Gamma = 0.85$ and $\Delta = -0.87$.

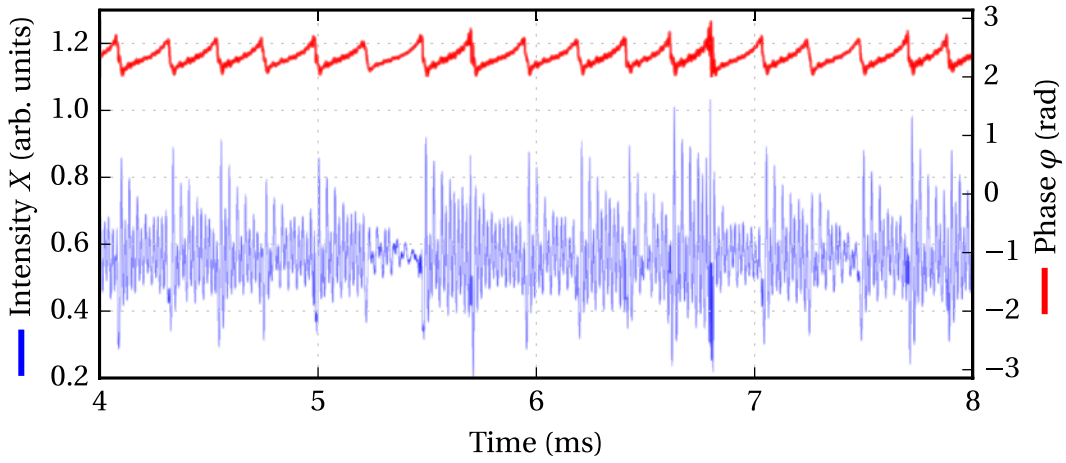

Figure II.16: Experimental time series in the bounded chaos regime.

Experimental observation

The particular bounded phase chaotic regime is located in quite small regions of the parameter space, so that fine control of the experimental parameters is needed if one hopes to observe it. Unfortunately, the injection strength Γ depends on a lot of

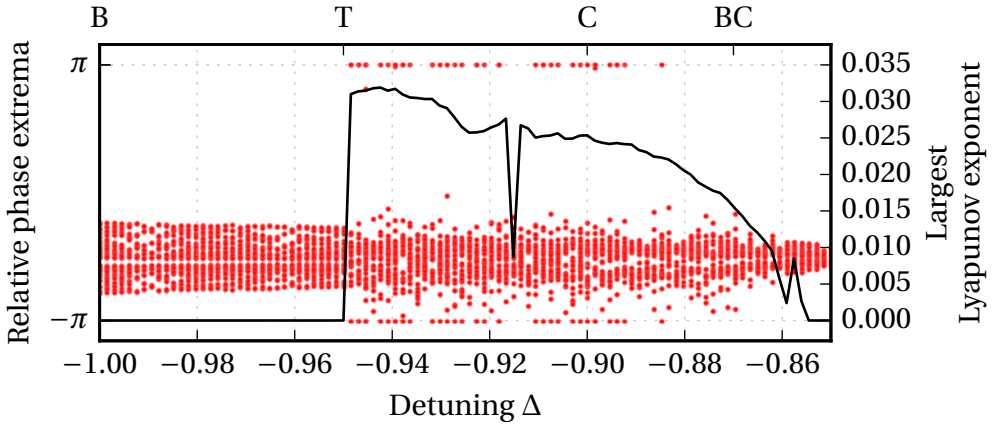

Figure II.17: Simulated bifurcation diagram of phase extrema for $\Gamma = 0.85$. Final state at each point is taken as the initial conditions for the next point, as Δ is decreased. The largest Lyapunov exponent is computed for each point and plotted as the solid black line. The B, T, C, and BC labels correspond to the ones from Fig. II.14

parameters, such the mode matching between the cavity and injected fields, so that its absolute value cannot be measured easily. However, there is a range $0.8 < \Gamma < 1.1$ for which chaotic bounded phase is predicted on the border of the locking range. This is highlighted on Fig. II.17, which shows the superposition of the numerical bifurcation diagram with the value of the largest Lyapunov exponent. As the free-running beatnote frequency is quite stable thanks to the single-mode pump diode, the detuning can be controlled precisely. The injection rate is set to a value in the correct region, using the fact that the half locking range is Γf_R. Then the detuning is slowly changed until the system leaves the locking range. This method allows to observe experimentally this peculiar regime. However, the system usually remains in this regime for less than a minute, because the drift of the injection rate and detuning will slowly drag it out of the bounded phase region, or back into the locking range.

Fig. II.16 show the demodulated time evolution we observed, and Fig. II.18 its complex plane counterpart. As anticipated, the phase features small chaotic oscillations, with amplitude less than 1 rad. On a time scale of 250 µs, the phase rises, and then drops to its start value again. These pseudo-cycle have varying periods and amplitudes, and are associated with amplitude bursts, modulated with faster oscillations.

Phase noise properties

When the phase difference between the modes is constant or bounded, we can consider that the frequency difference is locked on the reference. On the electrical

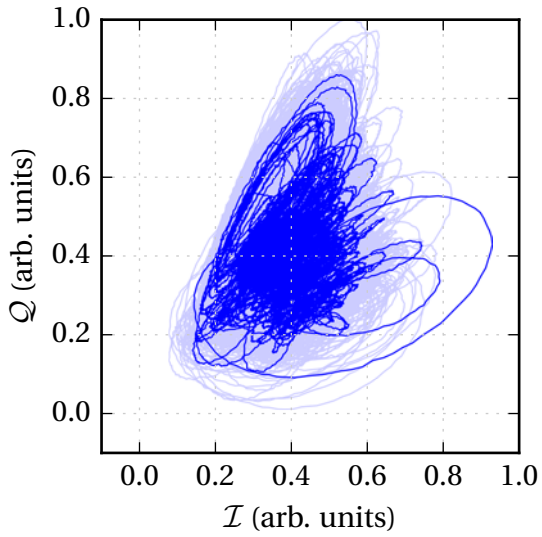

Figure II.18: Complex plane visualization of the experimental time series from Fig. II.16, showing bounded phase chaos. Light blue region corresponds to a recording of 100 ms, while dark blue is 4 ms.

spectrum, this corresponds to a sharp stable peak at $2f_{\mathrm{AO}}$. But if we look more closely, the reference signal is transfered to the output beatnote by a non-linear coupling inside the laser. Consequently, additional noise coming from other sources, may very well be superimposed on the output frequency. This can be quantified experimentally and numerically in terms of phase noise of the output, as defined in Section 3*a*.

Experimentally, the phase noise was measured in the different regimes using the recorded demodulated phase from the Rohde&Schwarz FSV. The demodulation has a maximum bandwidth of 30 MHz. Then, the phase noise was computed from the power spectral density of the phase φ using a multitaper method [Prieto09]. At low offset frequencies, we see here that frequency-shifted feedback effectively transfers the long-term stability of the reference to the beatnote, either in the locked or bounded phase regimes, as the phase noise level is at least 30 dB below the free-running level. This feature seem to be generic in system with Hopf bifurcations, and subsists on simpler models [Romanelli14]. Even in the chaotic bounded phase regime, the phase noise at 100 Hz from the carrier is reduced by the same amount. However, either periodic bounded phase oscillations, or chaotic ones add their footprint on the phase noise: sharp peaks at the cycle frequency for the first ones, and a continuous spectrum for the second. For the latter, broad peaks at harmonics of 5 kHz are seen, and they indeed correspond to the pseudo-frequency of the chaotic spikes.

As a test of the accuracy of the numerical model, phase noise was also computed numerically, by introducing Gaussian white noise on η, Δ and Γ. A few methods were

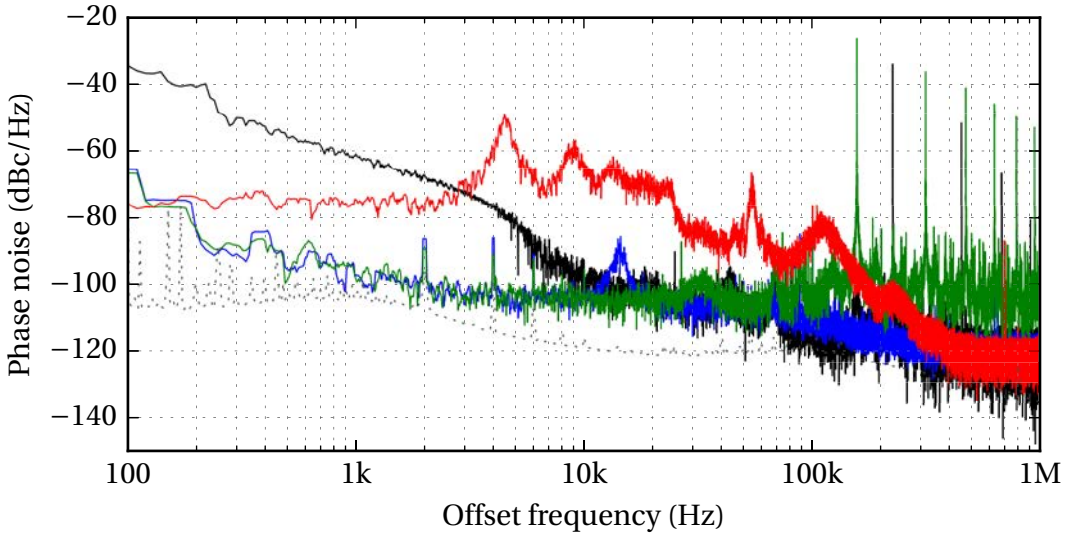

Figure II.19: Phase noise in different regimes, measured by demodulating the output beatnote, and calculated from the phase with a multitaper method. Legend: ▬ Free running, ▬ locked, ▬ bounded phase, ▬ chaotic bounded phase. Gray dotted line: reference oscillator.

used, but did not seem to give very different results (see Annex D). Fig II.20 shows the simulated phase noise in the different regimes: locked, unlocked, bounded, and bounded chaotic. It is qualitatively similar to the experimental observations, and leads to the same conclusions. Quantitative agreement was not sought, as it would require a more precise characterization of the relevant experimental noise sources to be inserted in the model.

4*a* Influence of the feedback delay

Until now, we have neglected the time lag associated with the reinjected field. Indeed, this time was very small compared to the response time of the laser. However, the goal of Chapter III will be to apply a similar synchronization mechanism to semiconductor lasers for which the intrinsic time dynamics are much faster, so that this delay will likely become a key component in the observed behaviors. In order to make a first step toward this, we added an artificial delay in our setup, in the form of a fiber coil inserted in the feedback arm. The modification of the setup is shown on Fig. II.21. The quarter wave plate and the mirror have been removed, and the light is now injected into a single-mode Hi-1060 fiber. We then add a coil of fiber in order to delay the signal, and finish with a fibered Faraday mirror. This component associates a polarization-rotating device (Faraday rotator) and a mirror, so that the two polarization modes are correctly swapped before being sent back to the laser. This setup is particularly

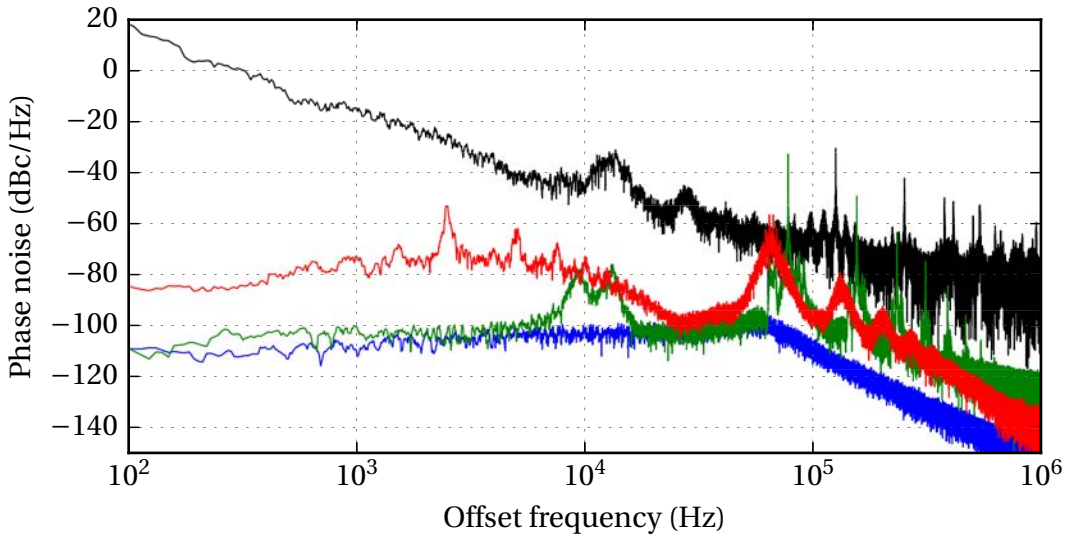

Figure II.20: Simulated phase noise in different regimes, for $\Gamma = 0.9$. Legend: Free running ($\Delta = 1.8$), locked ($\Delta = 0.8$), bounded phase ($\Delta = 1.1$), chaotic bounded phase ($\Delta = 0.91$).

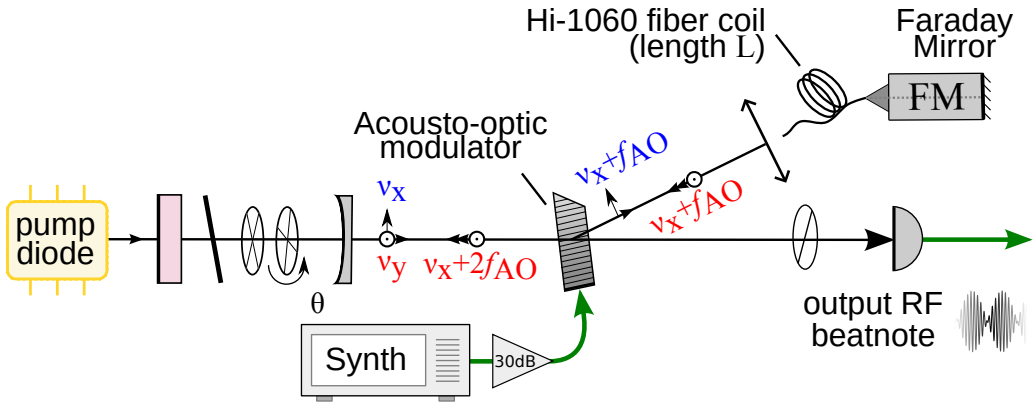

Figure II.21: Experimental setup with fibered end of feedback arm, including a fiber coil as an artificial delay.

interesting, because it also allows to compensate the birefringence of the fiber. Indeed, the effects of the birefringence on the way to the mirror are compensated by the same effects on the way back, so that after the round-trip the polarization state are still aligned with those of the input.

Three fiber lengths have been used: 10 m, 30 m and 100 m. They correspond to time delays of respectively 0.1 µs, 0.3 µs and 1 µs, which, normalized to the oscillation relaxation time scale give τ values of 0.05, 0.15 and 0.5. A 5 km fiber coil was available in the lab. Its use was planned, as it would have created a delay of 50 µs (or 25 in normalized units).

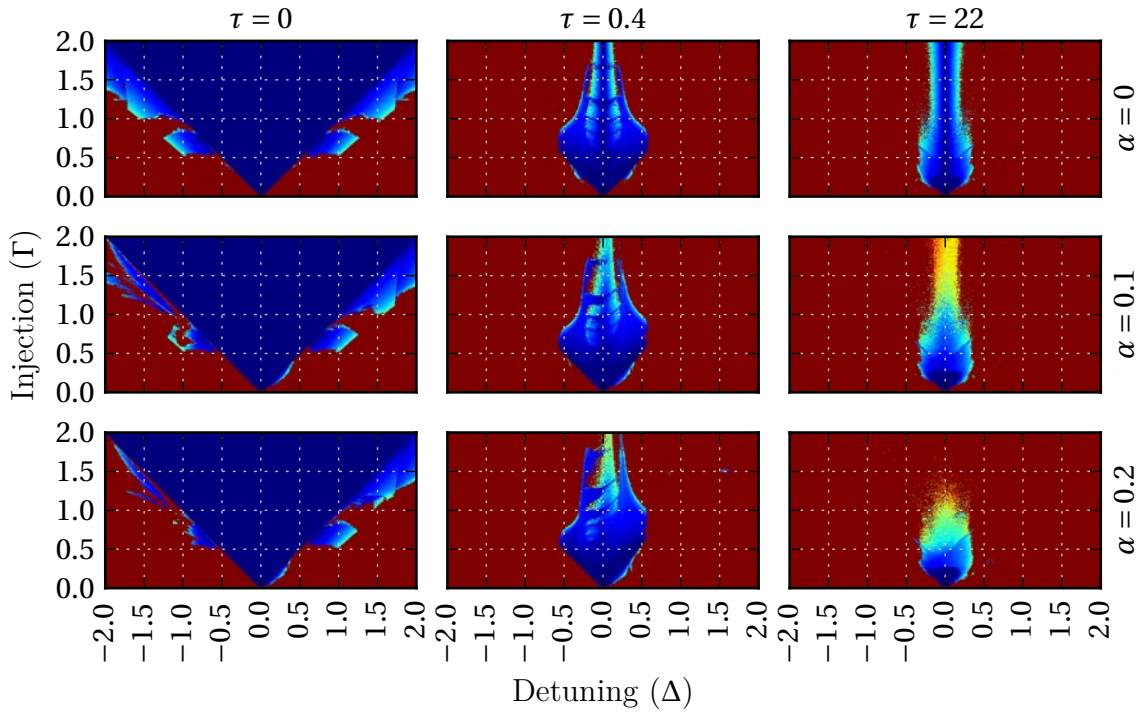

Figure II.22: Map of the phase extrema obtained for $\beta = 0.2$ and different values of α and τ.

Introducing a time delay $\tau \neq 0$ turns the rate equations II.4 into delayed differential equations (DDE). The RADAR5 code, a numerical integrator specifically designed for such equations was used to integrate them. It relies on an implicit Runge-Kutta method, using collocations based on Radau nodes, and is well adapted to stiff equations [Guglielmi05]. As it is an old FORTRAN program, a Python wrapper was specifically developed (see Annex E). Mappings of the dynamics were computed for varying Δ and Γ in the resonant injection regime. For each point of parameters, the stationary phase difference φ was recorded, and plotted in Fig. II.22. As can be seen in these maps, the primary effect of a non-zero delay is to dramatically reduce the locking range as soon as the injection level Γ exceeds 0.5. This effect can already be seen for quite small delays, here $\tau = 0.4$, and indeed for larger delays, such as $\tau = 22$.

Experimentally, a reduced locking range has been also observed for large delays. While the 10 m and 30 m fiber coils ($\tau = 0.05$ and 0.15 respectively) barely affect the dynamics, using a 100 m coil ($\tau = 0.5$) results in a reduction of the locking range for small injection rates, and in its disappearance for larger values of Γ. This can be seen on Fig. II.23, where the maximum amplitude of the beatnote has been recorded while the detuning was swept, and the injection rate kept constant. The smallest amplitude corresponds to the locked state, where the beatnote is not modulated by the dynamical output of the laser. While the locking range does not vary appreciably

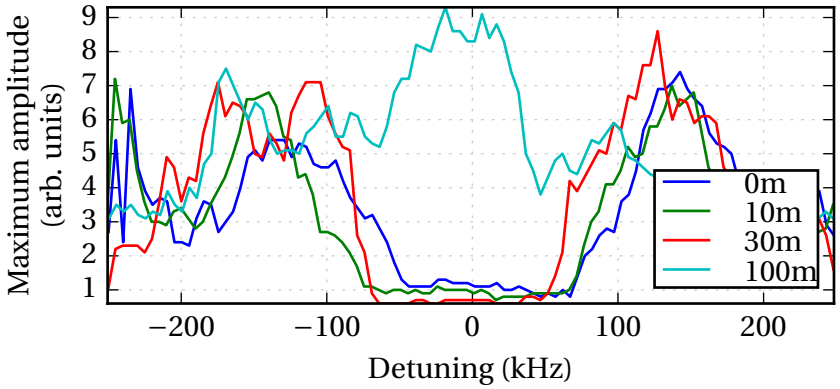

Figure II.23: Maximum amplitude of the beatnote during a detuning sweep, for $\Gamma = 1.2$. The feedback delay was varied using different fiber lengths.

for the two first fiber length, we see that it has disappeared when the feedback time is further increased. This is confirmed by Fig. II.24, where the 100 m coil was used, and the feedback strength Γ was changed. While for lower Γ we still notice a locking range, it vanishes for higher values. These observations match correctly the numerical predictions from Fig. II.22

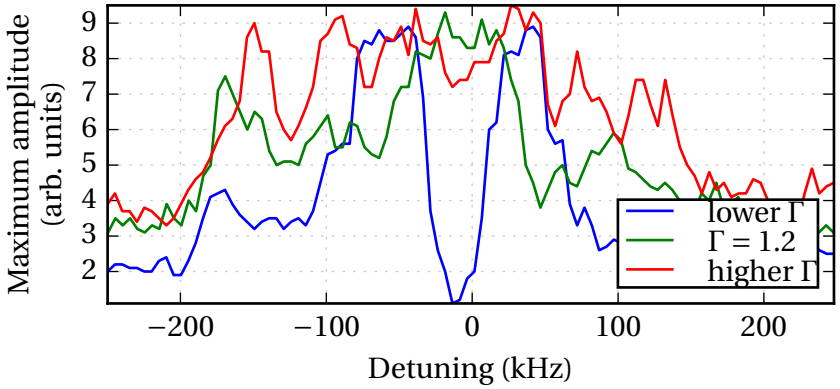

Figure II.24: Maximum amplitude of the beatnote during a detuning sweep, for a fixed fiber length of 100 m, corresponding to a normalized delay $\tau = 0.5$. The feedback strength is changed from $\Gamma < 1.2$ to $\Gamma > 1.2$.

Experimentally, we observed another effect of the delay on the stability of the beatnote, that is not accounted for in the model. Indeed, as the light travels in the fiber, it accumulates an optical phase $2\pi\nu_{x,y}\frac{n_f L}{c}$ where n_f is the optical index of the fiber. This index is prone to slow thermal and mechanical drifts, may be slightly modified by acoustic noise, and can also include a dependency on the optical frequency. This phase adds to the optical feedback phase ψ included in the model in Eq. II.2b. While this feedback phase could be removed from the rate equations by selecting an appropriate

phase reference in the normalization of $\mathcal{E}_x$, it is nevertheless reported on the output RF phase of the beatnote $\varphi = \varphi_x - \varphi_y$. In short, even though it can not affect the dynamics of the laser, it is still present in the RF output phase. While this goes unnoticed when this term is constant, this means that any perturbation of the feedback phase is reported on the RF phase of the beatnote. Experimentally, this means that for the 100 m coil, the synchronized state will nevertheless feature a slow phase drift, depending on the temperature, acoustic noise, etc. Countermeasures were investigated, such as sealing the fiber coil in a vacuum chamber in order to reduce the acoustic and thermal fluctuations, but no significant enhancement could be noticed up to a surrounding pressure of 1×10^{-2} mbar. This actually prevented us from using any delay longer than 100 m. Namely, the planned 5 km coil could not be used, because it would result in an excessive phase drift, and in the inability to observe the locked state anymore.

In order to see if this low-frequency phase noise is indeed reported from the optical feedback phase, or if there is also an additional noise of intrinsic dynamical origin, we computed numerically the phase noise for various values of α, β and τ. This is summarized in Fig. II.25. If one look at the experimental values $\alpha = 0.2$ and $\beta = 0.2$ in the rightmost panel of the second line, we can see that the phase noise is 20 to 30 dB higher at low offset frequencies when the delay is not zero. We can thus expect that the observed phase noise comes not only from the optical phase variations, but also from the fact that the synchronization quality is degraded by the delay. We note that the added phase noise at low offset frequencies does not grow monotonously with delay, as $\tau = 0.4$ has a higher noise than $\tau = 22$. Also, this degradation completely disappears for other values of α and β, for which the phase noise appears to be insensitive to the delay.

To sum up the study on the delay, we notice again a good model-experiment agreement. The main consequence of the delay, in the range of values we could explore, is a disappearance of the locking range in favor of phase drift or chaotic oscillations. In this region, we have observed that it is much easier to obtain a stable regime combining chaotic spiking and bounded phase. This was not investigated in depth, but was thought to be a good candidate as a signal generator for chaotic LIDAR-RADAR applications [Lin04a; Lin04b]

4b Bounded chaotic "spike triggering" (excitable-like)

As could be seen in the previous results, in the resonant injection regime ($\Gamma \lesssim 1$), our system features sharp transitions when leaving the locking region. When the detuning crosses a threshold value, the system jumps to an attractor which creates spiking dynamics, often with chaotic amplitude and pseudo-period. This effect of a

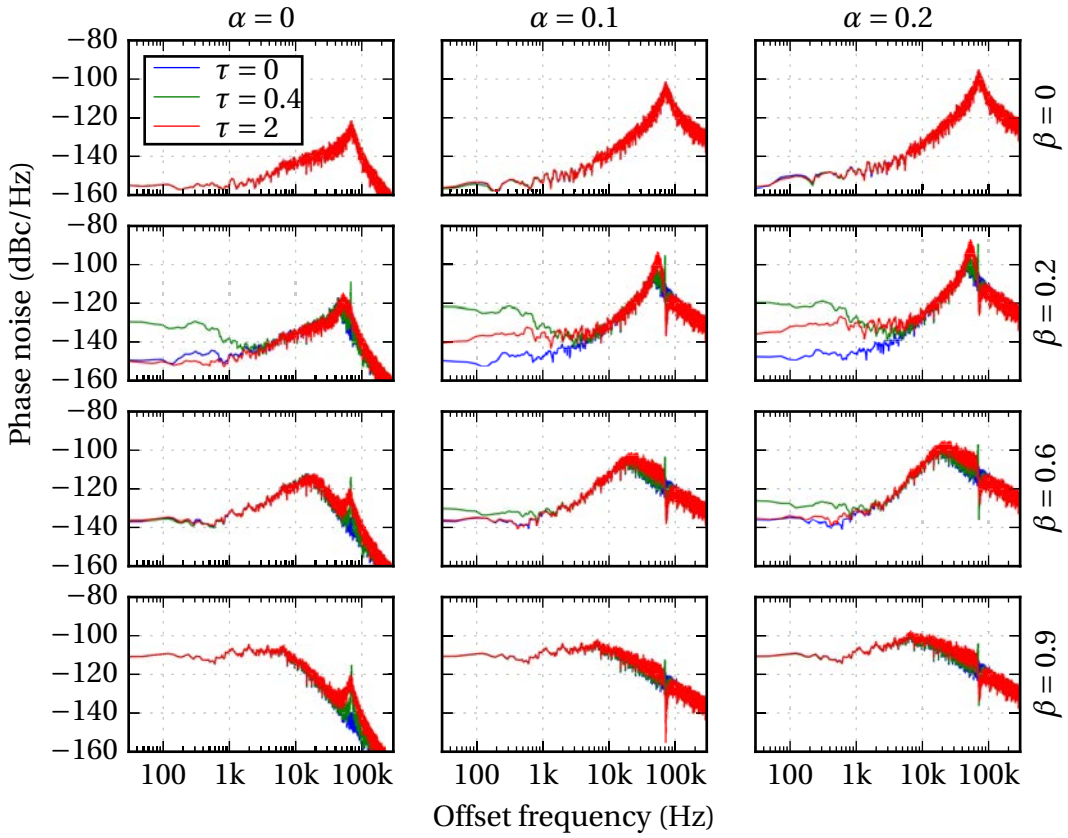

Figure II.25: Computed phase noise of the output beatnote for various parameters in the low injection regime ($\Delta = 0.01$, $\Gamma = 0.2$). Only pump noise has been considered as the noise source.

spiking behavior, triggered by a small change in a parameter, resembles interestingly to a phenomenon known as excitability. This term was originally introduced to describe biological phenomena, namely those happening in particular neurons [Hodgkin52]. Afterwards, a similar behaviors has been reported numerous times in all kind of dynamical systems, from optically injected semiconductor lasers [Turconi13], to optical torque wrenches [Pedaci10]. The perturbation can come from an external source, but can also be driven by noise [Lindner04]. While the exact definition of an excitable phenomenon may sometimes be a matter of debate, we will here retain two of the main characteristics, which are (i) the existence of a threshold on the perturbation of the parameters needed to trigger the event; (ii) this response does not depend on the amplitude of the perturbation [Izhikevich07].

In our case, the attractor associated with the event is chaotic, so that we have to dismiss a third condition in the definition of an excitable phenomenon, that is required by some authors for the usage of the term excitable, and that is that the event has to follow a reproducible, always identical trajectory. This is not strictly true in our

case, although the events are indeed similar, and most importantly their characteristics (amplitude and duration) do not depend on the excitation. For that reason, we will refer to this perturbation-induced spiking phenomenon as “excitable-like”. The fact that it happens on a bounded phase chaotic attractor gives another unique property to this phenomenon: indeed, the beatnote phase will remain bounded during the event, which is a very unusual feature for an excitable system, where the event is on the contrary often characterized by a phase jump [Kelleher09].

A numerical study was carried out in the case $\beta = 0.6$ and $\alpha = 0$ in [Romanelli16]. The main results are reproduced here in Fig. II.26 and Fig. II.27. The first one shows the threshold value, and is obtained by doing multiple numerical experiments of a detuning “kick”. Also highlighted is the fact that the amplitude of the response does not vary appreciably with the amplitude of the perturbation. The second figure concerns the existence of a refractory time, i.e. a time after a trigger during which the system cannot be excited again, that is often found in excitable systems [Garbin17]. The figure has been produced by changing the delay between two consecutive perturbations.

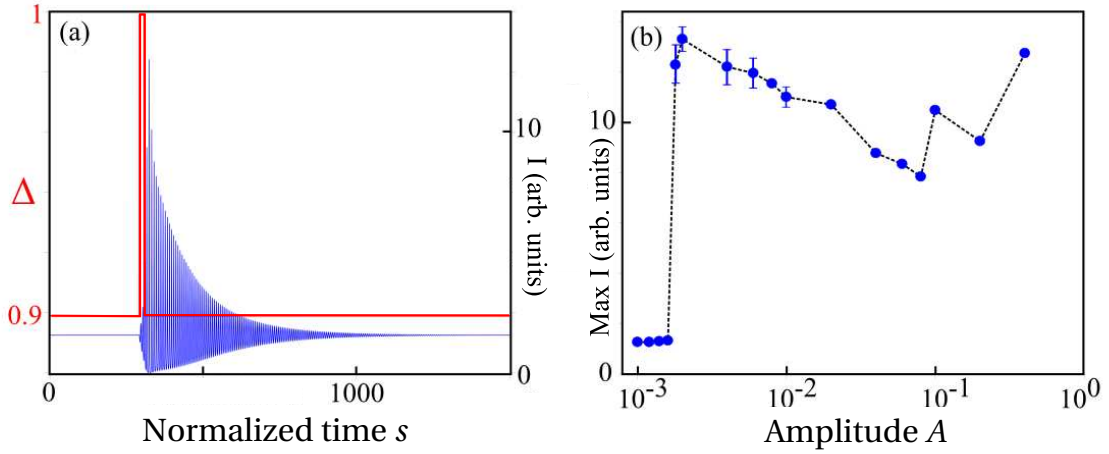

Figure II.26: (a) Numerical response to a perturbation of a detuning, showing the spiking effect on the amplitude (b) Maximum amplitude response for different perturbations. The points correspond to the mean value over slightly different initial conditions.

Experimental evidences of the features (i, threshold) and (ii, independence of response to the amplitude of the perturbation) of excitability were clearly observed. For the observation of the threshold, the detuning was set close to the border of the locking range, and was modulated with an amplitude of ±0.6. The output beatnote intensity was recorded along with the modulating signal, and the results in Fig. II.28 show clearly that the spiking is only triggered when the perturbation crosses a certain threshold value. However, this threshold value varies slightly at each cycle of the modulation, because of the unavoidable experimental drift of the mean detuning and injection rate.

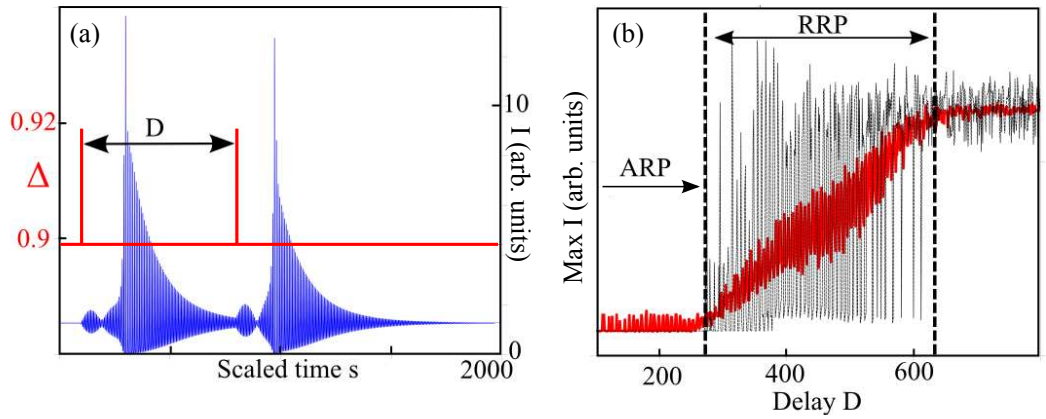

Figure II.27: (a) Response to two consecutive excitations separated by delay D. (b) Maximum amplitude observed after the second perturbation, for different values of D. Black lines: single realization; red line: mean value. ARP stands for absolute refractory period, while RRP stands for relative refractory period.

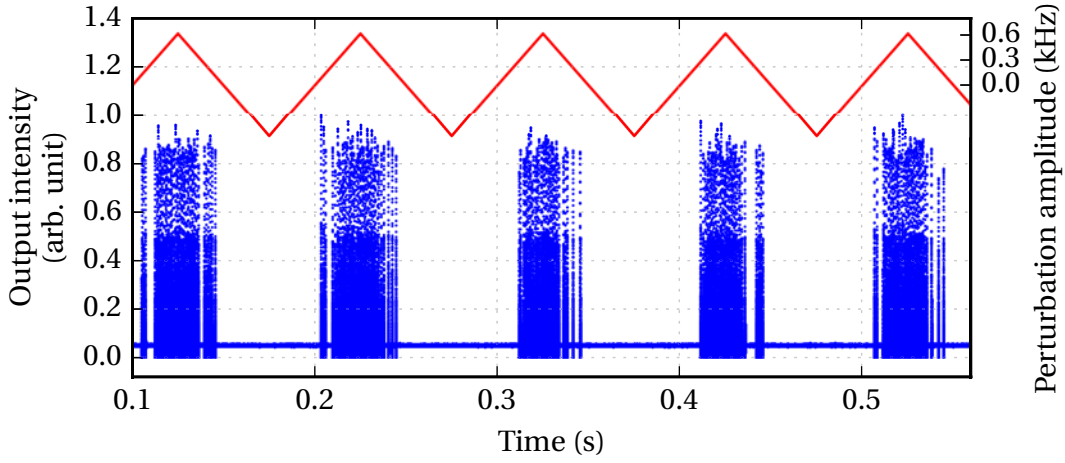

Figure II.28: Experimental manifestation of the excitable threshold. The detuning is changed periodically, and the beatnote is recorded.

For the refractory time, an example is shown on Fig. II.29. The system was excited by a sharp change in the detuning, then a second excitation was made after a given time. When the delay between the two kicks is too small, for instance on the upper panel, the second excitation is ignored, the cycle ends and the system goes back to its quiescent state. However, when the time between the two kicks is greater than the refractory time, another event is correctly triggered (lower panel).

To sum up, as this system features a threshold between a steady state region and an attractor, the observation of an excitable-like phenomenon is rather unsurprising. However, what we observe is quite unique, as the attractor is of chaotic nature. The result is that the event spikes, while very similar, each differs in shape, amplitude and

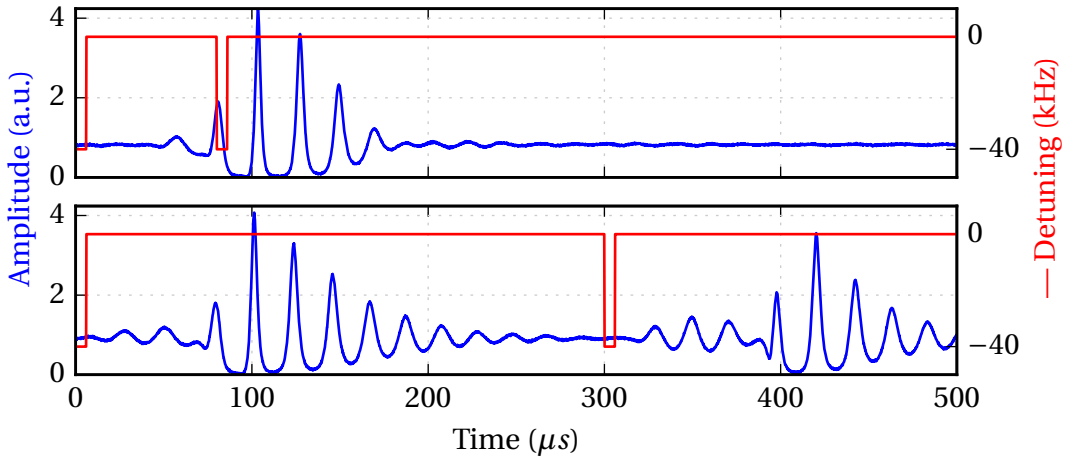

Figure II.29: Experimental observation of the refractory time, by exciting the system with two steps of detuning, separated by a different delay.

duration. Yet, it succeeds in maintaining the main properties of an excitable system, thus proving their robustness even in presence of chaos. On a side note, given the ubiquitous character of excitable behaviors, we expect this phenomenon to be found in other systems.

4c Arguments in favor of a non-zero α

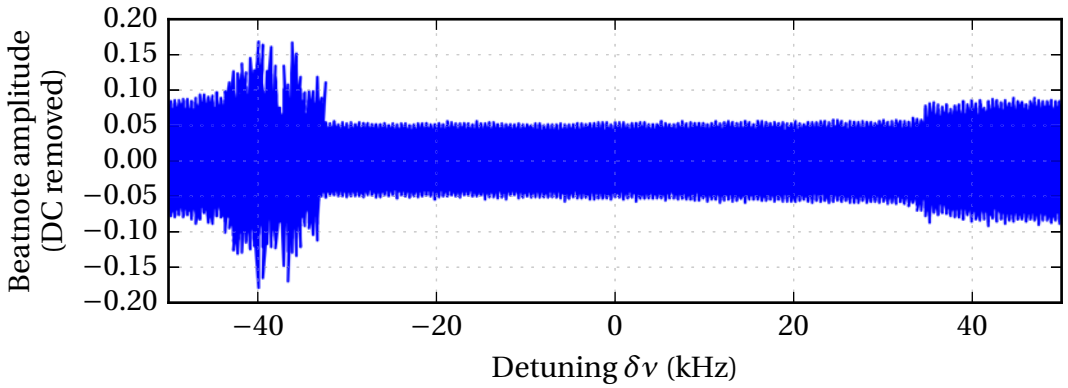

Figure II.30: Experimental recording the beatnote while varying the detuning Δ with a triangle modulation, across and outside of the locking range. The trace width corresponds to the unresolved oscillations at $2f_{\mathrm{AO}}$

We have yet to explain the reason why a non-zero linewidth enhancement factor has been included in the model. Indeed, it is very uncommon in solid-state lasers and there is only a few references of it in the literature. The study which resembles the most

with our setup has been undertaken for a Nd:YVO4 solid-state laser [Fordell05]. Its authors used a pump modulation method to obtain a value of $\alpha = 0.25 \pm 0.13$. They also proceeded to an experimental mapping of the dynamics under injection [Valling05], which showed clearly a locking range asymmetry, well explained by a non-zero α. Also, an unexpectedly high value of $\alpha \approx 1$ has been reported in a microchip Nd:YAG laser. In that case, it has been measured using an injection method based on the change in relaxation oscillation frequency [Szwaj04].

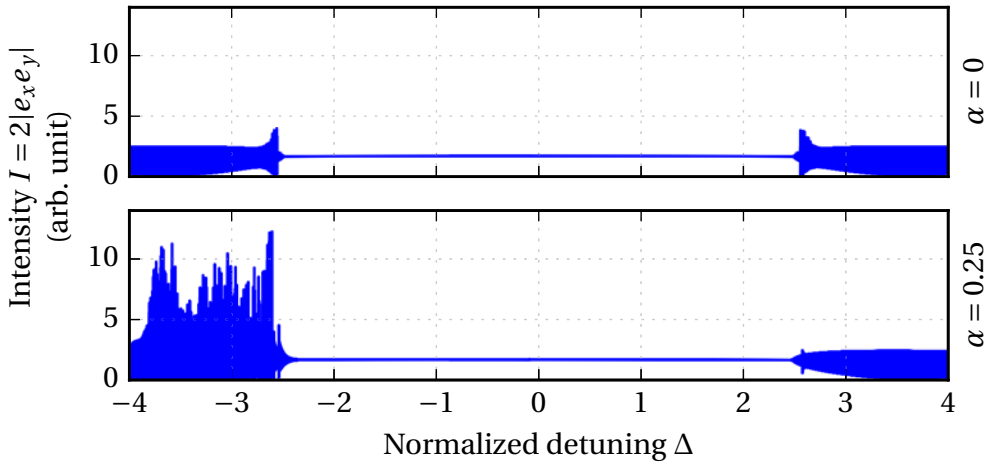

Figure II.31: Computed values of the beatnote intensity for varying detuning Δ, with a zero and non-zero value of α.

In our case, the first experimental hint of a non-zero α factor was the observation of an asymmetry of the unlocking mechanism with respect to the detuning. This is shown on Fig. II.30, where the detuning has been swept across the locking range and outside of it, and the beatnote amplitude has been recorded. It is clear that while for $\Delta > 0$ a smooth bifurcation is observed, it is not the case for $\Delta < 0$, for which a more complicated transition happens. This asymmetry is a clear evidence of a non-zero linewidth enhancement factor. Indeed, if one looks again at the model II.4, we see that for $\alpha = 0$, a change $\Delta \to -\Delta$ is equivalent to taking the complex conjugate of the equation of e_y. This is not the case anymore for $\alpha \neq 0$, and in that case, the observed asymmetry appears, as already noticed on Fig. II.11, for instance. The previous experimental figure can be compared to Fig. II.8 and Fig. II.31, which is its numerical counterpart, and replicates quite well the observed features.

For a more detailed insight, a complete mapping of the stationary phase extrema for various values of α and β has been calculated and is shown on Fig. II.32. Using these, we found other clues pointing toward a non-zero value of α, such as the shape of the bounded phase regions, that were also observed experimentally.

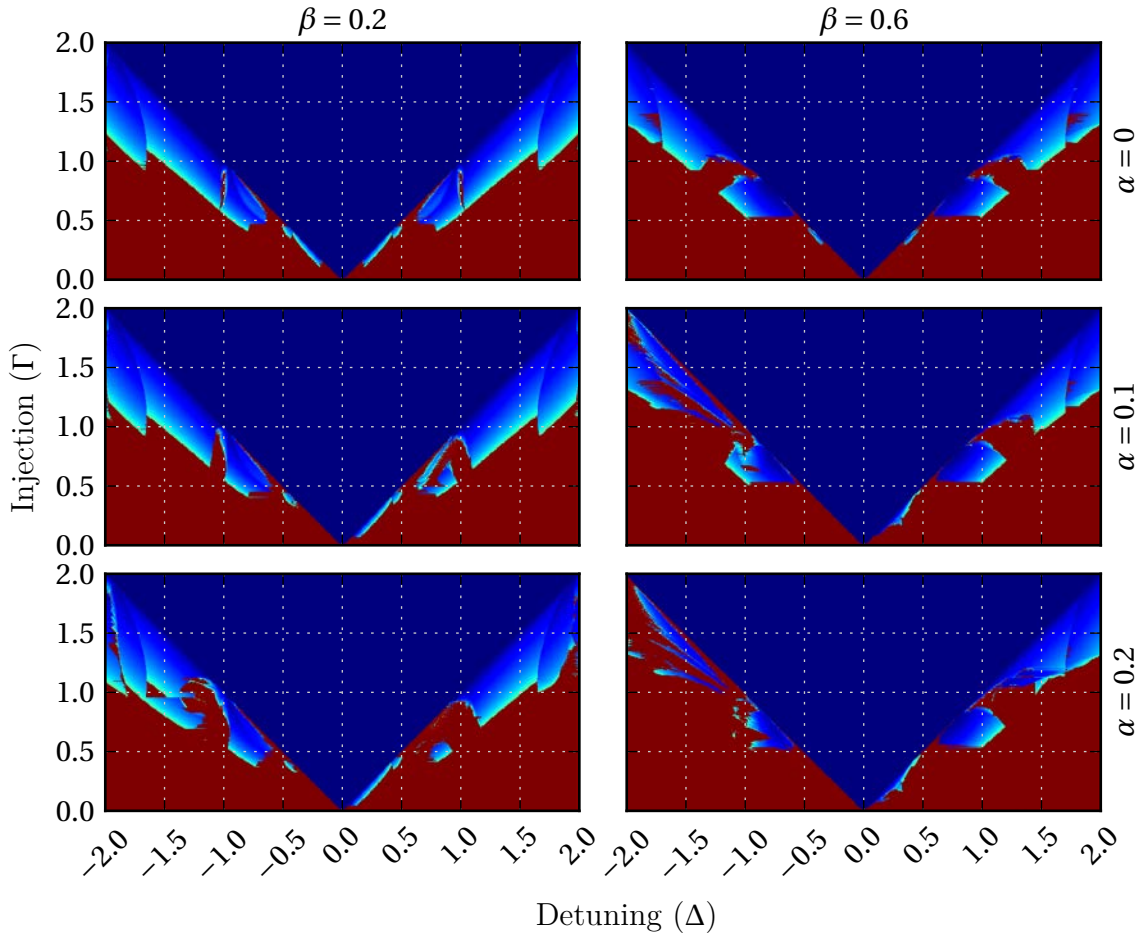

Figure II.32: Maps of the phase extrema difference $\max\varphi - \min\varphi$ for various values of α and β. No delay τ has been included.

4d Alternate results for $\alpha = 0$ and $\beta = 0.6$

As it was initially not known that a linewidth enhancement factor had to be included in order to account for the precise phenomena under frequency-shifted feedback, it had been ignored in preliminary simulations and previous works [Thévenin12c]. Also, in these studies, the coupling factor β was measured to be 0.6. This is likely due to a different setup of the pump, but the exact reason is not known yet. In any case, many investigations were made upon this assumption. We reproduce here some results obtained with these parameters, because they provide valuable informations, namely for different values of β factor, or assuming the linewidth enhancement factor α is neglected. For instance, Fig. II.33 is the counterpart of Fig. II.11, which shows the different regimes obtained in the resonant injection region ($\Gamma < 1$). Here, only $\Delta > 0$ is shown, as $\alpha = 0$ induces a symmetry with respect to the detuning. We notice that the same regimes, bounded phase, chaos, and the combination of the two, are similarly

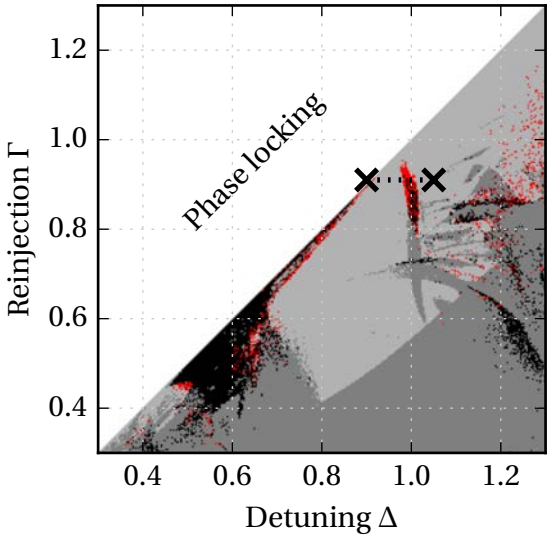

Figure II.33: Map of the different regimes for $\beta = 0.6$ and $\alpha = 0$. See Fig. II.11 for legend. Dashed line $\Gamma = 0.91$ is the line along which the bifurcation diagram of Fig. II.34 is computed.

found, but in different regions.

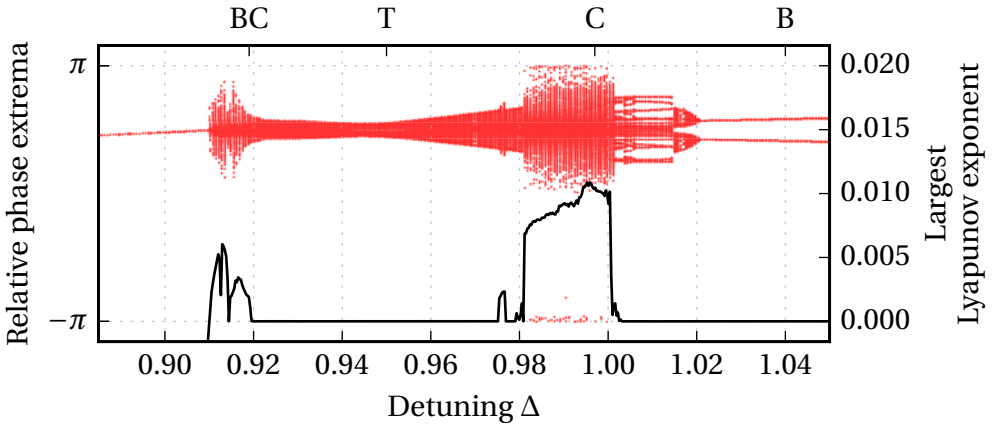

Figure II.34: Simulated bifurcation diagram of phase extrema for $\beta = 0.6$, $\alpha = 0$ and $\Gamma = 0.91$. Final state at each point is taken as the initial conditions for the next point, as Δ is increased. The largest Lyapunov exponent is computed for each point and plotted as the solid black line.

Finally, Fig. II.35 includes maps from Fig. II.32 and Fig. II.22, and shows the effect of a larger delay for different values of β. The conclusions obtained for $\alpha \neq 0$ still apply. All in all, these results also demonstrate a general reassuring feature of this system: even with slightly different parameters of the laser, nearly identical regimes can be found, although in slightly different locations of the (Δ, Γ) space.

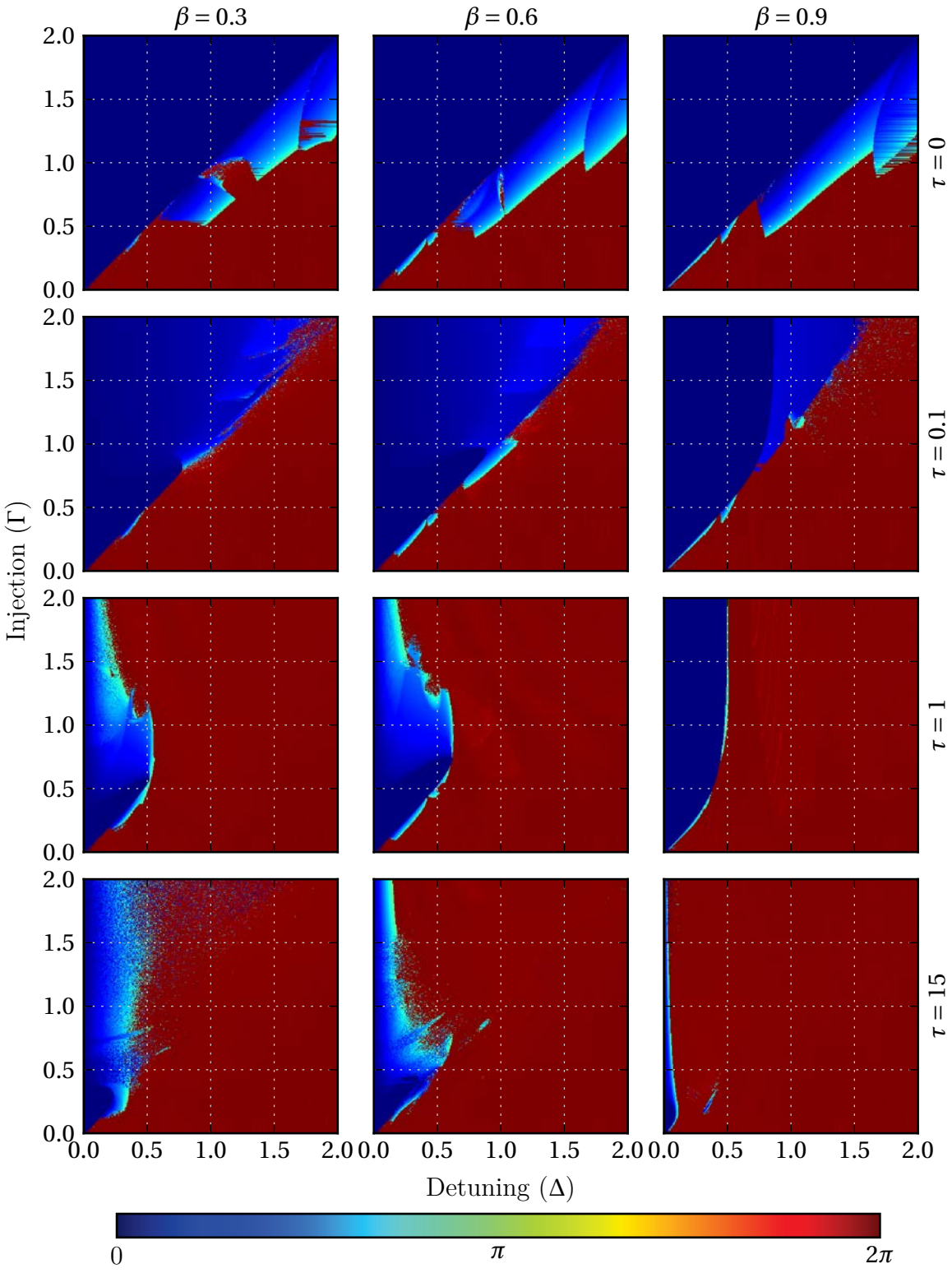

Figure II.35: Map of the phase extrema obtained for $\alpha = 0$ and different values of β and τ.

5 Application to the measurement of the small linewidth enhancement factor

In the previous section, we pointed out that experimental observations led to the inclusion of a non-zero α factor in the model. Qualitative observations showed that it should be in the 0.1–0.3 range for our Nd:YAG laser. But as we would like that the model matches as closely as possible the observations, a more precise measurement is needed.

However, it is quite clear that standard measurement techniques described in Section I.1*b* cannot be easily applied in this case. First, we expect a very low value of α and most methods have large uncertainties that would lead to a very high relative error. Second, we would like to avoid any changes of the intracavity power, so that we can safely rule out thermally-induced modifications in the optical index as the origin of the observed amplitude-phase coupling. Also, we would like to take advantage of our frequency-shifted feedback setup, and see whether it can be used to easily recover the linewidth enhancement factor.

With that in mind, several options were considered. The first one was to study how the antiphase oscillations frequency depends on α. Using computer algebra on the rate equations, it was found that it indeed depends strongly on α, but only within the locking range. This makes the measurement unusable, as when the beatnote is locked on the external reference, antiphase oscillations are only very weakly excited, and thus cannot be seen on the electrical spectrum.

Secondly, the frequency of the Hopf oscillations that appear when leaving the locking range were suspected to depend on α, but in fact we discovered that they did not (see Fig. II.36).

Finally, we derived a method based on the modulation of the detuning, that will be presented here, along with results obtained on the Nd:YAG laser. This method was also presented in [Thorette17].

5*a* Theory

As one of the main constraints was that the intracavity power should remain as constant as possible, we ruled out pump modulation, but also injection strength modulation. What remains is the frequency detuning that can be easily modulated as $\Delta = \Delta_0 + a\cos(2\pi f_M t)$ around a mean value Δ_0, effectively inserting a phase perturbation in the laser with amplitude a and frequency f_M. Intuitively, as the linewidth enhancement factor introduces a coupling between the amplitude and phase of the

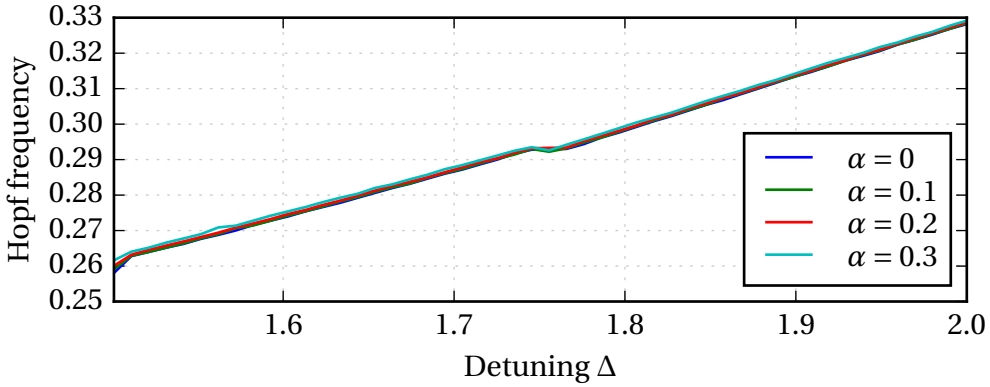

Figure II.36: Normalized frequency of the cycle oscillations when leaving the locking range, obtained numerically for $\Gamma = 1.5$, $\Delta > 0$, and various values of α.

optical field, we expected that a modulation of the detuning would have an effect on the output intensity if and only if $\alpha \neq 0$, and that this could be used to retrieve the value of α.

We recall the normalized rate equations with optical injection I.15, already presented in Chapter I.

$$\frac{\mathrm{d}E}{\mathrm{d}s} = \frac{1}{2}(1+i\alpha)NE + i\Delta E + \Gamma E_{\mathrm{inj}} \tag{II.11}$$

Here, E is the normalized intracavity field, N the active medium gain, Δ is the detuning between the injected field and the free-running laser frequency, Γ is the injection efficiency, and E_{inj} the injected field, whose frequency and phase are taken as reference. Separating phase and amplitude as $E = |E|e^{i\varphi}$ leads to:

$$\frac{\mathrm{d}|E|}{\mathrm{d}s} = \frac{1}{2}N|E| + \Gamma E_{\mathrm{inj}}\cos\varphi \tag{II.12a}$$

$$\frac{\mathrm{d}\varphi}{\mathrm{d}s} = \frac{1}{2}\alpha N + \Delta - \Gamma\frac{E_{\mathrm{inj}}}{|E|}\sin\varphi \tag{II.12b}$$

We consider small perturbations of the injection-locked, steady state regime. Thus, we write $x = \widehat{x} + \delta x$, where x stands for $|E|, \varphi, N$. $\widehat{x}$ denotes the steady state value of x and δx the small perturbation. Linearization of equation (II.12a) leads to:

$$\frac{\mathrm{d}\delta|E|}{\mathrm{d}s} = \frac{1}{2}\left(|\widehat{E}|\delta N + \widehat{N}\delta|E|\right) - \Gamma E_{\mathrm{inj}}\sin\widehat{\varphi}\delta\varphi \tag{II.13}$$

This shows clearly that amplitude response to a phase perturbation $\delta\varphi$ depends on

the quantity $\sin\widehat{\varphi}$. In particular, a zero response is expected when $\sin\widehat{\varphi} = 0$. Using the steady state of equation (II.12b), this condition becomes $\alpha\widehat{N}/2 = -\Delta$, which we can be transformed using (II.12a) to the more useful expression:

$$\Delta = \alpha\Gamma\frac{E_{\text{inj}}}{|\widehat{E}|} \equiv \Delta_m \tag{II.14}$$

This means that there is a particular value of the detuning, which we will now call Δ_m, that corresponds to a minimal amplitude response to a perturbation of the phase. This value, as expected, depends directly on α, so that is is zero when $\alpha = 0$. This confirms the fact that the linewidth enhancement factor is responsible for the phase to amplitude coupling. This detuning of minimal response Δ_m can surely be measured, so that to calculate α, it remains to measure the normalized injection rate $\Gamma E_{\text{inj}}/|\widehat{E}|$. Luckily, this value can be indirectly obtained, because it is closely related to the width of the locking region. Generally speaking, for the "semiconductor" model (II.11), the locking range in the low injection regime corresponds to $|\Delta| < \sqrt{1+\alpha^2}\Gamma$, as explained in I.2*a* and we obtain:

$$\frac{\alpha}{\sqrt{1+\alpha^2}} = \frac{\Delta_+ - \Delta_-}{2\Delta_m} \tag{II.15}$$

where Δ_+ and Δ_- are the upper and lower boundaries of the locking range.

Clearly this can be used to relate two simple experimental values to α, yet we see that the left-hand side of the equation grows as α^{-2} for large values of α. This makes any precise measurement impossible as soon as $\alpha > 1$. On the other hand, for low values, it scales as α, which makes this method well adapted to the low values expected for solid-state lasers.

5*b* Dual-frequency laser

This method, being based on injection, relies on a very stable master laser, all the more so because it uses precise frequency measurements. Interestingly, in our dual-frequency case we can bypass this requirement, and use the frequency-shifted feedback mechanism to inject one mode onto the other. This allows to have a very stable injection, with a stable and controllable detuning at the kHz scale. However, the coupling between the modes inside the gain medium makes the analysis slightly different from the simple injection case, and a more complex relation than Eq. II.15 has to be expected.

Starting from the FSF model (II.4), we linearize it around its steady state, insert a phase perturbation, and obtain the transfer function A for the output amplitude of the beatnote signal presented on Fig. II.37. There we can clearly see that its magnitude $|A|$

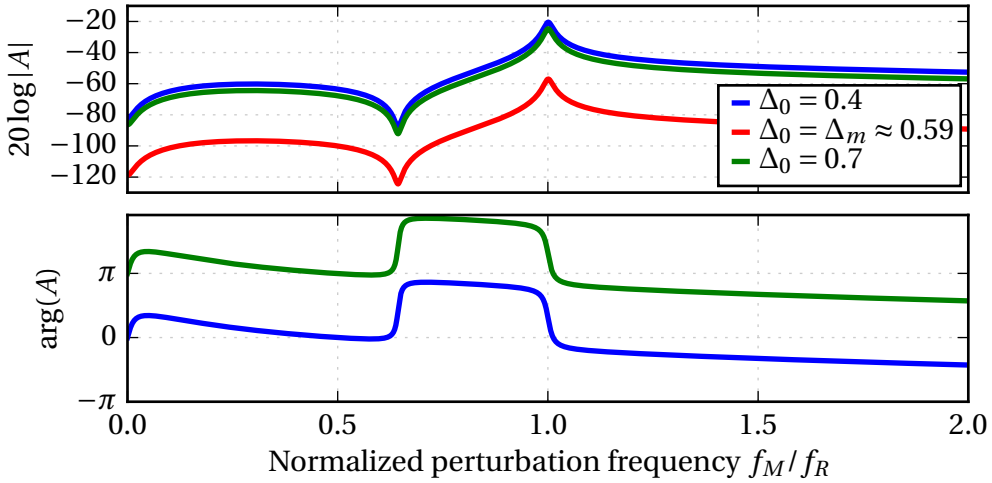

Figure II.37: Amplitude and phase of the transfer function from a detuning modulation to the beatnote amplitude, for varying values of the mean detuning Δ_0. Here, we have taken $\alpha = 0.25$ and $\Gamma = 0.25$.

shows an unsurprising peak at the frequency of the relaxation oscillations. Therefore, we will use $f_M = f_R$ as the modulating frequency in order to maximize the observed response. Then, we notice that the whole amplitude of the transfer function depends on the mean detuning Δ_0. This can be more clearly seen on Fig. II.38, which shows the value of the transfer function for the chosen modulation frequency. As expected, it exists a minimal value of the detuning Δ_m which corresponds to a canceling of the amplitude response. We note that it is also associated with a $-\pi$ phase shift of the response.

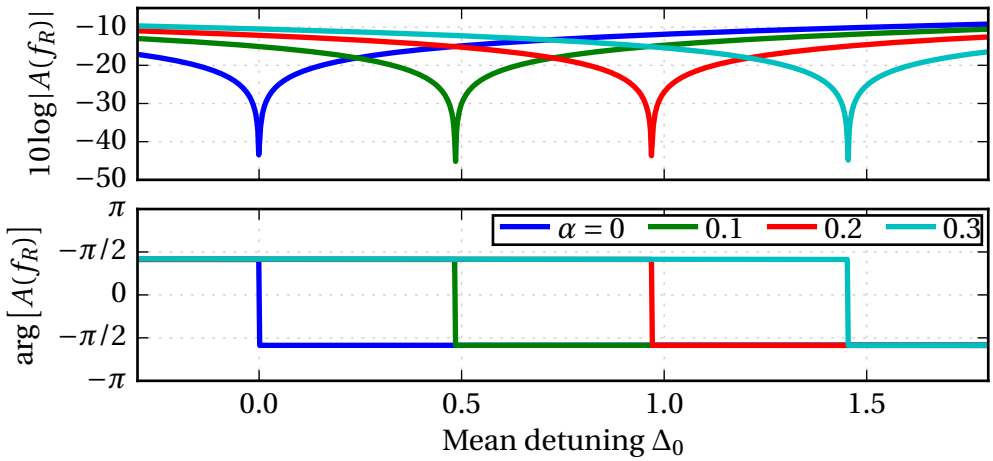

Figure II.38: Computed amplitude and phase of the transfer function, for a modulation at the relaxation oscillation frequency f_R, for varying values of the mean detuning Δ_0, and different values of α.

In order to compute an expression for this minimal detuning Δ_m, we can solve the equation obtained for the transfer function, which has a quite complicated expression, but is proportional to $2\Delta - \alpha(\beta+1)\widehat{m_y}$. Thus, we obtain the following conditions on the detuning, which can be made to look very similar to Eq. (II.15) obtained in the simple injection case.

$$\Delta_m = \frac{\alpha\widehat{m_y}}{2(\beta-1)} = \alpha\Gamma\left|\frac{\widehat{e_x}}{\widehat{e_y}}\right| \tag{II.16}$$

For low injection level, one can consider that $\widehat{e}_{x,y}$ do not differ appreciably from their equilibrium values in the free-running regime, so that equation (II.16) further simplifies to $\Delta_m = \alpha\Gamma$. In the general case $\widehat{e}_{x,y}$ has to be computed from the system equations (II.4a-c), and inserted into equation (II.16). This procedure leads to a 4th degree polynomial for $x = \Delta_m/\alpha$, as follows.

$$\begin{gathered}\Gamma^2\epsilon^2\left(\Omega^2-1\right)(\eta-1)x^4 + \Gamma\epsilon\left(\eta\Omega^2-\eta-2\Omega^2\right)x^3 + \\ \left(\Gamma^2\epsilon^2\left(\Omega^2-1\right)(\eta-1)-\Omega^2\right)x^2 + \Gamma\epsilon\left(-\eta\Omega^2-\eta+2\Omega^2\right)x + \Omega^2 = 0\end{gathered} \tag{II.17}$$

Here $\Omega = \frac{1-\beta}{1+\beta}$. This equation can be solved for a single real value. As we know that $\Delta \approx \Gamma\alpha$, we can set $y = 1+x$ and solve the previous equation at the order 2, so that:

$$\Delta_m = \alpha\Gamma(1 + f(\varepsilon\Gamma, \beta, \eta)) \tag{II.18}$$

where f is a "correction function" containing the needed terms for the dual-polarization case. It cancels for $\Gamma = 0$, and has the rather cumbersome expression to the first order in $\varepsilon\Gamma$:

$$\begin{aligned}f(\varepsilon\Gamma,\Omega,\eta) = \Big\{&\Gamma\varepsilon(\eta\Omega^2-2\eta-2\Omega^2) - \Omega^2 + \Big(-2\Gamma^2\varepsilon^2(-\eta^2\Omega^4/2 - \eta^2\Omega^2 + \eta^2 + 3\eta\Omega^4 + \eta\Omega^2 \\ &- 3\Omega^4 + \Omega^2) + 2\Gamma\varepsilon\Omega^2(-\eta\Omega^2 + \eta + 2\Omega^2) + \Omega^4\Big)^{\frac{1}{2}}\Big\} \Big/ \left(3\Gamma\varepsilon(-\eta\Omega^2 + \eta + 2\Omega^2) + \Omega^2\right)\end{aligned} \tag{II.19}$$

A plot of this correction function is shown on Fig. II.39, along with the exact result obtained from the roots of the 4th order polynomial.

This shows that for higher injection level, the minimal response detuning is not simply $\alpha\Gamma$, but also depends on other parameters of the model. These corrections will be taken into account in our measurements.

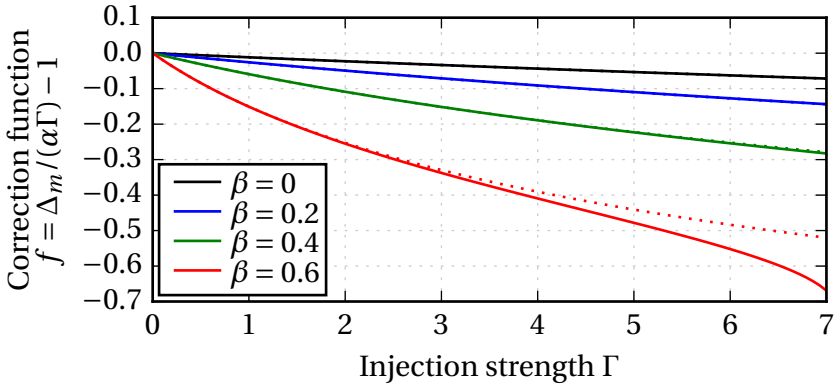

Figure II.39: Correction function $f(\varepsilon\Gamma, \beta, \eta)$ in function of Γ for various values of β. η is kept at 1.2 and ε at 0.01. Solid curves correspond to the approximate expression (II.19), while dotted curves are the exact values.

5c Result for Nd:YAG bulk laser

We applied the method to our laser, simply by frequency-modulating the acousto-optic signal f_{AO} at the frequency of the relaxation oscillations 65 kHz, with a small excursion of 10 kHz, so that $2f_{\mathrm{AO}} = f_0 + f_1\cos(2\pi f_M t)$). We monitored the electrical spectrum and the time evolution of the beatnote. The results can be seen on Fig. II.40, and the existence of a detuning of minimal response Δ_m is clearly highlighted on the time series, where the beatnote has a constant intensity, and is almost uncorrelated with the modulation signal. The phase shift that happens when the mean detuning crosses Δ_m, expected from Fig. II.38 is also clearly seen. On the electrical spectrum, the effect of the modulation are the sharp sidebands at $\pm f_R$ around the beatnote. These sidebands have the smallest height when $\Delta = \Delta_m$. In the experiments, we also notice that interestingly, these sidebands are not symmetric, as we would expect them to be. They are slightly unbalanced, and they only balance at their minimum level, i.e. when $\Delta_0 = \Delta_m$. While we do not find this asymmetry in our model, it proved to be quite useful in order to precisely locate the minimal response point, and thus to measure Δ_m.

Using this method, the value of Δ_m was measured for different values of the injection rate. The power applied on the acousto-optic modulator was changed, and each time, the detuning was varied so that we could locate the two borders of the locking range and the minimal response frequency. This measurement was repeated multiple times, and the results are shown on Fig. II.41.

Then, equation (II.18) allow to extract an estimation of α from the measured values. From each point of the Fig II.41, a value of α can be estimated, so that the final result

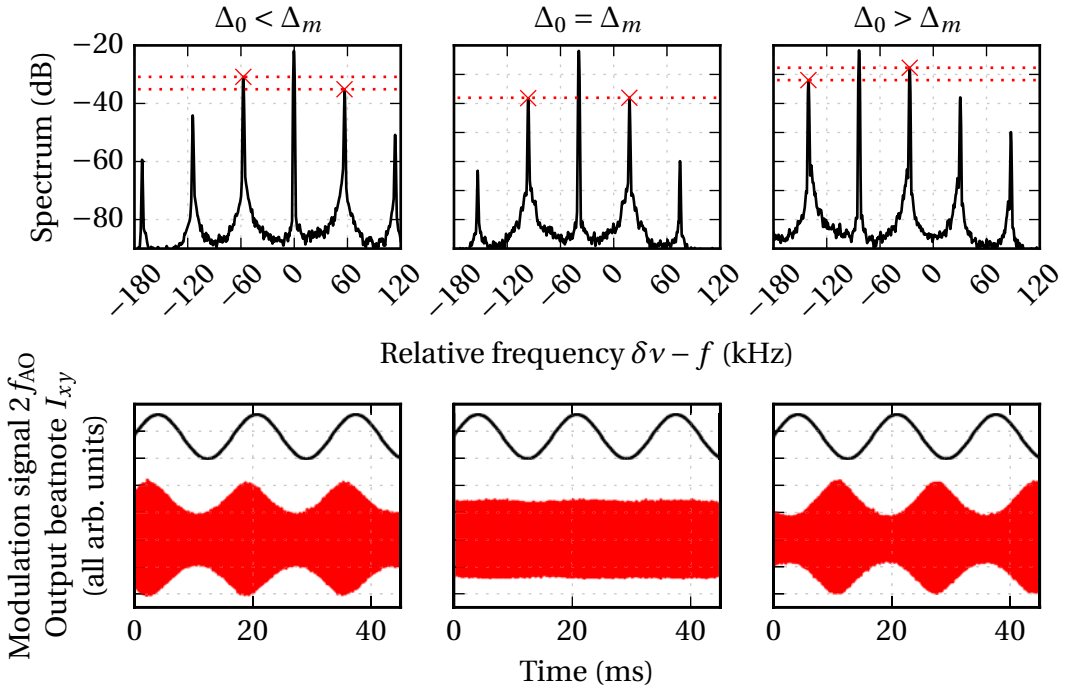

Figure II.40: Experimental electrical spectrum of the beatnote, for different values of the mean detuning $\Delta_0 < \Delta_m$, $\Delta_0 = \Delta_m$ and $\Delta_0 > \Delta_m$ (with $\Delta_0 = (\delta\nu - f_0)/f_R$), and the associated time series (black: modulation signal, red: output beatnote $I_{xy} = |e_x + e_y|^2$). This shows that the balance of the two sidebands at $\pm f_R$ corresponds to minimal amplitude response, and to π phase shift between $\Delta_0 > \Delta_m$ and $\Delta_0 < \Delta_m$.

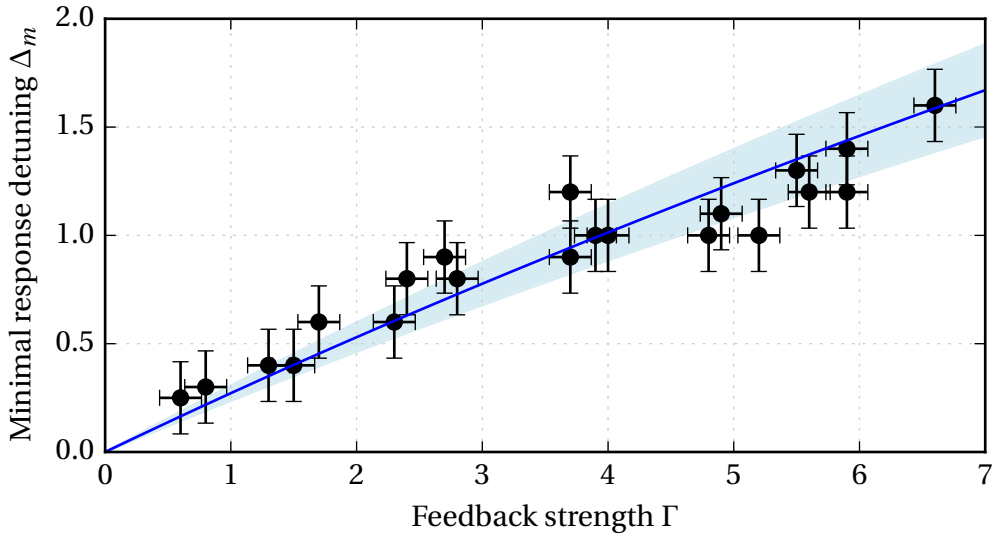

Figure II.41: Measured values of the minimal response detuning Δ_m for different injection strength. The blue curve shows the best fit with Eq. II.18 and the filled region the associated uncertainty.

can be obtained simply by averaging.

$$\alpha = \left\langle \frac{\Delta_m}{\Gamma(1 + f(\varepsilon\Gamma, \beta, \eta))} \right\rangle \tag{II.20}$$

As the uncertainty on a single measurement $\delta\alpha$ is higher for low values of Γ, we have to use a weighted average with weights $1/\delta\alpha$, and we find a value of

$$\alpha = 0.28 \pm 0.04 \tag{II.21}$$

The uncertainty is computed from the precision of the frequency measurements, which we estimate to be around 8kHz, and also includes the uncertainties on β and η. This leads to a satisfying reduced chi-squared value of 1.15. We can note here that this measurement achieves very good relative precision of 14%, better than other similar measurement [Fordell05; Villafranca07].

This value can be compared to the one found in a Nd:YVO_4 laser in [Fordell05], $\alpha = 0.24 \pm 0.13$, with which it seems compatible. Although these are only two measurements, this might suggest a weak influence of the crystalline matrix on the linewidth enhancement factor. We have not found yet the physical origin of this phase-amplitude coupling. In semiconductor mediums, it can be linked to an asymmetry of the gain curve. This hypothesis is tested for a Nd:YAG laser in Annex. B, but it does not allow to reproduce our quite high value of α.

Other hypotheses have been suggested, but they could not be investigated during this work. For instance, it could be related to some unnoticed thermal effects, although the fact that the effect has the same scale in the much more thermally unstable Nd:YVO4 makes this doubtful. A longitudinal unhomogeneity of the population of ions in the crystal would probably induce a coupling between the phase of the field and the gain, so this could also be investigated. Other authors have suggested an acoustic coupling in the crystal, namely with standing acoustic waves [Fordell05]. This would probably suggest a dependence on the geometry of the crystal.

6 Fiber laser

Fiber lasers, while being more compact and practical, do not differ strongly from solid-state lasers in their principle, and we expect that many of the previously developed concepts can be reused on them quite easily. Indeed, dual-frequency dual-polarization lasers have been observed in fibered form for a few years [Loh97], and have been studied for applications in heterodyne microwave generation [Leng06; Maxin11]. In that case, simple forms of stabilization techniques based on feedback have also been

proposed [Liang14]. In our lab, dual-frequency fiber lasers are studied for their potential use in optically-carried microwave signal generation. We thus are interested in applying the FSF method to these lasers in order to stabilize their output beatnote. We can also expect to do a measurement of the linewidth enhancement factor.

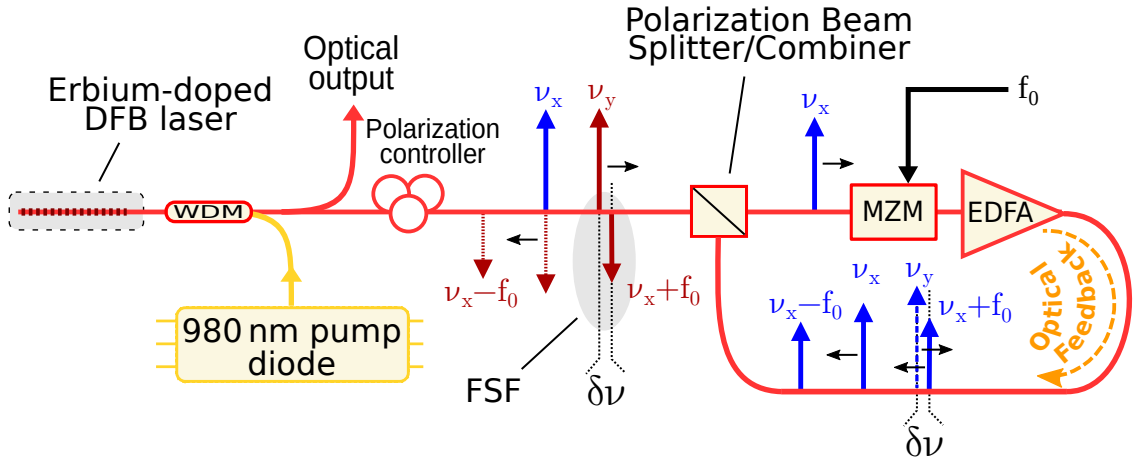

Figure II.42: Frequency-shifted feedback applied to a dual-polarization dual-frequency fiber laser. Colors on arrows indicate the two orthogonal polarizations.

The laser under consideration is a 33 mm-long Erbium-doped fiber, on which a Bragg grating is photo-induced using an UV interference pattern. It has been provided by the iXblue society[3] in the framework of the EDA contract EOFIL. A π phase shift in the motif of optical index creates a cavity with an estimated effective length of 2.6 mm, enclosed between very efficients "mirrors" of transmission −35 dB on pump side (co-propagating output), and −51 and the other side (co-propagating output). The process of engraving leaves a residual birefringence in the fiber, that induces a frequency separation between the two orthogonal modes of polarization, allowing dual-frequency dual-polarization output. Thus, the frequency of the beatnote depends mostly on the manufacturing process. For now, beatnotes up to 3 GHz have been obtained, and a 1 GHz beatnote will be used in the following. These lasers are pumped using a 980 nm laser diode and outputs at 1532 nm, typically in the power range of 100 µW on the contra-propagating side. More technical details on these lasers can be found in [Guionie18a].

We applied a frequency-shifted feedback scheme similar to the one of Fig. II.5, but in an all-fibered setup, presented on Fig. II.42. While the laser itself sits on a SMF fiber, the feedback loop uses polarization-maintaining (PM) fiber. This is why a polarization controller had to be added at the contra-propagating output, and before the first PM component: a polarization beam splitter/combiner (PBS/C) that redirects the two polarization modes x and y on each of its outputs. One of them, here x, goes through

[3] https://photonics.ixblue.com/

an amplitude modulator (MZM)[4] driven by the reference synthetizer at f_0, that creates sidebands at $\nu_x \pm f_0$, then through an amplifier (EDFA) that also contains an isolator. This allows to create a one-way loop, as it blocks the other polarization y, coming from the other port of the PBS/C. The modulated and amplified signal then enters the other port of the PBS/C, so that it is reinjected into the laser, with orthogonal polarization y. Three frequencies are injected on the mode y: two non-resonants ν_x and $\nu_x - f_0$, and a resonant one $\nu_x + f_0$, with a remaining detuning $\delta\nu = \nu_y - \nu_x - f_0$. We see here that the only difference with the previous setup (Fig. II.5) is the presence of two non-resonant frequencies in the injection.

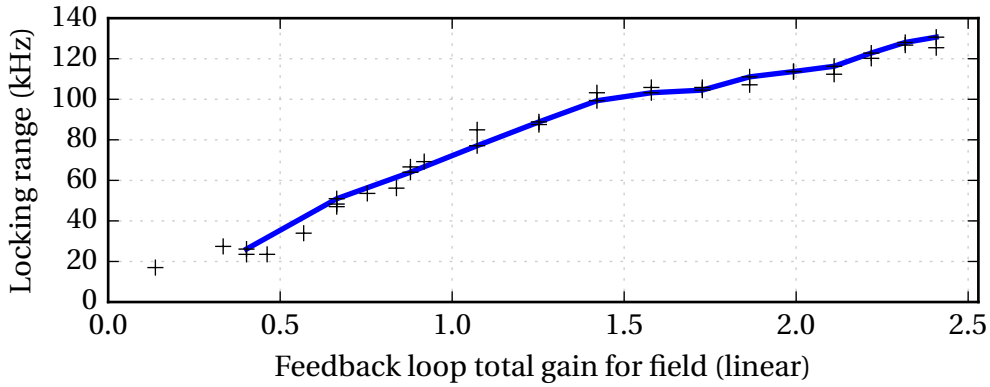

Figure II.43: Measured locking range with FSF applied on an Erbium fiber laser.

While this is preliminary work, the results are good, and a locking range is observed, that grows with injected power, as shown on Fig. II.43. Locking does not start as soon as the gain of the amplifier is non-zero, because some losses in the feedback loop have to be compensated before. After that, a linear rise of the locking range with the total loop gain is observed. Very interestingly, we see that if a wide locking range is not needed, the loop can be made even simpler by replacing the amplifier by an isolator. Indeed, we still observe 50 kHz of locking range for a gain of 1.

Phase noise measurements show the very good transfer of spectral purity from the reference to the beatnote. For instance, levels of -104 dBc/Hz at 1 kHz offset from the carrier have been obtained, as can be seen on Fig. II.44. As a comparisons, other stabilization methods based on a phase-locked loop using changes in the pump power work very well and provide a wider locking range, but currently reach a limit on phase noise at -75 dBc/Hz for the same 1 kHz offset [Guionie18a].

If we dive deeper in the details of the FSF, we notice that there are strong differences

[4] Fibered acousto-optic modulators barely go beyond 1 GHz, and such high-frequency models were not available in our lab. Instead, we used an amplitude modulator. While it does not only shift the frequency of the signal, but rather creates sidebands around it, we will see that it is not a problem in our case.

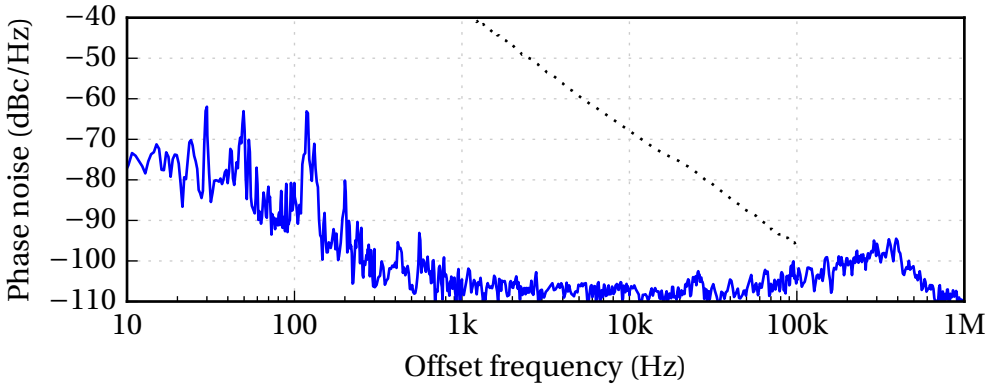

Figure II.44: Phase noise measured on the locked fiber laser. Dotted curve is the free-running phase noise, obtained by an indirect method (see [Guionie18a]).

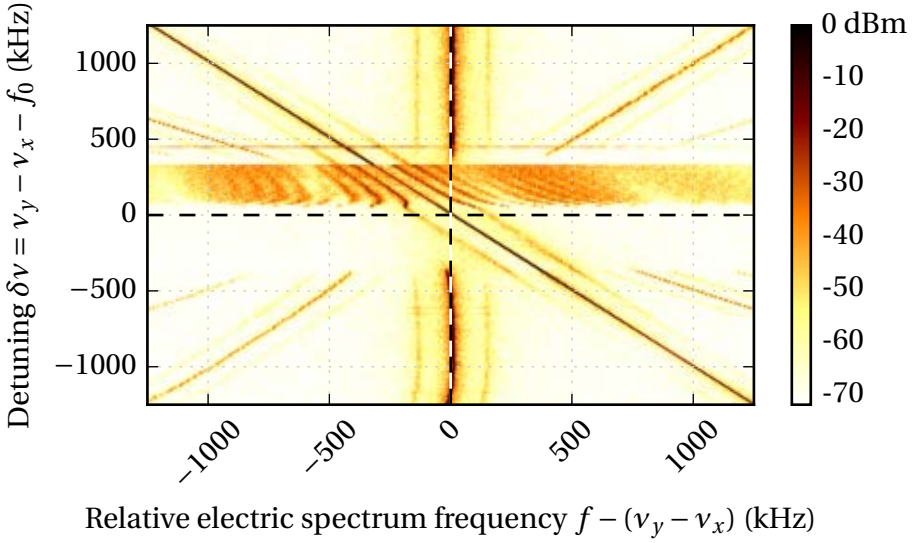

Figure II.45: Asymmetry of the locking range for the fiber laser, with a gain of ≈ 5 in the feedback loop.

between this laser and the previous Nd:YAG solid-state case. One of the obvious feature is the strong asymmetry of the locking range, that can be noticed as soon as we leave the very low injection regime $\Gamma \ll 1$. Fig. II.45 shows an example of a typical spectrogram, recorded during a sweep of the detuning, where the asymmetry can be clearly observed.

Some of these features could be explained by a large value of α. A rough estimate, based on locking range asymmetry and bifurcation diagrams (see Fig. II.46) is that α is in the range 2–3 [Guionie18b]. This preliminary result seem to agree well with previous suggestions in the literature for such lasers [Rønnekleiv01], although some debate and

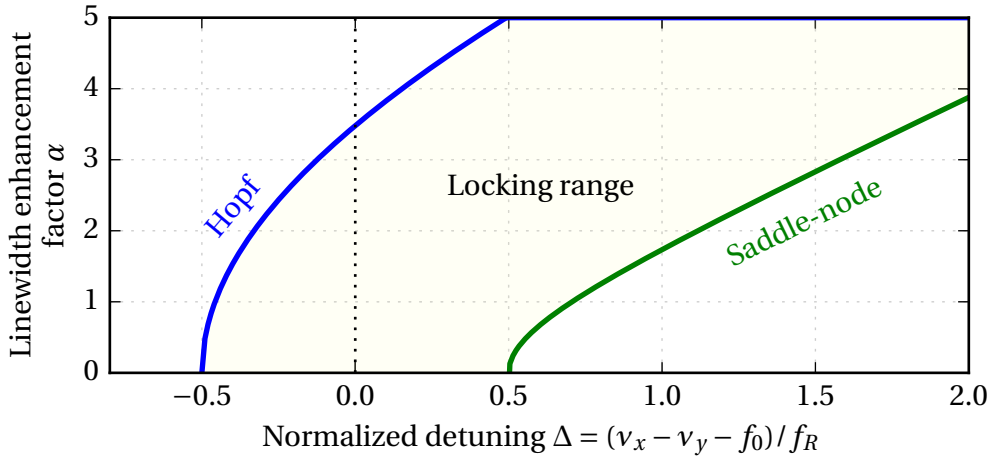

Figure II.46: Bifurcation diagram showing the influence of α on the locking range, for $\Gamma = 0.5$. Other parameters have been measured for the fiber laser, and are $\varepsilon = 1 \times 10^{-4}$, $\beta = 0.65$ and $\eta = 1.2$.

contradictory measurement exist [Foster07]. This means that the method proposed in Section 5 cannot be applied. It has been attempted with poor results. While the minimal response detuning Δ_m could indeed be located (see Fig. II.47), how it relates to α is a more complex problem, and is under study in the lab. Also, here we have used the same equations that we derived for the four-level Nd:YAG, but Er:glass is a three-level system, so slight changes should be taken into account [Kervevan07].

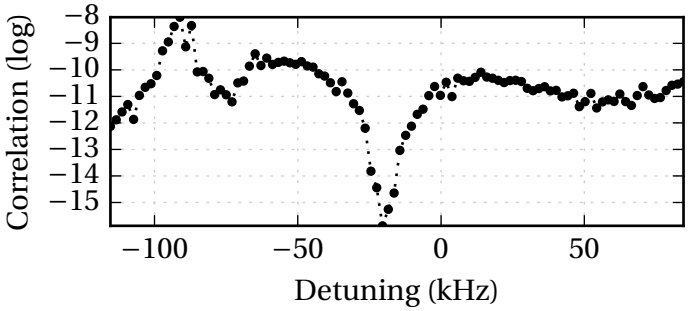

Figure II.47: Correlation between the beatnote amplitude and the phase modulating signal, for different values of the detuning.

7 Conclusions

In this chapter, we have explored many of the different behaviors offered by a frequency-shifted feedback mechanism in a dual-polarization dual-frequency laser. By seeking an excellent agreement with a rate equation model even in the complex resonant regions, we were brought to make precise measurements of the parameters of the laser. This allowed us to identify the existence of an unexpected linewidth enhancement factor, that plays an important role in the injection dynamics.

We have seen that experimental observation of full synchronization (locking), partial synchronization (bounded phase), and chaotic synchronization (bounded chaos) could be fully reproduced with the rate equations model, and that conversely the model could be used to predict new regimes, which were then experimentally observed. Namely, we report the unique bounded phase chaotic regime, which combines chaotic oscillations, and very good stability, as the phase noise measurements did show. On the verge of the locking range, we also observed an excitable-like phenomenon with unique synchronization properties.

The measurement method that was developed for α could be applied to other solid-state lasers using different gain mediums. We tried to use it on a Er^{3+}-doped laser, developed in the framework of the COMTONIQ project [Danion14], but it was not stable enough to measure precisely locking ranges and the minimal detuning. Similarly, it was tried on a Erbium-doped DFB fiber laser, for which it was found unsuited as α was estimated to be above 1. Nevertheless, this study should be continued, as it may give clues to the potential contribution of α to the AM/FM noise conversion process during low phase noise microwave or THz generation [Quinlan11; Rolland14].

Finally, this study proved that this system is very versatile and can be used in a number of ways, from synchronization to chaotic dynamics, and even as a measurement tool for α and maybe other parameters. As it is quite simple, we expect it to be further studied and that the principle can inspire other designs, with the benefit of building on a well-studied reference experiment.

CHAPTER III

SYNCHRONIZATION AND COMPLEX DYNAMICS OF TWO COUPLED SEMICONDUCTOR LASERS

WHILE the previous chapter has been devoted to the study of FSF in solid-state lasers, we will now make a step toward applications, and try to apply FSF to semiconductor lasers. Indeed, when it comes to practical uses, semiconductor lasers are the first choice in a number of domains, from telecommunications [Agrawal02] to spectroscopy [Sasada88]. Among their advantages are an easy frequency tuning through the pump current, integration with electronics, telecommunication wavelengths and facilitated mass production. We will also see that their dynamics under injection are more complex, and that the use of two separated lasers makes the FSF scheme less straightforward. In contrast with the previous chapter, we will not be able to delve into particular instabilities or dynamical regimes, nor will we attempt to obtain a strong quantitative model-experiment agreement. We will rather focus on some particular cases, with a focus on the influence of various parameters.

1 The dual-DFB component

A wide variety of active medium structures exist in the field of semiconductor lasers: from the double heterostructures of the first lasers, to the nanoscale arrangements that confine electrons and holes in the more recent devices. Two-dimensional confinement is obtained by using large inclusions called quantum wells, one-dimensional confinement using elongated structures known as quantum wires, and the more recent quantum dots, as punctual structures, provide “zero-dimensional” confinement [Arakawa82]. Quantum confinement is the use of structures at the nanometer scale that allow to finely control the quantum density of states. The global idea is that

the shape of these structures can force them to act as similarly as possible to a single "artificial atom". This can help inducing desirable properties in terms of wavelength control, temperature sensitivity, low threshold current, high efficiency, low linewidth, etc. Recently, intermediate structures, such as quantum dashes have been used. Being slightly elongated, they combine feature from quantum wire and quantum dots, and may be easier to grow on substrates [Wang01].

In the microwave photonics and telecommunications domains, a key requirement is current modulation efficiency, as high modulation bandwidths allow fast data exchange. The component on which we will focus, being developed in this framework, was specifically engineered so that it can reach a larger than 10 GHz modulation bandwidth, while also keeping a sub-MHz linewidth, and a high output power (in the 10 mW range).

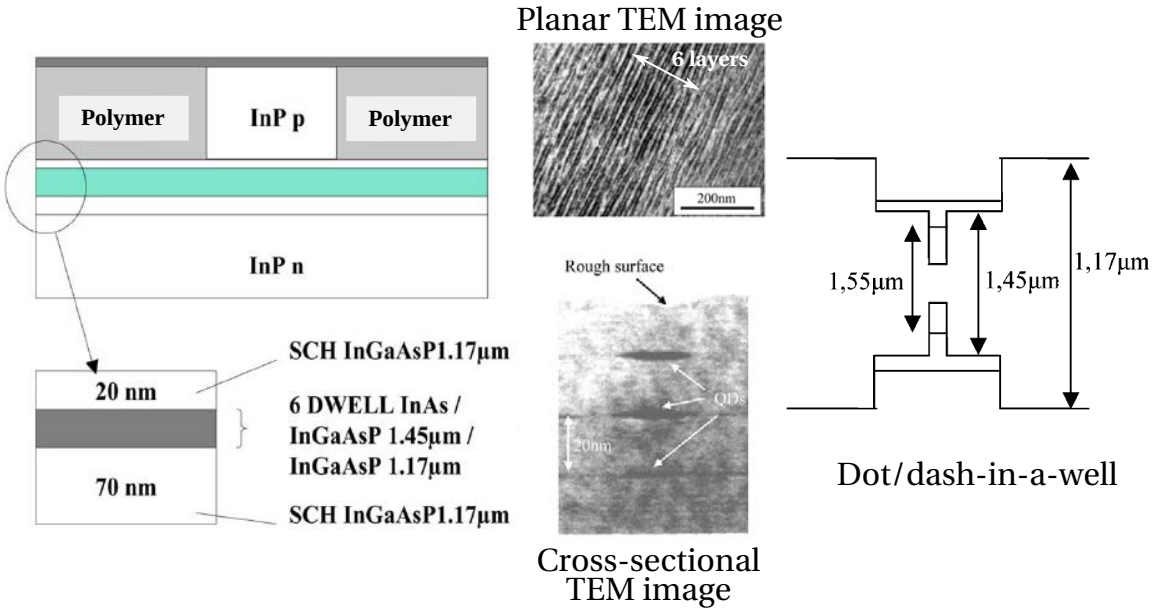

Figure III.1: Description of the DWELL active medium used, and transmission electronic microscope (TEM) pictures. Adapted from [Lelarge07] and [Dagens08]. SCH: Separated confinement heterostructure.

The active medium, designed by the III-V Lab[1], is of quantum dash-in-a-well (DWELL) type (Fig. III.1). This type of active medium strives to combine the foremen-tioned advantages of quantum dots, while overcoming their well-known limitation in modulation bandwidth [Kamath97]. As the performances of quantum-dots-based heterostructure strongly depends on the geometry of the confining nanostructures, it was proposed to insert the quantum dots in a supplementary well. This allows to enhance the confinement to approximately 0.15% per layer, as compared to the usual

[1] a joint lab between Thales Research and Technology France, Nokia Bell Labs France and CEA-Leti, 1 Avenue Augustin Fresnel, Campus Polytechnique, Palaiseau CEDEX

1% per well in quantum wells structures.

Our active medium, grown on a S-doped (001) InP substrate is based on six layers of 170 nm×15 nm InAs quantum dashes, each embedded in an InGaAsP quantum well of gap wavelength $\lambda_g = 1.45\,\mu m$. These layers contain a high density of dashes, around 2×10^{10} cm^2, and are separated by InGaAsP barriers of different gap $\lambda_g = 1.17\,\mu m$. This medium is described in more details in [Lelarge07]. Transverse optical confinement is obtained by using a separated confinement heterostructure (SCH) whose p-side and n-side are 20 nm and 70 nm respectively. This particular type of active medium showed good performances in direct pump current modulation, with bandwiths larger than 10 GHz [Dagens08]. Finally, the need for a small microwave linewidth, and thus a small optical linewidth, translates to a good quality factor of the cavity. This has driven the choice of DFB lasers with quite long (2.5 mm) cavities [Kogelnik72].

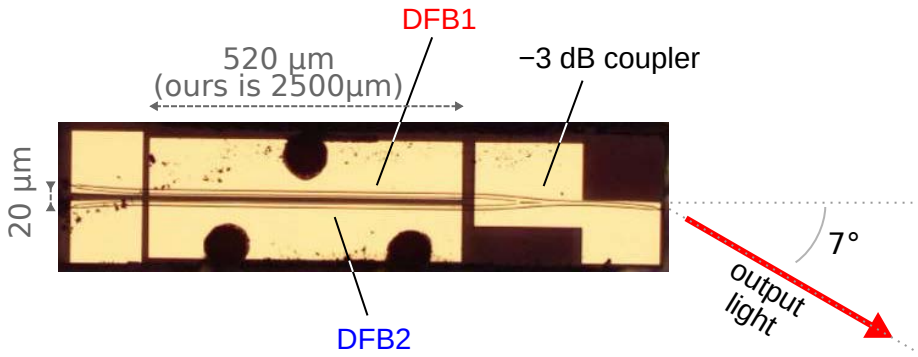

Figure III.2: Microscope photograph of a dual-DFB component, provided by III-V Lab. Here is a picture of a 520 µm long component. Our 2500 µm structure is similar.

The special components we used have been obtained in the framework of the EDA contract MINOTOR. They have been fabricated using gas source molecular beam epitaxy by III-V Lab in Palaiseau (France), and contain two DFB lasers, as described in the publication [van Dijk11] and pictured on Fig. III.2. They operate at wavelength around 1550 nm, and their cavities are separated by 20 µm in order to avoid direct coupling. The output light from each laser is combined by an on-chip −3 dB coupler. Pump current is provided on each laser independently. Additionally, one of them (DFB2) is driven by symmetrical electrical tracks, so that it can be modulated by an RF signal with correct impedance matching. For that reason it will sometimes be referred as the “RF” laser. The characteristic curve, showing the output power collected in the fiber in function of the pump current for each laser is shown on Fig. III.3. We see that they feature a threshold at ~ 80 mA, which is quite high for this kind of laser. The discrepancy between the curve of each laser is not a consequence of the design, nor a signature of the difference between the lasers, as both of them have the same threshold current. It rather reflects the fact that for aging reasons or due to fabrication issues, the on-chip coupler suffer from losses and is clearly asymmetric.

Evolutions of this type of component already exist, and the following versions tend to include more and more features, becoming full-fledged photonic integrated components (PIC). They include semiconductor optical amplifiers (SOA), electro-absorption modulators (EAM), and photodiodes [Kervella14]. The long-term objective of these developments is to have a compact heterodyne source of microwaves on an optical carrier, with a high stability and spectral purity, all integrated on a single component.

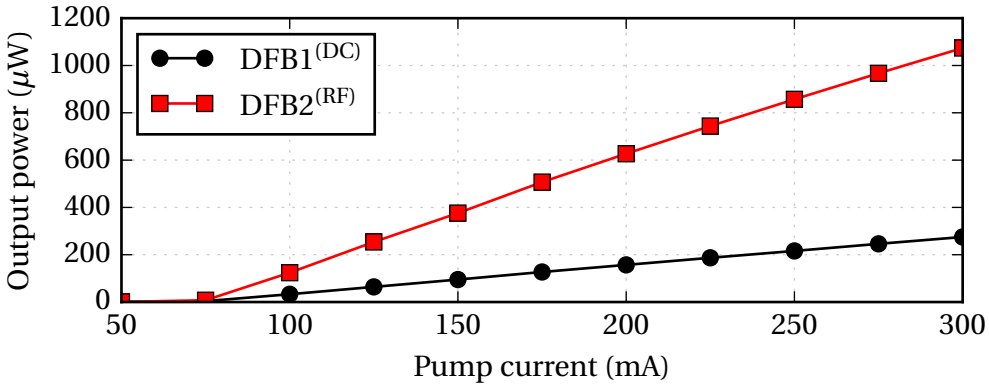

Figure III.3: Optical power collected in the fiber in function of the applied pump current for each laser of the component.

1a Tunability

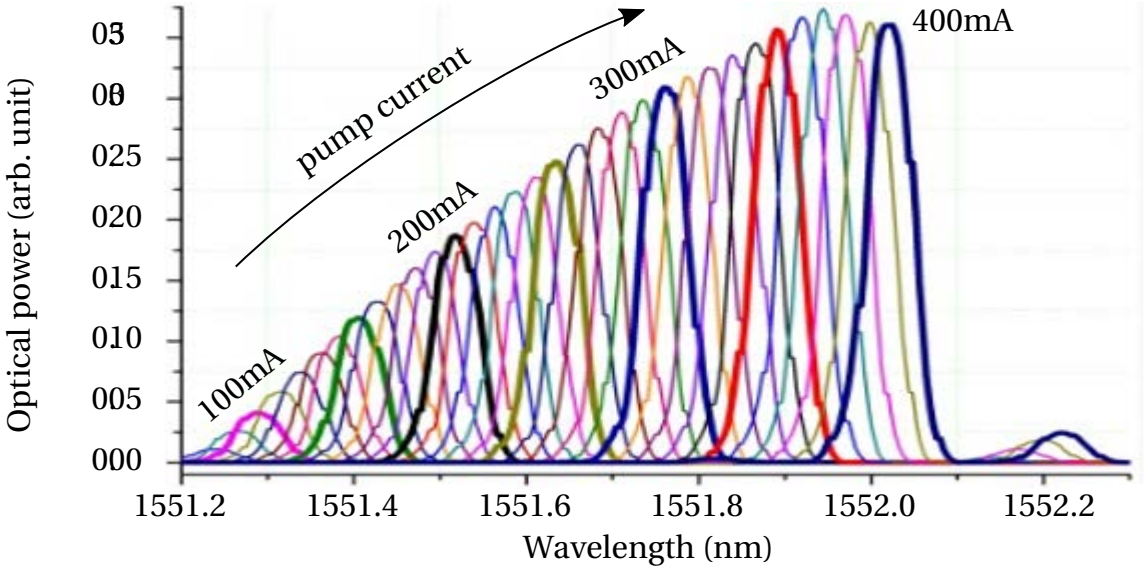

Figure III.4: Shift in the optical spectrum of one laser while varying its pump current by steps of 10 mA. Bold lines correspond to the indicated pump currents.

The output wavelengths ν_1 and ν_2 of each laser are greatly dependent on the pump current [Agrawal86], as clearly shown on Fig. III.4. Namely, we measured typical variations of the wavelength of 2.4 pm/mA (or in terms of frequency, 300 MHz/mA). Furthermore, the wavelength also depends on the temperature. In our setup, the mean temperature of the chip is stabilized by a Peltier element and a controller. This allowed us to measure variations of 0.1 nm/K, or equivalently for the frequency 13 GHz/K. These results are in agreement with values found in the literature for DFB lasers [Akiba82]. Note that in our device, the two effects are coupled. Indeed, the pump current applied to each laser locally heats the semiconductor. Given the proximity of the two lasers, mutual heating is unavoidable, so that changing the pump current of one laser affects both wavelengths.

Yet, we can still use the pump current of one laser to adjust their frequency difference. Fig. III.5 shows that a wide range of frequency differences $\nu_1 - \nu_2$, from nearly DC up to 14 GHz, can be obtained using this chip. In fact, similar components have been used to reach beatnote frequencies up to 100 GHz [van Dijk14].

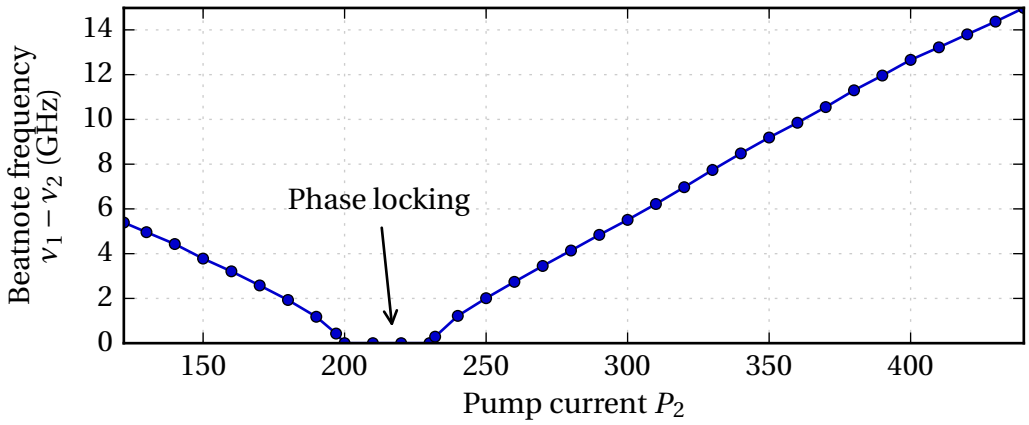

Figure III.5: Beatnote frequency measurement for different pumping currents of DFB2, while DFB1 is kept at $P_1 = 200$ mA.

On a small range of pump currents where the frequencies of the two lasers are closer to each other than 250 kHz, the beatnote disappears. This means that the frequency difference between the lasers have become so small that phase locking happened between them. This phenomenon can be explained by an unwanted small mutual injection, most probably in the optical coupler or at the output facet.

1b Frequency stability

One of the main interest of these dual-DFB components is that, being located on the same chip, the two lasers experience similar environmental noises and drifts. This

makes their frequency difference quite robust on long time scales. In order to quantify this, we used a high-precision heterodyne optical spectrum analyzer (Apex 2083A) to record the optical spectrum every ten seconds during a few hours. The results, including the evolution of the two peak frequencies and of their difference, are shown on Fig. III.6.

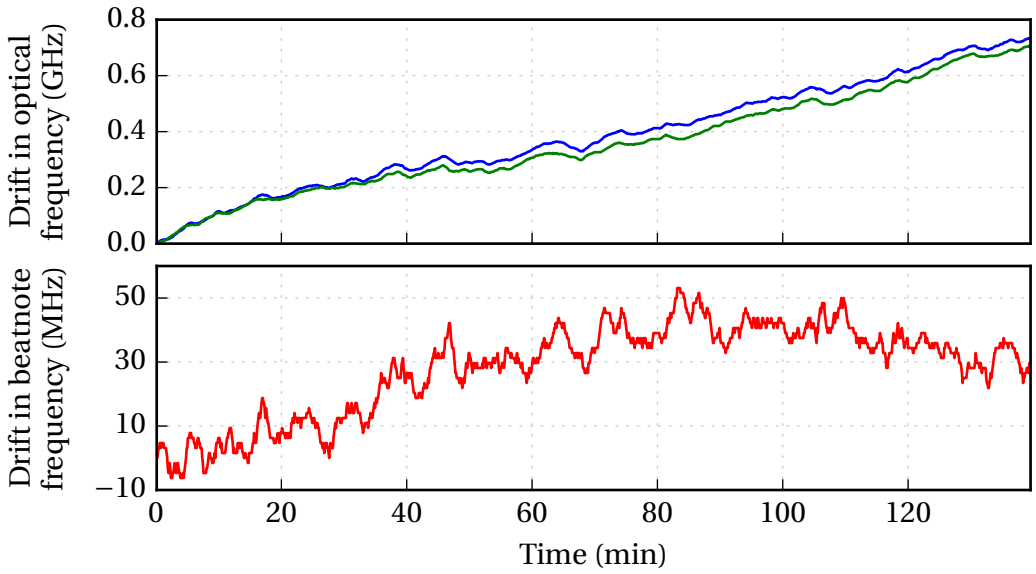

Figure III.6: Long-term natural drift of the optical frequencies of the two DFB. Lower panel show the drift of their difference, which starts around 10 GHz. This corresponds to the actual drift of the beatnote.

In this measurement, the drift of optical frequencies is monotonous, and quite stable at 5 MHz/min, or 80 kHz/s. However, we notice that the variations in frequency for the two lasers are strongly correlated, so that the frequency difference around 10 GHz vary as slowly as 80 kHz/min, for a maximum excursion of 50 MHz on a two hours scale. This confirms the gain in stability obtained by placing the two lasers close to each other on the chip.

1.c Linewidth

The free-running linewidth of the lasers has been measured using an auto-heterodyne setup, shown on Fig. III.7. The output light is split by a coupler, and on one of its arm it is frequency-shifted by 80 MHz by an acousto-optic modulator, while on the other arm it is delayed by a 700 m fiber coil. The two paths are coupled again, and the whole setup forms an unbalanced Mach-Zehnder modulator. Then, observation on a photodiode gives a single peak in the electrical spectrum at 80 MHz. The optical linewidth of the laser can be deduced from the electrical linewidth of this 80 MHz beatnote. In our case, it was measured to be around 300 kHz [van Dijk11]. We can compare the

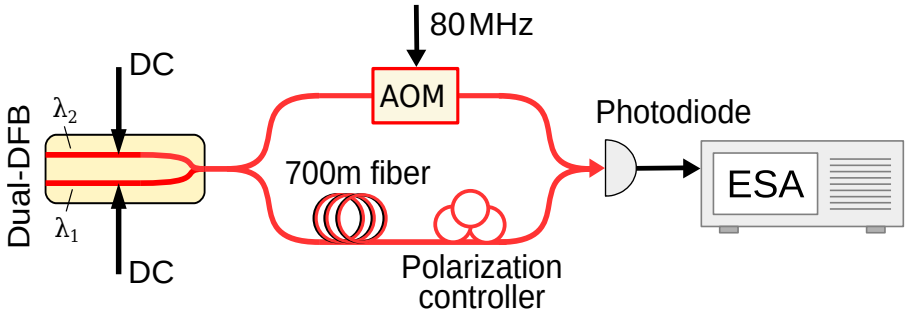

Figure III.7: Autoheterodyne measurement of the optical linewidth of the two lasers.

measured value with the standard Schawlow-Townes formula (I.11) for the full width at half maximum [Schawlow58]: $\Delta\nu = \left(1+\alpha^2\right)\frac{hc}{4\pi\lambda I_{\text{out}}\tau_p^2}$. Here I_{out} is the output power, supposing that all the cavity losses are caused by the output mirror (which is clearly not the case). If we use the value $\tau_p = 8\,\text{ps}$ measured in III.1*d*, $\alpha = 1$ from 1*e* and an output power of 1 mW, we obtain a rough estimation of 320 kHz, which is in the correct order of magnitude. This low linewidth, which corresponds to a large coherence length in fiber of 600 m, will allow coherent injection and feedback experiments for the lasers.

If the two lasers are independent, we expect the linewidth of the microwave beatnote to be the double of this value. This is confirmed by Fig. III.8, which shows the microwave beatnote and the associated Lorentzian fit with an electrical linewidth of 600 kHz. This confirms that the environmental noises experienced by the two lasers are strongly correlated, so that their contribution to the noise of the beatnote is greatly reduced.

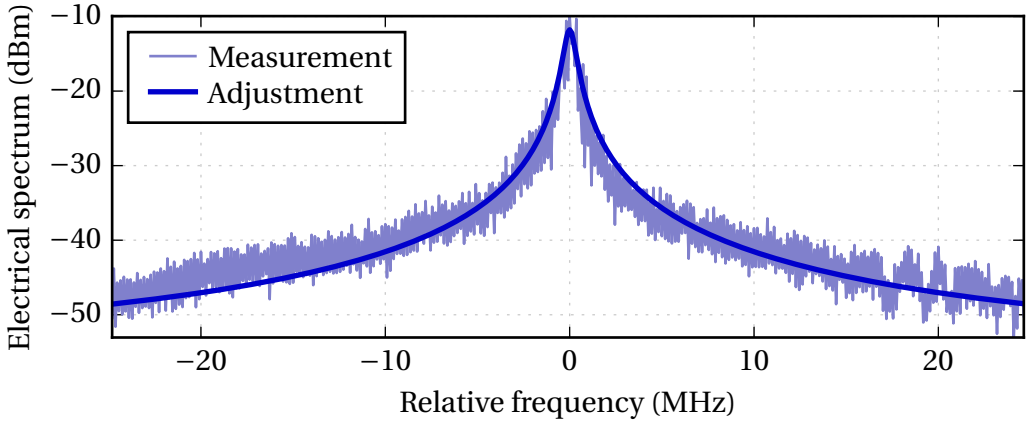

Figure III.8: Measurement and Lorentzian fit of the electrical linewidth of the beatnote. Obtained FWHM is 600 kHz.

As can be seen on Fig. III.9, we checked that this value does not significantly depends on the selected beatnote frequency, except for the expected decrease with pump power, and some experimental dispersion. These values are already on the very

lower end for semiconductor DFB lasers, where linewidth much larger than 1 MHz are common [Tkach86a][2]. Here the frequency quality comes from a combination of the particular active medium [Takano89; Lelarge07] and the long cavity design [Kogelnik72]. However, this linewidth still reflects a certain level of amplitude and phase noise which may be too high for critical applications, and justifies the need for a stabilization mechanism.

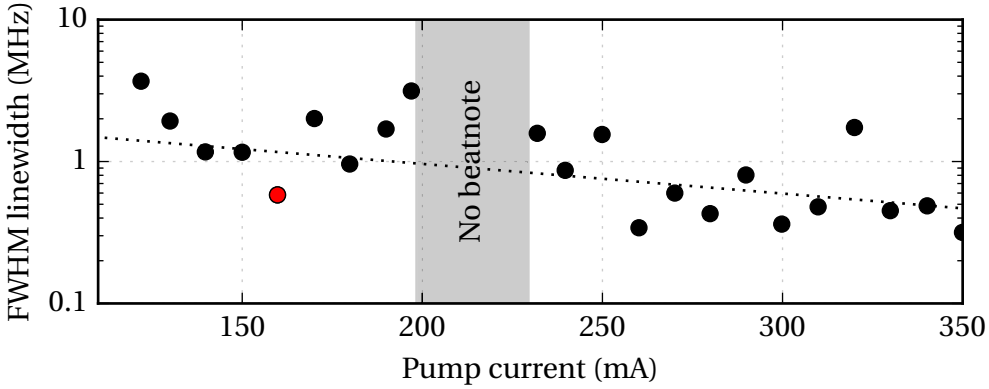

Figure III.9: Full-width at half maximum electric linewidth of the beatnote, for varying pump current of DFB2, while DFB1 is kept at $P_1 = 200\,\text{mA}$. Red dot corresponds to Fig. III.8. Dashed line in the best fit excluding points near the self-locking region.

1*d* Lifetimes measurements

As we are interested in precise numerical simulations of the dynamics under FSF, we need to characterize the time scales of the lasers, namely the lifetime of the carriers τ_c, and the lifetime of the photons in the laser cavity τ_p.

Principle

It appears that measuring the output intensity response to a modulation of the pump current is an efficient way to retrieve these two parameters. This can be seen from the following calculations. We start with a standard rate equations model for the optical intensity I and the normalized population inversion N, similarly to Eqs. (I.10) from Chapter I:

[2] See examples for commercial products:

- http://www.lightwavestore.com/product_datasheet/OSC-LDPM-C-011D_pdf1.pdf
- http://www.optilab.com/images/datasheets/DFB-1550-PM_09022016_v3.pdf
- https://www.furukawa.co.jp/fitel/english/active/pdf/signal/ODC-7R001G_FRL15DCWx-A8x-xxxxx-x.pdf

$$\frac{\mathrm{d}I}{\mathrm{d}t} = -\frac{I}{\tau_p} + 2gNI \tag{III.1a}$$

$$\frac{\mathrm{d}N}{\mathrm{d}t} = -\frac{N}{\tau_c} - 2gNI + \frac{1}{\tau_c}P \tag{III.1b}$$

Here P is the pump current and g the laser gain. The lasing steady-state solution is $\widehat{N} = P_{\mathrm{th}} = 1/(2g\tau_p)$ and $\widehat{I} = (\tau_p P - 1/2g)/\tau_c = \frac{\tau_p}{\tau_c}(P - P_{\mathrm{th}})$, where P_{th} is the threshold current. We are interested in the deviations from this steady state when the pump is modulated so that $P = \widehat{P} + \delta P$. We introduce $I = \widehat{I} + \delta I$ and $N = \widehat{N} + \delta N$, and at the first perturbation order we obtain:

$$\frac{\tau_c}{\frac{\widehat{P}}{P_{\mathrm{th}}} - 1}\frac{\mathrm{d}^2}{\mathrm{d}t^2}\delta I + \frac{\frac{\widehat{P}}{P_{\mathrm{th}}}}{\frac{\widehat{P}}{P_{\mathrm{th}}} - 1}\frac{\mathrm{d}}{\mathrm{d}t}\delta I + \frac{1}{\tau_p}\delta I = \frac{1}{\tau_c}\delta P \tag{III.2}$$

From this the frequency domain transfer function $H(\omega) = \widetilde{\delta I}/\widetilde{\delta P}$ is obtained by letting $\delta P = \widetilde{\delta P}e^{i\omega t}$ and $\delta I = \widetilde{\delta I}e^{i\omega t}$.

$$H(\omega) = \frac{\frac{\tau_p}{\tau_c}}{1 - \tau_c\tau_p\frac{P_{\mathrm{th}}}{\widehat{P}-P_{\mathrm{th}}}\omega^2 + i\frac{\widehat{P}}{\widehat{P}-P_{\mathrm{th}}}\tau_p\omega} \tag{III.3}$$

We define $\omega_R^2 = \left(\frac{\widehat{P}}{P_{\mathrm{th}}} - 1\right)/\tau_c\tau_p$, which corresponds to the pulsation of the relaxation oscillations, and to the cutoff frequency of the transfer function. Then, we let $\omega_R/2\zeta = (\widehat{P} - P_{\mathrm{th}})/(\tau_p\widehat{P})$ in order to obtain a second order low-pass filter.

$$H(\omega) = \frac{\tau_p/\tau_c}{1 + 2i\zeta\frac{\omega}{\omega_R} - \left(\frac{\omega}{\omega_R}\right)^2} \tag{III.4}$$

The corresponding gain $|H(\omega)|$ can be shown to reach its maximum for $\omega_{\mathrm{max}}^2 = \omega_R^2(1 - 2\zeta^2)$.

$$\omega_{\mathrm{max}}^2 = \frac{1}{\tau_c\tau_p}\left(\frac{\widehat{P}}{P_{\mathrm{th}}} - 1 - \frac{1}{2}\frac{\tau_p}{\tau_c}\left(\frac{\widehat{P}}{P_{\mathrm{th}}}\right)^2\right) = \underbrace{-\frac{1}{2\tau_c^2P_{\mathrm{th}}^2}}_{a}\widehat{P}^2 + \underbrace{\frac{1}{\tau_c\tau_pP_{\mathrm{th}}}}_{b}\widehat{P} \underbrace{-\frac{1}{\tau_c\tau_p}}_{c} = a\widehat{P}^2 + b\widehat{P} + c \tag{III.5}$$

This shows that if this maximum is measured for different values of the mean pump current $\widehat{P}$, all parameters can be retrieved using an order 2 polynomial fit on experimental data: $P_{\mathrm{th}} = -c/b$, $\tau_c = \sqrt{-b^2/2ac^2}$ et $\tau_p = \sqrt{-2a/b^2}$.

Results

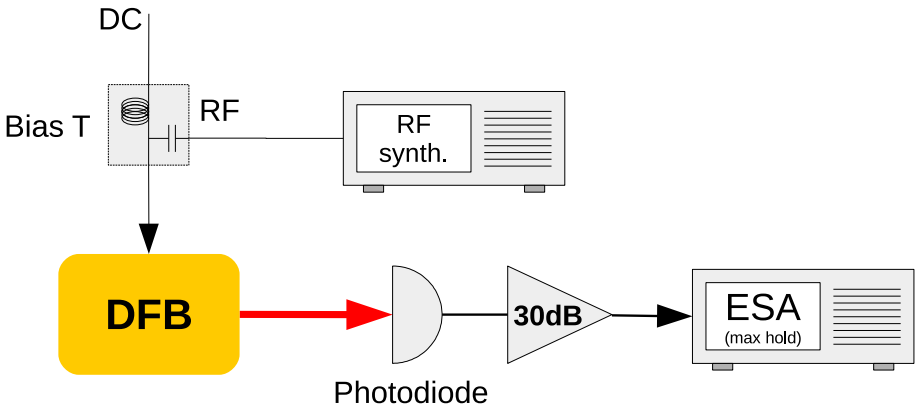

Figure III.10: Experimental setup used to measure the transfer function H of Eq. (III.3). The RF signal is superimposed to the pump current using a bias T, and the output signal is monitored on a Discovery 401HG photodiode, with a 20 GHz bandwidth.

Transfer functions for different pump currents have been measured by modulating it in the 1–12 GHz range using a bias T, as shown on Fig. III.10. Some results are shown on Fig. III.11. For each measurement, the maximum has been located, and reported on Fig. III.12. We notice that this setup measures the transfer function not only of the laser, but of the whole chain, from synthetizer to the ESA. We supposed that other components had weak influence on the result, mostly because we are interested only in the frequency of the maximum of the transfer function. However, this may explain the spurious oscillations observed on the results.

The least-square curve fit according to Eq. III.5 give $\tau_c = 60 \pm 18$ps for carriers, $\tau_p = 8 \pm 1$ps for photons and $P_{\text{th}} = 82 \pm 14$mA for the threshold current. The lifetime of the carriers is relatively small for a DFB laser, and can be related to the particular "quantum dashes" structure of the active medium. Finally, the ratio of the lifetimes is $\tau_p/\tau_c = 0.14 \pm 0.07$.

1.e Linewidth enhancement factor

When studying the behavior of semiconductor lasers under injection and feedback, the linewidth enhancement factor α is a key parameter. Therefore, we have to measure it beforehand. However, we are only interested in the intrinsic part of the phase-amplitude coupling, excluding any temperature effect. This excludes a large number of "AM/FM" methods based on pump current modulation. As we expect values $\alpha \gtrsim 1$, the method developed in the previous chapter (II.5) is not suited here. We settled on another injection method, described in [Hui90]. We first recall the principle here.

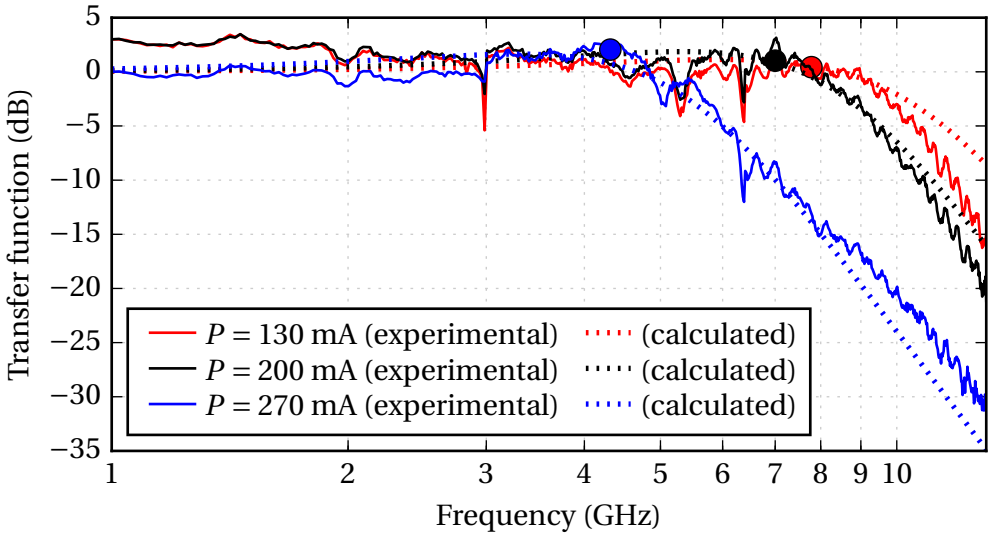

Figure III.11: Examples of measured transfer functions, for different pump currents. The dotted curves are their theoretical counterparts, using Eq. (III.3). The large dots corresponds to the measured maximums.

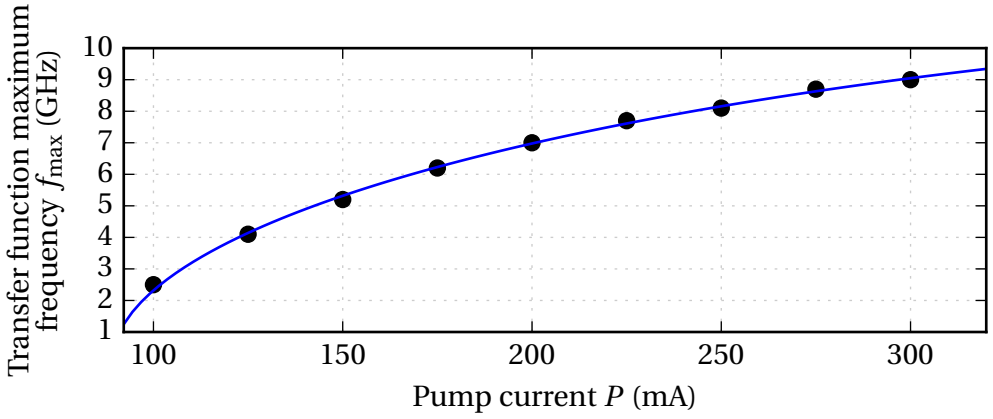

Figure III.12: Frequency of the transfer function maximum, for different values of the pump current. The blue curve is the best second-order polynomial fit, according to Eq. (III.5).

Principle

We start with already normalized rate equations (I.13) for an injected semiconductor laser, including the linewidth enhancement factor α. Here Δ quantifies the frequency detuning between the injected field E_{inj} and the cavity field E. The time scale is set to

match the relaxation oscillation with $s = 2\pi f_R t$.

$$\frac{\mathrm{d}E}{\mathrm{d}s} = \frac{1}{2}(1+i\alpha)NE - i\Delta E + \kappa E_{\mathrm{inj}} \tag{III.6a}$$
$$\frac{\mathrm{d}N}{\mathrm{d}s} = 1 - |E|^2 - \varepsilon N\left(1 + (r-1)|E|^2\right) \tag{III.6b}$$

Here we defined the pump factor $r = P/P_{\mathrm{th}}$ and the damping coefficient $\varepsilon = \sqrt{\frac{\tau_p/\tau_c}{r-1}}$. If we separate amplitude and phase by letting $E = Ae^{i\varphi}$, we obtain:

$$\frac{\mathrm{d}A}{\mathrm{d}s} = \frac{1}{2}NA + \kappa E_{\mathrm{inj}}\cos\varphi \tag{III.7a}$$
$$\frac{\mathrm{d}\varphi}{\mathrm{d}s} = \frac{1}{2}\alpha N - \Delta - \kappa\frac{E_{\mathrm{inj}}}{A}\sin\varphi \tag{III.7b}$$
$$\frac{\mathrm{d}N}{\mathrm{d}s} = 1 - A^2 - \varepsilon N\left(1 + (r-1)A^2\right) \tag{III.7c}$$

These equations give the following steady state:

$$\frac{1}{2}\widehat{N}\widehat{A} = -\kappa E_{\mathrm{inj}}\cos\varphi \tag{III.8a}$$
$$\frac{1}{2}\alpha\widehat{N} = \Delta + \kappa\frac{E_{\mathrm{inj}}}{\widehat{A}}\sin\varphi \tag{III.8b}$$
$$\widehat{A}^2 = \frac{1-\varepsilon\widehat{N}}{1+\varepsilon(r-1)\widehat{N}} \tag{III.8c}$$

If the injection is turned off, with $E_{\mathrm{inj}} = 0$, then $\widehat{N} = 0$ and $\widehat{A} = 1$. We notice that the same result is obtained in the case where $\varphi = \pi/2$. This corresponds to a particular value of the detuning Δ_m, for which we have:

$$\Delta_m + \kappa E_{\mathrm{inj}} = 0 \tag{III.9}$$

This means that when the detuning matches this particular value Δ_m, the output power from the laser is exactly the same as would have been observed without any injection. Then, combining equation (III.8a-b), we can also express φ:

$$\Delta = -\frac{\kappa E_{\mathrm{inj}}}{\widehat{A}}\left(\sin\varphi + \alpha\cos\varphi\right) \tag{III.10}$$

This means that the maximum value that $|\Delta|$ can take is given for $\cos\varphi - \alpha\sin\varphi = 0$,

i.e. $\tan\varphi = 1/\alpha$. This corresponds to $\sin\varphi + \alpha\cos\varphi = \sqrt{1+\alpha^2}$. In the low injection regime, it can be shown that this condition actually matches with the stable locking range [Mogensen85]. Furthermore, using Eq. (III.8c), we can show that $\widehat{A} \approx 1 + r\varepsilon\kappa E_{\text{inj}}\cos\varphi$ to the first order in $\varepsilon\kappa$, so that we have a locking range of:

$$|\Delta| < \Delta_0 \approx \kappa E_{\text{inj}}\sqrt{1+\alpha^2} \tag{III.11}$$

This allows to easily measure $\sqrt{1+\alpha^2} = -\Delta_0/\Delta_m$ and eventually we obtain the following formula:

$$\alpha = \sqrt{\left(\frac{\Delta_0}{\Delta_m}\right)^2 - 1} \tag{III.12}$$

In the case of a stronger injection, the relation between E_{inj}, Δ_0 and α becomes more complicated and has no analytical expression. It could nonetheless be computed numerically to extend the method. In the following measurement, we have ensured that we stayed in the weak injection regime by checking that the locking range remained roughly symmetric with respect to the detuning (see I.2*a*).

Experimental realization

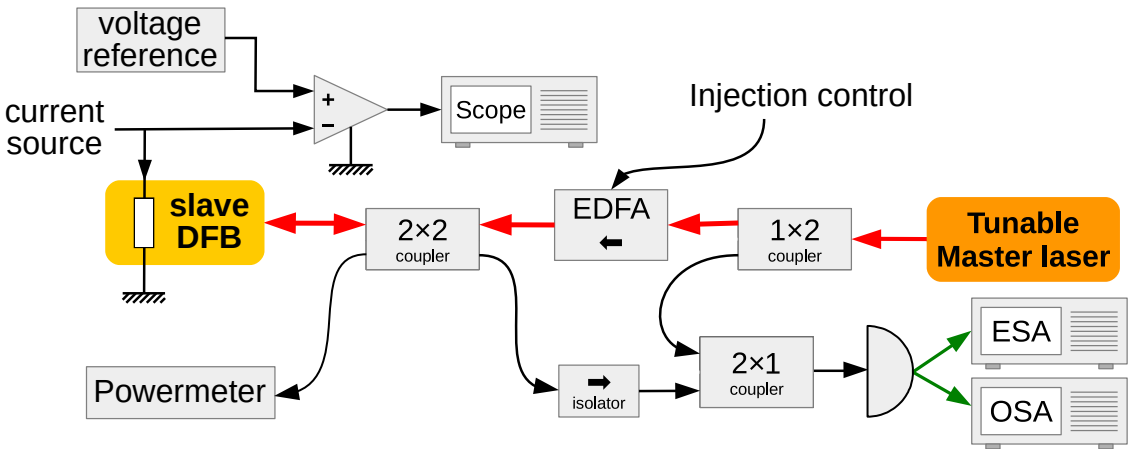

Figure III.13: Experimental setup used for measuring the linewidth enhancement factor.

We have to measure precisely the output power of the laser, in order to compare its level with and without injection. Unfortunately, the coupling from the output of the chip into the fiber is not very stable, so that the power measured in the fiber is not a reliable measurement.

It appears that the same information can be obtained by measuring the variations of the tension on the terminals of the laser diode, as it is proportional to the variation

of carrier density [Kazarinov74; Hui90]. However, the differences we want to measure around the 1 V mean value are weak, in the mV range. For that purpose, we used a differential amplifier (the 7A22 rack of a Tektronix 7603 analog oscilloscope) and a voltage reference set on the mean value (Adret voltage etalon, with voltage precision $\Delta V/V \approx 2\times 10^{-5}$). The whole setup is shown on Fig. III.13. To avoid any noise from the 50 Hz AC power supply, we set the oscilloscope's trigger on the "Line" option, use the shortest time scale possible, and read the useful value right after the triggering.

The master laser was a Tunics, with wavelength setting precision down to 0.01 nm, and a fine tuning capability of 2 GHz. The frequency detuning between master and slave lasers is controlled using the "TUNE" input of the Tunics laser. It has an effect of roughly 400 ± 10 MHz/V in the ± 7 V range[3]. An external amplifier (EDFA) was also used to control the injected power. Monitoring of the state laser is done by an heterodyne setup. Its output is mixed with the output of the master laser, and the observation of the electrical spectrum of their beatnote allows to discriminate locking from unlocking.

Finally, we see that the injection, even non-resonant (i.e. with a very large detuning compared to relaxation oscillations), leads to a small offset in the output frequency of the DFB of roughly $30\,\text{MHz}\times P_{\text{in}}/P_{\text{out}}$. This is probably due to a thermal effect, and was accounted for in the results, by subtracting this value from the measured frequencies.

Results

Measurements have been performed on each DFB laser. The frequencies have not been measured directly, but rather deduced from the control voltage V applied to the master laser. The measurement protocol is as follows:

1. Without injection (EDFA off), the master laser is tuned in order to observe a null beanote frequency on the spectrum analyser. The control voltage is stored as V_0, and the oscilloscope is adjusted to show a zero voltage.

2. Injection is turned on, and control voltage is varied until it reaches V_m, where a null voltage is observed again on the oscilloscope. This corresponds to an output power that is identical to the non-injected case.

3. Boundaries of the locking range are located by varying the detuning. Unlocking can be seen on the electrical spectrum. Thus V_+ and V_- are found.

4. Ultimately, we have $\frac{\Delta_0}{\Delta_m} = \frac{V_+ - V_-}{2(V_m - V_0)}$, from which α is deduced.

[3] Specifications are ± 10 V, but we noticed that it is not linear anymore when the voltage is too high.

Results are shown on Fig. III.14. As a comparison, this protocol has also been applied to a a commercial telecommunication DFB laser. This was done in order to validate the protocol, as expected values for this kind of laser is $\alpha \approx 2-3$. We used an Alcatel A1905 LMI 3CN00386NUAA laser diode, from which we had previously removed the integrated isolator. The estimated value of $\alpha \approx 2.4$ seems to be in good agreement with the literature for this type of DFB laser diodes [Kikuchi85; Osinski87]. This allows to put a high trust level on our measurement.

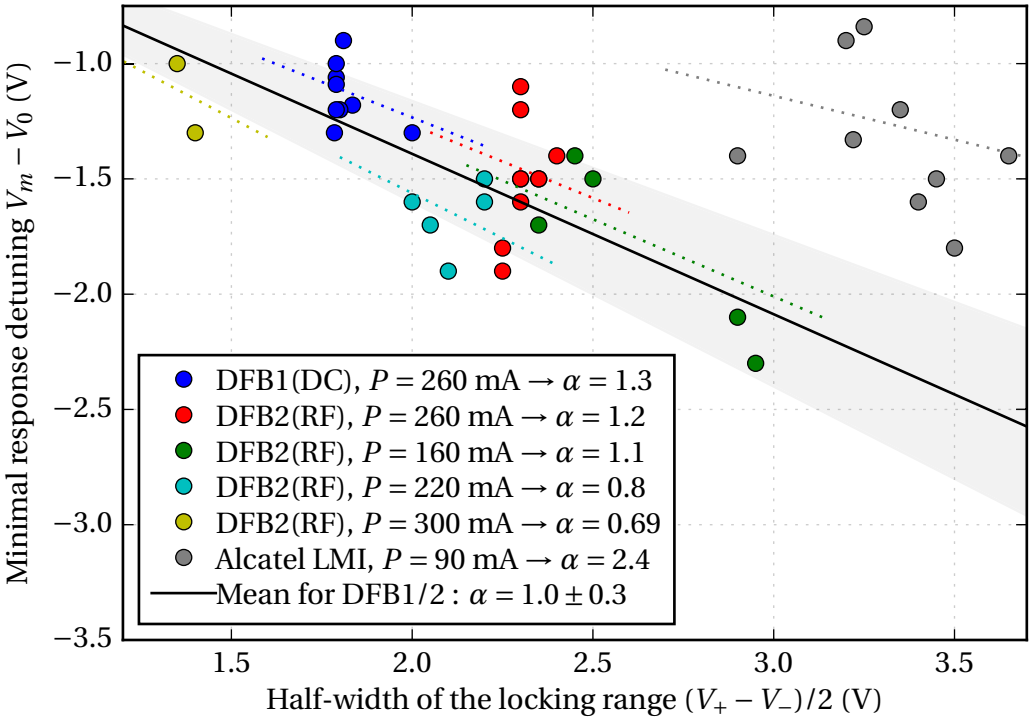

Figure III.14: Summary of the linewidth enhancement factor measurements. Points show measured values for different lasers and parameters. Dotted lines show the best fit for each set of measurement, while the solid line show the best fit taking in account every measurement on our lasers. Light gray region materializes the estimated error on the final value.

For the two lasers from the component under study, a value of α close to 1 is found for any injection rate and pump current. The mean value of all measurements, along with a coarse estimation of the error including measurement precision, dispersion and systematic error, lead to $\alpha = 1.0 \pm 0.3$. This surprisingly low value can be explained by the very particular QDash layer structure of the lasers, which was developed with a low linewidth in mind. This has already been observed in dot-in-a-well structures [Newell99] and also in dash-in-a-well in very similar configuration to ours [Moreau06]. A better correction of systematic errors, notably on frequency measurements could allow a more precise result. Yet, this is sufficient for our needs.

2 Setup and model for frequency-shifted feedback

With these precisely characterized components at hand, we subjected them to an optical feedback loop including an amplitude modulator, in an attempt to stabilize the frequency difference between the two lasers. This method is directly derived from the one we applied on solid-state lasers in the previous chapter. However, contrary to the dual-polarization solid-state lasers, the two different wavelengths have the same polarization, and thus cannot be easily separated. Also, non-resonant modulators at microwave frequencies (here we use 10 GHz) are Mach-Zehnder modulators (MZM), and do not allow pure frequency shifting. Instead, they create sidebands around the input frequency. All these constraints do not allow us to create a one-way injection from one laser to the other. We will have to take into account cross-injection and self-feedback for the two lasers. A fair part of this work corresponds to [Thorette19].

2a Experimental setup

The output light from the PIC is collected by a single-mode anti-reflection coated microlensed fiber. It is precisely placed in front of the output coupler by an XYZ micropositioner.

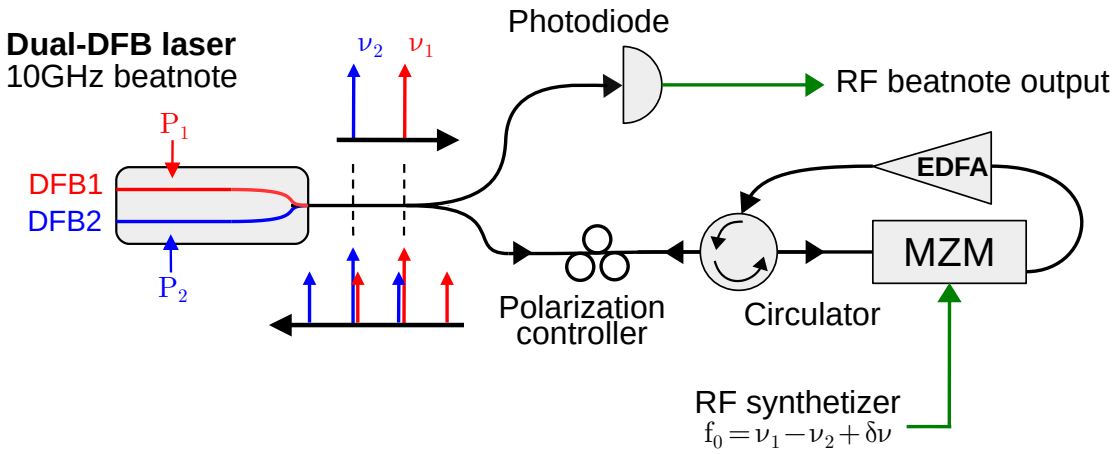

Figure III.15: Experimental setup of a fibered FSF scheme applied to the dual-DFB component. See text for details.

Once the light enters the fiber, it travels through an all-fibered polarization-maintaining (PM) loop, shown on Fig. III.15. A polarization controller is placed before the first PM element, in order to adjust the polarization axis and minimize the losses. The loop is formed by a circulator, of which two ports are linked by a Mach-Zehnder amplitude modulator (MZM, model Photline MX-LN-10 with 12 GHz bandpass) and a home-made Erbium-Doped Fiber Amplifier (EDFA). This last component was built

using a single stage of amplification, with the shortest possible length of doped fiber, here 1.5 m. This leads to a fiber length in the amplifier of only 5 m. Its optical gain for 100 µW of input power can reach 14 dB, and it can be used to completely block the signal when not pumped. The total length of fiber in the feedback loop is thus $L = 16$ m.

The amplitude modulator is fed with a tunable microwave signal at frequency f_0, generated by a low-noise synthetizer (Rohde&Schwarz SMF100A). It creates sidebands around each laser's optical frequency. When f_0 is close to the free-running frequency difference $\nu_1 - \nu_2$, one of the sidebands becomes resonant for the other laser, which leads to cross-injection between the lasers. The cross-injection strength is quantified by the modulation rate m, that we choose to define as:

$$\mathcal{E}_{\text{out}} = t_0 \mathcal{E}_{\text{in}} \left[\sqrt{1-m} + \sqrt{\tfrac{m}{2}} \left(e^{2i\pi f_0 t} + e^{-2i\pi f_0 t} \right) + ... \right] \tag{III.13}$$

where $\mathcal{E}_{\text{in}}$ and $\mathcal{E}_{\text{out}}$ are the input and output fields of the modulator, respectively. This convention was chosen so that for an optical input power I_0, the optical intensities after the modulator are $t_0(1-m)I_0$ for the carrier and $t_0 \frac{m}{2} I_0$ for the main sidebands. For reasons that will be explained shortly after, we are not interested in the harmonics of the modulation, and they are accounted for in the transmission coefficient t_0. As $m \leq 1$, unmodulated light usually remains at the output, so that self-feedback is also present for each laser.

Finally, a part of the output light is also routed to a 20 GHz photodiode, which records the beatnote between the different optical frequencies. This output signal in the microwave domain is then monitored on an electrical spectrum analyzer (ESA) and on a fast 11 GHz oscilloscope (LeCroy SDA11000). In order to keep the signal in the bandwidth of the oscilloscope, the 10 GHz beatnote is down-converted by multiplying it with a fixed signal at 9 GHz.

2b Delayed rate equations

Resonant approximation and the relevant terms

The setup on Fig. III.15 includes a large number of coupling and feedback between the lasers. Indeed, the amplitude modulator in the feedback loop creates sidebands around the optical frequency of each laser, so that the two original carriers, the four first-order sidebands, and also their possible harmonics are injected back into the cavity of the two lasers. However, as shown on Fig. III.16, the frequency driving the modulator f_0 is chosen close to the frequency difference of the lasers $\nu_1 - \nu_2 \approx 10$ GHz. The remaining frequency difference $\delta\nu = \nu_1 - \nu_2 - f_0$, called frequency detuning is always less than 500 MHz. This is why we are allowed to make the approximation that

only the two "quasi-resonant" injected fields for each laser contribute significantly to the dynamics.

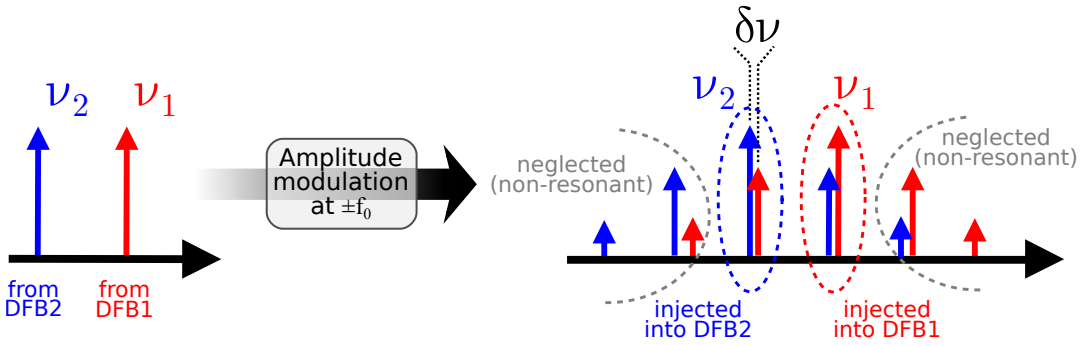

Figure III.16: Depiction of the different frequencies generated by the amplitude modulator, which are injected back into the lasers.

This hypothesis, which will be checked afterwards (see 3*a*), allows us to compare our setup to the more general problem of two coupled lasers, as depicted on Fig. III.17. Now, each laser experiences self-feedback, and also cross-injection from the other. We can notice here that the role of the frequency-shifting by $\pm f_0$ is only to make the frequency of each injecting field closer to the optical frequency of the injected laser. It creates a controllable frequency detuning $\pm\delta\nu$ in the mutual injection, that is small compared to the frequency difference.

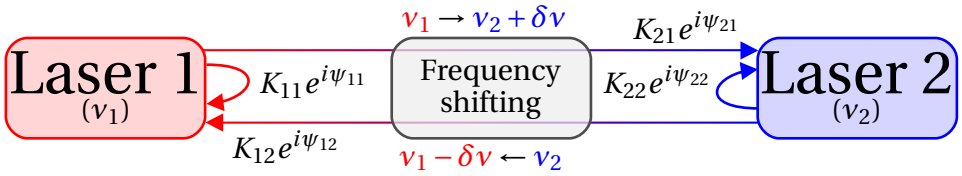

Figure III.17: Coupling mechanisms between the two lasers.

Rate equations and normalization

We can now use standard rate equations for class-B lasers [Erneux10; Siegman86] and include for each laser the appropriate delayed self-feedback and cross-feedback terms. Given the low linewidth of the lasers, we can still consider only coherent injection. The equations for the intracavity fields $\mathcal{E}_j$ and normalized population inversions N_j are:

$$\frac{\mathrm{d}\mathcal{E}_1}{\mathrm{d}t} = (1+i\alpha)gN_1\mathcal{E}_1 + 2i\pi\nu_1\mathcal{E}_1 + K_{11}\mathcal{E}_1(t-T_{11}) + K_{12}\mathcal{E}_2(t-T_{12})\cos(2\pi f_0 t) \quad \text{(III.14a)}$$

$$\frac{\mathrm{d}\mathcal{E}_2}{\mathrm{d}t} = (1+i\alpha)gN_2\mathcal{E}_2 + 2i\pi\nu_2\mathcal{E}_2 + K_{22}\mathcal{E}_2(t-T_{22}) + K_{21}\mathcal{E}_1(t-T_{21})\cos(2\pi f_0 t) \quad \text{(III.14b)}$$

$$\frac{\mathrm{d}N_1}{\mathrm{d}t} = -\frac{N_1}{\tau_c} - \left(\frac{1}{\tau_p} + 2gN_1\right)|\mathcal{E}_1|^2 + \frac{1}{\tau_c}P_1 \quad \text{(III.14c)}$$

$$\frac{\mathrm{d}N_2}{\mathrm{d}t} = -\frac{N_2}{\tau_c} - \left(\frac{1}{\tau_p} + 2gN_2\right)|\mathcal{E}_2|^2 + \frac{1}{\tau_c}P_2 \quad \text{(III.14d)}$$

The measurement of all the parameters having confirmed that we have two "identical" lasers, we consider the lifetimes, gain, linewidth enhancement factor and threshold current to be the same for both lasers. As the lasers we consider have a high pumping current, we can safely ignore any spontaneous emission term.

However, we allow the lasers to have different frequencies ν_j and pumping currents P_j. The $K_{ij} = \left|K_{ij}\right| e^{i\psi_{ij}}$ are complex coefficients quantifying the injection strengths, and T_{ij} is the time delay between the cavity field and injected field for each component. At the first order, they are just $T = nL/c$ with n the mean optical index of the fiber, but we allow them to be slightly offset from this mean value, so that $T_{ij} = T + \delta T_{ij}$. This permits to take into account unwanted effects such as frequency drifts of the lasers, variation of the fiber length and index, dispersion, additional phase shifts, etc.

We consider our fields to be monochromatic, and are only interested in their complex amplitude, so we place ourselves in the rotating frames $\mathcal{E}_1 = E_1 e^{i\xi} e^{2i\pi\nu_1 t}$ and $\mathcal{E}_2 = E_2 e^{2i\pi(\nu_1 - f_0)t}$. We introduced a constant phase ξ, which will be chosen later for convenience. Then, as the complex amplitudes are expected to vary slowly in comparison with the optical phases, we make the assumption that $E(t-T_{ij}) \approx E(t-T)$ for each field. This is very convenient, as the system now features a single constant delay.

We can also proceed to further normalizations $e_j = \frac{1}{2\pi f_R}\sqrt{\frac{g}{\tau_p}}\mathcal{E}_j$ and $m_j = \frac{g}{2\pi f_R}N_j$. We also introduce the pumping ratios $r_j = \tau_p g P_j$ and normalized damping coefficient $\varepsilon = \sqrt{\frac{\tau_p}{\tau_c(r_1-1)}}$. In order to obtain non-stiff equations, we also choose a time scale $s = 2\pi f_R^{(1)} t$, which is normalized to the frequency of the relaxation oscillations of the *first and less pumped laser* $f_R^{(1)} = \frac{1}{2\pi}\sqrt{\frac{r_1-1}{\tau_c\tau_p}}$. This leads to normalized delay $\tau = 2\pi f_R^{(1)} T$, detuning $\delta = (\nu_1 - \nu_2 - f_0)/f_R^{(1)}$, and injection strengths $\kappa_{ij} = \left|K_{ij}\right|/2\pi f_R^{(1)}$. Starting from the two field equations (III.14a–b) and neglecting the non-resonant sidebands of

the modulation, we obtain:

$$\frac{\mathrm{d}e_1}{\mathrm{d}s} = (1+i\alpha)\frac{m_1 e_1}{2} + \kappa_{11}\overbrace{e^{-2i\pi\nu_1 T_{11}+i\psi_{11}}}^{e^{i\varphi_1}} e_1(s-\tau) + \kappa_{12}\overbrace{e^{-2i\pi(\nu_1-f_0)T_{12}+i\psi_{12}-i\xi}}^{e^{i\varphi_x}} e_2(s-\tau) \tag{III.15a}$$

$$\frac{\mathrm{d}e_2}{\mathrm{d}s} = (1+i\alpha)\frac{m_2 e_2}{2} - i\delta e_2 + \kappa_{22}\overbrace{e^{-2i\pi(\nu_1-f_0)T_{22}+i\psi_{22}}}^{e^{i\varphi_2}e^{-i\delta\tau}} e_2(s-\tau) + \kappa_{21}\overbrace{e^{-2i\pi\nu_1 T_{21}+i\psi_{21}+i\xi}}^{e^{i\varphi_x}e^{-i\delta\tau}} e_1(s-\tau) \tag{III.15b}$$

Here, we have defined three phases of physical significance φ_1, φ_2 and φ_x that do not depend on the detuning. In equation (III.15b), we also notice a phase term $e^{-i\delta\tau}$ that does depend on the detuning. This was obtained using an approximation, namely that $\delta\nu \times T_{ij} \approx \delta\nu \times T$, i.e. we neglected the second-order terms $\delta\nu \times \delta T_{ij}$ that represent the variations of the microwave phase due to the small difference of delay in the different injected fields. Finally, for symmetry reasons, we have chosen ξ so that the same phase $e^{i\varphi_x}$ appears in both mutual injection terms. This cross-injection phase reads $\varphi_x = 2\pi\left(\frac{\nu_1-\nu_2}{2}T_{12} + \nu_1\frac{T_{12}+T_{21}}{2}\right) + \frac{\psi_{12}+\psi_{21}}{2}$. In contrast with the model from Chapter II, this means that we can no longer ignore the optical phase differences between the injected fields and the cavity fields. By comparing with the simple feedback case, i.e. the Lang-Kobayashi model (Section I.2*b*), we can even expect these phase parameters φ_j to play a key role in the dynamics. Finally, we obtain the following normalized model of rate equations:

$$\frac{\mathrm{d}e_1}{\mathrm{d}s} = (1+i\alpha)\frac{m_1 e_1}{2} + \kappa_{11}e^{i\varphi_1}e_1(s-\tau) + \kappa_{12}e^{i\varphi_x}e_2(s-\tau) \tag{III.16a}$$

$$\frac{\mathrm{d}e_2}{\mathrm{d}s} = (1+i\alpha)\frac{m_2 e_2}{2} - i\delta e_2 + \kappa_{22}e^{i\varphi_2}e^{-i\delta\tau}e_2(s-\tau) + \kappa_{21}e^{i\varphi_x}e^{-i\delta\tau}e_1(s-\tau) \tag{III.16b}$$

$$\frac{\mathrm{d}m_1}{\mathrm{d}s} = 1 - |e_1|^2 - \varepsilon m_1\left(1 + (r_1-1)|e_1|^2\right) \tag{III.16c}$$

$$\frac{\mathrm{d}m_2}{\mathrm{d}s} = \frac{r_2-1}{r_1-1} - |e_2|^2 - \varepsilon m_2\left(1 + (r_1-1)|e_2|^2\right) \tag{III.16d}$$

Injection rates

The setup described in Fig. III.15 corresponds to a particular form of the κ_{ij} coefficients, on which we will focus now. First, they have to take into account the asymmetric transmission t_j of the output mirrors and on-chip coupler between the two lasers, already mentioned and visible on Fig. III.3. It can be estimated when the two lasers are

pumped identically, and their output powers differ by $q = t_2/t_1 = I_2/I_1 = 0.25$. Second, it must include the modulation ratio m and the amplifier gain G. We add a parameter κ which account for the overall coupling efficiency between injected fields and the cavity of the lasers. This leads to:

$$\mathbb{K} = \begin{pmatrix} \kappa_{11} & \kappa_{12} \\ \kappa_{21} & \kappa_{22} \end{pmatrix} = G\kappa t_0 \begin{pmatrix} t_1\sqrt{1-m} & \sqrt{t_1 t_2}\sqrt{m/2} \\ \sqrt{t_1 t_2}\sqrt{m/2} & t_2\sqrt{1-m} \end{pmatrix} = \kappa_0 \begin{pmatrix} \sqrt{1-m} & \sqrt{qm/2} \\ \sqrt{qm/2} & q\sqrt{1-m} \end{pmatrix} \quad \text{(III.17)}$$

with $\kappa_0 = \kappa G t_0 t_1$ being an injection strength parameter. It can be controlled through the gain of the in-loop amplifier. However its absolute value depends on losses in the coupler and in the fiber injection, and cannot be measured precisely in our setup. Still, we will see in Section 2*d* that it can be estimated using an auxiliary experiment.

Summary of the parameters

Among the system's parameters, we will particularly focus on the influence of detuning δ, modulation ratio m, injection strength κ_0, and delay τ. The other parameters have been carefully measured in sections 1*d* and 1*e* for the DFB lasers and are kept fixed through the numerical study.

Relaxations oscillations of the least pumped laser are $f_R^{(1)} \approx 8\,\text{GHz}$. In order to obtain a frequency difference $\nu_1 - \nu_2$ around 10 GHz, we used $r_1 = 3$ and $r_2 = 4$. The fiber length of the whole feedback loop was $L \approx 16\,\text{m}$, which gives a large normalized delay $\tau = 4000$. All these parameters are summarized in Table III.1[4].

One must note that this kind of model has already been studied in the context of two semiconductor lasers, placed in front of each other and separated by a semi-reflecting mirror [Flunkert11; Wünsche05]. These dynamical studies focused on particular points, for instance the detrimental influence of noise on the synchronization stability, with the presence of a noise-induced on-off intermittency known as bubbling [Flunkert09]. Partial studies of the stability of the external cavity modes have also been done numerically [Hicke11].

[4] In the actual simulations we have taken $\varepsilon \approx 0.4$. This value is based on a previous measurement of $\tau_c/\tau_p = 0.3$, a value which differs slightly from the one found in Section 1*d*. However, it remains within the uncertainty range of the measurement, so the correction did not motivate a complete redo of the numerical simulations. The same thing happened for the linewidth enhancement factor, which was initially believed to be $\alpha = 1.2$, so this value is used in many following results.

Pumping ratio of laser 1	$r_1 = P_1/P_{\text{th}}$	3
Pumping ratio of laser 2	$r_2 = P_2/P_{\text{th}}$	4
Photon ("cavity") lifetime	τ_c	60 ± 18 ps
Population inversion lifetime	τ_p	8 ± 1 ps
Normalized damping factor	$\varepsilon = \sqrt{\frac{\tau_p}{\tau_c(r_1-1)}}$	0.2 (see footnote 4)
Linewidth enhancement factor	α	1.0 ± 0.3 (see footnote 4)
Relaxation oscillations frequency of laser 1	$f_R^{(1)}$	≈ 8 GHz
Output asymmetry	q	0.5
Normalized injection rate	κ_0	< 0.1
Normalized delay	τ	4000

Table III.1: Summary of parameters measured, and subsequently used for the following simulations.

Estimating the drift of the feedback phases

A rough estimate of the drift of the optical phases φ_j can be made from the drift of the lasers. As can be seen from Fig. III.6, the optical frequencies exhibit strongly correlated drifts of about 80 kHz/s. Recalling the definition of the optical feedback phases, we get for instance a variation of the self-feedback phase φ_1 for the first mode of 50 mrad/s. This means that a 2π variation of φ_1 takes approximately 2 min. However, we have to realize that φ_2 and φ_x will experience very similar drifts, as their variations are correlated to those of φ_1. Indeed, φ_2 can be written as:

$$\varphi_2 = \varphi_1 + 2\pi \frac{(\nu_1 - \nu_2)\, nL}{c} + \psi_{22} - \psi_{21} \tag{III.18}$$

Thus, if we ignore the phases ψ_{ij} for now, the variation of φ_2 with respect to φ_1 is ruled by the drift of the frequency difference $\nu_1 - \nu_2$, which, according to Fig. III.6, is ten times slower than the optical frequency drift, corresponding roughly to 60 MHz in two hours. This means that $\delta\varphi_2 - \delta\varphi_1$ takes around 20 min to make a 2π excursion.

Uncorrelated drifts between the phases φ_j can also happen, but are much slower, as the main contribution would be phase dispersion in the used SMF-28 fiber, which is roughly 15 ps/nm/km for our wavelength of 1550 nm. For our 17 m loop, and a frequency drift of 80 kHz/s, this corresponds to a phase difference drift of 0.2 mrad/s. However other perturbations can contribute and are difficult to quantify, for instance acoustic noise, thermal changes, phase shift in the output coupler, during the insertion in the microlensed fiber or in the modulator.

2c Analytical considerations

Analytical study of the system (III.16) is complicated in the general case. A few attempts have been made, for instance in [Flunkert11], but without the detuning term $-i\delta e_2$. Even so, only necessary conditions for the existence of a steady state could be found. Sufficient conditions, or arguments about the stability of the locking state do not exist to our knowledge. We present here the very beginning of a study, which allows to obtain an equation for the external cavity modes frequencies (see I.2*b*).

We start from a rotating steady state of Eqs. (III.16a-b) that corresponds to an external cavity mode (ECM). This means that the two fields have a constant amplitude but a rotating phase, so that $e_j = \widehat{e_j} e^{i\Omega s}$. Here, we require the external cavity mode pulsation Ω to be the same for the two fields, which is a necessary condition for a synchronized state. If we also define $\gamma = \arctan\alpha$ so that we can rewrite $1 + i\alpha = \sqrt{1+\alpha^2}e^{i\gamma}$, we obtain the following complex equations:

$$i\Omega = \sqrt{1+\alpha^2}e^{i\gamma}\frac{m_1}{2} + \kappa_{11}e^{i\varphi_1}e^{-\Omega\tau} + \kappa_{12}e^{i\varphi_x}e^{-\Omega\tau}\frac{\widehat{e_2}}{\widehat{e_1}} \tag{III.19a}$$

$$i\Omega = \sqrt{1+\alpha^2}e^{i\gamma}\frac{m_2}{2} - i\delta e_2 + \kappa_{22}e^{i\varphi_2}e^{-i\delta\tau}e^{-\Omega\tau} + \kappa_{21}e^{i\varphi_x}e^{-i\delta\tau}e^{-i\Omega\tau}\frac{\widehat{e_1}}{\widehat{e_2}} \tag{III.19b}$$

If we define $\widehat{e_2}/\widehat{e_1} = \rho e^{i\phi}$, multiply both sides by $e^{-i\gamma}$, and keep only the imaginary part of these equations, we have:

$$\Omega\cos\gamma = \kappa_{11}\sin(\varphi_1 - \Omega\tau - \gamma) + \kappa_{12}\rho\sin(\varphi_x - \omega\tau + \phi - \gamma) \tag{III.20a}$$

$$(\delta+\Omega)\cos\gamma = \kappa_{22}\sin\big(\varphi_2 - (\delta+\Omega)\tau - \gamma\big) + \kappa_{21}\frac{1}{\rho}\sin\big(\varphi_x - (\delta+\Omega)\tau - \phi - \gamma\big) \tag{III.20b}$$

From Eqs. (III.16c-d), we can estimate that for small ε, $\rho^2 \approx (r_2-1)/(r_1-1)$, so that we have two equations for two unknowns ϕ and Ω. If we change the variables to $x = \varphi_x - \gamma - \Omega\tau - \delta\tau/2$ and $y = \phi + \delta\tau/2$, then:

$$-\left(\frac{x-\varphi_x+\gamma}{\tau} + \frac{\delta}{2}\right)\cos\gamma = \kappa_{11}\sin\left(\varphi_1 + x - \varphi_x + \frac{\delta\tau}{2}\right) + \kappa_{12}\rho\sin(x+y) \tag{III.21a}$$

$$-\left(\frac{x-\varphi_x+\gamma}{\tau} - \frac{\delta}{2}\right)\cos\gamma = \kappa_{22}\sin\left(\varphi_2 + x - \varphi_x - \frac{\delta\tau}{2}\right) + \kappa_{21}\frac{1}{\rho}\sin(x-y) \tag{III.21b}$$

With these expressions, $\cos y$ and $\sin y$ can be expressed in terms of x, so that we

obtain a complicated equation for x governing the external cavity modes. It includes polynomial and trigonometric terms, so that even the number of solutions is not easily found.

Further simplification is obtained by defining $\tau' = \tau/\cos\gamma$, $\delta' = \delta\cos\gamma$, $\Phi_1 = \varphi_1 - \varphi_x + \delta\tau/2$ and $\Phi_2 = \varphi_2 - \varphi_x - \delta\tau/2$.

$$0 = \frac{x-\varphi_x+\gamma}{\tau'} + \frac{\delta'}{2} + \kappa_{11}\sin(\Phi_1+x) + \kappa_{12}\rho\sin(x+y) \tag{III.22a}$$

$$0 = \frac{x-\varphi_x+\gamma}{\tau'} + \frac{\delta'}{2} + \kappa_{22}\sin(\Phi_2+x) + \kappa_{21}\frac{1}{\rho}\sin(x-y) \tag{III.22b}$$

For instance, if we set $\kappa_{12} = \kappa_{21}$ and $\rho = 1$, we obtain the following transcendental equation for x, i.e. for the frequencies of the external cavity modes.

$$\begin{aligned} 4\kappa_{12}^2\sin^2(x)\cos^2(x) + \left(\kappa_{11}\sin(\Phi_1+x) - \kappa_{22}\sin(\Phi_2+x) + \delta'\right)^2\sin^2(x) \\ + \left(\kappa_{11}\sin(\Phi_1+x) + \kappa_{22}\sin(\Phi_2+x) + 2\frac{x-\varphi_x+\gamma}{\tau'}\right)^2\cos^2(x) = 0 \end{aligned} \tag{III.23}$$

and y can be recovered using $\tan y = \frac{\kappa_{11}\sin(\Phi_1+x)-\kappa_{22}\sin(\Phi_2+x)+\delta'}{\kappa_{11}\sin(\Phi_1+x)+\kappa_{22}\sin(\Phi_2+x)+2(x-\varphi_x+\gamma)/\tau'}\tan x$.

While these relationships do not give great insight on the physics at play, they have been used numerically, for instance in continuation algorithm, or more simply to compute initial values for faster time integration of the equations.

2.d Injection rate estimation

When defining the κ_{ij} (p. 114), we stressed that the absolute injection rate cannot be measured, as it depends on a number of unknown parameters. However, its value is the same in every injection experiment, so that we can estimate it by doing a simple injection experiment for which the behavior of the laser is well known.

Indeed, from equation (III.10), we see that injection rate can be related to the locking range:

$$|\Delta| < \sqrt{1+\alpha^2}\,\kappa\,\frac{|E_{\text{inj}}|}{|E|} \tag{III.24}$$

However $|E|$ cannot be measured, and we can only monitor the optical power in the output fiber $I_{\text{out}}^{(\text{fiber})} = t_C|E|^2$, where t_C is the transmission of the coupler. In the same way, the injected field can be only measured before entering the component, as

$t_C I_{\text{inj}}^{(\text{fiber})} = |E_{\text{inj}}|^2$.

If we recall that $\Delta = \delta\nu / f_R$, we have:

$$|\delta\nu| < \sqrt{1+\alpha^2}\,\kappa f_R t_C \sqrt{\frac{I_{\text{inj}}^{(\text{fiber})}}{I_{\text{out}}^{(\text{fiber})}}} \tag{III.25}$$

Thus, κt_C can be estimated from the width of the locking range if we measure the injected and output power in the fiber.

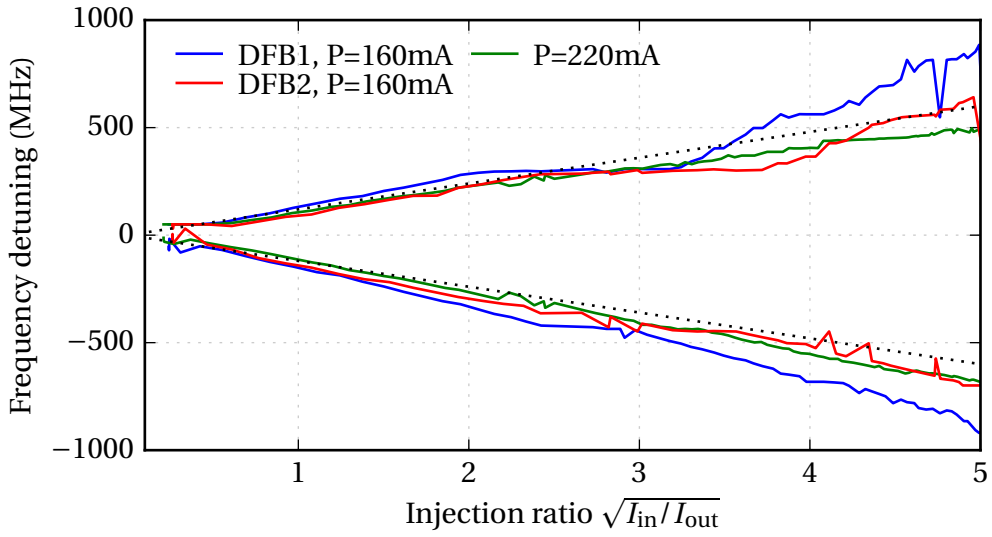

Figure III.18: Locking range boundaries in a simple injection experiment, with varying ratio of the power sent to the slave laser on the power collected in the fiber. The two lasers have been tested with different pumping rates. Dotted line is a rough fit of $\delta\nu = \pm 100\,\text{MHz} \times \sqrt{I_{\text{in}}/I_{\text{out}}}$.

We performed a simple injection experiment (such as the one in Fig. III.13), where we varied the frequency of the master laser while monitoring the output beat-note spectrum. A simple criterion was used for discriminating the unlocked state from the locked regime. In the locking range, no beatnote can be seen on the electrical spectrum, so that only measurement noise is observed. Using this criterion, the boundaries of the locking range were precisely located by a dichotomic search.

This was performed for 100 values of the injection levels, obtained by varying the pump current of an EDFA placed between the master and slave laser. Output and input power I_{in} and I_{out} in the fiber were recorded at each point. The results are shown in Fig. III.18 and confirm that we mostly stay in the weak injection regime. Indeed, the locking boundaries are the same for either sign of the frequency detuning, and the dependency on $\sqrt{I_{\text{in}}/I_{\text{out}}}$ is roughly linear.

From the results, we obtain $|\delta\nu| = 100\,\text{MHz} \times \sqrt{I_{\text{inj}}^{(\text{fiber})}/I_{\text{out}}^{(\text{fiber})}}$ for the two lasers, which in turn leads to an estimation of $\kappa t_C = 8 \times 10^{-3}$. If we come back to the physical units, and suppose the injection rate is only determined by the coupler and the lasers' output mirror transmission, we have $\kappa = K/2\pi f_R$ with $K = 1/\tau_p$ and we can estimate that $t_C = (\kappa t_C) \times 2\pi f_R \tau_p \approx 1.7 \times 10^{-2}$.

For our setup, we considered $\kappa_0 = G\kappa t_C$. We include in G all the losses in the loop, due to the couplers and also polarization losses due to the PM fiber. From a measurement we obtained $G^{\text{dB}} = -10\,\text{dB} + G_{\text{EDFA}}^{\text{dB}}$, so that finally $\kappa_0 = G_{\text{EDFA}} \times 8 \times 10^{-4}$.

2e Modulation ratio

The Mach-Zehnder modulator was calibrated with respect to its RF input power and DC bias, as shown on Fig. III.19. While the dependence on DC bias is expected to fluctuate, we can find the maximum modulation rate expected for a given RF input signal. We notice that every modulation rate up to 0.95 can be obtained by selecting the correct DC bias and input power. In our experiment, this will allow high levels of cross-injection with low self-feedback for each lasers.

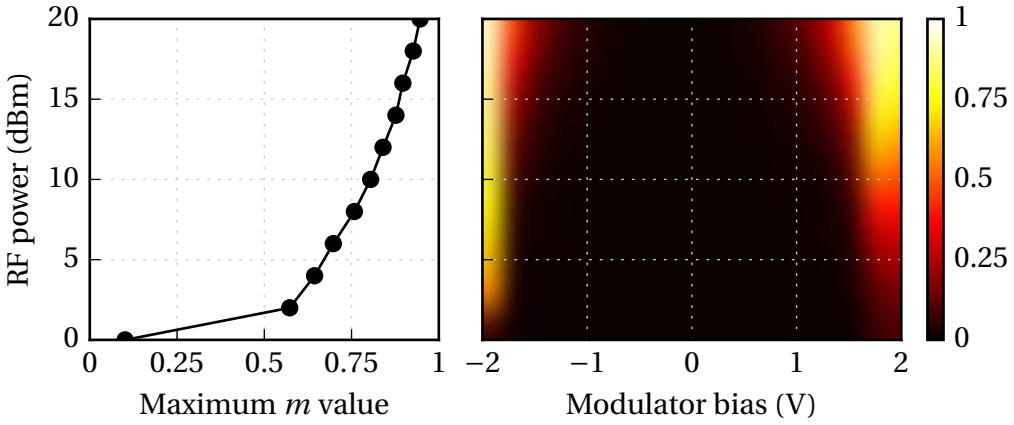

Figure III.19: Right panel: modulation ratio (as defined in Eq. (III.13)) of the MZM for varying RF power and DC bias. This was experimentally measured using a high-resolution optical spectrum analyzer (Apex 2083A). Left panel: maximum value obtained for each RF power.

3 Comparison of numerical and experimental results

In the following section, we will study the outcome of the FSF mechanism for varying parameters. The experimental observables are related to the microwave beatnote, namely its amplitude $X = |e_1 e_2|$ and its relative phase with respect to the synthetizer

reference $\theta = \arg\left(e_1 e_2^*\right)$. Namely, in dynamical regimes, the criterion $\max\theta - \min\theta$ will often be used to separate "locked" and "bounded" states from "phase drift" regimes.

3*a* Observed regimes

Experiments

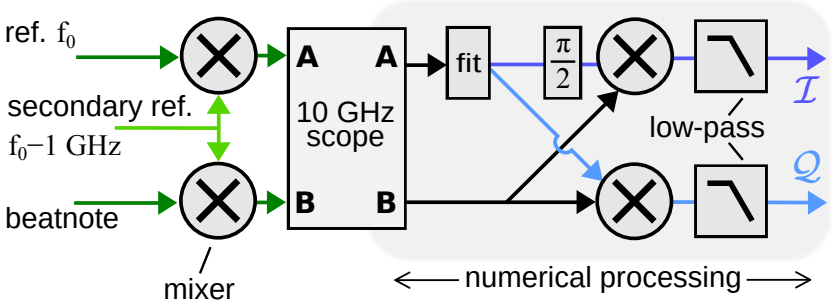

Figure III.20: Experimental setup used for the demodulation. The beatnote and reference signal are both down-converted at 1 GHz by mixing them with a synthetizer at 9 GHz. The time series are recorded by a fast oscilloscope, then numerically processed. First, the reference is fitted with a sinusoidal waveform to remove noise. It is then used to obtain the signal quadratures $\mathcal{I}$ and $\mathcal{Q}$, which in turn allow to retrieve the amplitude X and phase θ.

In all the study, the free-running beat-note is set at 10 GHz, and the relaxation oscillations of the least pumped laser are $f_R^{(1)} = 8$ GHz. If we set $m = 0.8$ and vary the frequency detuning, very different regimes can be experimentally observed, as shown on Fig. III.21. The amplitude and phase time series have been obtained from the oscilloscope traces, and numerically demodulated at the frequency f_0, according to the scheme described in Fig. III.20. However, only a weak signal was obtained after the down-mixing process, so the amplitude signal is very weak and show mostly measurement noise.

One of the main results is that despite the complex injection scheme, this setup can be used to lock the frequency difference of the lasers on the external synthetizer. In that case, the output beatnote is a single tone of frequency f_0. This locked state will be further studied in section 3*f*.

As seen on Fig. III.21, other regime are observed. In the unlocked case, different periodic or quasi-periodic amplitude and phase modulation can be seen. This kind of features, with a period (or pseudo-period) of 2τ, is common in delayed systems [Dong17]. Finally, as in the case of solid-state lasers, there is also an intermediary bounded phase regime, where the RF phase θ oscillates in the $[-\pi, \pi]$ range.

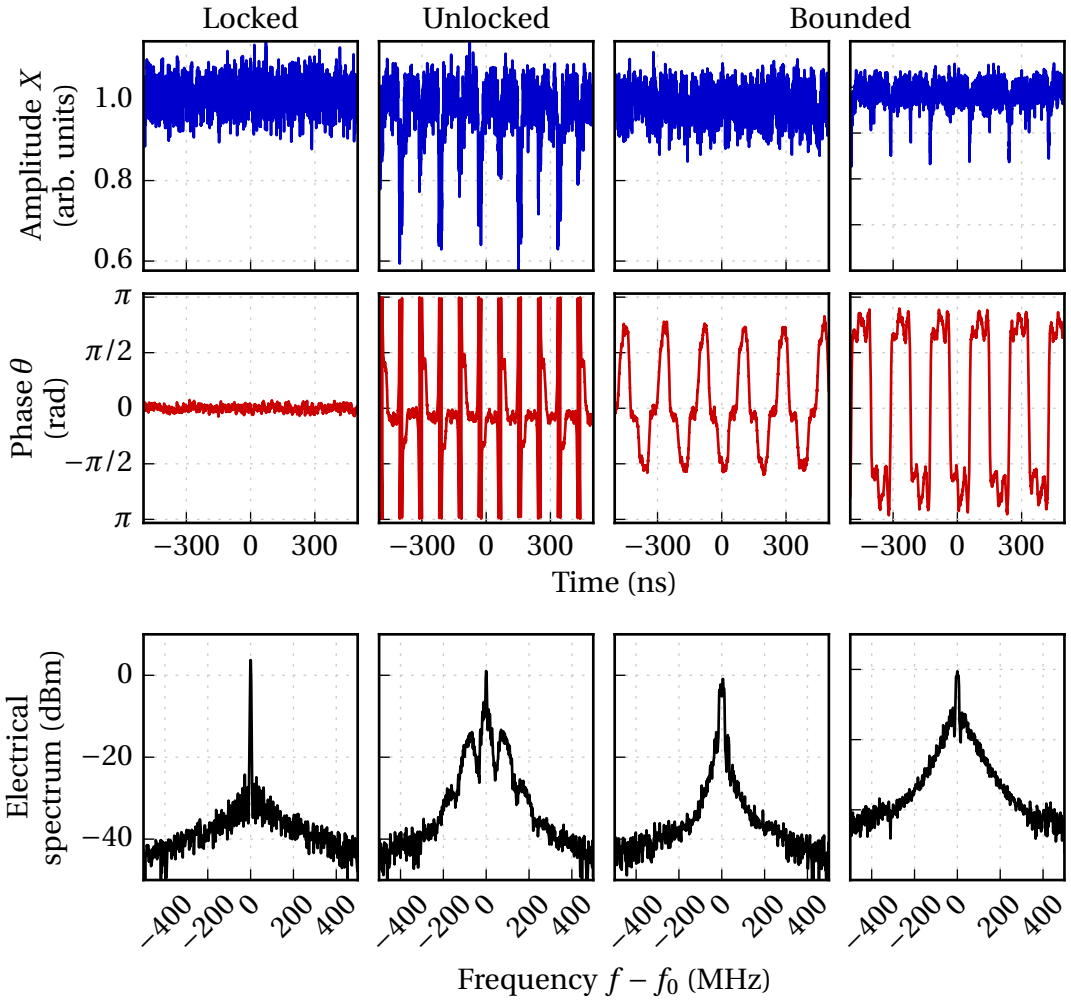

Figure III.21: Experimental time series and electrical spectrums, when the detuning $\nu_1 - \nu_2 - f_0$ are respectively 123 MHz, 29 MHz, −26 MHz and 174 MHz.

Simulations

Numerical simulations of Eqs. (III.16) have been made, again using the RADAR5 code [Guglielmi05] through a Python wrapper (see Annex. E). The large delay ($\tau = 4000$) forces us to run the integration for long times before reaching a stationary regime, to the point that in some cases, as long as $s > 10^7$ is needed.

Equations (III.16) and (III.19) show that the three optical phases φ_j play a role in the dynamics of the locking, a property also shown in Section I.2*b* for a system with a single self-feedback [Green10]. Indeed, performing numerical integrations of the model with the same parameter set except for feedback phases already leads to a wide variety of results, as shown on Fig. III.22. We notice that at least four different regimes can be obtained only by varying the feedback phases, and that they roughly match experimentally observed regimes.

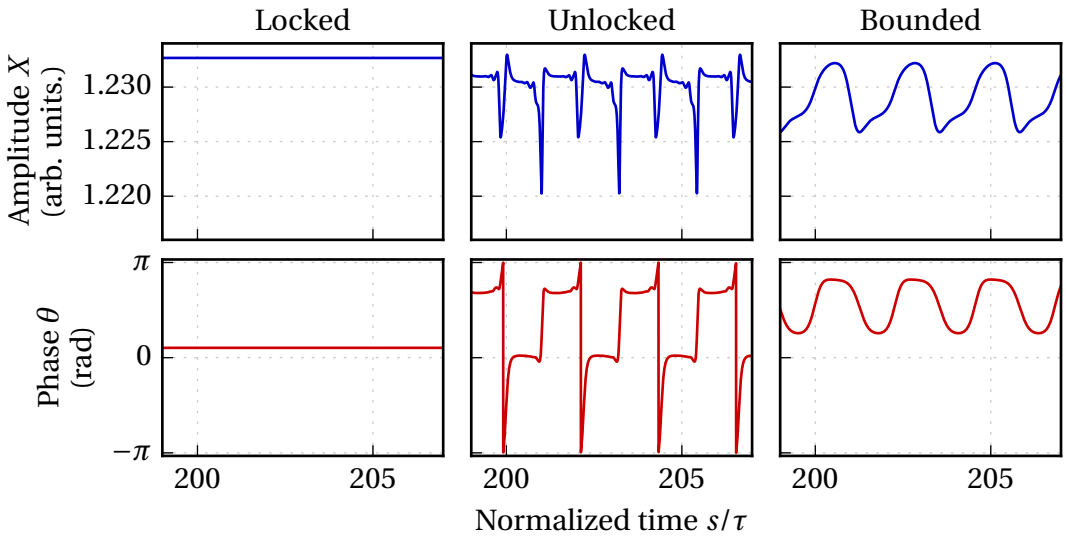

Figure III.22: Example of very different long-term phase and beatnote intensity behaviors obtained by choosing different feedback phases. In the three cases $\delta = 0.002$, $\kappa_0 = 0.01$, $m = 0.8$. Locked: $\varphi_{1,2,x} = 0, 0, 0$. Unlocked $\varphi_{1,2,x} = 0, -1.3, 2$. Bounded phase $\varphi_{1,2,x} = -2, -2.16, 1$ (all phases in radians).

"Full" model simulations

If we recall the first paragraph of Section 2*b*, the simulated model arises from an approximation made on the setup from Fig. III.15. Indeed, we supposed that the only terms relevant to the dynamics are the "resonant" fields, i.e. those injected with a small frequency detuning, either 0 or $\pm\delta\nu$. In the previous sections, and in the following, we confirm that they are indeed sufficient to reproduce the observed behaviors. Yet, as an extra check, numerical simulations have also been made including all the non-resonant terms. This full system of delayed differential equations, which cannot be made autonomous, is noticeably slower to integrate, by a factor of ten. For a comparison, Fig. III.22 has been reproduced, as the equivalent result is shown on Fig. III.23.

From this figure, it is clear that the only effect of the extra terms, which all have a detuning larger that $f_R^{(1)}$, is to add a very small overmodulation (see inset in top-left panel). This confirms that the non-resonant contributions can be safely neglected, at least if we avoid particular cases that may present strong resonances, such as $f_0 \approx f_R^{(1)}$. For such cases, we did not check numerically or experimentally if the hypothesis could still hold.

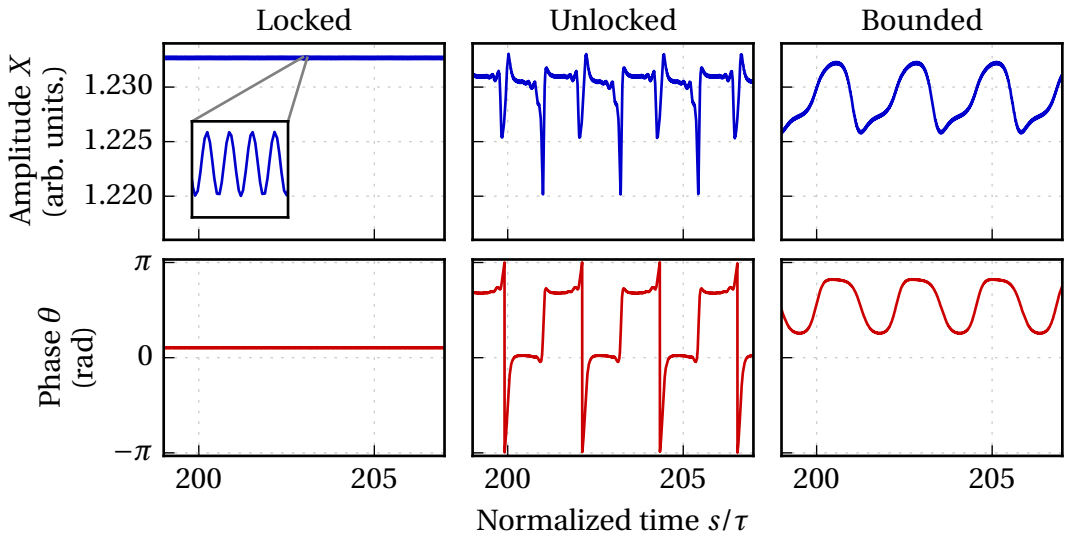

Figure III.23: Duplicate of Fig. III.22, calculated including all the non-resonant terms necessary to the full description of the setup from Fig. III.15.

3b Multistability

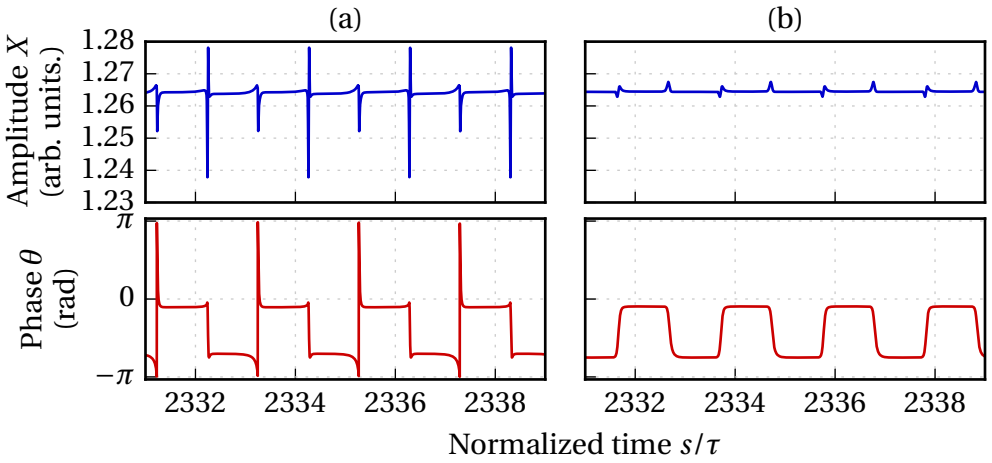

Figure III.24: Time evolution for the same set of parameter but different initial conditions, showing that the system is multistable.

In the previous chapter, at II.3*b* we have already encountered multistability. As it is also very common in semiconductor lasers under optical injection [Wieczorek05] or feedback [Lenstra91], it is not surprising that it is present in our particular case. For a given set of parameters, it is possible that more than one stable orbit exist. An example is shown on Fig. III.24, where we have chosen $\delta = -0.008$, $\kappa_0 = 0.04$, $m = 0.8$ and $\varphi_{1,2,x} = -0.79, -1.63, -1.75$. Then numerical integration has been performed, starting

from two different initial conditions for $s \leq 0$. In the first case (a): $e_1 = 0.01, e_2 = 0, m_j = 0$, and in the second case (b): $e_1 = 0.01, e_2 = 0.01i, m_j = 0$. Two different oscillating regimes, one of bounded phase, and one unbounded with sharper oscillations are seen.

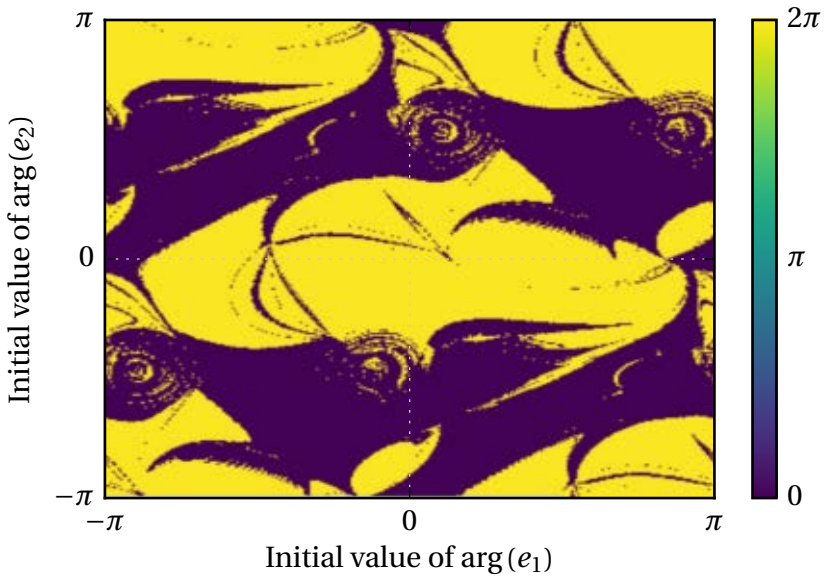

Figure III.25: Final value of $\max\theta - \min\theta$ for 400×400 different initial values of e_1 and e_2, showing a cut through the attraction basins for the two final states.

Attraction basins, i.e. the sets of initial conditions leading to each final state, often take very complicated shapes in such systems (see Fig. II.13). Here Fig. III.25 show a cut through the attraction basin for the two previous states. We have fixed the initial amplitude $|e_j| = 1$ and varied the initial phase of each field. The difference of phase extrema $\max\theta - \min\theta$ was recorded. The resulting picture show that the frontier between the two attraction basins is very complex, and looks fractal.

3c Phase dependency

We already saw in Fig. III.22 that very different regimes could be obtained only by changing the feedback phases $\varphi_{1,2,x}$. However, these parameters are difficult to control experimentally, and will experience drifts over time due to drift of the optical frequency of the lasers (see Section 1*b*), and to the fibered nature of the feedback loop. Yet a stable locking over long periods may be desired for applications such as a low noise microwave photonics oscillator. For that purpose, a high sensitivity on feedback phases may be detrimental. Thus, it becomes interesting to investigate how sensitive the system is to these parameters.

However, the parameter space to explore is the $[-\pi, \pi]^3$ cube, which is quite large

as each individual integration time is in the few minutes range. To address this problem, a Monte-Carlo method has been employed: we have performed numerical integrations with 50 different feedback phase values, taken from Halton sequences[5]. Multistability was accounted for by taking 5 different initial conditions for each phase triplet. These initial conditions were taken close to estimated external cavity mode, which were computed using Eq. III.23, so that the integration of lengthy transitory regimes could be avoided. For each integration, the phase difference in the steady state (for $s > 10^7$) was computed from $e_1 e_2^*$, and its extrema were recorded. The mean value of $\max\theta - \min\theta$ for different values of m, κ_0 and τ is shown on the maps in Fig. III.26.

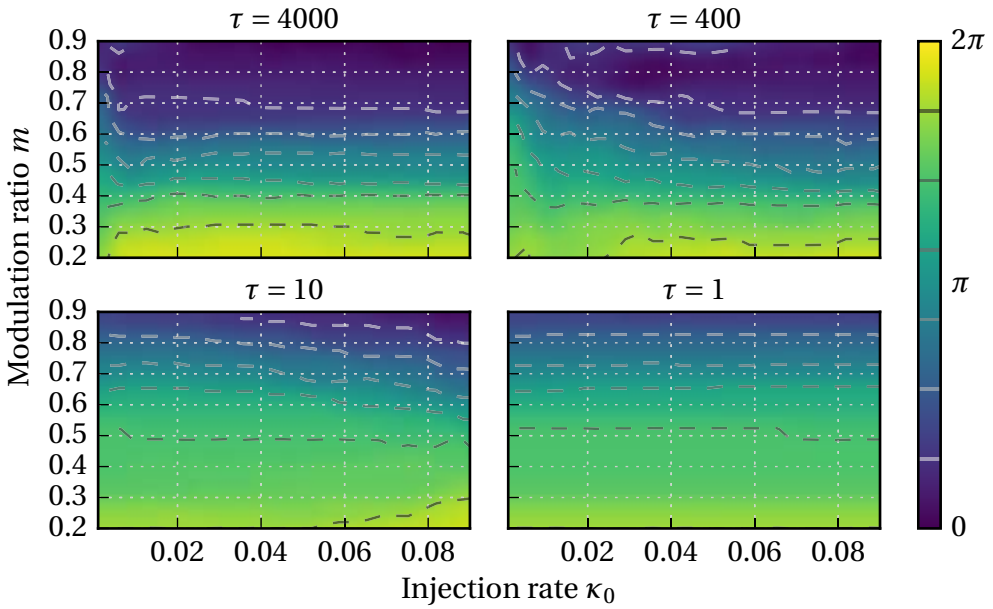

Figure III.26: Mean value of the difference on phase extrema $\max\theta - \min\theta$, averaged on 50 different feedback phases values $\varphi_{1,2,x}$. Here we have taken $\delta = 0$.

We notice that the mean value never reaches zero, which means there always exists a non-empty subset of the $(\varphi_1, \varphi_2, \varphi_x)$-space that leads to an unlocked regime. However, the volume of this subset becomes very small, down to about 3% of the feedback phase space when using a high modulation ratio $m \approx 0.8$. For $\tau = 400$ a higher injection level κ_0 is needed to mitigate phase dependency. When the delay becomes smaller, for $\tau = 10$, a very high modulation rate $m \approx 0.9$ is needed to reach the same levels. This suggests that the system becomes very sensitive to self-feedback, and this should obviously be avoided. Surprisingly, in that aspect, a large delay seems to have a stabilizing effect. We also notice that the influence of κ_0 seems to be quite weak in the

[5]Halton sequences come from an algorithm generating pseudo-random points on any set, with low discrepancy, i.e. they are "evenly" distributed, and thus well suited for integrating a function over a large set [Halton64].

10^{-2}–10^{-1} range.

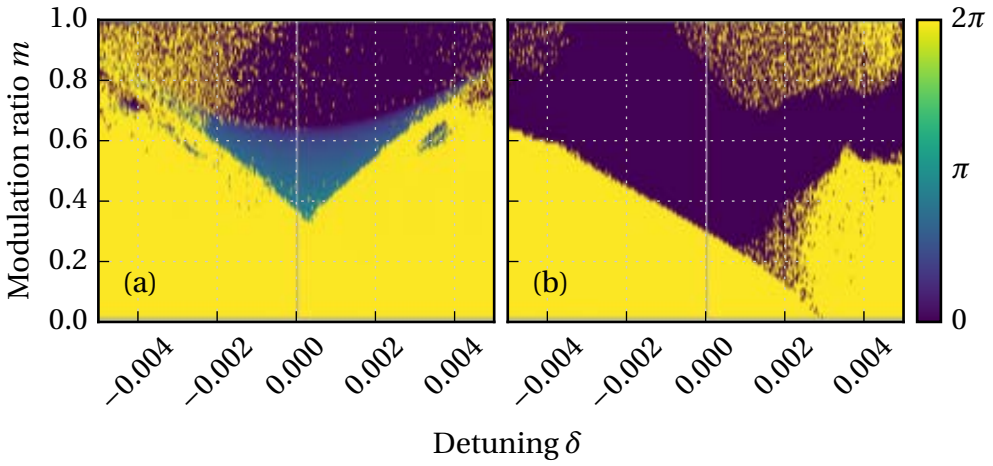

Figure III.27: Examples of the difference of phase extrema $\max\theta - \min\theta$ in the steady state. Integrations were performed for $\kappa_0 = 0.01$, ignoring the $e^{-i\delta\tau}$ in Eqs. (III.16). This highlights the effect of pure detuning, i.e. without its consequence in the feedback phases. Feedback phases are (a) $\varphi_{1,2,x} = 0.12, -2.72, 0.65$ and (b) $\varphi_{1,2,x} = 2.35, 3.33, -0.5$.

The feedback phases also interact with other parameters. For instance, Fig. III.27 shows that different steady states are obtained for varying detuning and modulation ratio, but that the picture is greatly modified if one selects another set of feedback phases.

3*d* Influence of frequency detuning: locking range

In injection-locking systems including a frequency detuning, one expects the presence of a limited locking range. It usually grows with injection level, but is largely dependent on the linewidth enhancement factor α. In our case, and as already seen in Fig. III.27, we expect the locking range to also depend on the three feedback phases. This complicates the definition and observation of the locking region. Integrating over the feedback phase space, or in other terms computing a mean value over all possible feedback phases, similarly to what had been done for Fig. III.26 allows to overcome this problem.

With $\kappa_0 = 0.04$ and $\tau = 4000$, numerical integrations were performed for different values of the detuning. For each value of δ, 50 triplets of feedback phases were used, and for each triplet multiple initial conditions were tried. The results are seen on Fig. III.28. As in the previous section, we notice that the dependency on the feedback phases is greatly reduced for higher m, but also that the region for which locking is

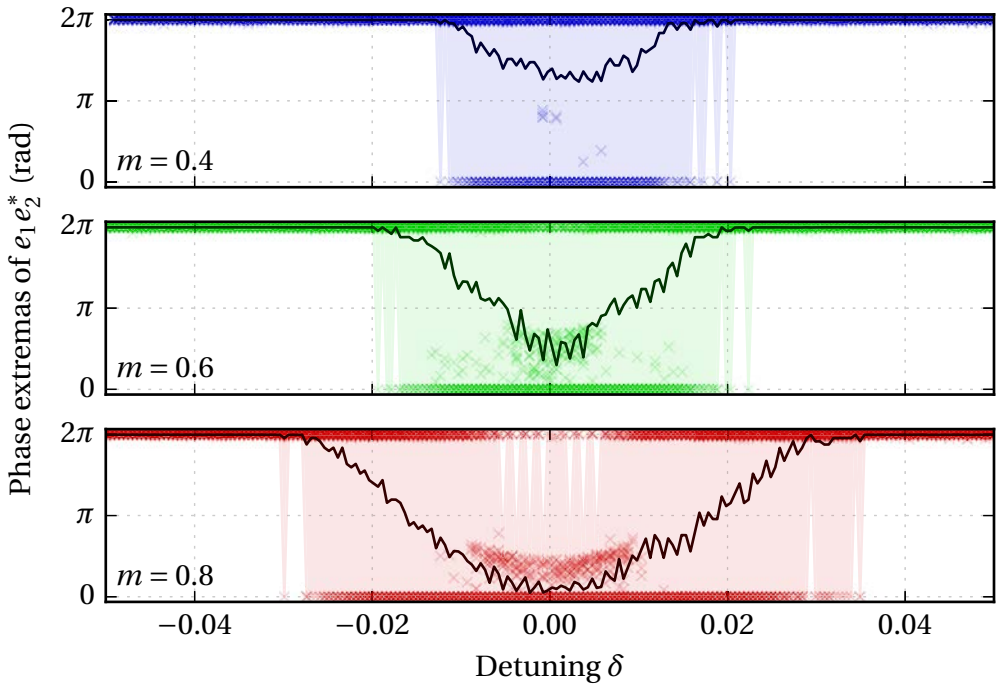

Figure III.28: Numerical integrations with varying detuning δ. Each × point corresponds to different feedback phases φ_j and different initial conditions, and the reported value is the stationary difference of output phase extrema $\max\theta - \min\theta$. Solid line shows the corresponding mean value for each δ, and filled region helps seeing the range where there is at least one phase combination that makes locking possible.

possible is enhanced. We stress that this happens at constant κ_0, which means that the total injected intensity is the same, but is more balanced toward cross-injection than self-feedback.

This figure also shows that while there is indeed a maximal locking range, there is no minimal locking range. This fact, highlighted by the solid line, which corresponds to the mean value and never reaches zero, can be related to Fig. III.26. It reflects the fact for any frequency detuning, there is always one combination of feedback phases that forbid stable locking.

Finally it can be noted that a lot of points do not lie on the 0 or 2π line. They correspond to an oscillating output phase θ that remains bounded in the $[0, 2\pi]$ interval, that is bounded phase dynamics, already seen on Fig. III.22. Here we see that this feature is more prominent with high modulation rates $m > 0.5$, and for lower values of the absolute detuning δ, i.e. near the center of the locking region.

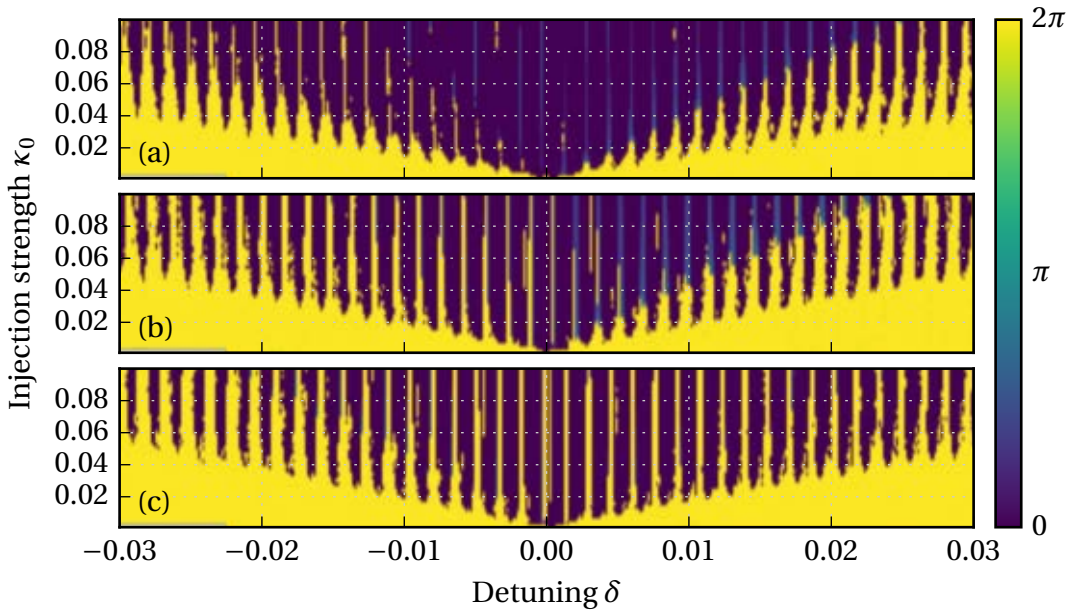

Figure III.29: Difference of phase extrema $\max\theta - \min\theta$ in the stationary regime for varying parameters. Locking bands appear when detuning changes on a short time scale so that feedback phases can be considered constant. Other parameters are $m = 0.8$ and $\tau = 4000$. The three panels show different behaviors for different feedback phases: $\varphi_{1,2,x} = (-1.77, -0.97, 0.68)$ for (a), $(0.88, -0.74, -0.075)$ for (b) and $(-0.69, 1.36, 1.18)$ for (c).

3e Locking bands

Previous computations with random φ_j (Fig. III.28) intended to stress the fact that optical feedback phases, that may not be controlled precisely, can alter the stability of the locking. Conversely, we can assume fixed φ_j, and see how the locking changes with the detuning δ. Indeed, we see in equation (III.16b) that the two injected terms include an additional detuning-dependent phase $e^{-i\delta\tau}$. As seen on Fig. III.29, this effective feedback phase variation breaks the locking range into periodic locking bands, with periodicity $2\pi/\tau$. However, the shape of the bands, and how they vary with κ_0 still depends on the optical phases φ_j. Between the stable bands, and depending on the other phases, we observe either complete unlocking or bounded phase with 2τ-periodic output.

These locking bands are also observed experimentally. We have varied the detuning in small steps, and recorded the electrical spectrum of the beatnote as well as time series at each step. On Fig. III.30, the locking bands expected from the numerical simulations appear clearly. This alone is an interesting result, as it confirms that the feedback phases φ_j vary on slower time scales than the measurement time, i.e. a

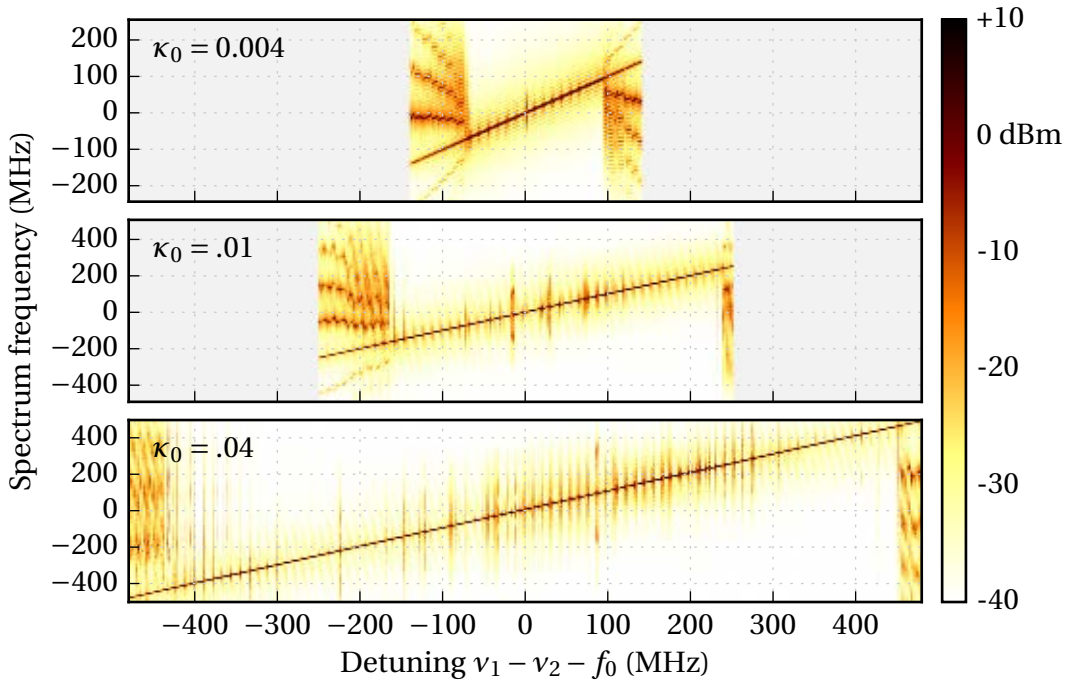

Figure III.30: Experimental spectrograms as a function of the detuning. Modulation ratio is set to maximum $m \approx 0.9$. For different injection strength κ_0, the control frequency f_0 is swept around the free-running beatnote $\nu_1 - \nu_2$. The electrical spectrum is recorded at each point, and plotted vertically.

few minutes. Indeed, if they were to vary faster, the locking bands would blurred or erratically spaced, as we previously noticed on Fig. III.29 that their shape depends on the feedback phases. Locking regions, where the electrical spectrum features only one peak at f_0, alternate with unlocking zones, where a wider spectrum can be seen. The spacing of $1/T = 12.5$ MHz between the locking bands is also observed. As in Fig. III.28, the locking range depends on the injection strength κ_0, and can reach roughly 800 MHz.

Although electrical spectrums allow to discriminate between locked and non-locked regions, it does not give any information about the phase dynamics between the locking range. A more detailed view of the beatnote phase extrema can be seen on Fig. III.31 for $\kappa_0 = 0.04$. We clearly see locking bands where $\max\theta - \min\theta = 0$, bounded phase regions, and an example of an unbounded zone at $\delta \approx 0$.

3*f* Overall stability and phase noise

In spite of the feedback phase dependency predicted before, the locked state proves to be very robust in our experimental conditions, with no other isolation scheme than

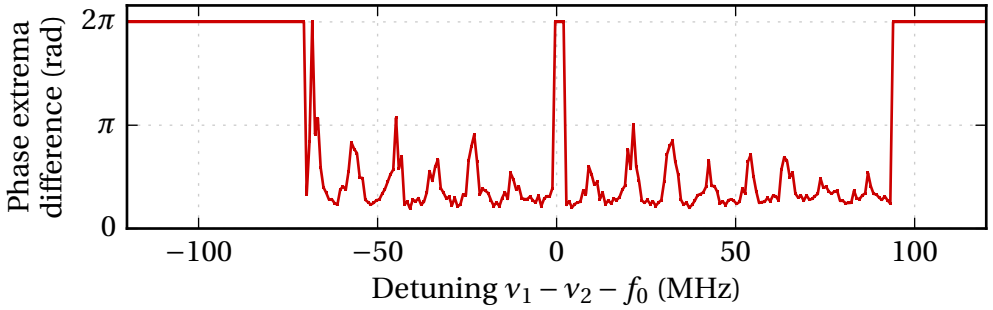

Figure III.31: Phase extrema with varying detuning, for $\kappa_0 = 0.04$ and $m = 0.8$. The phase does not go to zero because of experimental noise.

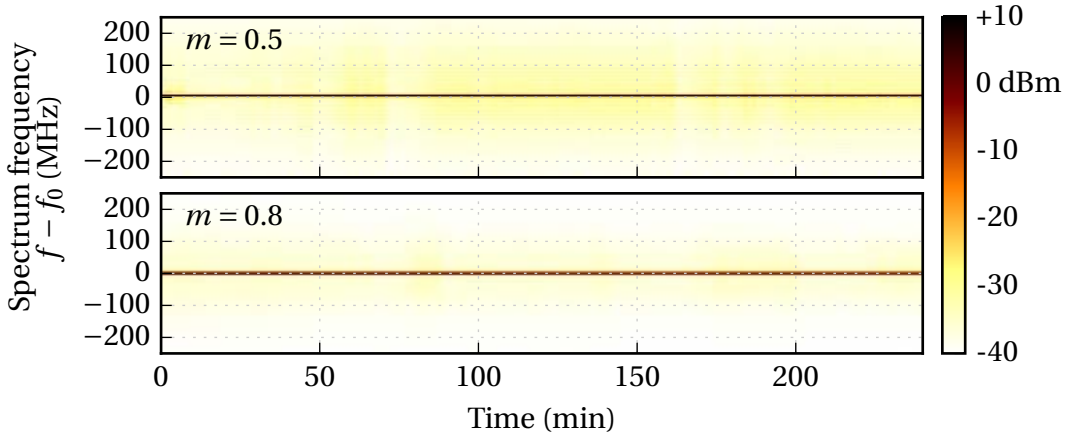

Figure III.32: Long-term spectrograms of the beatnote, showing the stability for two values of m.

a pressured-air table and a closed box above the setup. For different values of the modulation rate, we recorded the beatnote spectrum every ten seconds for several hours, and as shown on Fig. III.32, it remains locked on the reference. This locking has been observed for more than 12 hours with $m \approx 0.8$, and surprisingly more than 4 hours with $m \approx 0.5$. This suggests that the optical feedback phases vary very slowly, leading to a sturdy stabilization scheme.

On the short time scale, measurements of the electrical phase noise of the output beatnote have been performed in different regimes, as seen in Fig. III.33. They prove that the stability of the reference is almost completely transfered on the frequency difference of the lasers (the 3 dB difference is not significant, and could be due to elements of the detection chain).

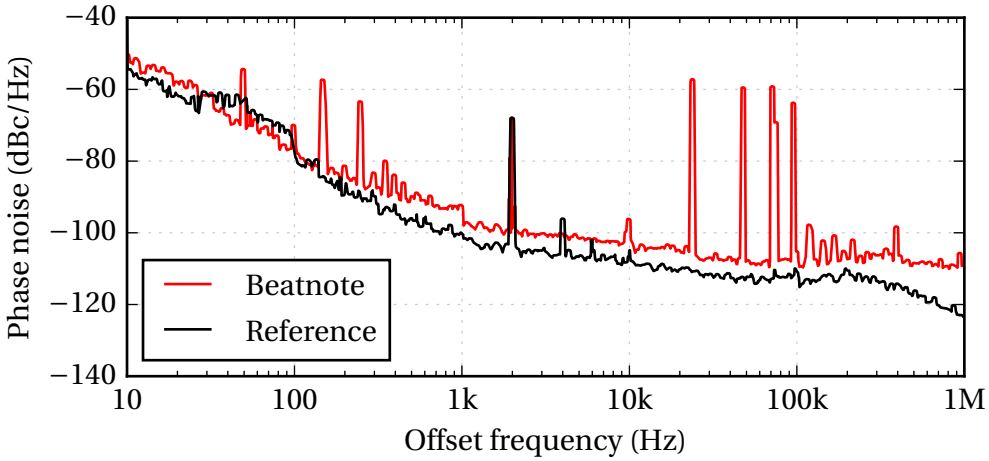

Figure III.33: Phase noise of the output beatnote, measured on a PN9000 phase noise analyzer.

4 Conclusions

We applied a method derived from frequency-shifted feedback to two semiconductor lasers contained on a single component. It allowed the successful stabilization of the frequency difference between the lasers on a microwave synthetizer at 10 GHz. The particular constraints associated with the components led to the fact that both cross-injection and self-feedback had to be applied on the lasers.

Observed experimental features, from stable locking, to bounded phase oscillations, 2τ-periodic motifs, or locking bands have been correctly obtained in numerical simulations. The influence of the injection rate, modulation ratio and detuning have been studied, with an emphasis on how they contribute to the sensitivity to the optical feedback phases. We showed that a high modulation ratio has to be preferred for non phase-dependent stabilization, and it slightly enlarges the locking range. This means that cross-feedback is the main stabilizing mechanism in that case, while the remaining self-feedback has a destabilizing effect. We also showed briefly that the feedback length, or delay, is not the most prominent parameter. This opens the way to similar, yet more compact schemes. This study is not exhaustive, and interesting comparisons could be made using a higher linewidth enhancement factor, or slightly different modulation mechanism. For instance, even though it was not developed in this chapter, we have spent some time experimenting with the replacement of the modulator by a resonant frequency shifter at 12 GHz provided by the Leonardo company (Italy) in the framework of the EDA contract HIPPOMOS. The observed behaviors are remarkably similar, and allow for a successful locking.

Even though the stabilization technique was applied to a particular dual-DFB component, the numerical model is very generic, and applies to two more separated lasers as well. With this viewpoint, we prove here that frequency-shifted feedback is an effective way to stabilize the frequency difference of two semiconductor lasers. Furthermore, it could be tightly integrated on a single component containing the feedback loop itself. The development of stabilization techniques being a central point for future heterodyne microwave generators, we expect this method to be very relevant. To illustrate this, a step toward a useful use case will be made in the next chapter.

CHAPTER IV
HYBRID OPTO-ELECTRONIC OSCILLATOR

IN the previous chapter, we developed a method that allows to synchronize the frequency difference of two lasers on a reference oscillator. However, as frequency rises, electronic oscillators of good quality may not be available, or may become too expensive, too large, or very sensitive to noises (see Fig. I.7). This motivates the search for self-referenced microwave oscillators using optical components.

1 The opto-electronic oscillator

1.a Principle

In the framework of microwave signal generation, it is usual to use electronic synthetizers. However, they are most commonly based on a frequency multiplication cascade, which means that the phase noise will tend to degrade as the frequency rises. Starting on a different ground, the opto-electronic oscillator was developed on the idea of generating a microwave frequency using a highly selective resonant loop the combines optical and electronic elements. The most common setup uses an optical resonator as a very sharp frequency filter. However, this resonator, either a long fiber coil [Yao96] or a specially engineered micro-resonator [Ilchenko08], usually has a large number of harmonic resonances. Thus an electronic microwave filter of larger bandwidth is also used in order to select a single resonance of the optical filter. This is summarized on the principle setup, shown in Fig. IV.1.

This kind of device is very mature, and it provides almost unmatched performances when it comes to very low phase noises even for high frequency carriers. For instance, a table-top realization with off-the-shelf components allowed us to reach -125 dBc/Hz

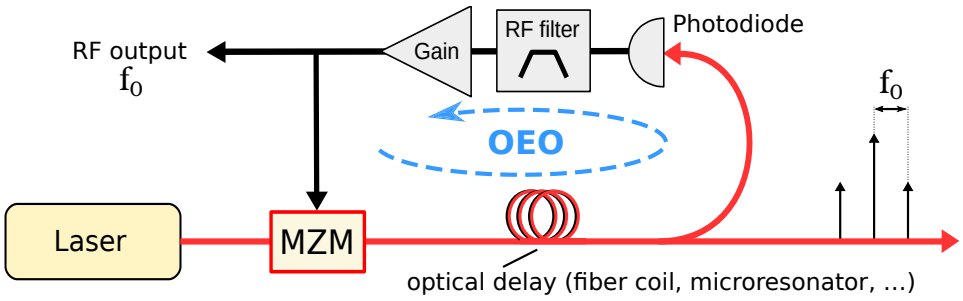

Figure IV.1: Principle of an opto-electronic oscillator.

at 10 kHz from the carrier as can be seen on Fig. IV.2. Then, the output microwave frequency is only limited by the capabilities of the modulator, photodiode and electrical filter. Current technology make it possible to build a robust OEO that operates up to 100 GHz. Furthermore, this can be done in extremely compact systems, down to chip-scale components [Maleki11]. Typical performances in miniaturized commercialized devices (μOEO from OEwaves) include a phase noise of -108 dBc/Hz for an offset frequency of 10 kHz from a 35 GHz carrier[1]. The main drawback of this kind of setup is that frequency tuning is often poor or non-existent. Indeed, the oscillation loop relies on two filtering elements, the resonator and a microwave filter. This makes continuous frequency tuning a complex problem. Tunability in steps has been achieved using special electric filters [Eliyahu03], optical filters [Xie13] or Brillouin scattering [Peng15].

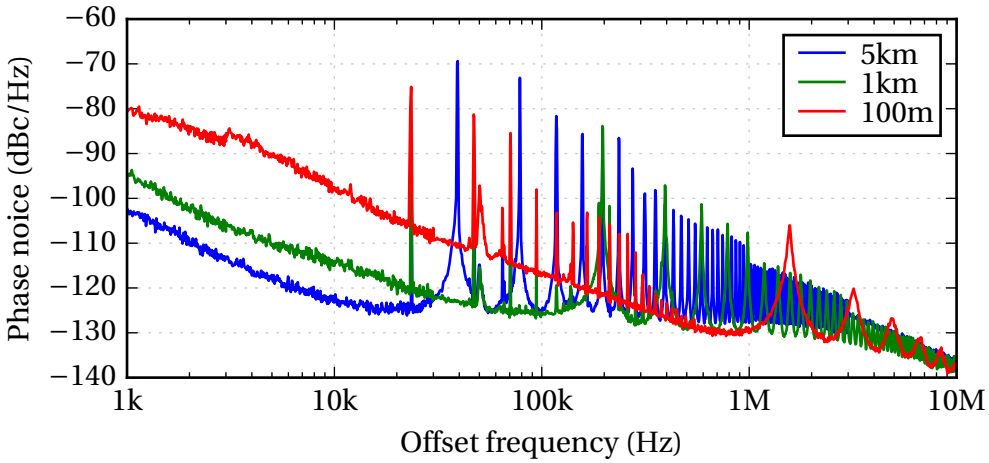

Figure IV.2: Phase noise measured on a simple 10 GHz opto-electronic oscillator we realized with a 1.55 µm laser source, a MZM modulator, and different fiber lengths.

[1] http://www.oewaves.com/micro-oeo

1 b Phase noise

The phase noise of an opto-electronic oscillator can be computed using models with growing complexity. However, a first order approach is the feedback oscillator model developed by Leeson [Leeson66]. In this model, adapted on Fig. IV.3 to the case of an OEO, we consider that the only noise source enters the system in the amplification stage. Then, by applying a standard linear analysis of feedback systems, we can compute the transfer function for this phase noise [Rubiola08].

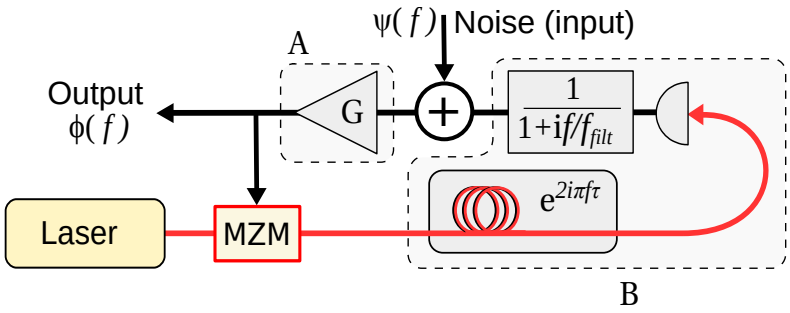

Figure IV.3: The Leeson model of an OEO, including amplifier noise, a filter and a delay line.

Here, the microwave bandpass filter centered on f_0 corresponds for the phase φ to a low-pass filter with a cutoff at half the bandwidth. If we suppose that it is a first-order filter, its transfer function is simply $\frac{1}{1+if/f_{\text{filt}}}$, where f is the offset frequency, and f_{filt} the cutoff frequency, i.e the half-bandwidth of the bandpass filter. The amplifier is linear, and appears as a single constant G. Finally, the delay due to the fiber coil corresponds to $\varphi(t-\tau)$, with $\tau = nL/c$ the time delay. In the frequency domain, this reads $e^{2i\pi f\tau}$. The transfer function from the noise input ψ before the amplifier to the output phase ϕ reads:

$$H(f) = \frac{\varphi(f)}{\psi(f)} = \frac{A}{1-AB} = G\frac{1+i\frac{f}{f_{\text{filt}}}}{1+i\frac{f}{f_{\text{filt}}} - Ge^{-2i\pi f\tau}} \tag{IV.1}$$

The amplitude of this transfer function is plotted on Fig. IV.4. This shape is typical of an opto-electronic oscillator, and very similar to the measurement of Fig. IV.2. At lower frequency, we see a decrease with slope $-20\,\text{dB/decade}$. Then it reaches a minimum, and what follows are sharp harmonic peaks that correspond to the resonances of the delay line. The cutoff frequency, corresponding to the first minimum before the delay resonances is sometimes called the Leeson frequency $f_L = 1/(2\tau)$. This simple model teaches us that the typical phase noise of an opto-electronic oscillator features two distinctive traits: a first-order low-pass filtering with cutoff frequency f_L all the smaller if the delay is long, and sharp peaks at each harmonic resonance of the

delay. The latter are indeed unwanted, and methods to mitigate this extra noise will be discussed in Section 2*c*.

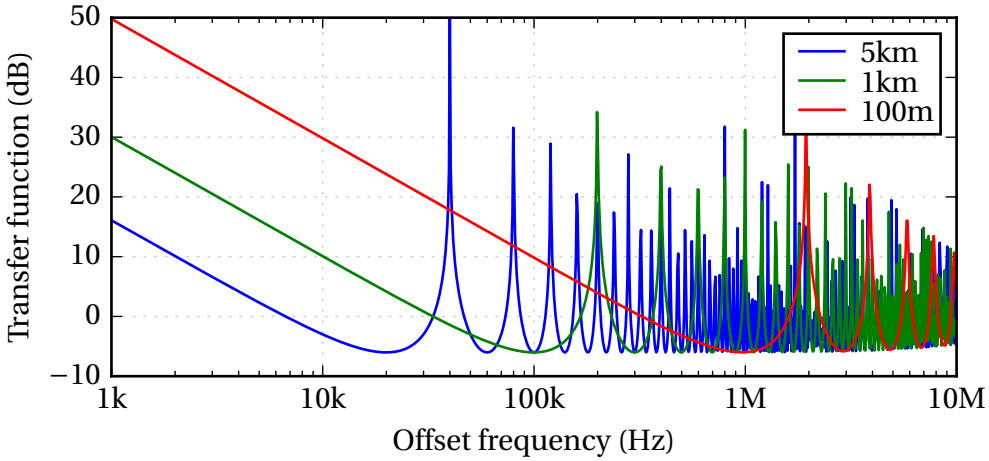

Figure IV.4: Transfer function for the phase noise in the Leeson model. Here we have taken $G = 1$, a filter bandwidth of 5 MHz and various fiber lengths.

1*c* Dispersion losses in long fiber links

Even though opto-electronic oscillator can generate microwave signals of very high purity over optical carriers, their output is not well suited as a carrier for transmission in fiber links. Indeed, as the microwave signal is contained in two sidebands at $\pm f_0$ created by a MZM around the main carrier, it is very sensitive to chromatic dispersion in fibers [Smith97]. The following simple calculation highlights the process.

If the input signal of the MZM has a pulsation Ω, the electrical field contains three pulsations ω, $\omega \pm \Omega$. After propagation in a fiber, the amplitudes E_j and phases ϕ_j may be different for each, so that the total field writes:

$$\mathcal{E} = E_0 e^{i\omega t} + E_1 e^{i\phi_1} e^{i(\omega+\Omega)t} + E_2 e^{-i\phi_2} e^{i(\omega-\Omega)t} \tag{IV.2}$$

Observed on a photodiode, the intensity is as follows.

$$I = |\mathcal{E}|^2 = E_0^2 + E_1^2 + E_2^2 + E_0 E_1 e^{i\phi_1} e^{i\Omega t} + E_0 E_2 e^{-i\phi_2} e^{-i\Omega t} + E_1 E_2 e^{i(\phi_1+\phi_2)} e^{2i\Omega t} + \text{c.c.} \tag{IV.3}$$

We are only interested in the microwave signal at frequency Ω, which is:

$$X(t) = E_0\left[E_1 e^{i\phi_1} e^{i\Omega t} + E_2 e^{-i\phi_2} e^{-i\Omega t} + \text{c.c.}\right] = 2E_0\left[E_1\cos(\Omega t + \phi_1) + E_2\cos(\Omega t + \phi_2)\right] \tag{IV.4}$$

Finally its power spectral density is:

$$|\widetilde{X}(\Omega)| = 2E_0\left|E_1 e^{i\phi_1} + E_2 e^{i\phi_2}\right| = 2E_0\sqrt{E_1^2 + E_2^2 + 2E_1E_2\cos(\phi_1 - \phi_2)} \tag{IV.5}$$

Which allows the following extrema:

$$\left|\widetilde{X}_{\min}\right| = 2E_0\,|E_1 - E_2| \tag{IV.6}$$
$$\left|\widetilde{X}_{\max}\right| = 2E_0(E_1 + E_2)$$

Thus, the ratio describing the maximum signal losses caused by the dispersion in the fiber is:

$$\left|\frac{\widetilde{X}_{\min}}{\widetilde{X}_{\max}}\right| = \frac{|E_1 - E_2|}{E_1 + E_2} \tag{IV.7}$$

Dual sidebands setup, such as any modulator-based oscillator, correspond to $E_1 \approx E_2$ because the chromatic losses are very low in a fiber. This means that they are very sensitive to dispersion and that very high modulation losses are to be expected after being propagated in a fiber. On the contrary, a true single-sideband setup, i.e. with $E_2 = 0$, cannot experience dispersion losses. In these particular use cases, this is a clear advantage of heterodyne-bases oscillators over other methods. We will see later that our modulation scheme may rather generate a weakly dual sideband signal, where $E_2 \ll E_1$. This lead to quite low maximum losses, around $1 - E_2/E_1$, or in term of intensities $1 - \sqrt{I_2/I_1}$.

2 Long-delay setup

Building on the stabilization scheme developed in Chapter III, we will show that it can be turned into a standalone oscillator, by inserting it in an opto-electronic loop inspired by the OEO principle. However, as what we have developed is a method of stabilizing the frequency difference between the two lasers, we expect to keep the property that the output signal is composed only of the two optical wavelengths. Hence, in contrast with standard OEO, the output will be nearly single-sideband microwave signal over an optical carrier.

2a Setup

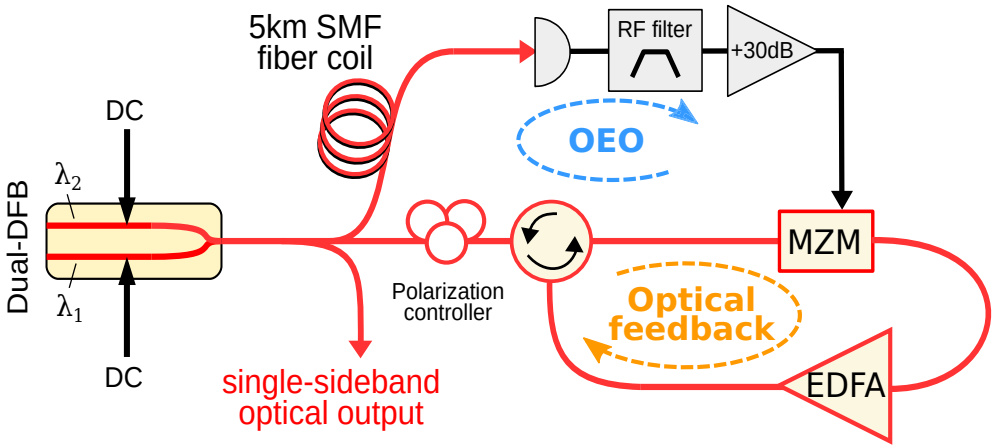

Figure IV.5: Hybrid opto-electronic oscillator, directly derived from the FSF technique.

The setup presented in Fig. IV.5 (and photographed on Fig. IV.6) is directly derived from the one shown in Fig. III.15. In fact, we can consider it to be the closed-loop form of the previous one, where the output goes through a feedback branch, and then back into the input, i.e. the microwave reference fed into the modulator [Vallet16]. For convenience, we will keep the frequency difference tuned at 10 GHz.

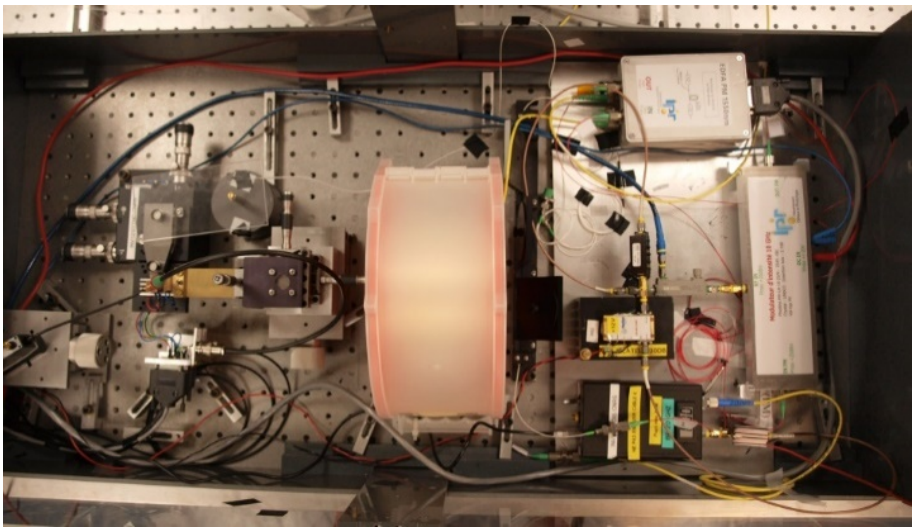

Figure IV.6: Photograph of the setup described on Fig. IV.5.

After leaving the dual-DFB chip, the light goes through a 80/20% fiber coupler. The smallest fraction goes into the optical frequency-shifted feedback arm, where it experiences amplitude modulation and amplification before being directed back into the PIC. The other fraction is delayed by a 5 km SMF fiber coil (corresponding to a Leeson frequency f_L = 7 kHz), and reaches a fast photodiode (Discovery 401HG),

from which the microwave signal is obtained. It is filtered by a custom-made[2] very sharp RF bandpass filter, centered around 10 GHz and with a bandwith of 3.8 MHz, the characteristics of which are shown on Fig. IV.7. Finally, building on the knowledge from the open-loop system, we know that a high modulation rate in the MZM in beneficial, so an amplification stage is added in order to reach around +20 dBm level on the modulator.

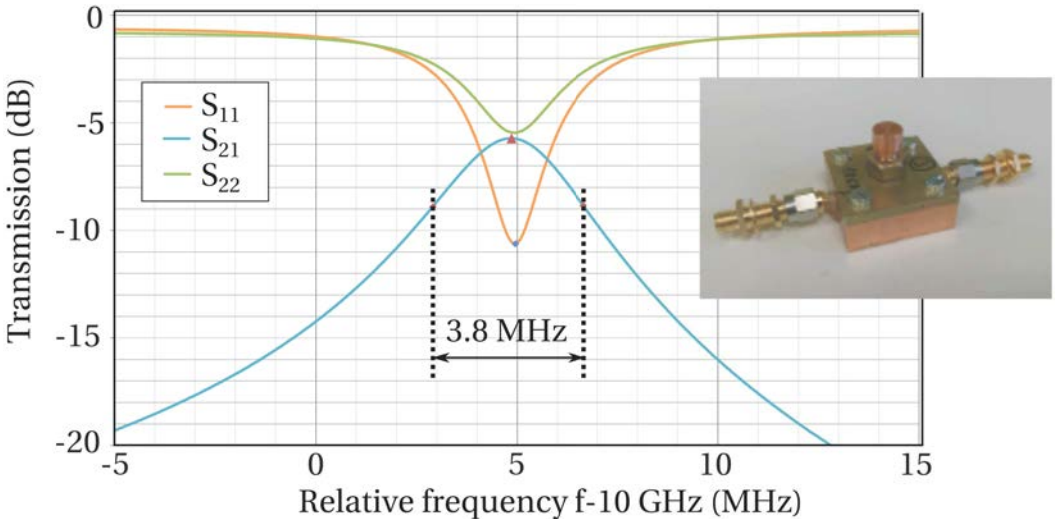

Figure IV.7: Characteristic of the custom-made narrow bandpass filter. Here, the useful transmission is the S_{21} curve between the two ports of the filter.

2b Performances and challenges

When the free-running beatnote of the lasers is set close to the resonant frequency of the filter, stable oscillation occurs, as seen on the electrical spectra of Fig. IV.8. A rejection of 40 dB between the main peak and the spurious sidebands can be observed. Before reaching this result, several lengths of fiber have been tested, as it is known that this length, that determines the width of the resonances, is a crucial parameter in OEO designs [Zhang15]. The different attempts have been reported on Fig. IV.9, and one can see that while 0 m and 700 m are clearly insufficient, no difference can be seen between 5 km and 20 km. This means that the phase noise is not limited anymore by the quality of the resonator, but by other noises in the system. We noticed that the optimum sits between 5 km and 10 km, so this first value has been used.

[2]Designed and realized by O. Llopis, LAAS Laboratory, Toulouse, France, in the framework of the EDA contract HIPPOMOS.

Phase noise of the beatnote has been measured using an Aeroflex 3254 ESA (Fig. IV.10, next page). At 10 kHz offset from the carrier, the value of −95 dBc/Hz is a good step toward the typical requirement of −110 dBc/Hz in radar systems, for instance. However at high offset frequencies, we clearly see spurious resonances as high as −70 dBc/Hz at multiples of 40 kHz that directly come from the delay element, here the 5 km-long fiber coil. Also found in standard OEO, this feature limits the phase noise performances of the oscillator. Furthermore, in our case, the long-term stability is altered by mode hopping between these resonances.

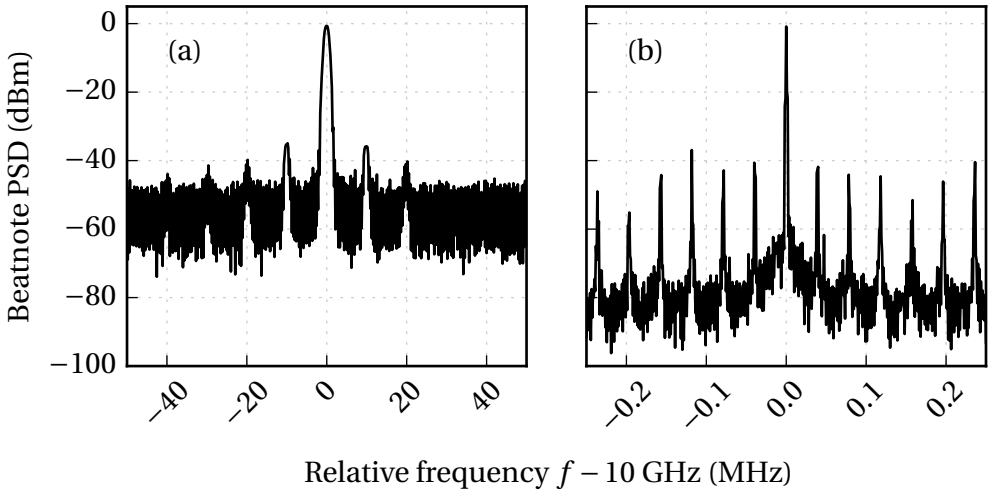

Figure IV.8: Electrical spectrum of the output beatnote. Relative bandwidth is 1 MHz for (a) and 1 kHz for (b).

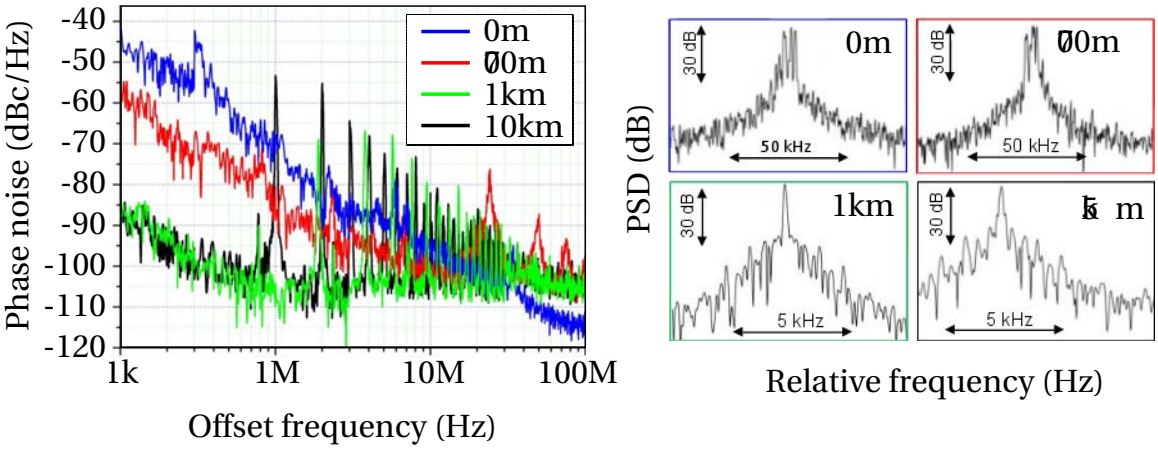

Figure IV.9: Influence of the fiber delay length on the output phase noise and electrical linewidth.

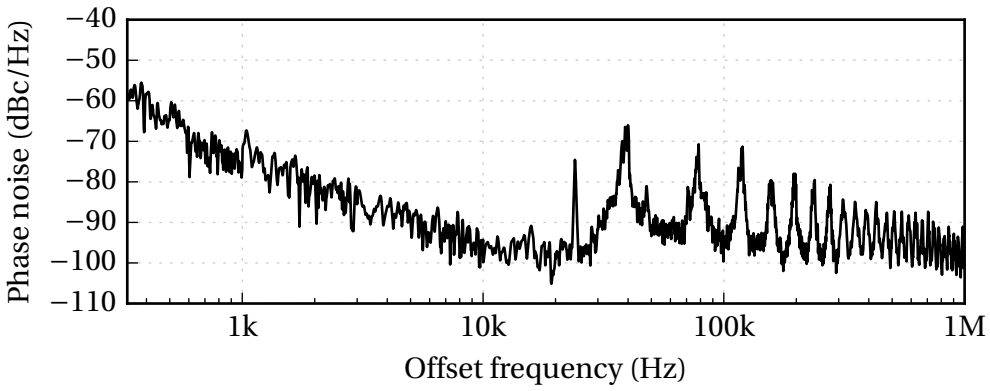

Figure IV.10: Phase noise around the 10 GHz carrier in the long feedback setup.

2c Dual-loop

In order to remove these unwanted phase noise peaks, several solutions have been proposed for OEO engineering. The most complex of them include the usage of two injection-locked oscillators, for instance two OEO with different characteristics, in what is called a Dual Injection-Locked (DIL) OEO setup [Zhou05]. Also, a coupled combination of an OEO and an electronic oscillator has been proposed [Lee08]. But the simplest solution is to reduce the periodicity of the phase filter, by using two different delays, and combining their output. This produces a RF interferometer, and can be done either electronically, by using two photodiodes [Yao98], or with all-optical means [Yang07].

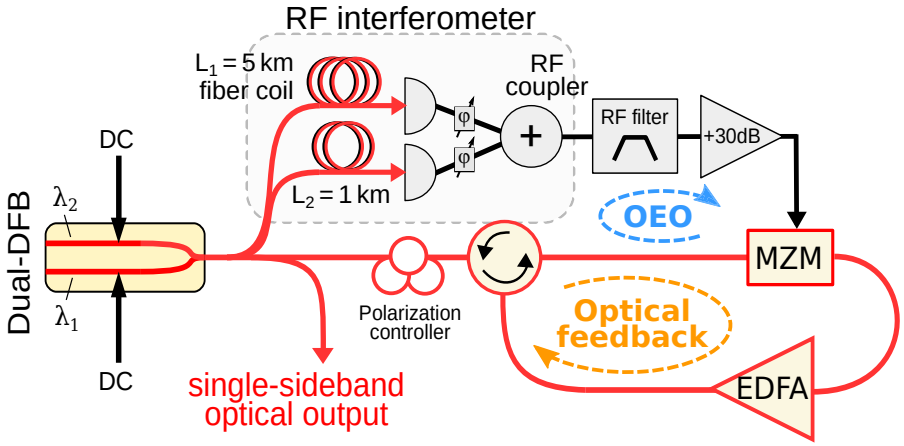

Figure IV.11: Dual-delay setup, using two fiber coils to create a RF interferometer and reduce the number of resonant modes.

Here we implement the simple dual-delay solution from [Yao98] by using two SMF28 fiber coils of length $L_1 = 5\,\text{km}$ and $L_2 = 1\,\text{km}$, that end on two Nortel PP-10G photodiodes. Each output goes through a microwave phase shifter, which can be used

to adjust the relative phase of the two arms, and they are summed by a RF mixer. The optical feedback loop is unchanged, as seen on Fig. IV.11. The optical intensities on the two photodiodes, initially unbalanced because of the different fiber lengths, were adjusted using a slightly lossy connector.

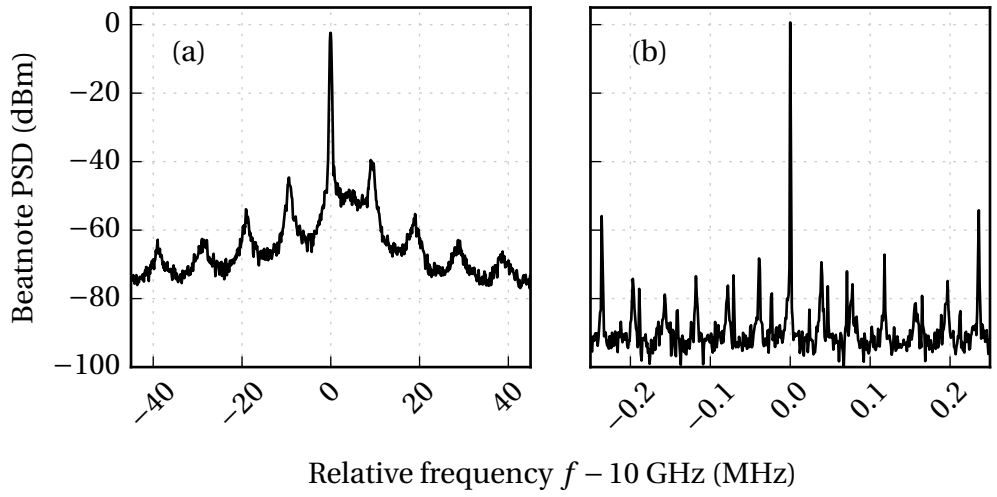

Figure IV.12: Electrical spectrum with the two-coil setup. Relative bandwidth is 0.3 MHz for (a) and 0.2 kHz for (b).

Beatnote spectrum and phase noise have been measured using a Rohde&Schwarz FSW, and what can be seen on Fig. IV.12 and Fig. IV.13 is a clear reduction of the parasitic resonances caused by the delay line. For instance, the first phase noise resonance has been damped by 30 dB, the second by 10 dB, and the third has completely disappeared. On the electrical spectrum, the sidebands due to the delay line have also been widely reduced, with a minimum rejection of 60 dB. On the larger span of the electrical spectrum, we note that external cavity modes of the FSF loop, spaced by $1/T = 12.5$ MHz are much more visible, not being drowned in delay resonances anymore.

It should be noted that the length of the two fibers have been chosen quite arbitrarily. Indeed, precise tuning of the setup is possible, but highly depends on the noise sources, and requires their characterization. That next step is out of the scope of this work, but would allow to precisely reduce a larger number of harmonics of the delay resonances. For instance, in standard OEOs it has allowed reduction of the maximum level of spurious resonances from −90 dBc/Hz down to −120 dBc/Hz [Lelievre17].

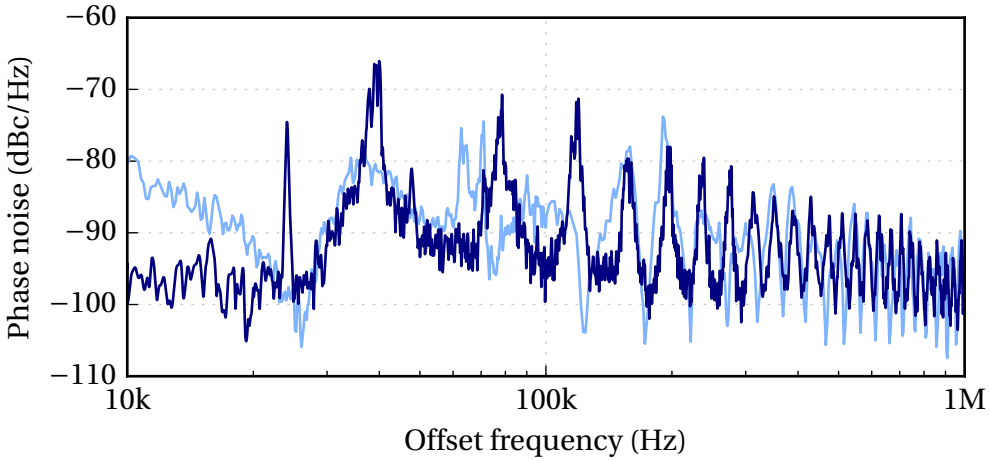

Figure IV.13: Reduction of the spurious high-frequency phase noise resonances using a dual-loop scheme (light blue curve). The phase noise for the single-loop scheme is recalled for comparison (dark blue curve).

3 Shorter delays, towards integration

As can be seen on Fig. IV.12, peaks due to the external cavity modes appear on the electrical spectrum. However, as they are located outside of the bandpass of the RF filter, they cannot resonate. But they prevent us to use a filter with a larger bandwidth, otherwise the frequency locking becomes very sensitive to unwanted "mode hops", where the resonant frequency jumps from one external cavity mode to another one. Yet, we would like to use a RF filter as wide as possible, for tunability reasons, but also because the use of a custom-made very sharp filter makes the setup very specific. We will see here that another possibility is to move away the external cavity resonances, by shortening the optical feedback loop.

3*a* Straight feedback and direct modulation

If we consider the optical feedback loop from Fig. IV.11, it contains a large number of elements, namely an optical coupler, a polarization controller, a circulator, a modulator and an amplifier. This puts a lower limit on the length that can be reached for this system.

However, a slight modification of the setup allows for a much shorter feedback. Indeed, sidebands around the optical carrier can also be generated by using direct modulation of the laser's pump current. Then a simple reflection can be used to generate a frequency-shifted feedback. This is particularly tempting on our kind of

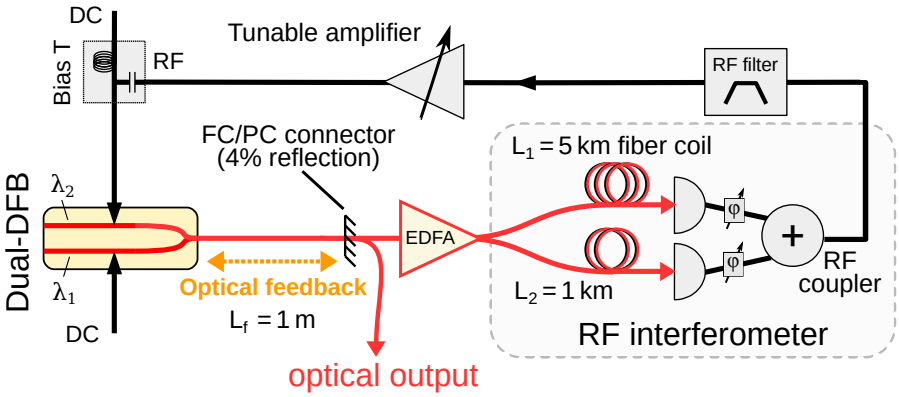

Figure IV.14: Short-loop hybrid opto-electronic oscillator, where direct modulation is used to create the injection sidebands.

components, because they have been specifically engineered for data transmission, and their modulation bandwidth has a 14 GHz cutoff frequency. In practice, only one of the two lasers has been connected with tracks that allow to feed it with a microwave signal. We have combined the DC pump current with the microwave signal using a bias T. Using a synthetizer, we checked that the modulation is indeed linear for our range of powers, as shown on Fig. IV.15

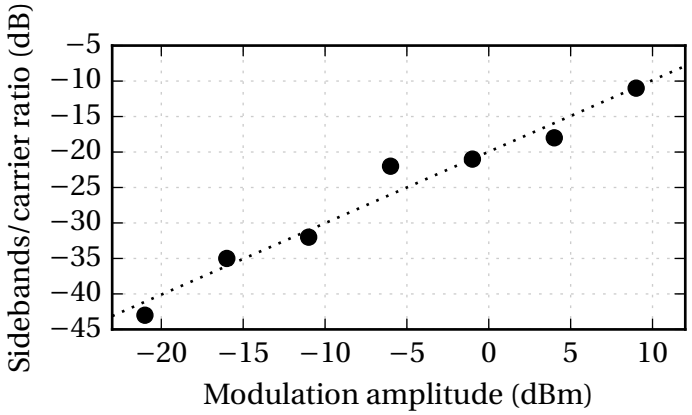

Figure IV.15: Pump modulation efficiency of DFB2, measured as the ratio of the sidebands at 10 ± 2 GHz over the carrying beatnote at 10 GHz.

The full setup, shown on Fig. IV.14, differs from all the previous ones because the coupling mechanism is not exactly the same. Indeed, there is no resonant injection from the unmodulated laser (DFB1) into the modulated one (DFB2). In terms of Eq. (III.16), this corresponds to $\kappa_{21} = 0$. However, we noticed that stable phase locking is still possible and very stable in this configuration. With this setup, all fibered components are removed, allowing an optical feedback path as short as wanted. We choose not to cut our microlensed fiber, and connected it to a FC/PC connector which generates a 4% reflection, so that the round-trip feedback length is roughly $L_f \approx 2$ m.

This corresponds to a much smaller delay $T = 10\,\text{ns}$ ($\tau = 500$ in the normalized units of previous chapter), and to an external cavity frequency of $\nu_f = 100\,\text{MHz}$.

This wider spacing of the external cavity modes allows to release the constraint on the RF filter, so we settle on a more standard filter, model Lorch CF7 with a $-3\,\text{dB}$ bandwidth of 80 MHz.

An extra EDFA with a low gain of 6 dB was added in front of the OEO part, so that the two OEO photodiodes, model Nortel PP-10G, receive 1 mW each. The rest of the OEO loop is nearly the same, with length $L_1 = 5\,\text{km}$. For the second coil, the length was slightly modified to $L_2 = 1.1\,\text{km}$, as it was noticed that it allowed for better results.

The power on the output photodiode, on which the phase noise and spectrum are measured is 200 µW. The results, obtained using a Rohde&Schwarz FSWP phase noise analyzer, are shown on Fig. IV.16 and IV.17.

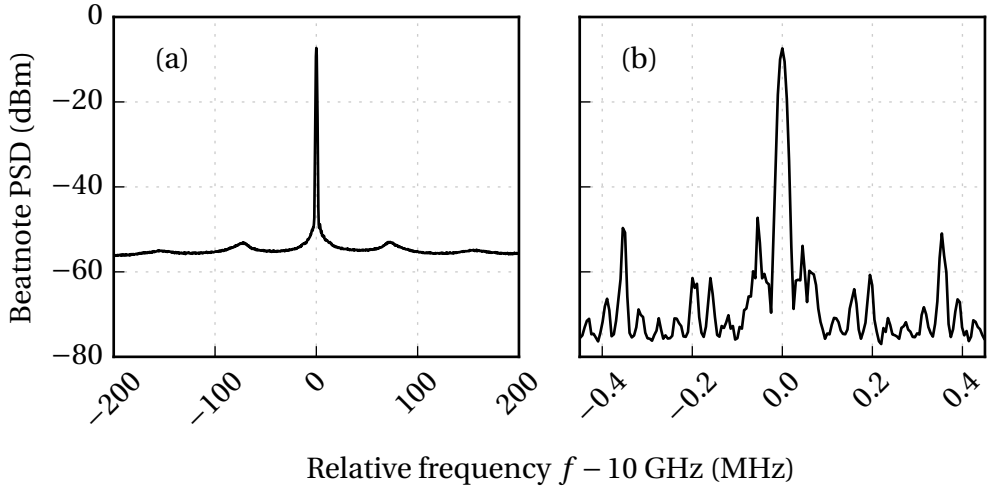

Figure IV.16: Spectrum in the short feedback setup. Relative bandwidth is 1 MHz for (a) and 10 kHz for (b).

On the electrical spectrum (Fig. IV.16), and in strong contrast with Fig. IV.12, external cavity modes can hardly been seen. No mode hops are observed, and the system remains stable for days. The smaller span shows similar performances compared to the long-feedback setup.

On the phase noise measurement (Fig. IV.17), one can notice that a low level of $-70\,\text{dBc/Hz}$ is reached at an offset frequency of 1 kHz from the carrier, and $-100\,\text{dBc/Hz}$ at 10 kHz. This compares well with the long delay setup (Fig. IV.10). At higher offset frequencies, the benefit of the dual-loop OEO is still present, with results similar to those from Fig. IV.13. However, these performances are now obtained with a much simpler setup, using standard components except for the PIC.

However, compared to the previous setups with an external modulator, it may seem

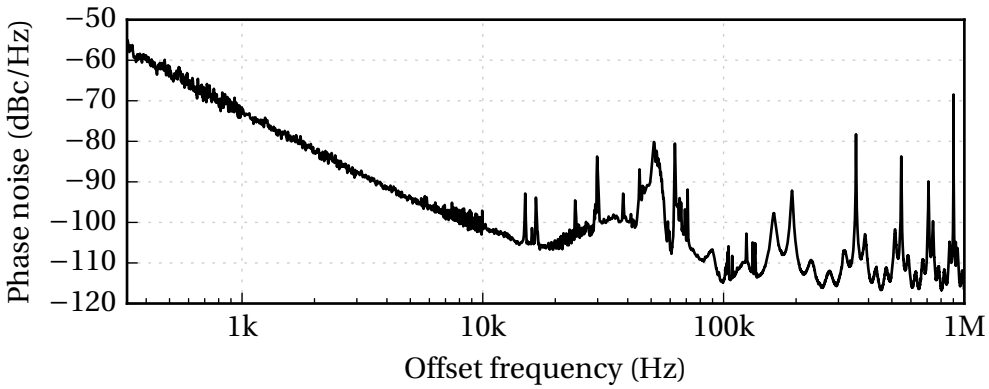

Figure IV.17: Phase noise around the 10 GHz carrier in the short feedback setup.

that the output from this configuration is not a true dual-frequency signal, because it contains the two sidebands around ν_2 created by the pump current modulation. Still, if we look at Fig. IV.18, which shows the output optical spectrum, we see that this extra sideband at λ_3 is 15 dB below the level of λ_1. If this signal were to be submitted to dispersion fading in a fiber link, the calculations from Section 1*c* show that the losses of modulation depth would be less than 1.6 dB. To sum up, the sidebands created for the purpose of stabilization mechanism are very small, and do not affect the output signal, which remains nearly single-sideband. This particular work has been published more concisely in [Thorette18].

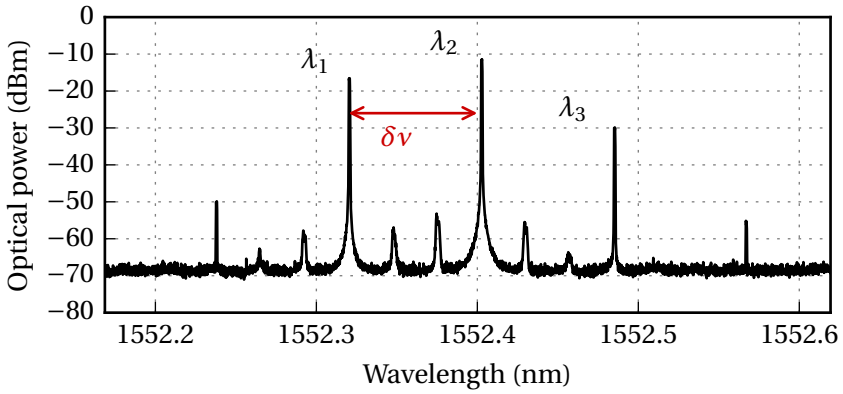

Figure IV.18: Output optical spectrum in the short feedback setup. The residual peaks under 50 dBm are either higher-order harmonics or parasitic, caused by the heterodyne scheme inside the high-resolution OSA (Apex 2083A).

4 Transfer functions: towards a full model of the hybrid OEO.

Characteristics of opto-electronic oscillator can be computed using simple models, such as [Yao96] or more complex ones [Levy09]. They are often linear models, similar to the one presented in 1*b*, that use transfer functions for the small variations of the microwave phase. They involve the characterization of the components and noise sources, and allow to predict the output phase noise of the oscillator. This process is very useful in OEO design, because it can be used to determine the desired features of the components, and guide the engineering when precise performances are required.

In our case, a non-linear element is at the center of the setup, namely the combination of the two injected lasers. However, when a stable regime has been reached, it can be considered that the two lasers and their optical injection loop will act as a linear filter for the microwave phase. This is shown on Fig. IV.19, where the dashed box containing the FSF mechanism can be considered as a replacement for the modulating part of an OEO.

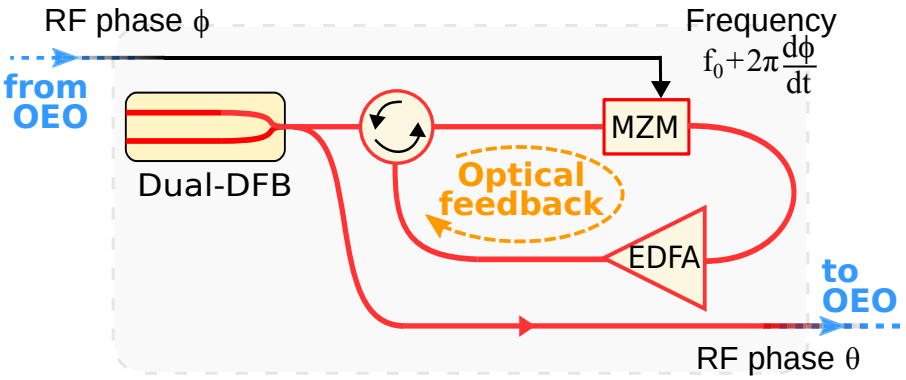

Figure IV.19: Dual-DFB with frequency-shifted feedback, seen as the modulating element of an OEO loop.

Then, the transfer function of this element for the microwave phase can indeed be computed using the model of Eqs. (III.16) presented in the previous chapter. Indeed, a perturbation $\delta\phi$ of the RF phase, reaching the input of the modulator, is included in the change $\psi_{12} = \widehat{\psi_{12}} + \delta\phi$, $\psi_{21} = \widehat{\psi_{21}} + \delta\phi$. In the normalized model, this corresponds to a detuning perturbation so that $\varphi_x = \widehat{\varphi_x} + \delta\phi$.

In a small signal regime, we can proceed to a linearization of the model around the external cavity mode with frequency Ω. We define $e_j = (\widehat{e_j} + \delta e_j)e^{i\omega s}$ and $m_j = \widehat{m_j} + \delta m_j$. If we notate all variables as a vector $u = (e_1, e_2, m_1, m_2)$ and $\delta u = (\delta e_1, \delta e_2, \delta m_1, \delta m_2)$, so that the full evolution is described by $\mathrm{d}u/\mathrm{d}s = f(u(s), u(s-\tau))$, we obtain the following time evolution equation:

$$\frac{\mathrm{d}}{\mathrm{d}s}\delta u = \mathbf{J}\delta u + \mathbf{J}_\tau \delta u(s-\tau) + b\frac{\mathrm{d}\delta\phi}{\mathrm{d}s} \tag{IV.8}$$

with the matrix $\mathbf{J} = \frac{\mathrm{d}f}{\mathrm{d}u(s)}$, $\mathbf{J}_\tau = \frac{\mathrm{d}f}{\mathrm{d}u(s-\tau)}$ and the vector $b = \frac{\mathrm{d}f}{\mathrm{d}\varphi_x}$. If we further define $\delta u = \widetilde{\delta u} e^{ixs}$ and $\delta\phi = \widetilde{\delta\phi} e^{ixs}$, we obtain the following linear system:

$$\left(ix - \mathbf{J} - \mathbf{J}_\tau e^{-ix\tau}\right)\widetilde{\delta u} = ixb\widetilde{\delta\phi} \tag{IV.9}$$

This can be solved to obtain the frequency-dependent response $\widetilde{\delta u} = r(x)\widetilde{\delta\phi}$. From this quantity, the output phase $\theta = \arg(e_1 e_2^*)$ can be recovered, as $\theta = \theta_0 + g(u_0)\delta u$ with the line vector $g(u_0) = \frac{\mathrm{d}\arg(e_1 e_2^*)}{\mathrm{d}u}(u_0)$.

Ultimately, the transfer function for the microwave phase is obtained as $H(x) = \mathrm{d}\widetilde{\theta}/\mathrm{d}\widetilde{\delta\phi} = gr(x)$. With physical units, we have $H(f) = gr(f/f_R)$.

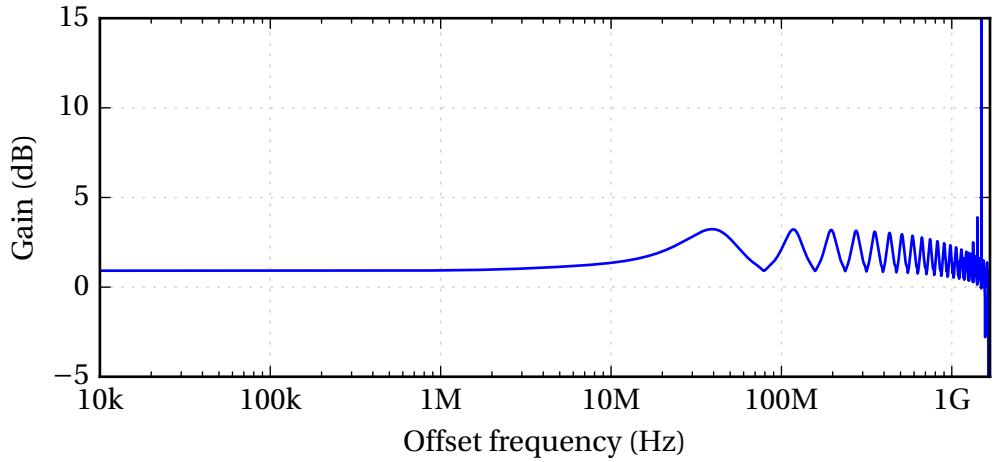

Figure IV.20: Computed transfer functions for the open-loop model.

The result for $\delta = 0$, and typical experimental values $m = 0.8$, $\kappa_0 = 0.04$ and $\tau = 4000$ is shown on Fig. IV.20. Except for small oscillations, with an amplitude less than 3 dB, and for spurious peaks at $f > 0.15 f_R$, the transfer function is rather flat, from the viewpoint of its contribution to the output phase noise. The resonances at higher offset frequencies are not fully understood, and their amplitude and position seem to depend on the parameters of the model. However, in an OEO configuration, they would in any case be filtered by the microwave filter of the loop. Even more so, the relevant offset frequencies for phase noise are usually less than 1 GHz, which corresponds to the non-resonant region of the transfer function. This tells us that the input phase noise ϕ is transparently transferred on the output microwave phase θ by the frequency-shifted feedback mechanism. This may not be necessarily true for other values of

the parameters, but then the model can be used to compute the effect. We note that this transfer function could also be measured experimentally using a vectorial network analyzer, but this was left out of the scope of this work.

4*a* On-chip feedback

As shortening the feedback arm is a valuable option to suppress external cavity modes, it is natural to consider placing it on the laser component itself. While we saw in Fig. III.26 that a very short feedback is not necessarily the best choice, feedback integration is nevertheless an interesting option when it comes to robustness and reproducibility of the setup.

Such experiments have already been done by P. Primiani and colleagues from III-V Lab, using the next generation of dual-DFB components. These PIC include a lot more features than only two DFB lasers. Indeed, the 4.4 mm×700 µm wafer includes, besides the two lasers, multiple semiconductor amplifiers (SOA), two electro-absorption modulators (EAM), and two uni-travelling carrier (UTC) photodiodes [van Dijk14]. These components are intended to be used as high-power and large bandwidth heterodyne transmitters. However, a preliminary experiment to use these components in a hybrid OEO configuration, similar to what we presented before. We report here the principle on Fig. IV.21 and their main results that are also described in [Primiani16].

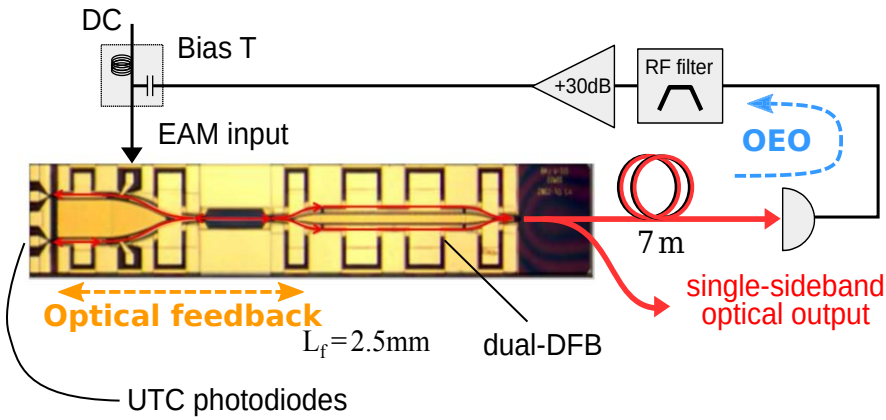

Figure IV.21: Very short feedback experiment, with integrated modulator.

One of the internal photodiode has been diverted from its usage, and was used as a reflector. This creates a feedback into the lasers, with a total length roundtrip length of 2.5 mm. This corresponds to a delay $T \approx 50$ ps, so that external cavity modes are $\nu_f \approx 20$ GHz apart and only one is allowed to oscillate. The setup has been closed with an OEO loop including a 7 m-long fiber as a delay element and a filter around 20 GHz. It successfully allow a self-stabilization of the beatnote, and the corresponding

output spectrum and phase noise are shown in Fig. IV.22. At 10 kHz offset from the carrier the phase noise level is −85 dBc/Hz and we notice a low level of −120 dBc/Hz at 1 MHz from carrier. These preliminary results are encouraging, as they show that the FSF principle can be deployed on-chip, with no other frequency limitation than that of the integrated modulator. With very few modification, an self-stabilized heterodyne source at 40 GHz could be built.

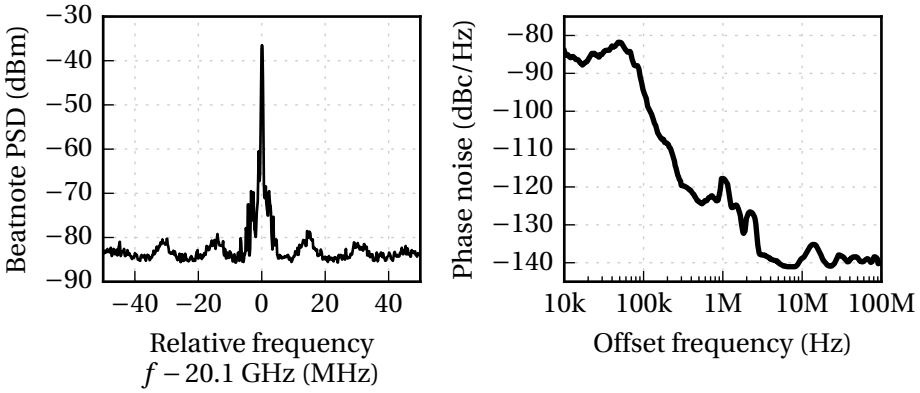

Figure IV.22: Spectrum and phase noise in the integrated exploratory experiment. Results reproduced from colleagues [Primiani16].

5 Perspectives

In this chapter, we showed a few proof-of-concept setups that allowed us to combine our beatnote locking method with opto-electronic resonant loops. Indeed, using the fact that frequency-shifted feedback allows to stabilize the beatnote on a reference signal, we used an optical delay and an electronic filter to stabilize it on a delayed version on itself, or equivalently, on a resonance peak of an optical resonator. This creates a hybrid opto-electronic oscillator, which generates its microwave signal using a heterodyne combination rather than with a modulator. Consequently, the optical output signal contains mainly two optical frequencies, and can be used for single-sideband modulation. This is an advantage as it exhibits a full modulation depth, and is insensitive to chromatic dispersion when traveling in fibers.

We then showed that various modifications to this principle can be made, for instance by using standard OEO techniques for enhancing the phase noise. On that topic, several other improvements based on other OEO could be used, such as dual-injected OEO, usage of high-quality factor, thermally stabilized microresonator instead of fiber coils. Additionally, we showed that a more optimized frequency-shifted feedback scheme (here, a shorter one) could help achieving better stability. Good prospects of integration can also be made, as photonic integrated components including modulating elements and feedback have already been made. Finally, using the model from Chapter III, and adding complementary experimental measurements of the transfer functions, we would have all the ingredients for a careful and precise engineering of a injection-based heterodyne opto-electronic oscillator up to 100 GHz.

CONCLUSIONS AND PERSPECTIVES

ALTHOUGH this work did venture in the quite different areas of dual-polarization solid-state lasers and semiconductor lasers, the unifying thread has been the quest for a nearly all-optical beatnote stabilization method. Indeed, the capability to control precisely optical beatnotes is part of the current endeavor in microwave photonics, that strives toward hybrid opto-electronic methods of very high quality microwave signal generation and transportation over fibered networks. In this framework, the current study focused on two cases, with the will to combine precise results and in-depth investigation with the outlining of general behaviors. This was done in the hope that the developed methods will be modified and adapted to practical cases where they could prove their usefulness in potentially very different forms from the models found in this work.

While hidden between the same term “frequency-shifted feedback”, the method developed for the dual-polarization dual-frequency lasers of Chapter II shows many differences compared to the one applied to the dual-DFB semiconductor component from Chapter III. In the first case, the good theoretical and experimental knowledge of the Nd:YAG dual-mode lasers allowed for fine measurement and control of the parameters. Furthermore, the low frequency difference and the fact that the two frequencies are produced on orthogonal polarizations allowed to inject exactly one mode into the other to provoke phase synchronization. The relative simplicity of the setup allowed a very good agreement between the experimental study and the numerical model, and comparisons between the two viewpoints allowed for interesting findings. One of the main results is that there is a locking region of the parameters in which phase synchronization happens, and the frequency difference can be externally controlled. Furthermore, phase noise measurements show that in this case the stability of the reference is well transposed on the beatnote.

Outside of this locking regions, bounded phase phenomenon are found, that allow for a kind of frequency locking with phase oscillations. Also, chaotic dynamics are frequent, and we have shown that the combination of bounded phase regimes and chaos exist. In this unique kind of regime, frequency locking is strongly maintained,

as seen on the phase noise measurements, but small chaotic oscillations of the phase and amplitude of the beatnote are present. An interesting use case of such regimes would be telemetric applications, with what is called chaotic detection. Such systems use chaotic signals to achieve non-ambiguous cross-correlation between an emitted and a reflected wave [Lin04b]. Here, we combine a chaotic regime with a very stable RF-over-optical carrier, so it could be used as a source for a chaotic LIDAR-RADAR. Preliminary work is in progress on this topic in the lab.

In this FSF setup, we have explored the influence of various parameters, most notably the frequency detuning and injection strength, but also the potential time delay in the feedback arm, the coupling between modes in the gain medium, and the linewidth enhancement factor α. For the latter, whose presence was an unexpected surprise along the road, we showed that our setup could be used to make a very precise measurement of its value. Yet, the question of its physical origin remains, and more investigation on this topic is needed. For instance, we planned a similar measurement in other types of rare-earth doped materials, which we expect to unveil interesting physics in solid-state active media. Similarly, some questions on the coupling coefficient β between the polarization modes remain to be answered, namely its dependence on the pump polarization and beam geometry. These problems are currently under study.

Finally, while this study for a low frequency beatnote in a table-top setup has few direct applications, we saw recently that it may advantageously be applied to very similar while much more convenient and versatile dual-frequency fiber lasers. This topic is an important part of an ongoing PhD within the EOFIL project [Guionie18b].

Long-term perspectives include the possibility to transpose this technique to multimode lasers, as mode-locked dual-polarization sources are currently meeting a particular interest in spectroscopy applications [Thévenin12b; Link16]. We also wonder how it could apply on spatially multimode lasers, such as ones using conical refraction phenomenon [Abdolvand10].

The transposition to the semiconductor chip, with separated lasers, came in as a more industry-driven case. Indeed, these unique components including two DFB had been specifically designed for heterodyne microwave generation and data communication. They came with the constraint of combined outputs on a single polarization, and their use case with the need of a beatnote in the tenth of GHz. It was quickly discovered that frequency-shifted feedback could be very successfully applied to this system as well, but the analysis of the outcome and synchronization conditions proved to be much more complicated. Indeed, instead of a one-direction coupling between the two modes, we now had a bidirectional and strongly delayed coupling between the lasers, along with feedback for each of them. Each of these four interactions has

a different strength, and comes with a dependency on the optical phases, that are not controlled and drift in time. Yet, the rate equation models allowed us to replicate the observed breaking of the locking range into bands, and most of the dynamical regimes. Importantly, it also showed that the dependency on the uncontrolled feedback optical phases could be lessened by reducing the amount of self-feedback for each laser. Taking this into account, very good stability of the synchronization could be obtained.

From a laser dynamics point of view, it would be interesting to explore the instabilities found in this system, notably because it is driven by a long delay. Indeed, such large-delay systems are known to present very rich dynamics [Barland16; Yanchuk17]. Also, it is known that some instabilities can be used in microwave applications, such as period-one-based microwave oscillation, signal regeneration, modulation bandwidth enhancement, etc. so this area could be explored.

Going a step further into practical usage, we proposed in Chapter IV an architecture derived of an opto-electronic oscillator (OEO) that relies on frequency-shifted feedback instead of on a straight modulator for the generation and control of the microwave phase. We showed that while keeping most of the advantages of the OEO, this could be used to directly generate a nearly single-sideband microwave signal over an optical carrier. Moreover, this system has good potentiality for direct on-chip inclusion in photonic integrated components. Work in this direction is in under progress, and a complete integration of the OEO, using a for instance ring resonators as an integrated delay line is the next milestone. This could be achieved thanks to an emerging technology combining silicium and InP wafers, developed at III-V Lab [Primiani15]. Further design of hybrid OEOs will also benefit from our good knowledge of the frequency-shifted feedback system.

To sum up in a sentence, we have explored the technique of frequency shifted feedback in its various displays, and found it is quite robust and that it can be applied in a vast panel of cases. Building on this ground, we hope that in a not too distant future it can be modified, adapted, and transposed to other systems.

ANNEXES

A Eigenstates of a cavity with two quarter-wave plates

In this annex we will recall some results on the polarization eigenmodes for a laser cavity containing (i) a phase anisotropy, (ii) two quarter-wave plates. For this, we will resort on the standard Jones matrix formalism [Jones41] to describe the change in polarization associated to optical elements.

Arbitrary phase anisotropy

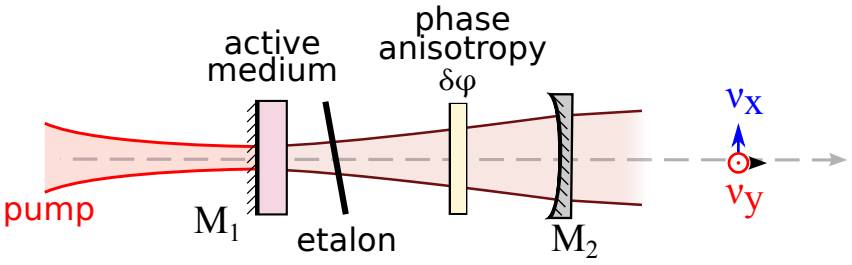

Figure A.1: Cavity including an arbitrary phase anisotropy $\delta\varphi$.

We first consider a cavity of length L containing an arbitrary phase anisotropy $\delta\varphi$, as pictured on Fig. A.1. The anisotropic element can be described by the following Jones matrix:

$$\mathbf{M} = \begin{pmatrix} e^{i\delta\varphi/2} & 0 \\ 0 & e^{-i\delta\varphi/2} \end{pmatrix} \tag{IV.10}$$

We want to determine the polarization eigenstates of the cavity, i.e. the polarization state of the field that remains unchanged after a round-trip in the cavity. For a monochromatic wave of frequency ν, the corresponding matrix is simply $\mathbf{M} = \mathbf{M_1}^2 e^{2i\pi\nu L/c}$. Note that here we have ignored the changes of the field amplitude, and more generally the effect of the active medium. The corresponding eigenmodes of

the field are simply $\mathbf{E}_+ = \begin{pmatrix} 1 \\ 0 \end{pmatrix}$ and $\mathbf{E}_- = \begin{pmatrix} 0 \\ 1 \end{pmatrix}$, and the associated eigenvalues are $\lambda_\pm = 2\pi\nu_\pm L/c \pm \delta\varphi$. As one requires that $\lambda_\pm = 2k\pi$ with k an integer. This gives us the two main properties of such cavity, which are:

$$\mathbf{E}_+ \perp \mathbf{E}_- \rightarrow \text{the two polarization modes are orthogonal} \tag{IV.11a}$$

$$\nu_+ - \nu_- = \frac{c}{2L} \times \frac{\delta\varphi}{2\pi} = \text{FSR} \times \frac{\delta\varphi}{2\pi} \tag{IV.11b}$$

Two quarter-wave plate

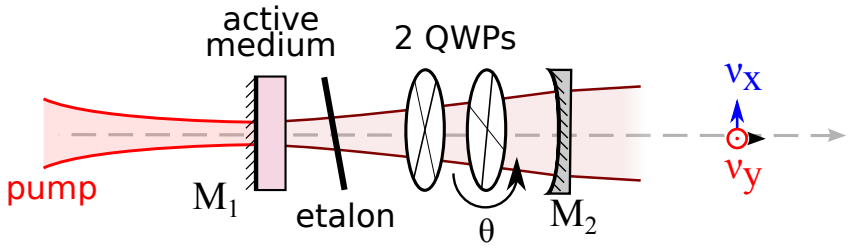

Figure A.2: Cavity including two quarter-wave plates, with an angle θ between them.

Let us consider a cavity including two quarter-wave plates between two mirrors M_a and M_b as in Fig. A.2 [Kastler70; Le Floch73]. There is an angle θ between the optical axes of the two plates. We want to determine the polarization eigenstates of the cavity, i.e. the polarization state of the field that remains unchanged after a round-trip in the cavity. Starting from active medium (left mirror) and moving from left to right, the Jones matrix of a cavity round-trip reads:

$$\mathbf{M} = \mathbf{M}_1\mathbf{M}_2^2\mathbf{M}_1, \tag{IV.12}$$

where $\mathbf{M}_1$ and $\mathbf{M}_2$ are the Jones matrices of the two QWPs. We can choose the optical axis of the first one as the x-axis, so $\mathbf{M}_1 = \begin{pmatrix} e^{i\phi/2} & 0 \\ 0 & e^{-i\phi/2} \end{pmatrix}$, with $\phi = \pi/2$. In order to write $\mathbb{M}_2$, we must apply a rotation of an angle θ:

$$\begin{aligned} \mathbf{M}_2 &= \begin{pmatrix} \cos\theta & \sin\theta \\ -\sin\theta & \cos\theta \end{pmatrix} \begin{pmatrix} e^{i\phi/2} & 0 \\ 0 & e^{-i\phi/2} \end{pmatrix} \begin{pmatrix} \cos\theta & -\sin\theta \\ \sin\theta & \cos\theta \end{pmatrix} \\ &= \begin{pmatrix} 1 + i(1-2\sin^2\theta) & -2i\sin\theta\cos\theta \\ -2i\sin\theta\cos\theta & 1 - i(1-2\sin^2\theta) \end{pmatrix}, \end{aligned} \tag{IV.13}$$

and then

$$\mathbf{M}_2^2 = 2i \begin{pmatrix} 1-2\sin^2\theta & -2\sin\theta\cos\theta \\ -2\sin\theta\cos\theta & -(1-2\sin^2\theta) \end{pmatrix}. \tag{IV.14}$$

We can now compute the Jones matrix of the cavity round-trip (IV.12):

$$\mathbf{M} = \mathbf{M}_1\mathbf{M}_2^2\mathbf{M}_1 = 2i\begin{pmatrix} 1-2\sin^2\theta & 2i\sin\theta\cos\theta \\ 2i\sin\theta\cos\theta & 1-2\sin^2\theta \end{pmatrix}, \tag{IV.15}$$

We can compute the eigenvalues $\lambda_\pm$ of $\mathbf{M}$ by solving $\det(\mathbf{M}-\lambda)=0$:

$$\lambda_\pm = 1-2\sin^2\theta \pm 2i\sin\theta\cos\theta = \cos 2\theta \pm i\sin 2\theta = e^{\pm i2\theta}. \tag{IV.16}$$

By solving $\mathbf{M}\mathbf{v}_\pm = \lambda_\pm\mathbf{v}_\pm$, one has the polarization eigenvectors $\mathbf{v}_\pm$:

$$\mathbf{v}_\pm = \begin{pmatrix} 1 \\ \pm 1 \end{pmatrix} \tag{IV.17}$$

It is seen that, at point A, the field is linearly polarized, at $\pm 45°$ with respect to the optical axis of QWP_1. A field propagating from left to right, having a polarization state corresponding to $\mathbf{v}_\pm$ at point A, acquires a circular polarization between the two QWPs, and is again linearly polarized after the QWP_2, at $\pm 45°$ with respect to the optical axis of QWP_2. If the mirror M_2 plays the role of the output coupler of the cavity, the output field is linearly polarized and its polarization direction depends on the angle θ.

Between the QWPs, each mode features a slightly more complicated polarization. Indeed, the two circularly polarized waves in each direction have an opposite rotation. This stationary structure of helicoidal polarization is often referred as "twisted modes" [Kastler70].

A monochromatic wave of frequency ν bouncing between the mirrors of the cavity accumulates a phase $\varphi = 2\pi\nu/c2L \pm 2\theta$. If one requires $\varphi = 2\pi k$ with k an integer, one gets the cavity eigenfrequencies $\nu_\pm$:

$$\nu_\pm = \frac{c}{2L}\left(k \pm \frac{\theta}{\pi}\right) \tag{IV.18}$$

One can see from the previous equations that the cavity eigenstates have a frequency splitting

$$\nu_+ - \nu_- = \frac{c}{2L}\frac{2\theta}{\pi} \tag{IV.19}$$

In particular, this frequency difference can be tuned mechanically, by rotating one of the quarter wave plates (usually one choses not to rotate the QWP close to the output mirror, in order not to change the polarization state of the output field).

B Estimation of α from gain asymmetry

The aim of this section is to examinate whether the low asymmetry of the Nd:YAG gain curve is sufficient to explain the value $\alpha = 0.28$ of the linewidth enhancement factor measured in II.5*c*. Indeed, if we recall Section 1*b*, the linewidth enhancement factor is defined as:

$$\alpha \equiv -\frac{\partial\chi_r/\partial N}{\partial\chi_i/\partial N} = \frac{1}{\lambda}\frac{\partial n/\partial N}{\partial\mathcal{G}/\partial N} \tag{IV.20}$$

with $\frac{\partial\mathcal{G}}{\partial N} = \lambda\sigma(\lambda)$. As the electric susceptibility $\chi = \chi_r + i\chi_i$ is supposed to be an analytical function, its real and imaginary parts are linked by the Kramers-Kronig formula, so that:

$$\frac{\partial\chi_r}{\partial N} = \frac{1}{\pi}\int_{-\infty}^{\infty}\frac{\partial\chi_i}{\partial N}(k') \times \frac{dk'}{k'-k} \tag{IV.21}$$

where $k = 1/\lambda$ is the wave number. If the integral does not converge, we will take the principal Cauchy value.

Thus, knowing the gain curve $\sigma(\lambda)$, we can estime α for a given value of the lasing wavelength λ.

$$\alpha(\lambda) = \frac{1}{\lambda\sigma(\lambda)} \times \frac{1}{\pi}\int_{-\infty}^{\infty}\frac{k'\sigma(k')dk'}{k'-k} = \frac{1}{\sigma(\lambda)} \times \frac{1}{\pi}\int_{-\infty}^{\infty}\frac{\sigma(\lambda')d\lambda'}{\lambda'-\lambda} \tag{IV.22}$$

We now have to compute the real part $f_1(\lambda)$ of an analytical function whose imaginary part $f_2(\lambda)$ has a Lorentzian shape:

$$f_2(\lambda) = \frac{1}{1+\left(\frac{\lambda-\lambda_0}{\mu}\right)^2} \tag{IV.23}$$

We know that:

$$f_1(\lambda) = \frac{1}{\pi}\int_{-\infty}^{\infty}\frac{1}{1+\left(\frac{\lambda'-\lambda_0}{\mu}\right)^2} \times \frac{d\lambda'}{\lambda'-\lambda} \tag{IV.24}$$

We start by using the offset $u = \lambda' - \lambda$, and introduce $\Delta = \lambda - \lambda_0$.

$$f_1(\lambda) = \frac{\mu^2}{\pi}\int_{-\infty}^{\infty}\frac{1}{\mu^2+(u-\Delta)^2} \times \frac{du}{u} \tag{IV.25}$$

This can be rewritten as:

$$f_1(\lambda) = \frac{1}{\pi}\frac{\mu^2}{\Delta^2+\mu^2}\int_{-\infty}^{\infty}\frac{1}{u} + \frac{2\Delta-u}{u^2-2\Delta u+\Delta^2+\mu^2}du \tag{IV.26}$$

The first term $\int_{-\infty}^{\infty} du/u$ has a principal value of zero, as it is an odd function integrated on a symmetric interval, and can be eliminated. For the second term, let us defined the translation $x = u - \Delta$. Then:

$$f_1(\lambda) = \frac{1}{\pi}\frac{\mu^2}{\Delta^2+\mu^2}\int_{-\infty}^{\infty}\frac{\Delta-x}{x^2+\mu^2}dx \tag{IV.27}$$

Again, the term $\int_{-\infty}^{\infty} x/(x^2+\mu^2)dx$ has a principal value of zero, and there remains:

$$f_1(\lambda) = \frac{1}{\pi}\frac{\Delta\mu^2}{\Delta^2+\mu^2}\int_{-\infty}^{\infty}\frac{dx}{x^2+\mu^2} = \frac{1}{\pi}\frac{\Delta\mu^2}{\Delta^2+\mu^2}\times\frac{\pi}{\mu} = \frac{\Delta\mu}{\Delta^2+\mu^2} \tag{IV.28}$$

Eventually:

$$f_1(\lambda) = \frac{(\lambda-\lambda_0)/\mu}{1+\left(\frac{\lambda'-\lambda_0}{\mu}\right)^2} = \frac{\lambda'-\lambda_0}{\mu}\times f_2(\lambda) \tag{IV.29}$$

We will now use the data on the gain of Nd:YAG, taken from the article [Kushida68], and summarized in the following table:

Level	R_1	R_2
Wavelength	$\lambda_1 = 1064.5\,\text{nm}$	$\lambda_2 = 1064.1\,\text{nm}$
FWHW	$\mu_1 = 0.238\,\text{nm}$	$\mu_1 = 0.294\,\text{nm}$
Intensity (cross-section)	$\sigma_1 = 1.7\times10^{-19}\,\text{cm}^{-2}$	$\sigma_2 = 8.0\times10^{-19}\,\text{cm}^{-2}$

On Fig. B.1, we plotted the gain curve for clarity, and the estimated value of α in function of the lasing wavelength. If the laser operates on the maximum of the gain curve, the value for the linewidth enhancement factor is $\alpha = 0.06$. This does not agree with the measured values in Chapter II, so that two hypothesis have to be considered. Either the laser does not operate at the maximum of gain, or another mechanism is at the root of the observed linewidth enhancement factor. It could go from subtle thermal effects, to acoustic effects in the crystal, as suggested in [Fordell05]. More investigation is needed to understand the origin of this non-zero Henry factor.

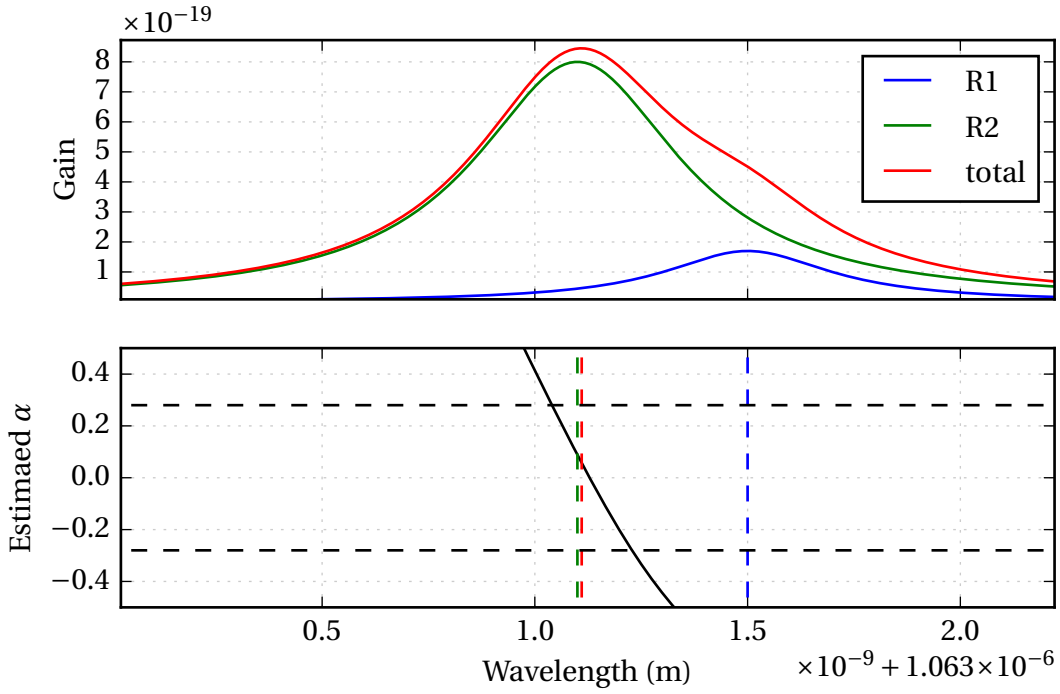

Figure B.1: Estimation of α using a Kramers-Kronig method.

C Coupling factor β for an non-isotropic pumping

Calculations for the coupling factor β between the different populations in a solid-state laser have been already made in [Schwartz09], and they allow to estimate the coupling in the case of a (111) or (100)-cut crystal, taking in account a slight ellipticity of the dipole interaction. However, it relies on the assumption that the pumping is the same for all populations. While this appears reasonable for the case of an unpolarized pump, and maybe for a circular pump, this becomes questionable for a linearly or elliptically polarized pump.

The population of active dipoles involved into the laser gain can be split into three groups according to their orientation, so that each of them associated with a polarization direction. The following calculations attempt to take in account a different pumping rate for each of theses 3 populations N_i in the (111)-cut case, which corresponds to our laser from Chapter II.

We define a 2×3 matrix $\mathbf{C} = c_{ij}$ as the interaction matrix between each each polarization of the field, and each population. At the first order, the dipole interaction gives $c_{ij} = \cos^2(\widehat{\mathbf{x}_j, \mathbf{u}_i})$. Then, let the diagonal 3×3 matrix $\mathbf{W}$ represent the different pumping rates W_k associated with each polarization.

With these notations, Equations (5) and (6) from [Schwartz09], describing the populations $\mathbf{N}$ and laser gain $\boldsymbol{\gamma}$ at equilibrium, become:

$$\mathbf{N} = \mathbf{W}\tau_c(\mathbf{1} - \mathbf{C}\mathbf{J}) \text{ with } \mathbf{J}_i = I_i / I_i^s \tag{IV.30a}$$

$$\boldsymbol{\gamma} = \sigma c \mathbf{C}^T \mathbf{N} \tag{IV.30b}$$

Here I_i is the intensity of the mode i, while I_i^s is the corresponding saturated intensity. σ is the cross-section of the interaction. The coupling coefficient $\mathcal{C}$ is defined with respect to the small variation of intensity and gain around the equilibrium:

$$\mathcal{C} = \frac{\frac{\Delta I_x}{\Delta \gamma_y} \times \frac{\Delta I_y}{\Delta \gamma_x}}{\frac{\Delta I_x}{\Delta \gamma_x} \times \frac{\Delta I_y}{\Delta \gamma_y}} \tag{IV.31}$$

If we study the small variations of Eqs. IV.30, we obtain

$$\Delta \boldsymbol{N} = \mathbf{W}\tau_c \mathbf{C}\Delta\mathbf{J} \tag{IV.32a}$$

$$\Delta\boldsymbol{\gamma} = \sigma c \mathbf{C}^T \Delta\mathbf{N} \tag{IV.32b}$$

Thus, $\Delta\boldsymbol{\gamma} = \sigma c \tau_c \mathbf{C}^T\mathbf{W}\mathbf{C}\Delta\mathbf{J}$ where $\mathbf{A} = \sigma c \tau_c \mathbf{C}^T\mathbf{W}\mathbf{C}$ is a square matrix. This gives $\Delta\mathbf{J} = \mathbf{A}^{-1}\Delta\boldsymbol{\gamma}$.

The terms appearing in th expression of $\mathcal{C}$ can be written:

$\frac{\Delta I_i}{\Delta\gamma_j} = I_i^s \frac{\Delta J_i}{\Delta\gamma_j} = I_i^s \frac{(\mathbf{A}^{-1}\Delta\boldsymbol{\gamma})_i}{\Delta\gamma_j} = I_i^s (\mathbf{A}^{-1})_{ij}$ car a priori, $\frac{\Delta\gamma_i}{\Delta\gamma_k} = \delta_{ik}$.

If we define $\mathbf{B} = \mathbf{A}^{-1}$, the coupling coefficient is:

$$\mathcal{C} = \frac{B_{12}B_{21}}{B_{11}B_{22}} \tag{IV.33}$$

We can express the terms by computing $\mathbf{A}$.

$$\mathbf{A} = \begin{bmatrix} W_0 c_{00}^2 + W_1 c_{01}^2 + W_2 c_{02}^2 & W_0 c_{00}c_{10} + W_1 c_{01}c_{11} + W_2 c_{02}c_{12} \\ W_0 c_{00}c_{10} + W_1 c_{01}c_{11} + W_2 c_{02}c_{12} & W_0 c_{10}^2 + W_1 c_{11}^2 + W_2 c_{12}^2 \end{bmatrix} \tag{IV.34}$$

Then its inverse is straightforwardly:

$$\mathbf{B} = \frac{1}{\det\mathbf{A}} \begin{bmatrix} W_0 c_{10}^2 + W_1 c_{11}^2 + W_2 c_{12}^2 & -W_0 c_{00}c_{10} + W_1 c_{01}c_{11} + W_2 c_{02}c_{12} \\ -W_0 c_{00}c_{10} + W_1 c_{01}c_{11} + W_2 c_{02}c_{12} & W_0 c_{00}^2 + W_1 c_{01}^2 + W_2 c_{02}^2 \end{bmatrix} \tag{IV.35}$$

We obtain this expression of $\mathcal{C}$ in function of the pumping rates and the light-matter interaction terms.

$$\mathcal{C} = \frac{(W_0 c_{00}c_{10} + W_1 c_{01}c_{11} + W_2 c_{02}c_{12})^2}{\left(W_0 c_{00}^2 + W_1 c_{01}^2 + W_2 c_{02}^2\right)\left(W_0 c_{10}^2 + W_1 c_{11}^2 + W_2 c_{12}^2\right)} \tag{IV.36}$$

We note that for the isotropic case $W_k = 1$, the expression from [Schwartz09] is found again:

$$\mathcal{C}_{\text{isotropic}} = \frac{(c_{00}c_{10} + c_{01}c_{11} + c_{02}c_{12})^2}{\left(c_{00}^2 + c_{01}^2 + c_{02}^2\right)\left(c_{10}^2 + c_{11}^2 + c_{12}^2\right)} \tag{IV.37}$$

We will now choose a basis for the modes $\mathbf{E_x} = \mathcal{E}_x \mathbf{u_x}$ et $\mathbf{E_y} = \mathcal{E}_y \mathbf{u_y}$ in the cavity. As we are in a (111)-cut crystal, the angle around the axis $\mathbf{u_1} + \mathbf{u_2} + \mathbf{u_3}$ is irrelevant. We follow Eq. 9 from [Schwartz09], and choose the same $\mathbf{x_1} = \frac{1}{\sqrt{2}} \begin{bmatrix} 1 \\ -1 \\ 0 \end{bmatrix}$ and $\mathbf{x_2} = \frac{1}{\sqrt{6}} \begin{bmatrix} 1 \\ 1 \\ -2 \end{bmatrix}$. This gives the following values for the interaction coefficients:

$$\mathbf{C} = \begin{bmatrix} \left(\frac{1}{\sqrt{2}}\cos\alpha + \frac{1}{\sqrt{6}}\sin\alpha\right)^2 & \left(\frac{1}{\sqrt{6}}\cos\alpha - \frac{1}{\sqrt{2}}\sin\alpha\right)^2 \\ \left(-\frac{1}{\sqrt{2}}\cos\alpha + \frac{1}{\sqrt{6}}\sin\alpha\right)^2 & \left(\frac{1}{\sqrt{6}}\cos\alpha + \frac{1}{\sqrt{2}}\sin\alpha\right)^2 \\ \frac{1}{3}\sin\alpha^2 & \frac{1}{3}\cos\alpha^2 \end{bmatrix} \tag{IV.38}$$

We now have to choose an expression for the pumping rates. We suppose that the pump beam is centered, so that its polarization is orthogonal to the (111) axis, i.e. parallel to $\mathbf{x_1}$.

We can reasonably choose $W_k = \cos^2(\widehat{\mathbf{x}_\theta, \mathbf{u_k}})$ where $\mathbf{x}_\theta = \cos\theta \mathbf{x_1} + \sin\theta \mathbf{x_2}$, θ being the angle between $\mathbf{E_x}$ and the pump polarization.

We check that indeed $\sum_k W_k = 1$. Then,

Which finally leads to a complicated expression for $\mathcal{C}$, which, contrary to the symmetric case, depends on both α and θ, and not only on their difference. Some curves are shown on Fig. C.1. We note that there are some symmetries $\mathcal{C}\left(\alpha + \frac{\pi}{4}\right) = \mathcal{C}\left(\frac{\pi}{4} - \alpha\right)$, but also $\mathcal{C}(-\alpha, \theta) = \mathcal{C}(\alpha, -\theta)$. As the dependency on α is maintained, the angle between the axes of the crystal and the cavity field is relevant, and care should be taken in the experiments. This preliminary study should be continued, for instance by a proper comparison with more measurements, or by considering an elliptical pump polarization.

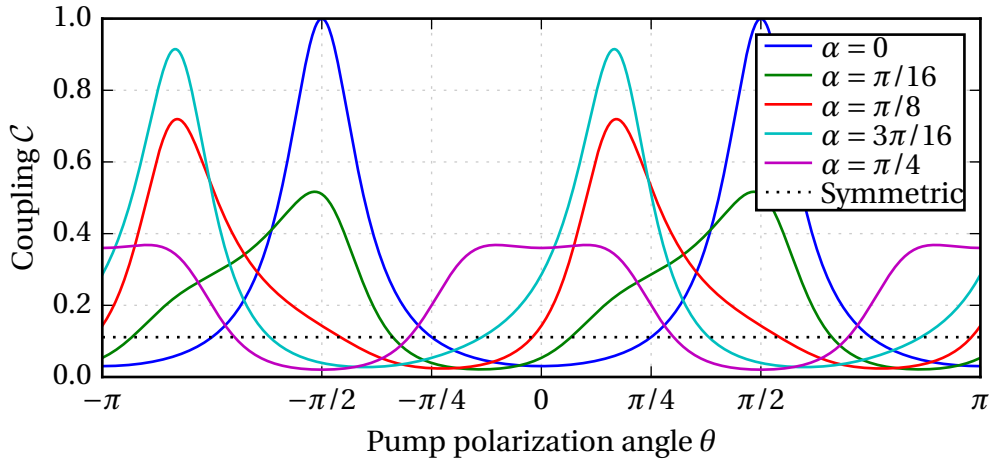

Figure C.1: Coupling coefficient for varying angle between the cavity and the linear pump polarization axis.

D Comparison of integrators for phase noise calculation

Numerical computation of the phase noise can be done from the rate equations using different methods. First, an "analytical" phase noise could be obtained from a linearization around the steady state. Alternatively, a "Langevin" approach can be used, that consist in adding noise terms to the equations, and proceeding to their time integration. Such equations are called stochastic differential equations (SDE), and the different process for their integration has been the topic of a substantial literature [Honeycutt92]. In our case, we compared four methods listed here. The results, shown on Fig. D.1 seem to indicate that they all have similar outcome in our case, so that the fastest one (precomputed noise) has been used.

- **Milstein method**. This technique is the only one that guarantees convergence, as long as the step is kept low.
- **Runge-Kutta, order 4, with same noise for all stages.**
- **Runge-Kutta, order 4, with different noise at each stage.** A different value of the noise terms was drawn at each substage of the RK method.
- **Higher order method (RADAR5), with precomputed noise.** Finally, our usual integrator is used, with noise added as a precomputed time-dependent function containing Gaussian noise with the desired bandwidth.

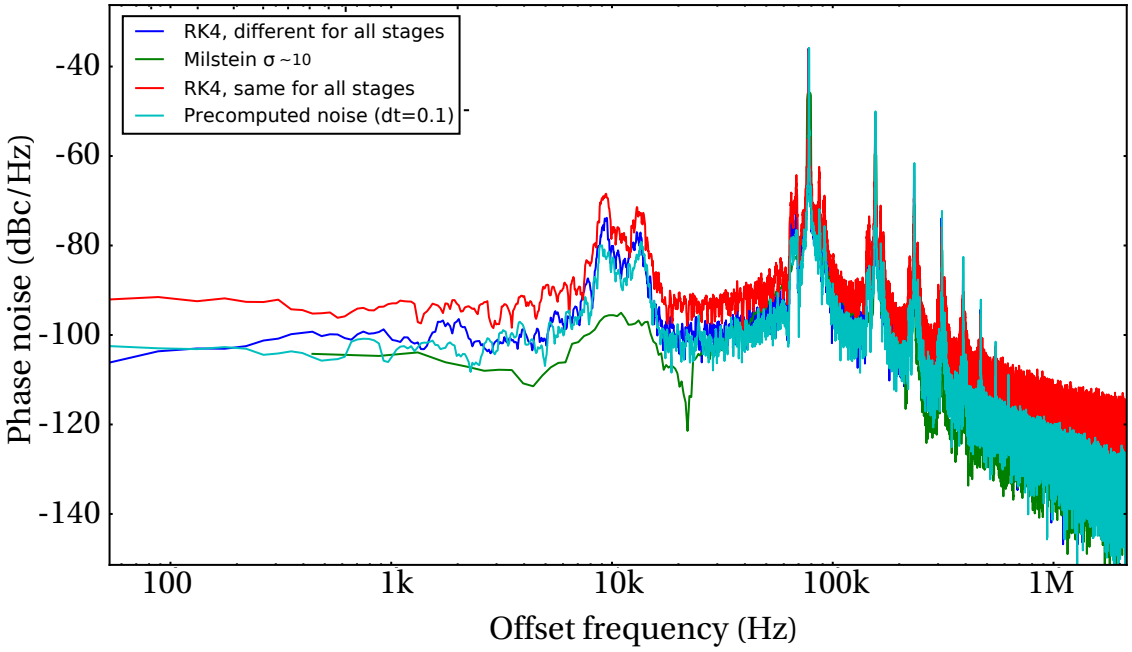

Figure D.1: Comparison of calculated phase noise for different SDE integration methods.

E A Python wrapper for the DDE integrator RADAR5

Available solutions

The integration of delayed differential equations (DDE) has an extra level of complexity compared to ordinary differential equations (ODE). Indeed, it is not sufficient to integrate the evolution at given times. The integrator must also have a way to compute past values at arbitrary times. Indeed, these values are needed to estimate the delayed terms. Thus, at least an interpolation mechanism is needed, but more complex schemes can also be developed.

The most common integrator appears to be the "`dde23`" included in Matlab. As we use Python for numerical computations and treatments, and even though Python-Matlab bridges exist, this would have been a cumbersome solution. The available Python solution seem to be the following:

- `PyDDE` (https://github.com/hensing/PyDDE): only accepts Python functions for right-hand side, so slow performances are to be expected.
- `pydelay` (http://pydelay.sourceforge.net/): has been considered, but as a code generator, it involves lengthy compilation phases at runtime.
- `jitcdde` (https://github.com/neurophysik/jitcdde): looks promising, but only appeared recently. It was not available at the beginning of this work.

We note that all these solvers are based on Bogacki-Shampine method [Shampine01]. Another integration method, based on collocation points and Radau nodes exist, and is particularly well adapted to stiff problems. This is interesting, as we can expect some stiffness in our models. The only implementation seem to be the FORTRAN code `RADAR5` [Guglielmi05], which can be found on http://www.unige.ch/~hairer/software.html.

Features

A Python wrapper was written in C, in order to encapsulate the call to the main integration routine, and the different user-provided callbacks it uses. Compared to most other solutions, it was written with execution speed in mind. Thus, it can accept as right-hand side callback either a Python function, but also compiled code, or C code, which will be compiled internally using the `tcc` embedded compiler (https://bellard.org/tcc/).

Please note that all the capabilities of the FORTRAN code are not wrapped yet. Here is what is currently available:

- Integration of DDE specified by Python function or runtime-compiled C code.
- Constant or time-dependant initial conditions, with interpolation if needed.
- Constant, variable-dependant, or time-dependant delay.

Here is what is not implemented:

- User-specified Jacobian, and delay-components Jacobian.
- Implicit systems and mass matrix
- Advanced breakpoints detection

Installation

The code was published under the name `radar5` version 0.1 on the official PyPi repository: https://pypi.org/project/radar5/. This makes easy installation possible using the command "`pip install radar5`".

On Windows, this will install binary packages, which have been compiled for Python 2.7 and 3.6, in 32 and 64 bits declinations. Please note that they have been built against a recent version of numpy. Updating your version of numpy can be required if you run into the error "`RuntimeError: module compiled against API version 0xc but this version of numpy is 0x9`". If you have installed Python using Anaconda, you can do this by running the "`conda upgrade numpy`" command. If you have only used pip, run "`pip install --upgrade numpy`".

On Linux systems, no binary package are provided, but building is easy as long as you have a FORTRAN compiler. It can be usually obtained under the name `gfortran` on your package manager. Be careful if you have installed numpy by your own means (probably through the system package manager). In that case it is strongly suggested that you do not install a concurrent version through pip. This can be avoided using the following command: "`pip install --no--deps radar5`". This will build the package against the systemwide version of numpy version.

Please note that this program has not been tested on OSX yet.

A very simple example can be run straight away to check if the installation went well:

```
import radar5
radar5.test()
```

If you have matplotlib installed, a window with two oscillating curves should pop up.

ASSOCIATED PUBLICATIONS

The following publications and public communications have been done during this work.

Articles

- A. Thorette, M. Romanelli, M. Brunel, and M. Vallet. "Frequency-Locked Chaotic Opto-RF Oscillator". *Opt. Lett.* **41**.12 (2016), pp. 2839–2842
- M. Romanelli, A. Thorette, M. Brunel, T. Erneux, and M. Vallet. "Excitable-like Chaotic Pulses in the Bounded-Phase Regime of an Opto-Rf Oscillator". *Phys. Rev. A* **94**.4 (2016), p. 043820
- A. Thorette, M. Romanelli, and M. Vallet. "Linewidth Enhancement Factor Measurement Based on FM-Modulated Optical Injection: Application to Rare-Earth-Doped Active Medium". *Opt. Lett.* **42**.8 (2017), pp. 1480–1483
- A. Thorette, M. Romanelli, S. Bouhier, F. Van Dijk, M. Vallet, and M. Alouini. "Hybrid Opto-Electronic Oscillator for Single-Sideband Microwave Photonics". *Electron. Lett.* **54**.11 (2018), pp. 706–708
- A. Thorette, M. Romanelli, and M. Vallet. "Synchronization of Two DFB Lasers Using Frequency-Shifted Feedback for Microwave Photonics". *IEEE J. Quantum Electron.* **accepted** (2019)

Posters

- A. Thorette, M. Romanelli, M. Brunel, and M. Vallet. "Régime chaotique verrouillé en fréquence d'un oscillateur opto-hyper." *19ème Rencontres du Non-Linéaire (RNL) 2016*, Paris, France.
- A. Thorette, M. Romanelli, M. Brunel, and M. Vallet. "Oscillateur opto-RF chaotique verrouillé en fréquence." *COLOQ 2016*, Bordeaux, France.
- A. Thorette, M. Romanelli, M. Brunel, and M. Vallet. "Bounded-phase chaotic dynamics in a vectorial laser." *CLEO/Europe-EQEC 2017*, Munich, Germany.

Conferences talks

- A. Thorette, M. Romanelli, and M. Vallet. "Optical injection method for the measurement of small linewidth enhancement factor in solid-state lasers." *CLEO/Europe-EQEC 2017*, Munich, Germany.
- A. Thorette, P. Primiani, M. Romanelli, M. Alouini, F. Van Dijk, and M. Vallet. "Self-stabilized optoelectronic oscillator using optical feedback on integrated heterodyne source." *CLEO/Europe-EQEC 2017*, Munich, Germany.
- A. Thorette, P. Primiani, M. Romanelli, M. Alouini, F. Van Dijk, and M. Vallet. "Self-stabilization of the beat-note of monolithic DFB lasers for microwave signal generation." *International Symposium on Physics and Applications of Laser Dynamics (IS-PALD) 2017*, Paris, France.
- M. Guionie, A. Thorette, M. Romanelli, A. Carré, G. Loas, E. Pinsard, L. Lablonde, B. Cadier, M. Alouini, M. Vallet, and M. Brunel. "Lasers à fibre bifréquences stabilisés par réinjection optique" *JNOG 2018*, Toulouse, France.
- A. Thorette, M. Romanelli, and M. Vallet. "Synchronisation de deux lasers DFB par réinjection décalée en fréquence, pour applications en photonique micro-onde." *JNOG 2018*, Toulouse, France. *(invited speaker)*

REFERENCES

[Abbott16] B. P. Abbott, R. Abbott, T. D. Abbott, M. R. Abernathy, F. Acernese, K. Ackley, C. Adams, T. Adams, P. Addesso, R. X. Adhikari, et al. "GW151226: Observation of Gravitational Waves from a 22-Solar-Mass Binary Black Hole Coalescence". *Phys. Rev. Lett.* **116** (2016), p. 241103. (↑ pp. 17, 33)

[Abdolvand10] A. Abdolvand, K. G. Wilcox, T. K. Kalkandjiev, and E. U. Rafailov. "Conical Refraction Nd:KGd(WO4)2 Laser". *Opt. Express* **18** (2010), p. 2753. (↑ p. 156)

[Acernese09] F. Acernese et al. "Laser with an In-Loop Relative Frequency Stability of 1.0 × 10 - 21 on a 100-Ms Time Scale for Gravitational-Wave Detection". *Phys. Rev. A* **79** (2009). (↑ p. 17)

[Adler46] R. Adler. "A Study of Locking Phenomena in Oscillators". *Proc. IRE* **34** (1946), pp. 351–357. (↑ p. 34)

[Agrawal02] G. P. Agrawal. *Fiber-Optic Communication Systems*. OCLC: 845720693. New York, NY: Wiley-Interscience, 2002. (↑ pp. 17, 95)

[Agrawal84] G. Agrawal. "Line Narrowing in a Single-Mode Injection Laser Due to External Optical Feedback". *IEEE J. Quantum Electron.* **20** (1984), pp. 468–471. (↑ p. 36)

[Agrawal86] G. P. Agrawal and N. K. Dutta. *Long-Wavelength Semiconductor Lasers*. Van Nostrand Reinhold electrical/computer science and engineering series. New York: Van Nostrand Reinhold, 1986. (↑ pp. 22, 99)

[Agrawal93] G. Agrawal and C. Bowden. "Concept of Linewidth Enhancement Factor in Semiconductor Lasers: Its Usefulness and Limitations". *IEEE Photonics Technol. Lett.* **5** (1993), pp. 640–642. (↑ pp. 26, 29)

[Akiba82] S. Akiba, K. Utaka, K. Sakai, and Y. Matsushima. "Temperature Dependence of Lasing Characteristics of InGaAsP/InP Distributed Feedback Lasers in 1.5 *M*m Range". *Jpn. J. Appl. Phys.* **21** (1982), pp. 1736–1740. (↑ p. 99)

[Alouini01] M. Alouini, B. Benazet, M. Vallet, M. Brunel, P. Di Bin, F. Bretenaker, A. Le Floch, and P. Thony. "Offset Phase Locking of Er,Yb:Glass Laser Eigenstates for RF Photonics Applications". *IEEE Photonics Technol. Lett.* **13** (2001), pp. 367–369. (↑ p. 19)

[Alouini98] M. Alouini, M. Brunel, F. Bretenaker, M. Vallet, and A. Le Floch. "Dual Tunable Wavelength Er,Yb:Glass Laser for Terahertz Beat Frequency Generation". *IEEE Photonics Technol. Lett.* **10** (1998), pp. 1554–1556. (↑ pp. 19, 45)

[Arakawa82] Y. Arakawa and H. Sakaki. "Multidimensional Quantum Well Laser and Temperature Dependence of Its Threshold Current". *Appl. Phys. Lett.* **40** (1982), pp. 939–941. (↑ p. 95)

[Arecchi65] F. Arecchi and R. Bonifacio. "Theory of Optical Maser Amplifiers". *IEEE J. Quantum Electron.* **1** (1965), pp. 169–178. (↑ p. 22)

[Armand69] M. Armand. "On the Output Spectrum of Unlocked Driven Oscillators". *Proc. IEEE* **57** (1969), pp. 798–799. (↑ p. 34)

[Audo18] K. Audo and M. Alouini. "Intensity Noise Cancellation in Solid-State Laser at 15 *M*m Using SHG Depletion as a Buffer Reservoir". *Appl. Opt.* **57** (2018), p. 1524. (↑ p. 28)

[Baili09] G. Baili, L. Morvan, M. Alouini, D. Dolfi, F. Bretenaker, I. Sagnes, and A. Garnache. "Experimental Demonstration of a Tunable Dual-Frequency Semiconductor Laser Free of Relaxation Oscillations". *Opt. Lett.* **34** (2009), pp. 3421–3423. (↑ p. 45)

[Barillet96] R. Barillet, A. Brillet, R. Chiche, F. Cleva, L. Latrach, and C. N. Man. "An Injection-Locked Nd:YAG Laser for the Interferometric Detection of Gravitational Waves". *Meas. Sci. Technol.* **7** (1996), pp. 162–169. (↑ p. 33)

[Barland16] S. Barland, M. Giudici, J. Javaloyes, and G. Tissoni. "Localized States in Semiconductor: Microcavities, from Transverse to Longitudinal Structures and Delayed Systems". *Nonlinear Optical Cavity Dynamics: From Microresonators to Fiber Lasers*. Wiley, 2016, pp. 77–106. (↑ p. 157)

[Barois14] T. Barois, S. Perisanu, P. Vincent, S. T. Purcell, and A. Ayari. "Frequency Modulated Self-Oscillation and Phase Inertia in a Synchronized Nanowire Mechanical Resonator". *New J. Phys.* **16** (2014), p. 083009. (↑ p. 61)

[Basov61] N. Basov, O. Krokhin, and Y. M. Popov. "Production of Negative Temperature States in Pn Junctions of Degenerate Semiconductors". *Sov Phys JETP* **13** (1961), pp. 1320–1321. (↑ p. 17)

[Bielawski92] S. Bielawski, D. Derozier, and P. Glorieux. "Antiphase Dynamics and Polarization Effects in the Nd-Doped Fiber Laser". *Phys. Rev. A* **46** (1992), p. 2811. (↑ p. 52)

[Blin00] S. Blin, G. M. Stéphan, R. Gabet, P. Besnard, and D. Kilper. "Amplification Process in a Laser Injected by a Narrow Band Weak Signal". *Europhys. Lett. EPL* **52** (2000), pp. 60–65. (↑ p. 34)

[Blin03] S. Blin, C. Guignard, P. Besnard, R. Gabet, G. M. Stéphan, and M. Bondiou. "Phase and Spectral Properties of Optically Injected Semiconductor Lasers". *Comptes Rendus Phys.* **4** (2003), pp. 687–699. (↑ p. 34)

[Blin17] S. Blin et al. "Coherent and Tunable THz Emission Driven by an Integrated III–V Semiconductor Laser". *IEEE J. Sel. Top. Quantum Electron.* **23** (2017), pp. 1–11. (↑ p. 44)

[Bogatov73] A. Bogatov, P. Eliseev, L. Ivanov, A. Logginov, M. Manko, and K. Senatorov. "Study of the Single-Mode Injection Laser". *IEEE J. Quantum Electron.* **9** (1973), pp. 392–394. (↑ p. 36)

[Bondu96] F. Bondu, P. Fritschel, C. N. Man, and A. Brillet. "Ultrahigh-Spectral-Purity Laser for the VIRGO Experiment". *Opt. Lett.* **21** (1996), pp. 582–584. (↑ p. 17)

[Braza90] P. A. Braza and T. Erneux. "Constant Phase, Phase Drift, and Phase Entrainment in Lasers with an Injected Signal". *Phys. Rev. A* **41** (1990), pp. 6470–6479. (↑ p. 60)

[Bretenaker90] F. Bretenaker and A. Le Floch. "The Dynamics of Spatially-Resolved Laser Eigenstates". *IEEE J. Quantum Electron.* **26** (Sept./1990), pp. 1451–1454. (↑ pp. 19, 44)

[Bretenaker91] F. Bretenaker and A. Le Floch. "Laser Eigenstates in the Framework of a Spatially Generalized Jones Matrix Formalism". *J. Opt. Soc. Am. B* **8** (1991), p. 230. (↑ p. 48)

[Broom70] R. Broom, E. Mohn, C. Risch, and R. Salathe. "Microwave Self-Modulation of a Diode Laser Coupled to an External Cavity". *IEEE J. Quantum Electron.* **6** (1970), pp. 328–334. (↑ p. 36)

[Brunel04] M. Brunel, N. D. Lai, M. Vallet, A. Le Floch, F. Bretenaker, L. Morvan, D. Dolfi, J.-P. Huignard, S. Blanc, and T. Merlet. "Generation of Tunable High-Purity Microwave and Terahertz Signals by Two-Frequency Solid State Lasers". *Proc. SPIE 5466*. Ed. by A. Stohr, D. Jager, and S. Iezekiel. 2004, p. 131. (↑ p. 19)

[Brunel05] M. Brunel, A. Amon, and M. Vallet. "Dual-Polarization Microchip Laser at 1553μm". *Opt. Lett.* **30** (2005), p. 2418. (↑ p. 45)

[Brunel16] M. Brunel, M. Romanelli, and M. Vallet. "Synchronization in Vectorial Solid-State Lasers". *Nonlinear Optical Cavity Dynamics: From Microresonators to Fiber Lasers*. Ed. by P. Grelu. Wiley, 2016, pp. 317–346. (↑ p. 47)

[Brunel97a] M. Brunel, F. Bretenaker, and A. Le Floch. "Tunable Optical Microwave Source Using Spatially Resolved Laser Eigenstates". *Opt. Lett.* **22** (1997), p. 384. (↑ p. 45)

[Brunel97b] M. Brunel, M. Vallet, A. Le Floch, and F. Bretenaker. "Differential Measurement of the Coupling Constant between Laser Eigenstates". *Appl. Phys. Lett.* **70** (1997), pp. 2070–2072. (↑ p. 55)

[Buczek73] C. Buczek, R. Freiberg, and M. Skolnick. "Laser Injection Locking". *Proc. IEEE* **61** (1973), pp. 1411–1431. (↑ p. 32)

[Bueno17] J. Bueno, D. Brunner, M. C. Soriano, and I. Fischer. "Conditions for Reservoir Computing Performance Using Semiconductor Lasers with Delayed Optical Feedback". *Opt. Express* **25** (2017), p. 2401. (↑ p. 37)

[Butcher98] P. N. Butcher and D. Cotter. *The Elements of Nonlinear Optics*. Reprinted. Cambridge studies in modern optics. OCLC: 245799372. Cambridge: Cambridge University Press, 1998. (↑ p. 24)

[Chakraborty88] T. Chakraborty and R. H. Rand. "The Transition from Phase Locking to Drift in a System of Two Weakly Coupled van Der Pol Oscillators". *Int. J. Non-Linear Mech.* **23** (1988), pp. 369–376. (↑ p. 61)

[Chartier00] T. Chartier, F. Sanchez, and G. Stéphan. "General Model for a Multimode Nd-Doped Fiber Laser. I: Construction of the Model". *Appl. Phys. B Lasers Opt.* **70** (2000), pp. 23–31. (↑ pp. 23, 52)

[Chinone78] N. Chinone, K. Aiki, and R. Ito. "Stabilization of Semiconductor Laser Outputs by a Mirror Close to a Laser Facet". *Appl. Phys. Lett.* **33** (1978), pp. 990–992. (↑ p. 36)

[Chlouverakis03] K. Chlouverakis, K. Al-Aswad, I. Henning, and M. Adams. "Determining Laser Linewidth Parameter from Hopf Bifurcation Minimum in Lasers Subject to Optical Injection". *Electron. Lett.* **39** (2003), p. 1185. (↑ p. 31)

[Chow83] W. Chow. "Theory of Line Narrowing and Frequency Selection in an Injection Locked Laser". *IEEE J. Quantum Electron.* **19** (1983), pp. 243–249. (↑ p. 30)

[Chuang14] C.-F. Chuang, Y.-H. Liao, C.-H. Lin, S.-Y. Chen, F. Grillot, and F.-Y. Lin. "Linewidth Enhancement Factor in Semiconductor Lasers Subject to Various External Optical Feedback Conditions". *Opt. Express* **22** (2014), p. 5651. (↑ p. 30)

[Czarny04] R. Czarny, M. Alouini, C. Larat, M. Krakowski, and D. Dolfi. "THz-Dual-Frequency Yb3+:KGd(WO4)2 Laser for Continuous Wave THz Generation through Photomixing". *Electron. Lett.* **40** (2004), p. 942. (↑ p. 45)

[Dagens05] B. Dagens, A. Markus, J. Chen, J.-G. Provost, D. Make, O. Le Gouezigou, J. Landreau, A. Fiore, and B. Thedrez. "Giant Linewidth Enhancement Factor and Purely Frequency Modulated Emission from Quantum Dot Laser". *Electron. Lett.* **41** (2005), p. 323. (↑ p. 30)

[Dagens08] B. Dagens et al. "High Bandwidth Operation of Directly Modulated Laser Based on Quantum-Dash InAs–InP Material at 1.55 μm". *IEEE Photonics Technol. Lett.* **20** (2008), pp. 903–905. (↑ pp. 96, 97)

[Danion14] G. Danion, C. Hamel, L. Frein, F. Bondu, G. Loas, and M. Alouini. "Dual Frequency Laser with Two Continuously and Widely Tunable Frequencies for Optical Referencing of GHz to THz Beatnotes". *Opt. Express* **22** (2014), pp. 17673–17678. (↑ pp. 19, 45, 94)

[Davies08] A. G. Davies, A. D. Burnett, W. Fan, E. H. Linfield, and J. E. Cunningham. "Terahertz Spectroscopy of Explosives and Drugs". *Mater. Today* **11** (2008), pp. 18–26. (↑ p. 18)

[Day92] T. Day, E. Gustafson, and R. Byer. "Sub-Hertz Relative Frequency Stabilization of Two-Diode Laser-Pumped Nd:YAG Lasers Locked to a Fabry-Perot Interferometer". *IEEE J. Quantum Electron.* **28** (1992), pp. 1106–1117. (↑ p. 19)

[de L Kronig26] R. de L. Kronig. "On the Theory of Dispersion of X-Rays". *J. Opt. Soc. Am.* **12** (1926), p. 547. (↑ p. 29)

[Dellunde95] J. Dellunde, C. R. Mirasso, M. C. Torrent, J. M. Sancho, and E. Hernández-García. "Transient Dynamics of a Single-Mode Semiconductor Laser Subjected to Both Optical Feedback and External Light Injection". *Opt. Quantum Electron.* **27** (1995), pp. 755–760. (↑ p. 39)

[Doedel12] E. J. Doedel and B. E. Oldeman. *AUTO-07P: Continuation and Bifurcatio Software for Ordinary Differential Equations*. 2012. (↑ p. 35)

[Dong17] J.-X. Dong, J.-P. Zhuang, and S.-C. Chan. "Tunable Switching between Stable and Periodic States in a Semiconductor Laser with Feedback". *Opt. Lett.* **42** (2017), pp. 4291–4294. (↑ p. 121)

[Drever83] R. W. P. Drever, J. L. Hall, F. V. Kowalski, J. Hough, G. M. Ford, A. J. Munley, and H. Ward. "Laser Phase and Frequency Stabilization Using an Optical Resonator". *Appl. Phys. B Photophysics Laser Chem.* **31** (1983), pp. 97–105. (↑ pp. 18, 43)

[Dumont14] P. Dumont et al. "Low-Noise Dual-Frequency Laser for Compact Cs Atomic Clocks". *J. Light. Technol.* **32** (2014), pp. 3817–3823. (↑ pp. 24, 45)

[Einstein17] A. Einstein. "Zur Quantentheorie Der Strahlung". *Phys. Z.* **18** (1917), pp. 121–128. (↑ p. 17)

[Eliyahu03] D. Eliyahu and L. Maleki. "Tunable, Ultra-Low Phase Noise YIG Based Opto-Electronic Oscillator" (2003), p. 3. (↑ p. 136)

[Engelborghs02] K. Engelborghs, T. Luzyanina, and D. Roose. "Numerical Bifurcation Analysis of Delay Differential Equations Using DDE-BIFTOOL". *ACM Trans. Math. Softw.* **28** (2002), pp. 1–21. (↑ p. 38)

[Erneux10] T. Erneux and P. Glorieux. *Laser Dynamics*. Cambridge: Cambridge University Press, 2010. (↑ pp. 19, 25, 28, 53, 55, 112)

[Fade12] J. Fade and M. Alouini. "Depolarization Remote Sensing by Orthogonality Breaking". *Phys. Rev. Lett.* **109** (2012). (↑ p. 45)

[Farinas95] A. D. Farinas, E. K. Gustafson, and R. L. Byer. "Frequency and Intensity Noise in an Injection-Locked, Solid-State Laser". *J. Opt. Soc. Am. B* **12** (1995), p. 328. (↑ p. 33)

[Federici10] J. Federici and L. Moeller. "Review of Terahertz and Subterahertz Wireless Communications". *J. Appl. Phys.* **107** (2010), p. 111101. (↑ p. 18)

[Flunkert09] V. Flunkert, O. D'Huys, J. Danckaert, I. Fischer, and E. Schöll. "Bubbling in Delay-Coupled Lasers". *Phys. Rev. E* **79** (2009). (↑ p. 115)

[Flunkert11] V. Flunkert. "Delayed Complex Systems and Applications to Lasers". PhD thesis. Teknische Universität Berlin II, 2011. (↑ pp. 115, 117)

[Fordell05] T. Fordell, S. Valling, and Å. M. Lindberg. "Modulation and the Linewidth Enhancement Factor of a Diode-Pumped Nd: YVO 4 Laser". *Opt. Lett.* **30** (2005), pp. 3036–3038. (↑ pp. 31, 78, 89, 164)

[Fortier11] T. M. Fortier et al. "Generation of Ultrastable Microwaves via Optical Frequency Division". *Nature Photonics* **5** (2011), p. 425. (↑ p. 19)

[Foster07] S. Foster. "Complex Susceptibility of Saturated Erbium-Doped Fiber Lasers and Amplifiers". *IEEE Photonics Technol. Lett.* **19** (2007), pp. 895–897. (↑ p. 93)

[Garbin17] B. Garbin, A. Dolcemascolo, F. Prati, J. Javaloyes, G. Tissoni, and S. Barland. "Refractory Period of an Excitable Semiconductor Laser with Optical Injection". *Phys. Rev. E* **95** (2017). (↑ p. 75)

[Gliese92] U. Gliese, T. Nielsen, M. Bruun, E. Lintz Christensen, K. Stubkjaer, S. Lindgren, and B. Broberg. "A Wideband Heterodyne Optical Phase-Locked Loop for Generation of 3-18 GHz Microwave Carriers". *IEEE Photonics Technol. Lett.* **4** (1992), pp. 936–938. (↑ p. 43)

[Gordon55] J. P. Gordon, H. J. Zeiger, and C. H. Townes. "The Maser—New Type of Microwave Amplifier, Frequency Standard, and Spectrometer". *Phys. Rev.* **99** (1955), pp. 1264–1274. (↑ p. 17)

[Green10] K. Green. "Bifurcation Analysis of Delay-Induced Periodic Oscillations". *J. Comput. Appl. Math.* **233** (2010), pp. 2405–2412. (↑ pp. 38, 122)

[Grillot11] F. Grillot, N. A. Naderi, J. B. Wright, R. Raghunathan, M. T. Crowley, and L. F. Lester. "A Dual-Mode Quantum Dot Laser Operating in the Excited State". *Appl. Phys. Lett.* **99** (2011), p. 231110. (↑ p. 43)

[Gu98] P. Gu, M. Tani, M. Hyodo, K. Sakai, and T. Hidaka. "Generation of Cw-Terahertz Radiation Using a Two-Longitudinal-Mode Laser Diode". *Jpn. J. Appl. Phys.* **37** (1998), pp. L976–L978. (↑ p. 43)

[Guglielmi05] N. Guglielmi and E. Hairer. *Users' Guide for the Code RADAR5-Version 2.1*. Tech. rep. Università dell'Aquila, Italy, 2005. (↑ pp. 71, 122, 171)

[Guionie18a] M. Guionie et al. "Beat Note Stabilization in Dual-Polarization DFB Fiber Lasers by an Optical Phase-Locked Loop". *Opt. Express* **26** (2018), pp. 3483–3488. (↑ pp. 90, 91, 92)

[Guionie18b] M. Guionie et al. "Lasers à fibre bifréquences stabilisés par réinjection optique". *Journées Nationales d'Optique Guidée (JNOG 2018)*. Toulouse, France, 2018, p. 4. (↑ pp. 92, 156)

[Haegeman02] B. Haegeman, K. Engelborghs, D. Roose, D. Pieroux, and T. Erneux. "Stability and Rupture of Bifurcation Bridges in Semiconductor Lasers Subject to Optical Feedback". *Phys. Rev. E* **66** (2002). (↑ p. 37)

[Hakki75] B. W. Hakki and T. L. Paoli. "Gain Spectra in GaAs Double-heterostructure Injection Lasers". *J. Appl. Phys.* **46** (1975), p. 1299. (↑ p. 30)

[Hall62] R. N. Hall, G. E. Fenner, J. D. Kingsley, T. J. Soltys, and R. O. Carlson. "Coherent Light Emission From GaAs Junctions". *Phys. Rev. Lett.* **9** (1962), pp. 366–368. (↑ p. 17)

[Hallal16] A. Hallal, S. Bouhier, and F. Bondu. "Frequency Stabilization of a Laser Tunable Over 1 THz in an All Fibered System". *IEEE Photonics Technol. Lett.* **28** (2016), pp. 1249–1252. (↑ pp. 19, 43)

[Halton64] J. H. Halton. "Algorithm 247: Radical-Inverse Quasi-Random Point Sequence". *Commun. ACM* **7** (1964), pp. 701–702. (↑ p. 126)

[Harder83] C. Harder, K. Vahala, and A. Yariv. "Measurement of the Linewidth Enhancement Factor α of Semiconductor Lasers". *Appl. Phys. Lett.* **42** (1983), pp. 328–330. (↑ p. 31)

[Haug67] H. Haug and H. Haken. "Theory of Noise in Semiconductor Laser Emission". *Z. Für Phys. Hadrons Nucl.* **204** (1967), pp. 262–275. (↑ p. 29)

[Henry82] C. Henry. "Theory of the Linewidth of Semiconductor Lasers". *IEEE J. Quantum Electron.* **18** (1982), pp. 259–264. (↑ pp. 26, 29)

[Henry86] C. Henry and R. Kazarinov. "Instability of Semiconductor Lasers Due to Optical Feedback from Distant Reflectors". *IEEE J. Quantum Electron.* **22** (1986), pp. 294–301. (↑ p. 19)

[Hicke11] K. Hicke, O. D'Huys, V. Flunkert, E. Schöll, J. Danckaert, and I. Fischer. "Mismatch and Synchronization: Influence of Asymmetries in Systems of Two Delay-Coupled Lasers". *Phys. Rev. E* **83** (2011), p. 056211. (↑ p. 115)

[Hilsum63] C. Hilsum and P. G. R. King. "Some Demonstrations of the Properties of Optical Masers". *Contemp. Phys.* **4** (1963), pp. 435–444. (↑ p. 36)

[Hodgkin52] A. L. Hodgkin and A. F. Huxley. "A Quantitative Description of Membrane Current and Its Application to Conduction and Excitation in Nerve". *J. Physiol.* **117** (1952), pp. 500–544. (↑ p. 74)

[Honeycutt92] R. L. Honeycutt. "Stochastic Runge-Kutta Algorithms. i. White Noise". *Phys. Rev. A* **45** (1992), p. 600. (↑ p. 169)

[Hugon11] O. Hugon, F. Joud, E. Lacot, O. Jacquin, and H. Guillet de Chatellus. "Coherent Microscopy by Laser Optical Feedback Imaging (LOFI) Technique". *Ultramicroscopy* **111** (2011), pp. 1557–1563. (↑ pp. 37, 62)

[Hui90] R. Hui, A. Mecozzi, A. D'ottavi, and P. Spano. "Novel Measurement Technique of α Factor in DFB Semiconductor Lasers by Injection Locking". *Electron. Lett.* **26** (1990), pp. 997–998. (↑ pp. 31, 104, 108)

[Hung15] Y.-H. Hung and S.-K. Hwang. "Photonic Microwave Stabilization for Period-One Nonlinear Dynamics of Semiconductor Lasers Using Optical Modulation Sideband Injection Locking". *Opt. Express* **23** (2015), pp. 6520–6532. (↑ p. 34)

[Huygens90] C. Huygens. *Correspondance*. **3**. M. Nijhoff, 1890. (↑ p. 32)

[Iiyama92] K. Iiyama, K.-i. Hayashi, and Y. Ida. "Simple Method for Measuring the Linewidth Enhancement Factor of Semiconductor Lasers by Optical Injection Locking". *Opt. Lett.* **17** (1992), p. 1128. (↑ p. 31)

[Ilchenko08] V. S. Ilchenko, J. Byrd, A. A. Savchenkov, A. B. Matsko, D. Seidel, and L. Maleki. "Miniature Oscillators Based on Optical Whispering Gallery Mode Resonators". IEEE, 2008, pp. 305–308. (↑ p. 135)

[Izhikevich07] E. M. Izhikevich. *Dynamical Systems in Neuroscience: The Geometry of Excitability and Bursting*. Computational neuroscience. OCLC: ocm65400606. Cambridge, Mass: MIT Press, 2007. (↑ p. 74)

[Jones41] R. C. Jones. "A New Calculus for the Treatment of Optical SystemsI Description and Discussion of the Calculus". *J. Opt. Soc. Am.* **31** (1941), p. 488. (↑ pp. 48, 159)

[Kamath97] K. Kamath, J. Phillips, H. Jiang, J. Singh, and P. Bhattacharya. "Small-Signal Modulation and Differential Gain of Single-Mode Self-Organized In0.4Ga0.6As/GaAs Quantum Dot Lasers". *Appl. Phys. Lett.* **70** (1997), pp. 2952–2953. (↑ p. 96)

[Kane05] D. M. Kane and K. A. Shore, eds. *Unlocking Dynamical Diversity: Optical Feedback Effects on Semiconductor Lasers*. Chichester, UK: John Wiley & Sons, Ltd, 2005. (↑ p. 37)

[Kastler70] A. Kastler. "Champ Lumineux Stationnaire à Structure Hélicoïdale Dans Une Cavité Laser. Possibilité d'imprimer Cette Structure Hélicoïdale à Un Milieu Matériel". *Compte-Rendu L'Académie Sci. B* **271** (1970), p. 999. (↑ pp. 160, 161)

[Kazarinov74] R. F. Kazarinov and R. A. Suris. "Heterodyne Reception of Light by an Injection Laser". *J. Exp. Theor. Phys.* **39** (1974), p. 522. (↑ p. 108)

[Kéfélian09] F. Kéfélian, H. Jiang, P. Lemonde, and G. Santarelli. "Ultralow-Frequency-Noise Stabilization of a Laser by Locking to an Optical Fiber-Delay Line". *Opt. Lett.* **34** (2009), p. 914. (↑ p. 18)

[Kelleher09] B. Kelleher et al. "Excitable Phase Slips in an Injection-Locked Single-Mode Quantum-Dot Laser". *Opt. Lett.* **34** (2009), p. 440. (↑ p. 75)

[Kelleher10] B. Kelleher, D. Goulding, B. B. Pascual, S. P. Hegarty, and G. Huyet. "Phasor Plots in Optical Injection Experiments". *Eur. Phys. J. D* **58** (2010), pp. 175–179. (↑ p. 60)

[Kelleher12] B. Kelleher, D. Goulding, B. B. Pascual, S. P. Hegarty, and G. Huyet. "Bounded Phase Phenomena in the Optically Injected Laser". *Phys. Rev. E* **85** (2012), p. 046212. (↑ p. 61)

[Kervella14] G. Kervella, J. Maxin, M. Faugeron, P. Berger, H. Lanctuit, G. Pillet, L. Morvan, F. van Dijk, and D. Dolfi. "Laser Sources for Microwave to Millimeter-Wave Applications". *Photonics Res.* **2** (2014), B70–B79. (↑ p. 98)

[Kervevan07] L. Kervevan, H. Gilles, S. Girard, and M. Laroche. "Beat-Note Jitter Suppression in a Dual-Frequency Laser Using Optical Feedback". *Opt. Lett.* **32** (2007), pp. 1099–1101. (↑ pp. 19, 46, 93)

[Kikuchi85] K. Kikuchi and T. Okoshi. "Measurement of FM Noise, AM Noise, and Field Spectra of 1.3 *M*m InGaAsP DFB Lasers and Determination of the Linewidth Enhancement Factor". *IEEE J. Quantum Electron.* **21** (1985), pp. 1814–1818. (↑ pp. 30, 31, 109)

[Kim06] D. I. Kim, D.-S. Lee, Y.-J. Park, G. U. Kim, and C.-M. Kim. "Phase Synchronization of Chaotic Lasers". *Opt. Express* **14** (2006), pp. 702–709. (↑ p. 34)

[Koechner06] W. Koechner. *Solid-State Laser Engineering*. **1**. Springer Series in Optical Sciences. New York, NY: Springer New York, 2006. (↑ p. 22)

[Kogelnik66] H. Kogelnik and T. Li. "Laser Beams and Resonators". *Appl. Opt.* **5** (1966), p. 1550. (↑ p. 50)

[Kogelnik72] H. Kogelnik and C. V. Shank. "Coupled-Wave Theory of Distributed Feedback Lasers". *J. Appl. Phys.* **43** (1972), pp. 2327–2335. (↑ pp. 97, 102)

[Kronauer82] R. E. Kronauer, C. A. Czeisler, S. F. Pilato, M. C. Moore-Ede, and E. D. Weitzman. "Mathematical Model of the Human Circadian System with Two Interacting Oscillators". *Am. J. Physiol.-Regul. Integr. Comp. Physiol.* **242** (1982), R3–R17. (↑ p. 61)

[Kushida68] T. Kushida, H. M. Marcos, and J. E. Geusic. "Laser Transition Cross Section and Fluorescence Branching Ratio for Nd 3 + in Yttrium Aluminum Garnet". *Phys. Rev.* **167** (1968), pp. 289–291. (↑ p. 163)

[Kuznetsov04] Y. A. Kuznetsov. *Elements of Applied Bifurcation Theory*. 3rd ed. Applied mathematical sciences. New York: Springer, 2004. (↑ p. 35)

[Lacot96] E. Lacot and F. Stoeckel. "Nonlinear Mode Coupling in a Microchip Laser". *JOSA B* **13** (1996), pp. 2034–2040. (↑ p. 56)

[Lai03] N. D. Lai, M. Brunel, and F. Bretenaker. "Green Two-Frequency Pulsed Laser: Intracavity Doubling of Helicoidal Eigenstates". *J. Opt. Soc. Am. B* **20** (2003), p. 662. (↑ p. 45)

[Lamb64] W. E. Lamb. "Theory of an Optical Maser". *Phys. Rev.* **134** (1964), A1429–A1450. (↑ p. 22)

[Lang80] R. Lang and K. Kobayashi. "External Optical Feedback Effects on Semiconductor Injection Laser Properties". *IEEE J. Quantum Electron.* **16** (1980), pp. 347–355. (↑ pp. 30, 37)

[Lax67] M. Lax. "Classical Noise. V. Noise in Self-Sustained Oscillators". *Phys. Rev.* **160** (1967), pp. 290–307. (↑ p. 29)

[Le Floch73] A. Le Floch and G. Stephan. "La Condition de Résonance Dans Les Lasers Anisotropes Contenant Des Lames Biréfringentes". *CR Acad Sci B* **277** (1973), pp. 265–268. (↑ p. 160)

[Lee08] K.-H. Lee, J.-Y. Kim, and W.-Y. Choi. "Injection-Locked Hybrid Optoelectronic Oscillators for Single-Mode Oscillation". *IEEE Photonics Technol. Lett.* **20** (2008), pp. 1645–1647. (↑ p. 143)

[Leeson16] D. B. Leeson. "Oscillator Phase Noise: A 50-Year Review". *IEEE Trans. Ultrason. Ferroelectr. Freq. Control* **63** (2016), pp. 1208–1225. (↑ p. 41)

[Leeson66] D. Leeson. "A Simple Model of Feedback Oscillator Noise Spectrum". *Proc. IEEE* **54** (1966), pp. 329–330. (↑ p. 137)

[Lelarge07] F. Lelarge et al. "Recent Advances on InAs/InP Quantum Dash Based Semiconductor Lasers and Optical Amplifiers Operating at 1.55 μm". *IEEE J. Sel. Top. Quantum Electron.* **13** (2007), pp. 111–124. (↑ pp. 96, 97, 102)

[Lelievre17] O. Lelievre et al. "A Model for Designing Ultralow Noise Single- and Dual-Loop 10-GHz Optoelectronic Oscillators". *J. Light. Technol.* **35** (2017), pp. 4366–4374. (↑ p. 144)

[Leng06] J. Leng, Y. Lai, W. Zhang, and J. Williams. "A New Method for Microwave Generation and Data Transmission Using DFB Laser Based on Fiber Bragg Gratings". *IEEE Photonics Technol. Lett.* **18** (2006), pp. 1729–1731. (↑ p. 89)

[Lenstra91] D. Lenstra. "Statistical Theory of the Multistable External-Feedback Laser". *Opt. Commun.* **81** (1991), pp. 209–214. (↑ p. 124)

[Levy09] E. C. Levy, M. Horowitz, and C. R. Menyuk. "Modeling Optoelectronic Oscillators". *J. Opt. Soc. Am. B* **26** (2009), pp. 148–158. (↑ p. 149)

[Li13] L. K. Li and M. P. Juniper. "Phase Trapping and Slipping in a Forced Hydrodynamically Self-Excited Jet". *J. Fluid Mech.* **735** (2013), R5. (↑ p. 61)

[Li14] W. Li, F. Kong, and J. Yao. "Stable and Frequency-Hopping-Free Microwave Generation Based on a Mutually Injection-Locked Optoelectronic Oscillator and a Dual-Wavelength Single-Longitudinal-Mode Fiber Laser". *J. Light. Technol.* **32** (2014), pp. 3572–3577. (↑ p. 45)

[Li97] S. Li, H. Ding, and K. Chan. "Erbium-Doped Fibre Lasers for Dual Wavelength Operation". *Electron. Lett.* **33** (1997), p. 52. (↑ p. 45)

[Liang14] Y. Liang, L. Jin, L. Cheng, and B.-O. Guan. "Stabilization of Microwave Signal Generated by a Dual-Polarization DBR Fiber Laser via Optical Feedback". *Opt. Express* **22** (2014), p. 29356. (↑ p. 90)

[Liao13] Y.-H. Liao and F.-Y. Lin. "Dynamical Characteristics and Their Applications of Semiconductor Lasers Subject to Both Optical Injection and Optical Feedback". *Opt. Express* **21** (2013), pp. 23568–23578. (↑ p. 39)

[Lin04a] F.-Y. Lin and J.-M. Liu. "Chaotic Radar Using Nonlinear Laser Dynamics". *Quantum Electron. IEEE J. Of* **40** (2004), pp. 815–820. (↑ p. 73)

[Lin04b] F.-Y. Lin and J.-M. Liu. "Chaotic Lidar". *IEEE J. Sel. Top. Quantum Electron.* **10** (2004), pp. 991–997. (↑ pp. 73, 156)

[Lindner04] B. Lindner. "Effects of Noise in Excitable Systems". *Phys. Rep.* **392** (2004), pp. 321–424. (↑ p. 74)

[Link16] S. M. Link, A. Klenner, and U. Keller. "Dual-Comb Modelocked Lasers: Semiconductor Saturable Absorber Mirror Decouples Noise Stabilization". *Opt. Express* **24** (2016), p. 1889. (↑ p. 156)

[Link17] S. M. Link, D. J. H. C. Maas, D. Waldburger, and U. Keller. "Dual-Comb Spectroscopy of Water Vapor with a Free-Running Semiconductor Disk Laser". *Science* **356** (2017), pp. 1164–1168. (↑ p. 45)

[Loas14] G. Loas, M. Romanelli, and M. Alouini. "Dual-Frequency 780-Nm Ti: Sa Laser for High Spectral Purity Tunable CW THz Generation". *IEEE Photonics Technol. Lett.* **26** (2014), pp. 1518–1521. (↑ p. 45)

[Loh97] W. Loh, J. de Sandro, G. Cowle, B. Samson, and A. Ellis. "40 GHz Optical-Millimetre Wave Generation with a Dual Polarisation Distributed Feedback Fibre Laser". *Electron. Lett.* **33** (1997), p. 594. (↑ pp. 45, 89)

[Lugiato15] L. Lugiato, F. Prati, and M. Brambilla. *Nonlinear Optical Systems*. Cambridge: Cambridge University Press, 2015. (↑ p. 22)

[Maiman60] T. H. Maiman. "Stimulated Optical Radiation in Ruby". *Nature* **187** (1960), pp. 493–494. (↑ p. 17)

[Maleki11] L. Maleki. "The Optoelectronic Oscillator". *Nat. Photonics* **5** (2011), p. 728. (↑ p. 136)

[Maxin11] J. Maxin, S. Molin, G. Pillet, L. Morvan, A. Mugnier, D. Pureur, and D. Dolfi. "Dual-Frequency Distributed Feedback Fibre Laser for Microwave Signals Generation". *Electron. Lett.* **47** (2011), pp. 816–818. (↑ p. 89)

[McKay09] A. McKay and J. Dawes. "Tunable Terahertz Signals Using a Helicoidally Polarized Ceramic Microchip Laser". *IEEE Photonics Technol. Lett.* **21** (2009), pp. 480–482. (↑ p. 45)

[McNeil15] B. McNeil. "Due Credit for Maxwell–Bloch Equations". *Nat. Photonics* **9** (2015), pp. 207–207. (↑ p. 22)

[Miles80] R. O. Miles, A. Dandridge, A. B. Tveten, H. F. Taylor, and T. G. Giallorenzi. "Feedback-induced Line Broadening in Cw Channel-substrate Planar Laser Diodes". *Appl. Phys. Lett.* **37** (1980), pp. 990–992. (↑ p. 36)

[Mogensen85] F. Mogensen, H. Olesen, and G. Jacobsen. "Locking Conditions and Stability Properties for a Semiconductor Laser with External Light Injection". *IEEE J. Quantum Electron.* **21** (1985), pp. 784–793. (↑ p. 107)

[Moller94] B. Moller, E. Zeeb, U. Fiedler, T. Hackbarth, and K. J. Ebeling. "Linewidth Enhancement Factor of Vertical-Cavity Surface-Emitting Laser Diodes". *IEEE Photonics Technol. Lett.* **6** (1994), pp. 921–923. (↑ p. 30)

[Montebugnoli05] S. Montebugnoli, M. Boschi, F. Perini, P. Faccin, G. Brunori, and E. Pirazzini. "Large Antenna Array Remoting Using Radio-over-Fiber Techniques for Radio Astronomical Application". *Microw. Opt. Technol. Lett.* **46** (2005), pp. 48–54. (↑ p. 18)

[Moreau06] G. Moreau, K. Merghem, A. Martinez, F. Lelarge, and A. Ramdane. "Low Linewidth Enhancement Factor (αH 0.5) of 9- Layer InAs/InP Quantum Dash Lasers Emitting at 1.55 Mm". *2006 International Conference on Indium Phosphide and Related Materials Conference Proceedings*. IEEE, 2006, pp. 116–118. (↑ pp. 30, 109)

[Morvan02] L. Morvan, N. D. Lai, D. Dolfi, J.-P. Huignard, M. Brunel, F. Bretenaker, and A. Le Floch. "Building Blocks for a Two-Frequency Laser Lidar-Radar: A Preliminary Study". *Appl. Opt.* **41** (2002), p. 5702. (↑ p. 45)

[Moses76] E. I. Moses, J. J. Turner, and C. L. Tang. "Mode Locking of Laser Oscillators by Injection-locking". *Appl. Phys. Lett.* **28** (1976), pp. 258–260. (↑ p. 34)

[Mouret13] G. Mouret, M. Guinet, A. Cuisset, L. Croize, S. Eliet, R. Bocquet, and F. Hindle. "Versatile Sub-THz Spectrometer for Trace Gas Analysis". *IEEE Sens. J.* **13** (2013), pp. 133–138. (↑ p. 18)

[Murakami03] A. Murakami. "Phase Locking and Chaos Synchronization in Injection-Locked Semiconductor Lasers". *IEEE J. Quantum Electron.* **39** (2003), pp. 438–447. (↑ p. 34)

[Naderi09] N. Naderi, M. Pochet, F. Grillot, N. Terry, V. Kovanis, and L. Lester. "Modeling the Injection-Locked Behavior of a Quantum Dash Semiconductor Laser". *IEEE J. Sel. Top. Quantum Electron.* **15** (2009), pp. 563–571. (↑ p. 30)

[Nathan62] M. I. Nathan, W. P. Dumke, G. Burns, F. H. Dill, and G. Lasher. "Stimulated Emission of Radiation from GaAs P-n Junctions". *Appl. Phys. Lett.* **1** (1962), pp. 62–64. (↑ p. 17)

[Nerin97] P. Nerin, P. Puget, P. Besesty, and G. Chartier. "Self-Mixing Using a Dual-Polarisation Nd:YAG Microchip Laser". *Electron. Lett.* **33** (1997), p. 491. (↑ p. 46)

[Newell99] T. C. Newell and K. J. Malloy. "Gain and Linewidth Enhancement Factor in InAs Quantum-Dot Laser Diodes". **11** (1999), pp. 1527–1529. (↑ pp. 30, 109)

[Nizette04a] M. Nizette and T. Erneux. "Stability of Injection-Locked CW-Emitting External-Cavity Semiconductor Lasers". *IEEE J. Sel. Top. Quantum Electron.* **10** (2004), pp. 961–967. (↑ p. 39)

[Nizette04b] M. Nizette and T. Erneux. "Bifurcations of Injection-Locked Semiconductor Lasers Subject to Optical Feedback". *Proceedings of SPIE*. **5452**. 2004, pp. 105–116. (↑ p. 39)

[Osinski87] M. Osinski and J. Buus. "Linewidth Broadening Factor in Semiconductor Lasers–An Overview". *IEEE J. Quantum Electron.* **23** (1987), pp. 9–29. (↑ pp. 30, 109)

[Ōtsubo17] J. Ōtsubo. *Semiconductor Lasers: Stability, Instability and Chaos*. Fourth edition. Springer series in optical sciences. OCLC: 990041689. Cham: Springer, 2017. (↑ p. 22)

[Otsuka92] K. Otsuka, P. Mandel, S. Bielawski, D. Derozier, and P. Glorieux. "Alternate Time Scale in Multimode Lasers". *Phys. Rev. A* **46** (1992), pp. 1692–1695. (↑ p. 56)

[Pal10] V. Pal et al. "Measurement of the Coupling Constant in a Two-Frequency VECSEL". *Opt. Express* **18** (2010), p. 5008. (↑ p. 56)

[Pantell65] R. Pantell. "The Laser Oscillator with an External Signal". *Proc. IEEE* **53** (1965), pp. 474–477. (↑ p. 32)

[Paquet16] R. Paquet, S. Blin, M. Myara, L. L. Gratiet, M. Sellahi, B. Chomet, G. Beaudoin, I. Sagnes, and A. Garnache. "Coherent Continuous-Wave Dual-Frequency High-Q External-Cavity Semiconductor Laser for GHz–THz Applications". *Opt. Lett.* **41** (2016), p. 3751. (↑ p. 44)

[Pedaci10] F. Pedaci, Z. Huang, M. van Oene, S. Barland, and N. H. Dekker. "Excitable Particles in an Optical Torque Wrench". *Nature Physics* **7** (2010), p. 259. (↑ p. 74)

[Pelusi97] M. D. Pelusi, H. F. Liu, D. Novak, and Y. Ogawa. "THz Optical Beat Frequency Generation from a Single Mode Locked Semiconductor Laser". *Appl. Phys. Lett.* **71** (1997), pp. 449–451. (↑ p. 45)

[Peng15] H. Peng, C. Zhang, X. Xie, T. Sun, P. Guo, X. Zhu, L. Zhu, W. Hu, and Z. Chen. "Tunable DC-60 GHz RF Generation Utilizing a Dual-Loop Optoelectronic Oscillator Based on Stimulated Brillouin Scattering". *J. Light. Technol.* **33** (2015), pp. 2707–2715. (↑ p. 136)

[Petermann88] K. Petermann. *Laser Diode Modulation and Noise*. **3**. Springer Science & Business Media, 1988. (↑ p. 22)

[Pickwell06] E. Pickwell and V. P. Wallace. "Biomedical Applications of Terahertz Technology". *J. Phys. Appl. Phys.* **39** (2006), R301–R310. (↑ p. 18)

[Pikovsky97] A. S. Pikovsky, M. G. Rosenblum, and J. Kurths. "Phase Synchronization in Driven and Coupled Chaotic Oscillators". *IEEE Trans. Circuits Syst. Fundam. Theory Appl.* **44** (1997), pp. 874–881. (↑ p. 34)

[Pillet08] G. Pillet, L. Morvan, M. Brunel, F. Bretenaker, D. Dolfi, M. Vallet, J.-P. Huignard, and A. Le Floch. "Dual-Frequency Laser at 1.5 μ m for Optical Distribution and Generation of High-Purity Microwave Signals". *J. Light. Technol.* **26** (2008), pp. 2764–2773. (↑ pp. 19, 44)

[Pillet14] G. Pillet, L. Morvan, L. Ménager, A. Garcia, S. Babiel, and A. Stöhr. "Dual-Frequency Laser Phase Locked at 100 GHz". *J. Light. Technol.* **32** (2014), pp. 3824–3830. (↑ p. 44)

[Prieto09] G. Prieto, R. Parker, and F. Vernon III. "A Fortran 90 Library for Multitaper Spectrum Analysis". *Comput. Geosci.* **35** (2009), pp. 1701–1710. (↑ pp. 41, 68)

[Primiani15] P. Primiani and F. van Dijk. "Étude préliminaire d'un oscillateur opto-électronique ultra compact utilisant des circuits photoniques intégrés". *Journées Nationales d'Optique Guidée (JNOG 2015)*. Rennes, France, 2015. (↑ p. 157)

[Primiani16] P. Primiani, F. van Dijk, M. Lamponi, M. Chtioui, M. Vallet, M. Romanelli, and M. Alouini. "Tunable Optoelectronic Oscillator Based on an Integrated Heterodyne Source". *Microwave Photonics (MWP), 2016 IEEE International Topical Meeting On*. IEEE, 2016, pp. 251–254. (↑ pp. 151, 152)

[Prokhorov58] A. Prokhorov. "Molecular Amplifier and Generator for Submillimeter Waves". *Essentials of Lasers*. Elsevier, 1958, pp. 85–87. (↑ p. 17)

[Provost11] J.-G. Provost and F. Grillot. "Measuring the Chirp and the Linewidth Enhancement Factor of Optoelectronic Devices with a Mach-Zehnder Interferometer". *IEEE Photonics J.* **3** (2011), pp. 476–488. (↑ p. 31)

[Quinlan11] F. Quinlan, T. M. Fortier, M. S. Kirchner, J. A. Taylor, M. J. Thorpe, N. Lemke, A. D. Ludlow, Y. Jiang, and S. A. Diddams. "Ultralow Phase Noise Microwave Generation with an Er: Fiber-Based Optical Frequency Divider". *Opt. Lett.* **36** (2011), pp. 3260–3262. (↑ p. 94)

[Radziunas07] M. Radziunas, A. Glitzky, U. Bandelow, M. Wolfrum, U. Troppenz, J. Kreissl, and W. Rehbein. "Improving the Modulation Bandwidth in Semiconductor Lasers by Passive Feedback". *IEEE J. Sel. Top. Quantum Electron.* **13** (2007), pp. 136–142. (↑ p. 36)

[Rogister01] F. Rogister, A. Locquet, D. Pieroux, M. Sciamanna, O. Deparis, P. Mégret, and M. Blondel. "Secure Communication Scheme Using Chaotic Laser Diodes Subject to Incoherent Optical Feedback and Incoherent Optical Injection". *Opt. Lett.* **26** (2001), pp. 1486–1488. (↑ p. 36)

[Rohde14] U. L. Rohde, A. K. Poddar, and D. Calbaza. "Searching For Low-Phase-Noise Synthesizers". *Microwaves & Radio Frequency* (2014), pp. 74–80. (↑ pp. 18, 41)

[Rolland11a] A. Rolland, M. Brunel, G. Loas, L. Frein, M. Vallet, and M. Alouini. "Beat Note Stabilization of a 10–60 GHz Dual-Polarization Micro-laser through Optical down Conversion". *Opt. Express* **19** (2011), p. 4399. (↑ p. 19)

[Rolland11b] A. Rolland, G. Loas, M. Brunel, L. Frein, M. Vallet, and M. Alouini. "Non-Linear Optoelectronic Phase-Locked Loop for Stabilization of Opto-Millimeter Waves: Towards a Narrow Linewidth Tunable THz Source". *Opt. Express* **19** (2011), p. 17944. (↑ p. 19)

[Rolland14] A. Rolland et al. "Narrow Linewidth Tunable Terahertz Radiation By Photomixing Without Servo-Locking". *IEEE Trans. Terahertz Sci. Technol.* **4** (2014), pp. 260–266. (↑ pp. 18, 45, 94)

[Romanelli14] M. Romanelli, L. Wang, M. Brunel, and M. Vallet. "Measuring the Universal Synchronization Properties of Driven Oscillators across a Hopf Instability". *Opt. Express* **22** (2014), pp. 7364–7373. (↑ pp. 47, 58, 61, 68)

[Romanelli16] M. Romanelli, A. Thorette, M. Brunel, T. Erneux, and M. Vallet. "Excitable-like Chaotic Pulses in the Bounded-Phase Regime of an Opto-Rf Oscillator". *Phys. Rev. A* **94** (2016), p. 043820. (↑ pp. 58, 75, 173)

[Rønnekleiv01] E. Rønnekleiv. "Frequency and Intensity Noise of Single Frequency Fiber Bragg Grating Lasers". *Opt. Fiber Technol.* **7** (2001), pp. 206–235. (↑ p. 92)

[RotaRodrigo14] S. Rota-Rodrigo, L. Rodriguez-Cobo, M. A. Quintela, J. M. Lopez-Higuera, and M. Lopez-Amo. "Dual-Wavelength Single-Longitudinal Mode Fiber Laser Using Phase-Shift Bragg Gratings". *IEEE J. Sel. Top. Quantum Electron.* **20** (2014), pp. 161–165. (↑ p. 45)

[Royset94] A. Royset, L. Bjerkan, D. Myhre, and L. Hafskjaer. "Use of Dispersive Optical Fibre for Characterisation of Chirp in Semiconductor Lasers". *Electron. Lett.* **30** (1994), pp. 710–712. (↑ p. 31)

[Rubiola08] E. Rubiola. *Phase Noise and Frequency Stability in Oscillators*. Cambridge: Cambridge University Press, 2008. (↑ pp. 40, 137)

[Salomon88] C. Salomon, D. Hils, and J. L. Hall. "Laser Stabilization at the Millihertz Level". *J. Opt. Soc. Am. B* **5** (1988), p. 1576. (↑ p. 18)

[Sanborn03] J. Z. Sanborn, C. Hellings, and T. D. Donnelly. "Breakdown of the Slowly-Varying-Amplitude Approximation: Generation of Backward-Traveling, Second-Harmonic Light". *J. Opt. Soc. Am. B* **20** (2003), pp. 152–157. (↑ p. 24)

[Sargent74] M. Sargent, M. O. Scully, and W. E. Lamb. *Laser Physics*. Reading, Mass: Addison-Wesley Pub. Co., Advanced Book Program, 1974. (↑ pp. 23, 27, 32, 55)

[Sasada88] H. Sasada. "1.5 *M*m DFB Semiconductor Laser Spectroscopy of HCN". *J. Chem. Phys.* **88** (1988), pp. 767–777. (↑ p. 95)

[Scalise04] L. Scalise, Y. Yu, G. Giuliani, G. Plantier, and T. Bosch. "Self-Mixing Laser Diode Velocimetry: Application to Vibration and Velocity Measurement". *IEEE Trans. Instrum. Meas.* **53** (2004), pp. 223–232. (↑ p. 36)

[Schawlow58] A. L. Schawlow and C. H. Townes. "Infrared and Optical Masers". *Phys. Rev.* **112** (1958), pp. 1940–1949. (↑ pp. 17, 22, 27, 29, 101)

[Schwartz09] S. Schwartz, G. Feugnet, M. Rebut, F. Bretenaker, and J.-P. Pocholle. "Orientation of Nd 3 + Dipoles in Yttrium Aluminum Garnet: Experiment and Model". *Phys. Rev. A* **79** (2009). (↑ pp. 52, 57, 165, 166, 167)

[Sciamanna15] M. Sciamanna and K. A. Shore. "Physics and Applications of Laser Diode Chaos". *Nat. Photonics* **9** (2015), pp. 151–162. (↑ pp. 19, 34)

[Shampine01] L. Shampine and S. Thompson. "Solving DDEs in Matlab". *Appl. Numer. Math.* **37** (2001), pp. 441–458. (↑ p. 171)

[Siegman86] A. E. Siegman. *Lasers*. OCLC: 14525287. Mill Valley, California: University Science Books, 1986. (↑ pp. 28, 48, 112)

[Simpson97] T. B. Simpson, J. M. Liu, K. F. Huang, and K. Tai. "Nonlinear Dynamics Induced by External Optical Injection in Semiconductor Lasers". **9** (1997), pp. 765–784. (↑ p. 34)

[Skokos10] C. Skokos. "The Lyapunov Characteristic Exponents and Their Computation". *Dynamics of Small Solar System Bodies and Exoplanets*. Ed. by J. J. Souchay and R. Dvorak. **790**. Berlin, Heidelberg: Springer Berlin Heidelberg, 2010, pp. 63–135. (↑ p. 63)

[Smith97] G. H. Smith, D. Novak, and Z. Ahmed. "Overcoming Chromatic-Dispersion Effects in Fiber-Wireless Systems Incorporating External Modulators". *IEEE Trans. Microw. Theory Tech.* **45** (1997), pp. 1410–1415. (↑ p. 138)

[Song15] J. Song, Z.-Q. Zhong, L.-X. Wei, Z.-M. Wu, and G.-Q. Xia. "Experimental Investigations on Nonlinear Dynamics of a Semiconductor Laser Subject to Optical Injection and Fiber Bragg Grating Feedback". *Opt. Commun.* **354** (2015), pp. 213–217. (↑ p. 39)

[Sprott94] J. C. Sprott. "Some Simple Chaotic Flows". *Phys. Rev. E* **50** (1994), pp. 647–650. (↑ p. 63)

[Statz60] H. Statz and G. DeMars. "Transients and Oscillation Pulses in Masers". *Quantum Electronics*. New York, NY: Columbia University Press, 1960, pp. 530–537. (↑ p. 27)

[Stover66] H. L. Stover and W. H. Steier. "Locking of Laser Oscillators by Light Injection". *Appl. Phys. Lett.* **8** (1966), pp. 91–93. (↑ p. 32)

[Strogatz01] S. H. Strogatz. *Nonlinear Dynamics and Chaos: With Applications to Physics, Biology, Chemistry, and Engineering*. 2. print. Studies in Nonlinearity. OCLC: 248691524. Cambridge, Mass: Perseus Books, 2001. (↑ p. 59)

[Svelto10] O. Svelto. *Principles of Lasers*. 5. ed. OCLC: 699877195. New York, NY: Springer, 2010. (↑ p. 21)

[Szwaj04] C. Szwaj, E. Lacot, and O. Hugon. "Large Linewidth-Enhancement Factor in a Microchip Laser". *Phys. Rev. A* **70** (2004). (↑ pp. 31, 78)

[Takano89] S. Takano, T. Sasaki, H. Yamada, M. Kitamura, and I. Mito. "Sub-MHz Spectral Linewidth in 1.5μm Separate-Confinementheterostructure (SCH) Quantum-Well DFB LDs". *Electron. Lett.* **25** (1989), p. 356. (↑ p. 102)

[Tan07] Y. Tan and S. Zhang. "Self-Mixing Interference Effects of Microchip Nd:YAG Laser with a Wave Plate in the External Cavity". *Appl. Opt.* **46** (2007), p. 6064. (↑ p. 46)

[Tartwijk95] G. H. M. van Tartwijk and D. Lenstra. "Semiconductor Lasers with Optical Injection and Feedback". *Quantum Semiclassical Opt. J. Eur. Opt. Soc. Part B* **7** (1995), pp. 87–143. (↑ p. 22)

[Thévenin11a] J. Thévenin, M. Romanelli, M. Vallet, M. Brunel, and T. Erneux. "Resonance Assisted Synchronization of Coupled Oscillators: Frequency Locking without Phase Locking". *Phys. Rev. Lett.* **107** (2011), p. 104101. (↑ pp. 46, 60, 61)

[Thévenin11b] J. Thévenin, M. Vallet, M. Brunel, H. Gilles, and S. Girard. "Beat-Note Locking in Dual-Polarization Lasers Submitted to Frequency-Shifted Optical Feedback". *JOSA B* **28** (2011), pp. 1104–1110. (↑ p. 58)

[Thévenin12a] J. Thévenin, M. Romanelli, M. Vallet, M. Brunel, and T. Erneux. "Phase and Intensity Dynamics of a Two-Frequency Laser Submitted to Resonant Frequency-Shifted Feedback". *Phys. Rev. A* **86** (2012). (↑ pp. 58, 62)

[Thévenin12b] J. Thévenin, M. Vallet, and M. Brunel. "Dual-Polarization Mode-Locked Nd:YAG Laser". *Opt. Lett.* **37** (2012), p. 2859. (↑ p. 156)

[Thévenin12c] J. Thévenin. "Accrochages de Fréquences Dans Les Lasers Vectoriels à État Solide: Étude Du Verrouillage de Modes Passif et de La Réinjection Décalée En Fréquence". PhD thesis. Université Rennes 1, 2012. (↑ pp. 19, 45, 52, 58, 79)

[Thomson82] D. Thomson. "Spectrum Estimation and Harmonic Analysis". *Proc. IEEE* **70** (1982), pp. 1055–1096. (↑ p. 41)

[Thorette16] A. Thorette, M. Romanelli, M. Brunel, and M. Vallet. "Frequency-Locked Chaotic Opto-RF Oscillator". *Opt. Lett.* **41** (2016), pp. 2839–2842. (↑ pp. 58, 65, 173)

[Thorette17] A. Thorette, M. Romanelli, and M. Vallet. "Linewidth Enhancement Factor Measurement Based on FM-Modulated Optical Injection: Application to Rare-Earth-Doped Active Medium". *Opt. Lett.* **42** (2017), pp. 1480–1483. (↑ pp. 82, 173)

[Thorette18] A. Thorette, M. Romanelli, S. Bouhier, F. Van Dijk, M. Vallet, and M. Alouini. "Hybrid Opto-Electronic Oscillator for Single-Sideband Microwave Photonics". *Electron. Lett.* **54** (2018), pp. 706–708. (↑ pp. 148, 173)

[Thorette19] A. Thorette, M. Romanelli, and M. Vallet. "Synchronization of Two DFB Lasers Using Frequency-Shifted Feedback for Microwave Photonics". *IEEE J. Quantum Electron.* **accepted** (2019). (↑ pp. 110, 173)

[Tkach86a] R. Tkach and A. Chraplyvy. "Phase Noise and Linewidth in an InGaAsP DFB Laser". *J. Light. Technol.* **4** (1986), pp. 1711–1716. (↑ p. 102)

[Tkach86b] R. Tkach and A. Chraplyvy. "Regimes of Feedback Effects in 1.5-*M*m Distributed Feedback Lasers". *J. Light. Technol.* **4** (1986), pp. 1655–1661. (↑ p. 36)

[Toffano92] Z. Toffano, A. Destrez, C. Birocheau, and L. Hassine. "New Linewidth Enhancement Determination Method in Semiconductor Lasers Based on Spectrum Analysis above and below Threshold". *Electron. Lett.* **28** (1992), pp. 9–11. (↑ p. 31)

[Tonouchi07] M. Tonouchi. "Cutting-Edge Terahertz Technology". *Nature Photonics* **1** (2007), p. 97. (↑ p. 18)

[Tredicce85] J. R. Tredicce, F. T. Arecchi, G. L. Lippi, and G. P. Puccioni. "Instabilities in Lasers with an Injected Signal". *J. Opt. Soc. Am. B* **2** (1985), p. 173. (↑ pp. 19, 33)

[Turconi13] M. Turconi, B. Garbin, M. Feyereisen, M. Giudici, and S. Barland. "Control of Excitable Pulses in an Injection-Locked Semiconductor Laser". *Phys. Rev. E* **88** (2013). (↑ p. 74)

[Uchida08] A. Uchida et al. "Fast Physical Random Bit Generation with Chaotic Semiconductor Lasers". *Nature Photonics* **2** (2008), p. 728. (↑ p. 36)

[Udem02] T. Udem, R. Holzwarth, and T. W. Hänsch. "Optical Frequency Metrology". *Nature* **416** (2002), p. 233. (↑ p. 17)

[Vahed11] H. Vahed, R. Kheradmand, H. Tajalli, G. Tissoni, L. A. Lugiato, and F. Prati. "Phase-Mediated Long-Range Interactions of Cavity Solitons in a Semiconductor Laser with a Saturable Absorber". *Phys. Rev. A* **84** (2011). (↑ p. 61)

[Vallet13] M. Vallet, J. Barreaux, M. Romanelli, G. Pillet, J. Thévenin, L. Wang, and M. Brunel. "Lidar–Radar Velocimetry Using a Pulse-to-Pulse Coherent Rf-Modulated Q-Switched Laser". *Appl. Opt.* **52** (2013), pp. 5402–5410. (↑ p. 45)

[Vallet16] M. Vallet, M. Romanelli, G. Loas, F. van Dijk, and M. Alouini. "Self-Stabilized Optoelectronic Oscillator Using Frequency-Shifted Feedback and a Delay Line". *IEEE Photonics Technol. Lett.* **28** (2016), pp. 1088–1090. (↑ p. 140)

[Valling05] S. Valling, T. Fordell, and Å. M. Lindberg. "Maps of the Dynamics of an Optically Injected Solid-State Laser". *Phys. Rev. A* **72** (2005). (↑ p. 78)

[van der Pol27] B. van der Pol. "VII. Forced Oscillations in a Circuit with Non-Linear Resistance. (Reception with Reactive Triode)". *Lond. Edinb. Dublin Philos. Mag. J. Sci.* **3** (1927), pp. 65–80. (↑ p. 32)

[van Dijk11] F. van Dijk, A. Accard, A. Enard, O. Drisse, D. Make, and F. Lelarge. "Monolithic Dual Wavelength DFB Lasers for Narrow Linewidth Heterodyne Beat-Note Generation". *Microwave Photonics, 2011 International Topical Meeting on & Microwave Photonics Conference, 2011 Asia-Pacific, MWP/APMP*. IEEE, 2011, pp. 73–76. (↑ pp. 97, 100)

[van Dijk14] F. van Dijk et al. "Integrated InP Heterodyne Millimeter Wave Transmitter". *IEEE Photonics Technol. Lett.* **26** (2014), pp. 965–968. (↑ pp. 99, 151)

[Verdeyen95] J. T. Verdeyen. *Laser Electronics*. 3rd ed. Prentice Hall series in solid state physical electronics. Englewood Cliffs, N.J: Prentice Hall, 1995. (↑ p. 21)

[Verschaffelt08] G. Verschaffelt, G. Van der Sande, J. Danckaert, B. Ségard, P. Glorieux, and T. Erneux. "Delayed Polarization Dynamics in Nd 3 + -Doped Yttrium-Aluminum-Garnet Lasers". *Phys. Rev. A* **77** (2008). (↑ p. 57)

[Villafranca07] A. Villafranca et al. "Linewidth Enhancement Factor of Semiconductor Lasers: Results from Round-Robin Measurements in COST 288". IEEE, 2007, pp. 1–2. (↑ pp. 32, 89)

[Wake95] D. Wake, C. Lima, and P. Davies. "Optical Generation of Millimeter-Wave Signals for Fiber-Radio Systems Using a Dual-Mode DFB Semiconductor Laser". *IEEE Trans. Microw. Theory Tech.* **43** (Sept./1995), pp. 2270–2276. (↑ p. 43)

[Wang01] R. Wang, A. Stintz, P. Varangis, T. Newell, H. Li, K. Malloy, and L. Lester. "Room-Temperature Operation of InAs Quantum-Dash Lasers on InP [001]". *IEEE Photonics Technol. Lett.* **13** (2001), pp. 767–769. (↑ p. 96)

[Wang94] W. Wang, K. Grattan, A. Palmer, and W. Boyle. "Self-Mixing Interference inside a Single-Mode Diode Laser for Optical Sensing Applications". *J. Light. Technol.* **12** (Sept./1994), pp. 1577–1587. (↑ p. 36)

[Westbrook87] L. Westbrook and M. Adams. "Simple Expressions for the Linewidth Enhancement Factor in Direct-Gap Semiconductors". *IEE Proc. J Optoelectron.* **134** (1987), p. 209. (↑ p. 30)

[Wieczorek05] S. Wieczorek, B. Krauskopf, T. Simpson, and D. Lenstra. "The Dynamical Complexity of Optically Injected Semiconductor Lasers". *Phys. Rep.* **416** (2005), pp. 1–128. (↑ pp. 34, 35, 55, 124)

[Wünsche05] H.-J. Wünsche et al. "Synchronization of Delay-Coupled Oscillators: A Study of Semiconductor Lasers". *Phys. Rev. Lett.* **94** (2005). (↑ p. 115)

[Xie13] X. Xie, C. Zhang, T. Sun, P. Guo, X. Zhu, L. Zhu, W. Hu, and Z. Chen. "Wideband Tunable Optoelectronic Oscillator Based on a Phase Modulator and a Tunable Optical Filter". *Opt. Lett.* **38** (2013), p. 655. (↑ p. 136)

[Xu14] K. Xu, R. Wang, Y. Dai, F. Yin, J. Li, Y. Ji, and J. Lin. "Microwave Photonics: Radio-over-Fiber Links, Systems, and Applications [Invited]". *Photonics Res.* **2** (2014), B54. (↑ p. 18)

[Yanchuk17] S. Yanchuk and G. Giacomelli. "Spatio-Temporal Phenomena in Complex Systems with Time Delays". *J. Phys. Math. Theor.* **50** (2017), p. 103001. (↑ p. 157)

[Yang07] J. Yang, Y. Jin-Long, W. Yao-Tian, Z. Li-Tai, and Y. En-Ze. "An Optical Domain Combined Dual-Loop Optoelectronic Oscillator". *IEEE Photonics Technol. Lett.* **19** (2007), pp. 807–809. (↑ p. 143)

[Yao09] J. Yao. "Microwave Photonics". *J. Light. Technol.* **27** (2009), pp. 314–335. (↑ p. 18)

[Yao96] X. S. Yao and L. Maleki. "Optoelectronic Microwave Oscillator". *J. Opt. Soc. Am. B* **13** (1996), pp. 1725–1735. (↑ pp. 135, 149)

[Yao98] X. S. Yao, L. Maleki, Y. Ji, G. Lutes, and M. Tu. "Dual-Loop Opto-Electronic Oscillator". *Frequency Control Symposium, 1998. Proceedings of the 1998 IEEE International*. IEEE, 1998, pp. 545–549. (↑ p. 143)

[Yu04] Y. Yu, G. Giuliani, and S. Donati. "Measurement of the Linewidth Enhancement Factor of Semiconductor Lasers Based on the Optical Feedback Self-Mixing Effect". *IEEE Photonics Technol. Lett.* **16** (2004), pp. 990–992. (↑ p. 31)

[Zeghlache95a] H. Zeghlache and A. Boulnois. "Polarization Instability in Lasers. I. Model and Steady States of Neodymium-Doped Fiber Lasers". *Phys. Rev. A* **52** (1995), p. 4229. (↑ p. 52)

[Zeghlache95b] H. Zeghlache and A. Boulnois. "Polarization Instability in Lasers. II: Influence of the Pump Polarization on the Dynamics". *Phys. Rev. A* **52** (1995), p. 4243. (↑ p. 57)

[Zhang15] L. Zhang, A. K. Poddar, U. L. Rohde, and A. S. Daryoush. "Self-ILPLL Using Optical Feedback for Phase Noise Reduction in Microwave Oscillators". *IEEE Photonics Technol. Lett.* **27** (2015), pp. 624–627. (↑ p. 141)

[Zhou05] W. Zhou and G. Blasche. "Injection-Locked Dual Opto-Electronic Oscillator with Ultra-Low Phase Noise and Ultra-Low Spurious Level". *IEEE Trans. Microw. Theory Tech.* **53** (2005), pp. 929–933. (↑ p. 143)

[Zhuang13] J.-P. Zhuang and S.-C. Chan. “Tunable Photonic Microwave Generation Using Optically Injected Semiconductor Laser Dynamics with Optical Feedback Stabilization”. *Opt. Lett.* **38** (2013), pp. 344–346. (↑ p. 34)

UNIVERSITE MATIERE BRETAGNE MOLECULES LOIRE ET MATERIAUX

UNIVERSITÉ DE RENNES 1

Title: Synchronization dynamics of dual-mode solid-state and semiconductor DFB lasers under frequency-shifted feedback.Applications to microwave photonics.

Keywords: laser dynamics, microwave photonics, injection-locking, synchronization

Abstract: The control of the frequency difference between two lasers is a cross-cutting challenge in many fields of photonics, either for the heterodyne generation of high-purity microwave beatnotes, or in metrology and telecom experiments. The comprehension of laser dynamics under various couplings has allowed to develop stabilization methods based on optical injection. In this work we study theoretically and experimentally a mechanism called *frequency-shifted feedback*, which allows to precisely lock the frequency difference between two lasers.

First, it is applied to a dual-frequency dual-polarization solid-state Nd:YAG laser, in order to lock the phases of its two orthogonal polarization modes. A model of rate equations is used to precisely describe the experiment, and allows to highlight partial "bounded phase" synchronization regimes. Furthermore, we show that in some cases this synchronization can subsist even with chaotic oscillations of the intensity and phase. The behavior is studied for varying values of the frequency detuning, injection rate, possible injection delay, and mode coupling in the active medium. We find that the a non-zero phase-amplitude coupling (linewidth enhancement factor) is needed in the model to account for experimental observation. This leads to the use of an ad-hoc technique to measure the low value of this usually neglected factor.

We then turn to a custom semiconductor component embedding two DFB lasers. In spite of a more complex coupling scheme and the large effective delays into play, phase locking of the two lasers is possible. Locking bands appear when the detuning changes, and this behavior can be replicated using a numerical model. This model also permit to determine working conditions minimizing the influence of uncontrolled optical feedback phases.

Finally, we demonstrate that this system can be integrated in a resonant loop not unlike an opto-electronic oscillator (OEO), that outputs a self-referenced, single sideband microwave signal over an optical carrier, with encouraging phase noise performances.

Titre : Dynamiques de synchronisation de lasers bifréquence à état solide et DFB soumis à une réinjection décalée en fréquence.Applications en photonique micro-onde.

Mots-clés : dynamique des lasers, photonique micro-onde, verrouillage par injection, synchronisation

Résumé : Le contrôle de la différence de fréquence entre deux lasers est un défi transversal pour la photonique, que ce soit dans un but de génération hétérodyne d'un battement micro-onde de grande pureté, ou pour des expériences de métrologie ou télécom. L'avancée des connaissances sur la dynamique des lasers soumis à divers couplages a permis le développement de méthodes de stabilisation basées sur l'injection optique. Nous étudions ici théoriquement et expérimentalement un mécanisme de *réinjection décalée en fréquence*, qui permet de verrouiller la différence de fréquence entre deux lasers.

Il est d'abord appliqué à un laser à état solide bi-polarisation bi-fréquence Nd:YAG afin de verrouiller en phase ses deux modes de polarisation orthogonaux. Un modèle type «rate equations» en bonne adéquation avec les expériences permet de mettre en lumière un certain nombre de régimes de synchronisation partielle dits de phase bornée. De plus, nous montrons que cet état peut subsister en présence d'oscillations chaotiques de l'intensité et de la phase. Le comportement est étudié pour différentes valeurs du désaccord de fréquence, du taux d'injection, du retard éventuel, et du couplage inter-modes. Enfin, la nécessité d'inclure un couplage phase-amplitude (facteur de Henry non-nul) dans le modèle a mené au développement d'une méthode pour mesurer ce coefficient habituellement négligé.

Nous nous tournons ensuite vers un composant semiconducteur original contenant deux lasers DFB. Malgré une plus grande complexité du couplage et des retards effectifs importants, il reste possible de synchroniser en phase ces lasers. Des bandes d'accrochages liées au retard sont observées, et reproduites à l'aide d'un modèle numérique, qui permet aussi de déterminer les conditions minimisant l'influence de phases optiques non maîtrisées.

Enfin, ce système peut être intégré dans une boucle résonante de type oscillateur opto-électronique (OEO) produisant un signal micro-onde auto-référencé à bande latérale unique sur porteuse optique, avec des bruits de phase encourageants.